



**University of
Nottingham**

UK | CHINA | MALAYSIA

**Performance Enhancement of Organic Solar Cells via Device
Engineering and Their Future Potential Applications**

Billy Fanady, BEng. (Hons.)

Thesis submitted to the University of Nottingham for the

Degree of Doctor of Philosophy in Chemical Engineering

March 2021

Abstract

Renewable energy sources are promising long-term solution to solve the energy supply crisis due to the excessive use of non-renewable fossil fuels. One of the options is solar energy, which can be harvested directly from sunlight using photovoltaic (PV) technology. In recent years, organic solar cells (OSCs) as the building blocks of organic PV technology have emerged in the PV field, enabling the realization of environmental-friendly and low-cost PV technology. However, issues related to efficiency performance still posed a major setback to commercialization of OSCs. In view of this, this study is conducted to present comprehensive understandings on how OSCs' performance in terms of optical, electrical, morphological and mechanical properties can be improved through device engineering strategy (interface and electrode engineering strategy). In addition, the potential applications of OSCs achieved via device engineering strategy are also being explored. In summary, the studies conducted can be divided into three main parts.

The first part focuses on improving OSCs' performance through interface engineering strategy for the realization of high-performing OSCs. Interface engineering on sol-gel zinc oxide (ZnO) electron-transporting layer (ETL) was conducted by introducing additional oxadiazole-based electron-transporting material called 2-(4-tert-butylphenyl)-5-(4-biphenyl)-1,3,4-oxadiazole (**PBD**) between ZnO ETL and photoactive layer. The significance of incorporating PBD on ZnO was demonstrated by investigating the change in optical, electrical and morphological properties of pristine ZnO ETL. The findings shown that additional PBD layer could improve pristine ZnO film's

conductivity, create better energy level alignment with the photoactive layer, smoothen ZnO film's morphology and improve ZnO film's hydrophobicity. All those factors crucially influenced the charge extraction, transport and recombination processes in OSCs, which were conducive for the enhancement in photovoltaic performance of ZnO/PBD-based device. In fact, through interface engineering strategy, inverted OSCs based on poly[(2,6-(4,8-bis(5-(2-ethylhexyl)thiophen-2-yl)-benzo[1,2-b:4,5-b']dithiophene))-alt-(5,5-(1',3'-di-2-thienyl-5',7'-bis(2-ethylhexyl)benzo[1',2'-c:4',5'-c']dithiophene-4,8-dione)] (**PBDB-T donor**) and 3,9-bis(2-methylene-((3-(1,1-dicyanomethylene)-6/7-methyl)-indanone))-5,5,11,11-tetrakis(4-hexylphenyl)-dithieno[2,3-d:2',3'-d']-s-indaceno[1,2-b:5,6-b']dithiophene (**IT-M acceptor**) could demonstrate ~7% increment in the photovoltaic performance from 10.8% (ZnO-based device) to 11.6% (ZnO/PBD-based device).

The second part focuses on improving OSCs' performance through electrode engineering strategy for the realization of high-performing flexible OSCs. Electrode engineering on poly(3,4-ethylenedioxythiophene)-poly(styrenesulfonate) (**PEDOT:PSS**) electrode was conducted by utilizing polyhydroxy compound dopant and gentle acid post-treatment method, specifically xylitol dopant and methanesulfonic acid (MSA) treatment. The significance of xylitol dopant and MSA treatment on PEDOT:PSS electrode was demonstrated by investigating the change in optical, electrical, morphological and mechanical properties of pristine PEDOT:PSS electrode. The findings shown that both doping and acid treatment on PEDOT:PSS electrode could improve the optical transparency of electrode, enhance electrode's conductivity and modify electrode's morphology. In addition, such treatment could also

provide electrode a stronger adhesion ability with the substrate, which were effective for improving the mechanical stability of electrode against extreme mechanical deformation. All those factors promoted the realization of high-performing flexible OSCs based on PEDOT:PSS electrode. In fact, through electrode engineering strategy, conventional OSCs based on poly[(2,6-(4,8-bis(5-(2-ethylhexyl-3-fluoro)thiophen-2-yl)-benzo[1,2-b:4,5-b']dithiophene))-alt-(5,5-(1',3'-di-2-thienyl-5',7'-bis(2-ethylhexyl)benzo[1',2'-c:4',5'-c']dithiophene-4,8-dione)] (**PBDB-T-2F/PM6 donor**) and 2,2'-((2Z,2'Z)-((12,13-bis(2-ethylhexyl)-3,9-diundecyl-12,13-dihydro-[1,2,5]thiadiazolo[3,4-e]thieno[2'',3''':4',5']thieno[2',3':4,5]pyrrolo[3,2-g]thieno[2',3':4,5]thieno[3,2-b]indole-2,10-diyl)bis(methanylylidene))bis(5,6-difluoro-3-oxo-2,3-dihydro-1H-indene-2,1-diylidene))dimalononitrile (**BTP-4F/Y6 acceptor**) could demonstrate an excellent photovoltaic performance of 14.2% with remarkable mechanical robustness against bending and folding.

The last part focuses on the application of device engineering, specifically electrode engineering as a continuation of study from the previous part. The desirable mechanical and optical properties of the engineered PEDOT:PSS could make PEDOT:PSS a great candidate for usage in foldable-flexible semi-transparent OSCs (FST-OSCs). FST-OSCs were fabricated similarly using engineered PEDOT:PSS electrode and PBDB-T-2F:Y6 photoactive layer system. As a result, high-performing FST-OSCs with over 10% efficiency and 21% average visible light transmittance, as well as excellent mechanical stability were obtained. The potential of such FST-OSCs for greenhouse application was investigated by incorporating them as part of roofs in the simulated greenhouse. Comparisons between plants grown under direct

sunlight with FST-OSCs roof and those under direct sunlight yielded remarkably similar results in terms of branch sturdiness and hypertrophic leaves, proving the significance of electrode engineering strategy in realizing high-performing FST-OSCs for practical greenhouse applications.

Publications

- **Billy Fanady**, Wei Song, Ruixiang Peng, Tao Wu & Ziyi Ge. *Efficiency enhancement of organic solar cells enabled by interface engineering of sol-gel zinc oxide with an oxadiazole-based material*. *Organic Electronics*, 2020. 76: 105483.
- Wei Song†, **Billy Fanady**†, Ruixiang Peng, Ling Hong, Lirong Wu, Wenxia Zhang, Tingting Yan, Tao Wu, Sanhui Chen & Ziyi Ge. *Foldable semitransparent organic solar cells for photovoltaic and photosynthesis*. *Advanced Energy Materials*, 2020. 10(15): 2000136. (co-first author)
- Sanhui Chen, Tingting Yan, **Billy Fanady**, Wei Song, Jinfeng Ge, Qiang Wei, Ruixiang Peng, Guohui Chen, Yingping Zou & Ziyi Ge. *High efficiency ternary organic solar cells enabled by compatible dual-donor strategy with planar conjugated structures*. *Science China Chemistry*, 2020. 63(7): 917-923.
- Jing Gao, Jinfeng Ge, Ruixiang Peng, Chang Liu, Liang Cao, Danli Zhang, **Billy Fanady**, Ling Hong, Erjun Zhou & Ziyi Ge. *Over 14% efficiency nonfullerene all-small-molecule organic solar cells enabled by improving the ordering of molecular donors via side-chain engineering*. *Journal of Materials Chemistry A*, 2020. 8(15): 7405-7411.
- Wei Song, Ruixiang Peng, Like Huang, Chang Liu, **Billy Fanady**, Tao Lei, Ling Hong, Jinfeng Ge, Antonio Facchetti & Ziyi Ge. *Over 14% efficiency*

folding-flexible ITO-free organic solar cells enabled by eco-friendly acid-processed electrodes. iScience, 2020. 23(4): 100981.

- Jinfeng Ge, Lingchao Xie, Ruixiang Peng, **Billy Fanady**, Jiaming Huang, Wei Song, Tingting Yan, Wenxia Zhang & Ziyi Ge. *13.34% efficiency non-fullerene all-small-molecule organic solar cells enabled by modulating the crystallinity of donors via a fluorination strategy.* Angewandte Chemie International Edition, 2020. 59(7): 2808-2815.
- Tingting Yan, Jinfeng Ge, Tao Lei, Wenxia Zhang, Wei Song, **Billy Fanady**, Danli Zhang, Sanhui Chen, Ruixiang Peng & Ziyi Ge. *16.55% efficiency ternary organic solar cells enabled by incorporating a small molecular donor.* Journal of Materials Chemistry A, 2019. 7(45): 25894-25899.
- Lirong Wu, Lingchao Xie, Hanmin Tian, Ruixiang Peng, Jiaming Huang, **Billy Fanady**, Wei Song, Songting Tan, Wengang Bi & Ziyi Ge. *Efficient ternary organic solar cells based on a twin spiro-type non-fullerene acceptor.* Science Bulletin, 2019. 64(15): 1087-1094.
- Tao Lei, Wei Song, **Billy Fanady**, Tingting Yan, Lirong Wu, Wenxia Zhang, Lingchao Xie, Ling Hong & Ziyi Ge. *Facile synthesized benzo[1,2-b:4,5-b']difuran based copolymer for both fullerene and non-fullerene organic solar cells.* Polymer, 2019. 172: 391-397.
- Ruixiang Peng, Wei Song, Tingting Yan, **Billy Fanady**, Yanbo Li, Qingfeng Zhan & Ziyi Ge. *Interface bonding engineering of a transparent conductive electrode towards highly efficient and mechanically flexible ITO-free*

organic solar cells. Journal of Materials Chemistry A, 2019. 7(18): 11460-11467.

- Wei Song, Wang Li, Ruixiang Peng, **Billy Fanady**, Jiaming Huang, Wenqing Zhu, Lingchao Xie, Tao Lei & Ziyi Ge. *Efficient enhancement of electron transport and collection capability in PTB7:PC71BM-based solar cells enabled by sulforhodamine cathode interlayers*. Chemistry Asian Journal, 2019. 14(9): 1472-1476.
- Huiqin Cui, Wei Song, **Billy Fanady**, Ruixiang Peng, Jianfeng Zhang, Jiaming Huang & Ziyi Ge. *Flexible ITO-free organic solar cells over 10% by employing drop-coated conductive PEDOT:PSS transparent anodes*. Science China Chemistry, 2019. 62(4): 500-505.

Acknowledgements

First and foremost, I would like to express my sincere gratitude to both my research supervisors, Prof. Tao Wu from the University of Nottingham Ningbo China and Prof. Ziyi Ge from Chinese Academy of Sciences, for giving me a remarkable doctoral research experience and providing constructive guidance and funding support throughout my study. I wish to acknowledge the valuable advices provided by Dr. Mengxia Xu (University of Nottingham Ningbo China) as my second supervisor for this thesis. Prof. Edward Lester from the University of Nottingham as my third supervisor, also enthusiastically assisted me in any way he could during my doctoral research.

Many thanks to Prof. Xi Fan and Dr. Ruixiang Peng, as lead teachers in Chinese Academy of Sciences, who imparted extensive knowledge of organic photovoltaic device fabrication to me and willingly to go the extra mile to steer me through my research. I would like to convey my heartfelt appreciation to Dr. Haitao Zhao, who encouraged me to venture into this wonderful journey. Additionally, special shoutout to my colleague, Wei Song, for his great assistance at every stage of my PhD research. I would like to thank my other colleagues in Chinese Academy of Sciences, Huiqin Cui, Jiaming Huang, Lirong Wu, Wenxia Zhang, Tingting Yan, Sanhui Chen, Jinfeng Ge, Jing Gao, Liang Cao, Danli Zhang, Tao Lei, Lingchao Xie, and Yanbo Li, for a treasured time spent together as a research team and in social settings. Without their tremendous understanding and encouragement, it would be impossible for me to accomplish my doctoral research in Chinese Academy of Sciences with my imperfect Chinese language. Lastly, I am truly grateful to my partner, Alecia and my

family, for their unconditional love, unwavering support and belief in me. Their care and encouragement are my motivation to strive forward.

I would also like to give my full acknowledgement to the following funding bodies for sponsoring the research:

- National Key Research and Development Program of China (2017YFE0106000)
- National Natural Science Foundation of China (51773212, 21574144, 21674123 and 61705240)
- National Science Fund for Distinguished Young Scholars (21925506)
- Zhejiang Provincial Natural Science Foundation of China (LR16B040002)
- Ningbo Municipal Science and Technology Innovative Research Team (2015B11002 and 2016B10005)
- Chinese Academy of Sciences Key Project of Frontier Science Research (QYZDB-SSW-SYS030)
- Chinese Academy of Sciences Key Project of International Cooperation (174433KYSB20160065)
- Ningbo S&T Innovation 2025 Major Special Programme (2018B10055)
- Ningbo Institute of Materials Technology and Engineering, Chinese Academy of Sciences for providing partial scholarship, experimental equipment, materials and facilities
- University of Nottingham Ningbo China for providing full scholarship

Table of Contents

ABSTRACT	I
PUBLICATIONS	V
ACKNOWLEDGEMENTS	VIII
TABLE OF CONTENTS	X
LIST OF FIGURES	XV
LIST OF TABLES	XXI
LIST OF ABBREVIATIONS	XXV
LIST OF CHEMICAL NAMES	XXVII
CHAPTER 1. INTRODUCTION	1
1.1 BACKGROUND.....	1
1.2 OVERVIEW OF SOLAR CELLS.....	3
1.2.1 Development history of solar cells.....	3
1.2.2 Organic solar cells (OSCs).....	8
1.2.3 Key challenges in OSCs.....	9
1.3 AIM AND OBJECTIVES	12
1.4 OUTLINE OF THESIS.....	13
CHAPTER 2. LITERATURE REVIEW	15
2.1 OVERVIEW OF OSCS	15
2.2 DEVELOPMENT OF OSCS.....	17
2.3 OPERATING PRINCIPLES OF OSCS	18
2.3.1 Exciton generation	19
2.3.2 Exciton diffusion.....	20
2.3.3 Exciton dissociation.....	20

2.3.4	Generation of CTE and free charge carrier	21
2.3.5	Charge transport to electrodes.....	21
2.4	PHOTOACTIVE LAYER CONFIGURATIONS IN OSCs.....	22
2.4.1	Single-layered Schottky-junction configuration.....	23
2.4.2	Bilayer heterojunction configuration.....	24
2.4.3	BHJ configuration.....	26
2.5	STRUCTURES OF OSCs	28
2.6	FABRICATION OF OSCs	31
2.6.1	Preparation techniques	32
2.6.2	Deposition techniques.....	33
2.7	KEY PERFORMANCE PARAMETERS IN OSCs.....	36
2.7.1	Open circuit voltage (V_{oc}).....	36
2.7.2	Short circuit current (J_{sc}).....	38
2.7.3	Fill factor (FF).....	41
2.7.4	Series and shunt resistances	43
2.7.5	External quantum efficiency (EQE).....	44
2.7.6	Power conversion efficiency (PCE)	45
2.8	PERFORMANCE ENHANCEMENT STRATEGIES IN OSCs.....	46
2.8.1	Material design.....	49
2.8.2	Morphology control	52
2.8.3	Device engineering	56
2.9	SUMMARY	63
CHAPTER 3. METHODOLOGY		65
3.1	INTRODUCTION.....	65
3.2	MATERIALS	65
3.3	INSTRUMENTS.....	67

3.4 DEVICE FABRICATIONS	68
3.4.1 Fabrication procedures for interface engineering study	69
3.4.2 Fabrication procedures for electrode engineering study.....	72
3.4.3 Fabrication procedures for application of electrode engineering study	75
3.5 DEVICE CHARACTERIZATIONS.....	75
3.5.1 $J-V$ measurement.....	75
3.5.2 EQE measurement.....	76
3.5.3 X-ray photoelectron spectroscopy (XPS) and ultraviolet photoelectron spectroscopy (UPS) measurement	77
3.5.4 UV-visible (UV-vis) measurement	78
3.5.5 Energy dispersive x-ray spectroscopy (EDS) measurement.....	79
3.5.6 Transmission electron microscopy (TEM) measurement.....	80
3.5.7 Atomic force microscopy (AFM) measurement.....	81
3.5.8 Contact angle measurement	82
3.5.9 Surface thickness measurement.....	82
3.5.10 Adhesion force measurement.....	83
3.5.11 Square resistance (R_{sq}) measurement	84
3.5.12 Colour coordinates	85
3.5.13 Flexibility and mechanical stability measurement	85
3.5.14 Plants growth	86
3.5.15 WF calculation.....	86
3.5.16 Conductivity calculation (interfacial layer).....	87
3.5.17 Conductivity calculation (electrode)	87
3.5.18 Exciton dissociation efficiency calculation	88
3.5.19 Charge mobility calculation	88
3.5.20 Figure of merit (FoM) calculation.....	89

3.5.21 Average visible transmittance (AVT) calculation	89
--	----

CHAPTER 4. PERFORMANCE ENHANCEMENT VIA INTERFACE ENGINEERING STRATEGY 90

4.1 SUMMARY	90
4.2 INTRODUCTION.....	91
4.3 RESULTS AND DISCUSSIONS	94
4.3.1 Elemental states.....	94
4.3.2 Work function	97
4.3.3 Optical properties.....	98
4.3.4 Electrical properties	99
4.3.5 Morphological properties	100
4.3.6 Photovoltaic performances.....	103
4.4 CONCLUSION	112

CHAPTER 5. PERFORMANCE ENHANCEMENT VIA ELECTRODE ENGINEERING STRATEGY..... 113

5.1 SUMMARY	113
5.2 INTRODUCTION.....	114
5.3 RESULTS AND DISCUSSIONS	116
5.3.1 Preliminary doping selection.....	116
5.3.2 Bonding properties.....	118
5.3.3 Optical properties.....	120
5.3.4 Electrical properties	122
5.3.5 Morphological properties	123
5.3.6 Mechanical stability	128
5.3.7 Photovoltaic performances.....	130
5.4 CONCLUSION	135

CHAPTER 6. APPLICATION OF FLEXIBLE SEMI-TRANSPARENT OSCS ACHIEVED THROUGH ELECTRODE ENGINEERING STRATEGY	137
6.1 SUMMARY	137
6.2 INTRODUCTION	138
6.3 RESULTS AND DISCUSSIONS	140
6.3.1 FST-OSCs	140
6.3.2 Photovoltaic performances	141
6.3.3 Application of FST-OSCs	147
6.4 CONCLUSION	150
CHAPTER 7. CONCLUSION AND FUTURE WORK	152
7.1 CONCLUSION	152
7.1.1 Interface engineering strategy	152
7.1.2 Electrode engineering strategy	153
7.1.3 Application of electrode engineering strategy	154
7.2 FUTURE WORK	155
BIBLIOGRAPHY	160
APPENDIX A: SUPPORTING INFORMATION	189
APPENDIX B: OTHER EXPERIMENTAL WORK	194

List of Figures

Figure 1.1 Global consumption of energy (measured in billion tons of oil equivalent) categorized based on fuel sources from 1970 to 2019 and further prediction to 2040 (British Petroleum, 2019).	2
Figure 1.2 Development of solar cells over the years for different PV technologies (National Renewable Energy Laboratory, 2020).....	6
Figure 1.3 Solar spectrum under air mass 1.5 global (AM1.5G) irradiance (Chang et al., 2018).	10
Figure 2.1 Key processes in OSCs (Kang et al., 2016).....	19
Figure 2.2 (a) Thermally evaporated photoactive layer (<i>p</i> -type donor) being sandwiched between two metal electrodes, one with higher WF (gold, Au) and another with lower WF (aluminium, Al). (b) Schematic of energy level diagram in Schottky-junction OSCs, where Schottky contact was formed with length <i>W</i> near the Al contact (Hoppe and Sariciftci, 2004).	24
Figure 2.3 (a) Photoactive layer consisting of <i>n</i> -type acceptor and <i>p</i> -type donor, placed between two metal electrodes, one with higher WF (gold, Au) and another with lower WF (aluminium, Al). (b) Schematic of energy level diagram in bilayer heterojunction OSCs, where donor (D) contacts Au electrode and acceptor (A) contacts Al electrode (Hoppe and Sariciftci, 2004).....	26
Figure 2.4 (a) Photoactive blend layer consisting of <i>n</i> -type acceptor and <i>p</i> -type donor, positioned between two metal electrodes, one with higher WF (gold, Au) and another with lower WF (aluminium, Al). (b) Schematic of energy level diagram in BHJ OSCs, where donor (D) contacts Au electrode and acceptor (A) contacts Al electrode (Hoppe and Sariciftci, 2004).	27

Figure 2.5 General structures of (a) conventional and (b) inverted OSCs (McAfee et al., 2015). Schematic of energy level diagram for (c) conventional OSCs and (d) inverted OSCs, where it shows electron's and hole's movements upon illumination (McAfee et al., 2015).	31
Figure 2.6 Illustration of spin coating process (Krebs, 2009).	35
Figure 2.7 Schematic of energy level diagram of BHJ OSCs (omitting interfacial layer, such as HTL and ETL) (Brebels et al., 2017).	37
Figure 2.8 The relationship of electron transfer, V_{oc} and J_{sc} to PCE (Schlenker and Thompson, 2011).	41
Figure 2.9 Typical current density vs voltage ($J-V$) curve in OSCs under illumination.	42
Figure 2.10 Typical molecular structure of organic materials, composed of backbone, side chain and substituent components (Zhou et al., 2012).	50
Figure 3.1 Shadow mask used for the deposition of MoO_3 and Ag.	72
Figure 3.2 Shadow mask used for the deposition of Al.	74
Figure 3.3 AM1.5G solar simulator (<i>left</i>) and digital source-measure meter (<i>right</i>).	76
Figure 3.4 Quantum efficiency measurement system.	77
Figure 3.5 XPS/UPS spectrometer.	78
Figure 3.6 UV-vis spectrophotometer.	79
Figure 3.7 EDS spectrometer.	80
Figure 3.8 TEM microscopy.	81

Figure 3.9 AFM microscopy.....	81
Figure 3.10 Contact angle measurement system.....	82
Figure 3.11 Surface profiler.....	83
Figure 3.12 Adhesion force measurement system.	84
Figure 3.13 4-Point probes measurement system.....	84
Figure 3.14 CIE1931 chromaticity coordinate program.	85
Figure 4.1 (a) Chemical structures of PBD electron-transporting materials. (b) XPS survey spectra of ZnO and ZnO/PBD on glass/ITO substrates; inset shows the enlarged N 1s spectra. The deconvoluted high-resolution (c) N 1s and (d) C 1s peaks of ZnO/PBD deposited on glass/ITO substrates.	95
Figure 4.2 High-resolution (a) Zn 2p and (b) O 1s peaks of ZnO and ZnO/PBD deposited on glass/ITO substrates.	96
Figure 4.3 UPS spectra of ZnO- and ZnO/PBD- modified ITO cathodes as compared to bare ITO cathode.	97
Figure 4.4 Transmittance spectra of ZnO and ZnO/PBD deposited on glass/ITO substrates as compared to bare glass/ITO.	98
Figure 4.5 Electrical conductivity of ZnO and ZnO/PBD interlayer.	100
Figure 4.6 AFM (5×5 μm) height and phase images of (a, d) ZnO, (b, e) ZnO/PBD and (c, f) ZnO/PBD/CB deposited on glass/ITO substrates.....	101

Figure 4.7 (a) XPS survey spectra of ZnO/PBD and ZnO/PBD/CB on glass/ITO substrates; inset shows the enlarged N 1s spectra. (b) High-resolution N 1s peak of ZnO/PBD/CB deposited on glass/ITO substrates.	102
Figure 4.8 Contact angle images when deionized water was dripped onto the (a) ITO/ZnO and (b) ITO/ZnO/PBD substrates.	103
Figure 4.9 (a) Device structure of inverted OSCs with ZnO/PBD ETL; inset shows the chemical structures of PBDB-T donor and IT-M acceptor. (b) Energy levels of materials used in the OSCs. (c) $J-V$ characteristics under standard AM1.5G illumination with 100 mW cm^{-2} light intensity, (d) EQE spectra, (e) J_{ph} versus V_{eff} curve and (f) J_{sc} and V_{oc} light intensity dependence curve of devices with or without optimized PBD interlayer.....	104
Figure 4.10 Absorption profiles of PBDB-T, IT-M and PBDB-T:IT-M blend film.	108
Figure 4.11 Electron mobility of devices with or without optimized PBD interlayer, measured using SCLC method.	111
Figure 5.1 Chemical structures of polyhydroxy compounds – ethylene glycol, xylitol dan dulcitol.	117
Figure 5.2 Comparison of R_{sq} and σ of PEDOT:PSS films (thickness: $\sim 90 \text{ nm}$) doped with various polyhydroxy compounds.	117
Figure 5.3 The schematic diagram of hydrogen bond and van der Waals bond effects on the substrate/electrode interfaces.	118
Figure 5.4 Adhesive force of as-cast PEDOT:PSS solution and PEDOT:PSS solution doped with xylitol; inset shows the process schematic for adhesion force measurement.	120

Figure 5.5 (a) Transmittance and reflectance spectra of glass/ITO, PET/ITO and PET/D-PEDOT:PSS. (b) Comparison of transmittance spectra of as-cast PEDOT:PSS and D-PEDOT:PSS films deposited on PET plastic substrates as compared to bare PET..... 121

Figure 5.6 (a) TEM images of the as-cast, xylitol-doped and xylitol-doped MSA-treated PEDOT:PSS films fabricated on PET plastic substrates. (b) The schematic diagram of morphology of the as-cast, xylitol-doped and xylitol-doped MSA-treated PEDOT:PSS films. (c) The schematic diagram of ionic and hydrogen bonding in as-cast, xylitol-doped and xylitol-doped MSA-treated PEDOT:PSS films. 125

Figure 5.7 AFM ($2 \times 2 \mu\text{m}$) height images of (a) as-cast PEDOT:PSS and (b) D-PEDOT:PSS films. EDS elemental mapping showing the distribution of S element in (c) as-cast PEDOT:PSS and (d) D-PEDOT:PSS films. Fitted S 2p XPS spectra of (e) as-cast PEDOT:PSS and (f) D-PEDOT:PSS films. 126

Figure 5.8 $R_{sq}/R_{sq(0)}$ of PET/D-PEDOT:PSS and PET/PEDOT:PSS (control samples) as a function of bending cycles; insets show the images of bending and folding test conducted using cylinder and ruler, respectively..... 129

Figure 5.9 (a) Chemical structures of PBDB-T-2F donor and Y6 acceptor. (b) Device structure of flexible OSCs incorporating D-PEDOT:PSS FTEs. (c) $J-V$ characteristics and (d) EQE spectra of devices based on PET/D-PEDOT:PSS and glass/ITO. (e) Normalized PCE of flexible OSCs based on D-PEDOT:PSS FTEs after subjected to bending (black), mid-device folding or folding between Al electrodes (red) and folding on top of the Al electrodes (blue). (f) Recent scatter plot report for PCE values of flexible OSCs with different FTEs; all data are listed in “Appendix A”. 131

Figure 6.1 (a) Optical properties of D-PEDOT:PSS fabricated on PET substrates. (b) Optical properties of PBDB-T-2F:Y6 photoactive layer film..... 141

Figure 6.2 (a) An installation of FST-OSCs as roofs in greenhouse. (b) Folding schematic diagram of FST-OSCs (folding between top Ag electrodes). (c) Typical $J-V$ characteristics

and (d) transmittance spectra of foldable-flexible semi-transparent devices. (e) Normalized PCE of FST-OSCs based on D-PEDOT:PSS FTEs after subjected to bending (orange), mid-device folding or folding between Ag electrodes (green) and folding on top of the Ag electrodes (red). (f) Recent scatter plot report for PCE and AVT values of semi-transparent OSCs; all data are listed in “Appendix A”. 142

Figure 6.3 Reflectance spectra of semi-transparent devices based on PET/D-PEDOT:PSS... 144

Figure 6.4 (a) Representation of the colour coordinates of fabricated FST-OSCs on a CIE 1931xyY chromaticity diagram. (b) Digital photographs taken with green leaves covered with FST-OSCs. 147

Figure 6.5 (a) Optical photograph of mung bean leaves changing in 9 days under direct sunlight (L), direct sunlight with FST-OSCs roof (S) and dark (D). (b) Optical photograph of mung beans, showing the stems length changing in 9 days under direct sunlight (L), direct sunlight with FST-OSCs roof (S) and dark (D). 148

List of Tables

Table 1.1 List of substrates and their corresponding information.....	65
Table 1.2 List of photoactive materials and their corresponding information.	66
Table 1.3 List of ETL and HTL materials and their corresponding information.	66
Table 1.4 List of solvents and their corresponding information.	66
Table 1.5 List of additives/dopants and their corresponding information.....	66
Table 1.6 List of electrode materials and their corresponding information.	67
Table 1.7 List of instrumentations and their corresponding information.	67
Table 1.8 Function of instrumentations used.	68
Table 2.1 Detailed photovoltaic parameters of inverted OSCs with ZnO and optimized ZnO/PBD interlayer.	105
Table 2.2 Optimization of PBD interlayer on ZnO film in terms of PBD concentration.....	105
Table 2.3 Optimization of PBD interlayer on ZnO film in terms of PBD film thickness.	105
Table 2.4 Optimization of PBD interlayer on ZnO film in terms of post-processing annealing treatment.....	106
Table 3.1 R_{sq} , σ and FoM values of D-PEDOT:PSS films when compared with different acid-treated PEDOT:PSS films.	122
Table 3.2 Detailed photovoltaic parameters of rigid and flexible OSCs based on D-PEDOT:PSS and ITO electrodes.	132

Table 4.1 Detailed photovoltaic parameters of FST-OSCs based on D-PEDOT:PSS with different cathode thicknesses.	143
Table A.1 Comparison of PCE values of flexible OSCs with different PEDOT:PSS-based FTEs.	189
Table A.2 Comparison of PCE values of flexible OSCs with different metal-based FTEs. ...	190
Table A.3 Comparison of PCE values of flexible OSCs with different carbon-based FTEs. .	190
Table A.4 Summaries of PCE and AVT values of recently reported rigid ST-OSCs – <i>Part 1</i>	191
Table A.5 Summaries of PCE and AVT values of recently reported rigid ST-OSCs – <i>Part 2</i>	192
Table A.6 Summaries of PCE and AVT values of recently reported flexible ST-OSCs.	193
Table B.1 Raw data of conventional PBDB-T:IT-M -based OSCs.....	194
Table B.2 Raw data of conventional PBDB-T:IT-M:PBI-Por -based OSCs (1% addition)....	195
Table B.3 Raw data of conventional PBDB-T:IT-M:PBI-Por -based OSCs (5% addition)....	196
Table B.4 Summary of conventional PBDB-T:IT-M:PBI-Por -based OSCs.	196
Table B.5 Raw data of conventional PBDB-T:IT-M:PBD -based OSCs (1% dopant).	197
Table B.6 Summary of conventional PBDB-T:IT-M:PBD -based OSCs.	197
Table B.7 Raw data of inverted PBDB-T:IT-M -based OSCs.	198
Table B.8 Raw data of inverted PBDB-T:IT-M:TFT-CN -based OSCs (1% addition).	199

Table B.9 Raw data of inverted PBDB-T:IT-M:TFT-CN -based OSCs (6% addition).	200
Table B.10 Raw data of inverted PBDB-T:IT-M:TFT-CN -based OSCs (1% dopant).	201
Table B.11 Raw data of inverted PBDB-T:IT-M:TFT-CN -based OSCs (6% dopant).	202
Table B.12 Summary of inverted PBDB-T:IT-M:TFT-CN -based OSCs.....	202
Table B.13 Raw data of conventional PBDB-T-2F:IT-4F -based OSCs.	203
Table B.14 Raw data of conventional PBDB-T-2F:IT-4F:PBD -based OSCs (1% dopant)...	204
Table B.15 Summary of conventional PBDB-T-2F:IT-4F:PBD -based OSCs.....	204
Table B.16 Raw data of conventional PBDB-T-2F:IT-4F:g-C ₃ N ₄ -based OSCs (1% dopant).	205
Table B.17 Summary of conventional PBDB-T-2F:IT-4F:g-C ₃ N ₄ -based OSCs.	205
Table B.18 Raw data of conventional PBDB-T-2F:Y6 -based OSCs.....	206
Table B.19 Raw data of conventional PBDB-T-2F:Y6:DRCN-5T -based OSCs (5% addition).	207
Table B.20 Raw data of conventional PBDB-T-2F:Y6:DRCN-5T -based OSCs (10% addition).	208
Table B.21 Raw data of conventional PBDB-T-2F:Y6:DRCN-5T -based OSCs (20% addition).	209
Table B.22 Summary of conventional PBDB-T-2F:Y6:DRCN-5T -based OSCs.	209
Table B.23 Raw data of conventional PBDB-T-2F:Y6:M2 -based OSCs (1% dopant).	210

Table B.24 Raw data of conventional PBDB-T-2F:Y6:M2 -based OSCs (5% dopant).	211
Table B.25 Summary of conventional PBDB-T-2F:Y6:M2 -based OSCs.....	211

List of Abbreviations

Abbreviation	Identification
λ	Wavelength
δ	Interfacial layer conductivity
σ	Electrode conductivity
σ_{dc}	Direct current conductivity
σ_{op}	Optical conductivity
μ	Charge mobility
ϵ_0	Permittivity of free space constant
ϵ_r	Relative dielectric constant
A	Acceptor
AFM	Atomic force microscopy
AM1.5G	Air mass 1.5 global
AVT	Average visible transmittance
BHJ	Bulk heterojunction
CPEs	Conjugated polyelectrolytes
CTE	Charge transfer exciton
D	Donor
D/A or D-A	Donor-acceptor
d , or L	Thickness of thin-film
e	Elementary charge
E	Energy or energy level
E_b	Binding energy
EDS	Energy dispersive x-ray spectroscopy
E_g	Optical bandgap
EQE	External quantum efficiency
ETL	Electron-transporting layer
FF	Fill factor
FoM	Figure of merit
FST-OSCs	Foldable-flexible semi-transparent organic solar cells
FTEs	Flexible transparent electrodes
G_0	Conductance
HOMO	Highest occupied molecular orbital
HTL	Hole-transporting layer
IPCC	Intergovernmental panel on climate change
J ; J_{sc} ; J_{max}	Current density ; Short circuit current ; Maximum current
J_0	Current density under dark condition
J_L	Current density under light irradiation

Abbreviation	Identification
J_{ph} ; J_{sc}	Photocurrent density ; Saturated photocurrent
LUMO	Lowest occupied molecular orbital
NWs	Nanowires
OLEDs	Organic light emitting diodes
OSCs	Organic solar cells
P	Light intensity
PCE	Power conversion efficiency
P(E,T)	Exciton dissociation efficiency or probability
P_{in}	Incident photon's power
PV	Photovoltaic
QDs	Quantum dots
RMS	Root-mean-square
R_s	Series resistance
R_{sh}	Shunt resistance
R_{sq}	Square resistance
S	Device active area
SADMs	Self-assembled dipole monolayers
SCLC	Space-charge limited current
SM	Small-molecular
TEM	Transmission electron microscopy
TFTs	Thin-film transistors
UPS	Ultraviolet photoelectron spectroscopy
UV ; UV-vis	Ultraviolet ; Ultraviolet – visible light
V ; V_{oc} ; V_{max}	Voltage ; Open circuit voltage ; Maximum voltage
V_{eff}	Effective voltage
WF or ϕ	Work function
XPS	X-ray photoelectron spectroscopy

List of Chemical Names

Abbreviation	Identification
Ag	Silver
Al	Aluminium
Au	Gold
Ba(OH) ₂	Barium hydroxide
Br-ITIC	Acceptor derived from ITIC
BTP-2F-ThCl	Acceptor derived from Y6
BTP-4Cl-BO or BTP-eC11	Acceptor derived from Y6
BTP-4F or Y6	2,2'-((2Z,2'Z)-((12,13-bis(2-ethylhexyl)-3,9-diundecyl-12,13-dihydro-[1,2,5]thiadiazolo[3,4-e]thieno[2'',3'':4',5']thieno[2',3':4,5]pyrrolo[3,2-g]thieno[2',3':4,5]thieno[3,2-b]indole-2,10-diyl)bis(methanylylidene))bis(5,6-difluoro-3-oxo-2,3-dihydro-1H-indene-2,1-diylidene))dimalononitrile
BTP-eC9	Acceptor derived from BTP-eC11
C	Carbon
C ₆₀	Fullerene
Ca	Calcium
CB	Chlorobenzene
CdTe	Cadmium telluride
CF	Chloroform
CIGS	Copper indium gallium selenide
CN	1-chloronaphthalene
CO ₂	Carbon dioxide gas
D18	Poly[(2,6-(4,8-bis(5-(2-ethylhexyl-3-fluoro)thiophen-2-yl)-benzo[1,2-b:4,5-b']dithiophene))-alt-5,5'-(5,8-bis(4-(2-butyloctyl)thiophen-2-yl)dithieno[3',2':3,4;2'',3'':5,6]benzo[1,2-c][1,2,5]thiadiazole)]
DIO	1,8-diiodooctane
D-PEDOT:PSS	PEDOT:PSS (PH1000) FTEs treated with xylitol dopant and MSA
DRCN-5T	2,2'-[(3,3'',3''',4'-tetraoctyl[2,2':5',2'':5'',2''':5''',2''''-quinquethiophene]-5,5''-diyl)bis[(Z)-methylidyne(3-ethyl-4-oxo-5,2-thiazolidinediylidene)]]bis-propanedinitrile
ECTBD ; PBQ10	Examples of donors
EDTA	Ethylenediaminetetraacetic acid
g-C ₃ N ₄	Graphitic carbon nitride
H	Hydrogen
IT-4F	3,9-bis(2-methylene-((3-(1,1-dicyanomethylene)-6,7-difluoro)-indanone))-5,5,11,11-tetrakis(4-hexylphenyl)-dithieno[2,3-d:2',3'-d']-s-indaceno[1,2-b:5,6-b']dithiophene
ITC-2Cl ; IXIC-4Cl	Examples of non-fullerene acceptors
ITCT	Acceptor derived from 4H-cyclopenta[b]thiophene-4,6(5H)-dione

Abbreviation	Identification
ITIC	3,9-bis(2-methylene-(3-(1,1-dicyanomethylene)-indanone))-5,5,11,11-tetrakis(4-hexylphenyl)-dithieno[2,3-d:2',3'-d']-s-indaceno[1,2-b:5,6-b']dithiophene
IT-M	3,9-bis(2-methylene-((3-(1,1-dicyanomethylene)-6/7-methyl)-indanone))-5,5,11,11-tetrakis(4-hexylphenyl)-dithieno[2,3-d:2',3'-d']-s-indaceno[1,2-b:5,6-b']dithiophene
ITO	Indium tin oxide
J71	Poly[[5,6-difluoro-2-(2-hexyldecyl)-2H-benzotriazole-4,7-diyl]-2,5-thiophenediyl][4,8-bis[5-(tripropylsilyl)-2-thienyl]benzo[1,2-b:4,5-b']dithiophene-2,6-diyl]-2,5-thiophenediyl]
MEH-PPV	Poly[2-methoxy-5-(2-ethylhexyloxy)-1,4-phenylenevinylene]
MoO ₃	Molybdenum oxide
MSA	Methanesulfonic acid
N	Nitrogen
N ₂	Nitrogen gas
O	Oxygen
P3HT	Poly(3-hexylthiophene-2,5-diyl)
PBD	2-(4-tert-butylphenyl)-5-(4-biphenyl)-1,3,4-oxadiazole
PBDB-T	Poly[(2,6-(4,8-bis(5-(2-ethylhexyl)thiophen-2-yl)-benzo[1,2-b:4,5-b']dithiophene))-alt-(5,5-(1',3'-di-2-thienyl-5',7'-bis(2-ethylhexyl)benzo[1',2'-c:4',5'-c']dithiophene-4,8-dione)]
PBDB-T-2Cl or PM7	Poly[(2,6-(4,8-bis(5-(2-ethylhexyl-3-chloro)thiophen-2-yl)-benzo[1,2-b:4,5-b']dithiophene))-alt-(5,5-(1',3'-di-2-thienyl-5',7'-bis(2-ethylhexyl)benzo[1',2'-c:4',5'-c']dithiophene-4,8-dione)]
PBDB-T-2F or PM6	Poly[(2,6-(4,8-bis(5-(2-ethylhexyl-3-fluoro)thiophen-2-yl)-benzo[1,2-b:4,5-b']dithiophene))-alt-(5,5-(1',3'-di-2-thienyl-5',7'-bis(2-ethylhexyl)benzo[1',2'-c:4',5'-c']dithiophene-4,8-dione)]
PBI-Por	Acceptor derived from perylene diimide
PC ₆₁ BM or PCBM	Acceptor derived from fullerene
PC ₇₁ BM	Acceptor derived from fullerene
PDINO	2,9-bis[3-(dimethylamino)propyl]anthra[2,1,9-def:6,5,10-d'e'f']diisoquinoline-1,3,8,10(2H,9H)-tetrone
PEDOT:PSS (4083) or 4083	Poly(3,4-ethylenedioxythiophene)-poly(styrenesulfonate) for HTL application
PEDOT:PSS (PH1000)	Poly(3,4-ethylenedioxythiophene)-poly(styrenesulfonate) for FTE application
PET	Polyethylene terephthalate
PFN	Poly[(9,9-bis(3'-(N,N-dimethylamino)propyl)-2,7-fluorene)-alt-2,7-(9,9-dioctylfluorene)]
PFN-Br	Poly(9,9-bis(3'-(N,N-dimethyl)-N-ethylammonium-propyl)-2,7-fluorene)-alt-2,7-(9,9-dioctylfluorene)dibromide
PTB7	Poly[[4,8-bis[(2-ethylhexyl)oxy]benzo[1,2-b:4,5-b']dithiophene-2,6-diyl][3-fluoro-2-[(2-ethylhexyl)carbonyl]thieno[3,4-b]thiophenediyl]]

Abbreviation	Identification
PTB7-Th	Poly[4,8-bis(5-(2-ethylhexyl)thiophen-2-yl)benzo[1,2-b;4,5-b']dithiophene-2,6-diyl-alt-(4-(2-ethylhexyl)-3-fluorothieno[3,4-b]thiophene-)-2-carboxylate-2-6-diyl]
S	Sulphur
Si	Silicon
T6Me ; IDTCN-O	Examples of non-fullerene acceptors
TFT-CN ; M2	OLED-based materials for study
TiO ₂	Titanium dioxide
WO _x	Tungsten oxides
Zn	Zinc
ZnO	Zinc oxide

Chapter 1. Introduction

1.1 Background

In the 21st century, the ever-increasing energy demand becomes a major worldwide concern due to the quick growth in global population by more than 5.5 billion people over a century (Roser et al., 2020). With the continuous rise in global energy demand and consumption, massive energy supply is needed more than ever. Over the past few decades, traditional sources of energy such as fossil fuels (coal, oil and natural gas) had dominated the market, covering more than 75% of world's energy supply as shown in **Figure 1.1** (British Petroleum, 2019). However, the combustion of fossil fuels is causing substantial greenhouse gases emissions (particularly carbon dioxide/CO₂ emissions) into the atmosphere. Based on studies reported by Intergovernmental Panel on Climate Change (IPCC), the global CO₂ concentration in the atmosphere had increased significantly over the past century and was highly associated with the combustion of fossil fuels (IPCC, 2015). Therefore, continuous dependency on fossil fuels as the primary energy sources will result in adverse environmental impacts (e.g., ozone depletion, global warming, etc). Not to mention, fossil fuels are facing resources depletion crisis due to their non-renewable nature. In view of these issues, alternatives to fossil fuels are needed with utmost urgency to mitigate greenhouse gases emissions and resolve the imminent depletion crisis of fossil fuel.

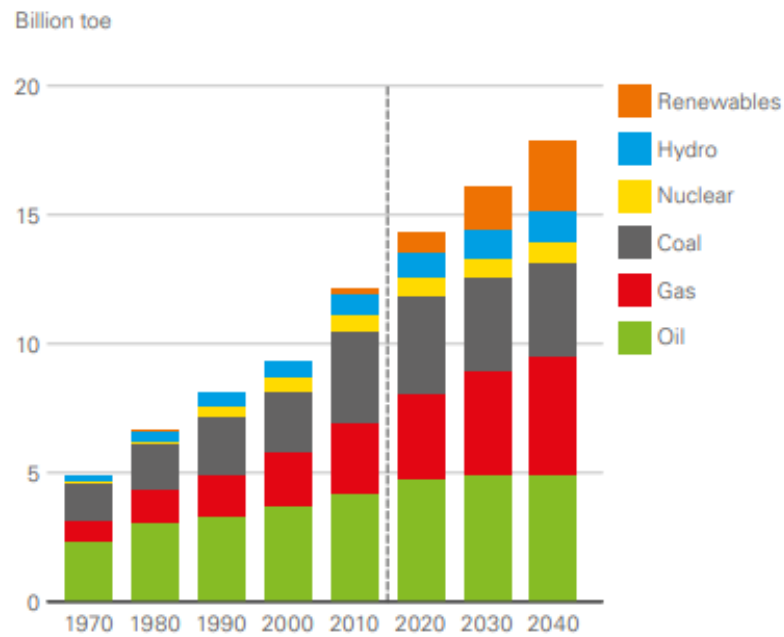


Figure 1.1 Global consumption of energy (measured in billion tons of oil equivalent) categorized based on fuel sources from 1970 to 2019 and further prediction to 2040 (British Petroleum, 2019).

Renewable energy sources, as replacement for non-renewable fossil fuels are ‘green’, clean and abundant in nature, providing a promising long-term solution to solve the energy supply crisis. Among them, solar energy appears to be one of the most ideal and encouraging renewable energy sources for sustainable development, as it can be harvested directly from sunlight using photovoltaic (PV) technology. Theoretically, sunlight is made up of photons, which contain a specific amount of energy. When the solar cell (building block of PV technology) is stroked by sunlight, it absorbs the extra energy to knock the electron loose, thereby allowing the electron to move freely. An additional electric field induced by the electrodes forces the free-moving electrons to move in the same direction for current generation. This process is often known as PV effect (Bagher, 2014), which is the key governing concept in all PV technologies to convert sunlight into electricity effectively. By using this technology,

electrical energy can be produced profusely from the inexhaustible and clean solar energy to meet the increasing demand for sustainable energy.

1.2 Overview of Solar Cells

Solar cells, as the building blocks of PV technology are mainly categorized into two classes, namely organic and inorganic solar cells (Huang and Deng, 2014). Since its discovery, inorganic solar cells have been dominating the PV market, particularly for silicon-based inorganic solar cells as it accounted for 95% of the total global PV production in 2019 (Philipps and Warmuth, 2020). However, due to complexity and cost issues in the manufacturing of silicon-based inorganic solar cells, several alternatives such as organic solar cells are being developed to replace them.

1.2.1 Development history of solar cells

Dating back to 1839, a French physicist named A. E. Becquerel, discovered the first PV effect from his experiment with platinum electrode in an electrolyte solution (U.S. Department of Energy, 2002, Four Peaks Technologies, 2011). Becquerel realized that voltage was developed when the electrode was exposed to light. In the 1870s, British electrical engineer and researchers discovered about the photoconductivity of selenium and its ability to produce electrical current when exposed to sunlight without any mechanical or thermal sources (U.S. Department of Energy, 2002, Four Peaks Technologies, 2011). Soon after in 1883, American inventor C. Fritts successfully made use of

selenium to construct the first working solar cells (U.S. Department of Energy, 2002, Four Peaks Technologies, 2011). The resulting cells had an electrical conversion efficiency of only 1% attributed to the properties of selenium.

The first photoelectric effect was discovered in 1887 by German physicist named H. R. Hertz (U.S. Department of Energy, 2002, Four Peaks Technologies, 2011). Hertz implied that matter could emit electrons when light was shined on it and ultraviolet (UV) light could provide better stimulus for this than visible light. The theories on photoelectric effect were later clarified by A. Einstein in 1905 (U.S. Department of Energy, 2002, Four Peaks Technologies, 2011). In his theory, Einstein postulated that light was composed of photons and photons carried varying amount of energy depending on the wavelength of light – greater energy corresponds to short wavelength. The experimental proof to support those theories was later conducted by R. Millikan in 1916 (U.S. Department of Energy, 2002, Four Peaks Technologies, 2011).

After almost a century, the development of solar cells continued in 1954, where D. M. Chapin, C. S. Fuller and G. L. Pearson developed the first practical solar cells made from silicon materials (Chapin et al., 1954). Efficiency of 6% was achieved for silicon solar cells, which was a milestone for a practical solar cell at that time. This efficiency was further enhanced to 14% in 1960s due to the intense researches in this field (U.S. Department of Energy, 2002, Four Peaks Technologies, 2011). In the early 1970s, cheaper silicon solar cells were designed using lower silicon purity grade materials (U.S. Department of Energy, 2002, Four Peaks Technologies, 2011). Since then, silicon solar cells started to gain popularity and dominance in various applications such as powering outer

space satellites, navigation warning lights, utilities, vehicles and many more. The pace of solar cells development never slowed down since 1970s as depicted in **Figure 1.2** (National Renewable Energy Laboratory, 2020). It was progressing much faster over the years leading to the emergence of three generation of solar cells, which were distinguished based on the key materials used for the light-absorbing layer or photoactive layer.

Silicon-based solar cells are the 1st generation solar cells, which are made from either monocrystalline or polycrystalline silicon (Battaglia et al., 2016, Raut et al., 2018, Liu et al., 2018). These solar cells are the most mature PV technologies on the market due to their remarkable efficiency of over 22% (Philipps and Warmuth, 2020) and excellent lifetime of 25 years (Jorgensen et al., 2008). Nonetheless, the production of these solar cells requires a thorough purification procedure and thicker silicon absorbing layer to obtain such high efficiency, which contributes to the high energy consumption and production cost (Hoppe and Sariciftci, 2004, Li et al., 2012b, Bagher, 2014). Thus, several alternatives to 1st generation solar cells are being studied and developed.

Best Research-Cell Efficiencies

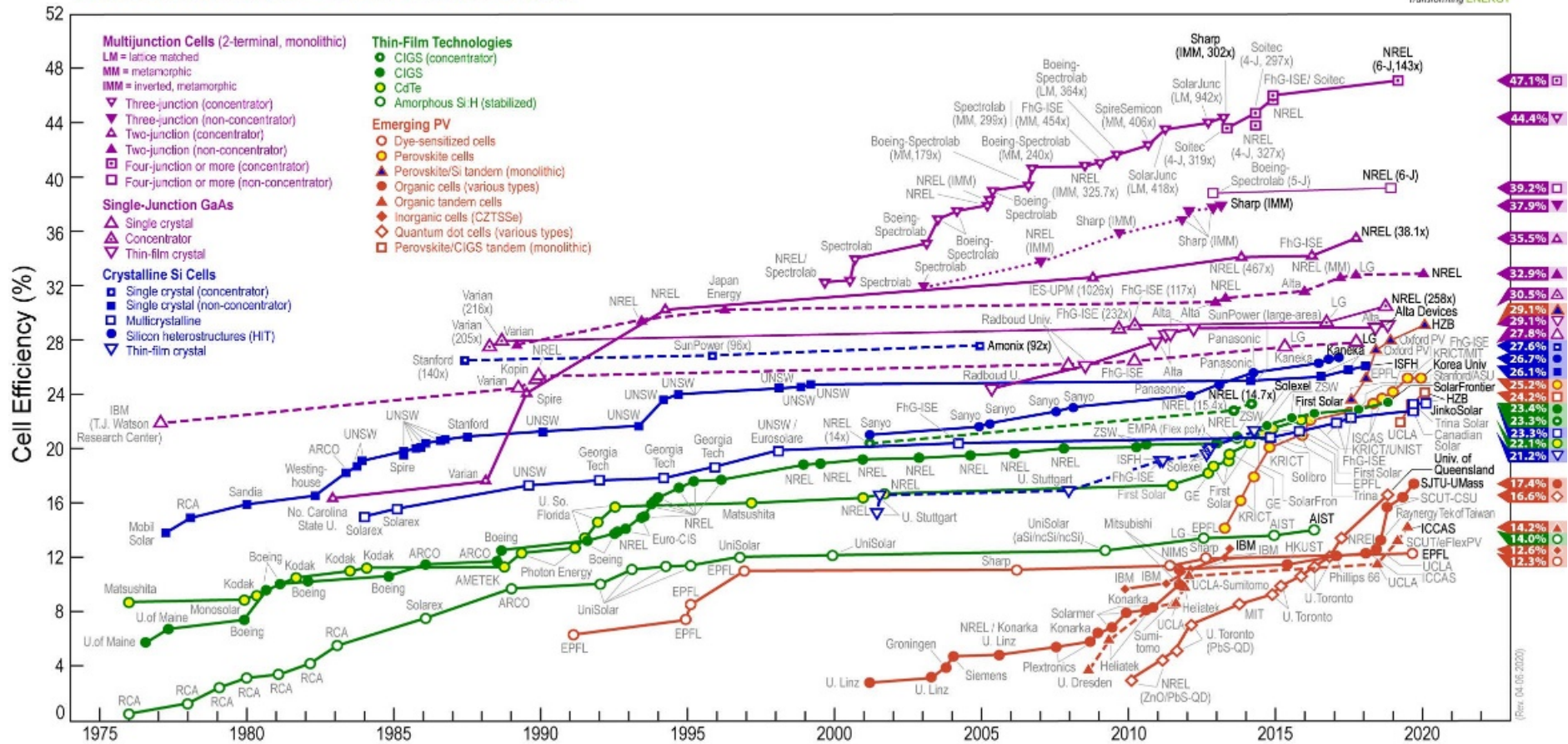


Figure 1.2 Development of solar cells over the years for different PV technologies (National Renewable Energy Laboratory, 2020).

The 2nd generation solar cells are thin-film solar cells classified into three different types: amorphous silicon, cadmium telluride (CdTe) and copper indium gallium selenide (CIGS) (Lee and Ebong, 2017, Raut et al., 2018). As compared to its predecessor, these solar cells are much more economical and have better absorption capability even with a thin photoactive layer. Each thin-film solar cell possesses its own unique characteristics. For instance, amorphous silicon solar cells may feature lower efficiency but are the most environmentally friendly when compared to CdTe and CIGS solar cells. CdTe solar cells can be considered as the lead candidate for 2nd generation PV technology as they have higher efficiency, yet various environmental hazards stemmed from the use of heavy metal cadmium. CIGS solar cells can absorb sunlight effectively in a much thinner photoactive layer, but the scarcity and toxicity of indium and gallium need to be taken into consideration. In view of those shortcomings, 3rd generation PV technologies are being introduced.

The newest technology in PV market is the 3rd generation solar cells, represented by nanocrystal or quantum dots (QDs) solar cells, organic solar cells (OSCs), perovskite solar cells, dye-sensitized solar cells and concentrated solar cells (Raut et al., 2018). These solar cells have the potential to be commercialized to replace the 1st generation silicon-based solar cells. As of now, most of the 3rd generation solar cells are still in the midst of developing, seeking for the right balance between efficiency, lifetime and cost to improve upon the first two generations.

1.2.2 Organic solar cells (OSCs)

OSCs or organic solar cells are thin-film solar cells, where the photoactive layers are made from organic semiconducting materials or carbon-based materials with backbones comprising of mainly C-C and C=C bond (Li et al., 2012a). In the last decade, OSCs have been gaining notable attentions over the other 3rd generation solar cells due to their promising potentials as substitutes for conventional silicon solar cells. Nonetheless, concerns regarding OSCs were raised in the past because of their low efficiency performances when compared to other inorganic PV technologies. It was the concerted efforts between chemists, physicists and engineers that managed to push the development progress of OSCs to reach a new milestone (Brabec, 2004, Jorgensen et al., 2008, Sista et al., 2011, Zhang and Wang, 2012, Zhou et al., 2012, Ameri et al., 2013, Heeger, 2014, McAfee et al., 2015, Yin et al., 2016, Carle et al., 2017, Cheng et al., 2018, Li et al., 2018, Yan et al., 2018, Upama et al., 2020). Resultantly, the performance of OSCs had increased rapidly from 2.9% in 1995 (Yu et al., 1995) to over 18% in 2020 (Liu et al., 2020).

The potential of OSCs arises from the fact that organic semiconductors are versatile in nature, which allow OSCs to have countless possible material combinations during fabrication process, providing great range of options for improvements. Also, OSCs have the following characteristics that made them far more superior than their inorganic counterparts (e.g., silicon) (Yin et al., 2016, Carle et al., 2017, Brebels et al., 2017, Li et al., 2018, Upama et al., 2020).

- i) Low carbon footprint with minimal use of non-abundant elements, making OSCs to be environmental-friendly and low-cost PV technology.
- ii) Lightweight and mechanically flexible, giving OSCs the possibility to be fabricated on a flexible substrate.
- iii) Ease of solution-processability at low temperature, allowing OSCs to be compatible for large-area manufacturing for commercialization purposes.
- iv) Flexibility for chemical tailoring where precise optimization of the desired properties (e.g., energy level and absorption spectra) of the materials are achievable.
- v) Semi-transparent to transparent nature of organic semiconductors results in stronger absorption coefficient in OSCs, which means that a high absorption can be obtained even in thin-film device with thickness less than 100 nm.

1.2.3 Key challenges in OSCs

Efficiency, lifetime and production cost are the three major obstacles that restrict the commercialization of OSCs (Jorgensen et al., 2008). Though OSCs may have lower cost of processing than their inorganic counterparts, efficiency and lifetime issues still need to be overcome to achieve comparable performance against mature silicon-based solar cells. These issues indeed remained as great challenges, causing the studies about organic photovoltaics to focus on the development of efficient and stable OSCs.

One of the key factors that have restricted the realization of efficient and stable OSCs is the limited absorption capability of OSCs, which affects the generation of charge carriers (Carle et al., 2017). For example, despite OSCs having high absorption coefficient, silicon solar cells still absorb light more effectively as the absorption spectrum extends up to 1100 nm – absorption from UV to infrared region (see **Figure 1.3**) (Hoppe and Sariciftci, 2004). Meanwhile, OSCs can only absorb light effectively up to the visible light region, limiting the possibility of harvesting solar photons in the higher wavelength region (see **Figure 1.3**) (Hoppe and Sariciftci, 2004). Theoretically, this is caused by the relatively high bandgap (E_g) of organic semiconductors (~ 2 eV), which is much higher than the value for silicon semiconductors (Coakley and McGehee, 2004, Gunes et al., 2007, Huang and Deng, 2014). This subsequently restricts the amount of incident solar light to be absorbed by OSCs. Hence, it is crucial to reduce the bandgap of organic semiconductors so that OSCs will have broader coverage of solar spectrum (UV to infrared region) to increase both their light absorption and charge generation capability.

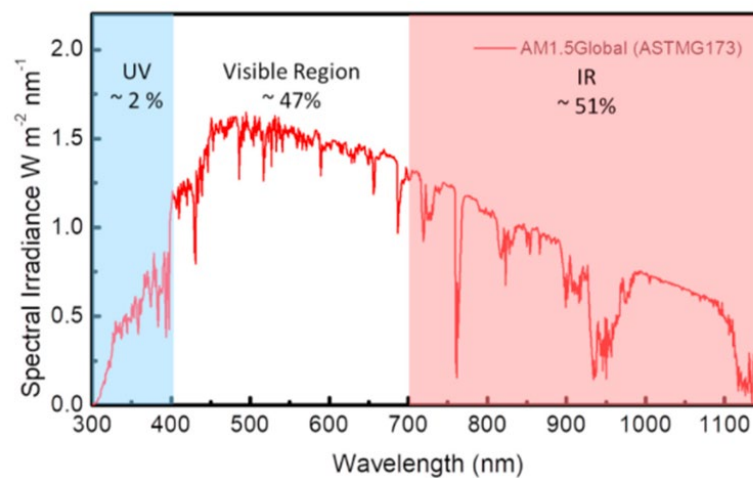


Figure 1.3 Solar spectrum under air mass 1.5 global (AM1.5G) irradiance (Chang et al., 2018).

Another factor that restricted the realization of efficient and stable OSCs is the low charge carrier mobility of OSCs, which affects the extraction of charge carriers (Carle et al., 2017). OSCs have lower charge carrier mobility, as the main transport mechanism in organic semiconductors is through hopping transport and not bandlike transport, which is the case for inorganic semiconductors (Hoppe and Sariciftci, 2004, Coakley and McGehee, 2004). Due to this reason, utilizing suitable materials that have good charge transporting properties are essential to promote better charge extraction and charge collection processes in OSCs.

Over the years, efforts to overcome the absorption and charge mobility issues in OSCs have been made to develop efficient and stable OSCs. One effective strategy is the copolymerization of donor and acceptor units into the same backbone (D-A copolymerization) (Zhang et al., 2015, Bang et al., 2017, Sun et al., 2020). Via this technique, organic semiconductors can have smaller bandgap due to the redistribution of frontier molecular orbitals, as well as higher charge carrier mobility caused by the change in aggregation behaviour. Other strategies such as by tuning the effective conjugation length and opting for quinoidal structure instead of aromatic were also proven to be useful (Cheng et al., 2009, Zhang and Wang, 2012, Chang et al., 2018). Due to those efforts, the performance of OSCs had risen to over 18% in 2020 (Liu et al., 2020). However, this efficiency performance was still lower than that of the other inorganic PV technologies (Philipps and Warmuth, 2020, National Renewable Energy Laboratory, 2020). Therefore, further enhancement in OSCs' performance is continuously required in the next couple of years for practical applications.

1.3 Aim and Objectives

Throughout the development of OSCs, three general approaches have been employed to boost OSCs' performance, namely material design (e.g., design and synthesis of novel organic material for photoactive layer), morphology control (e.g., morphology control of photoactive layer through post-production treatment) and device engineering (e.g., modification of electrode layer, interfacial layer or photoactive layer). Thus far, material design and morphology control of the photoactive layer have been the main focuses to improve OSCs' performance up to 15-18% range (Xu et al., 2019, Yuan et al., 2019, Cui et al., 2020, Luo et al., 2020, Liu et al., 2020, Sun et al., 2020). Meanwhile, device engineering gains less attention even though it plays an equally pivotal role to enhance OSCs' performance. In view of this, this study was conducted with the main aim of improving OSCs' performance using device engineering strategy, particularly via modification of interfacial layer and electrode layer (or interface and electrode engineering). Herein, different materials were chosen accordingly to modify the properties of pristine interfacial layer and electrode layer for better performing OSCs.

The objectives of this research are:

- i) To explore prospective of OSCs in supplying energy to meet global demand.
- ii) To provide an in-depth understanding of fundamental concepts of OSCs.

- iii) To study and demonstrate the potentials of device engineering, particularly interface and electrode engineering in enhancing OSCs' performance.
- iv) To present comprehensive ideas on how device engineering can improve device performance.
- v) To analyse the potential applications of high-performing OSCs achieved via device engineering.

1.4 Outline of Thesis

The outline of this research will be discussed in brief as follow. Chapter 1 introduces background information and problem statement of this study. It basically conveys the research gap and motivation to the readers. Ranges of solar cells are being introduced with the main focus on OSCs. The main aim and objectives of this study are presented as well.

Chapter 2 provides important and relevant technical information about OSCs that the readers need to understand before continuing further. This includes the development of OSCs over the years, operating principles of OSCs, photoactive layer configurations in OSCs, structures of OSCs and etc. Comprehensive insights on the key performance parameters of OSCs and relationships between them are also included here. This chapter discusses the previous work that have been studied or done to improve OSCs performance, which set clear opportunities for future research. A short summary regarding those research opportunities is presented at the end of this chapter.

Chapter 3 elaborates detailed information regarding the experimental work conducted for this study. This chapter aims to demonstrate a clear fabrication and performance measurement method for OSCs.

Chapter 4 discusses the interface engineering strategy to enhance OSCs' performance. This chapter is written based on published literature entitled "Efficiency enhancement of organic solar cells enabled by interface engineering of sol-gel zinc oxide with an oxadiazole-based material" (journal article: 10.1016/j.orgel.2019.105483). In here, interfacial layer engineering or interface engineering on zinc oxide (ZnO) electron-transporting layer (ETL) was performed via the incorporation of 2-(4-tert-butylphenyl)-5-(4-biphenyl)-1,3,4-oxadiazole (**PBD**) to form a hybrid electron-transporting bilayer.

Chapter 5 illustrates the electrode engineering strategy to improve OSCs' performance, which is based on the version of "Foldable semi-transparent organic solar cells for photovoltaic and photosynthesis" (journal article: 10.1002/aenm.202000136). Herein, electrode engineering was implemented on poly(3,4-ethylenedioxythiophene)-poly(styrenesulfonate) (**PEDOT:PSS**) electrode as indium tin oxide (ITO) alternatives, by adding xylitol dopant and utilizing methanesulfonic acid (MSA) post-processing treatment.

The study on device engineering continues in Chapter 6, where practical applications of device engineering strategy are being illustrated. This chapter covers the potential applications of high-performing OSCs achieved through electrode engineering strategy for greenhouse windows and/or roofs. A summary of the current study and discussion of future work are included in Chapter 7.

Chapter 2. Literature Review

2.1 Overview of OSCs

Though silicon-based inorganic solar cells had been dominating the global PV market, their complexity and cost issues had led to the emergence of several PV alternatives. OSCs being one of them, were gaining remarkable attentions in the last decades due to their promising potentials as future PV technology. Generally, OSCs are based on organic semiconducting materials, that can be further categorized into two major areas of polymeric and small-molecular (SM) materials (Brabec et al., 2010). Both materials have different characteristics and properties that will be discussed in the later parts.

Throughout the development of OSCs, it has been widely accepted that a combination of polymeric donor and SM acceptor as the photoactive layer is the most successful and prominent strategy for OSCs (Li et al., 2016, Zhao et al., 2017b, He et al., 2018, Zhang et al., 2018b, Xu et al., 2019, Yuan et al., 2019, Cui et al., 2020, Luo et al., 2020, Liu et al., 2020, Sun et al., 2020). Such combinations have propelled the efficiency performance of OSCs to over 15-18% range (Xu et al., 2019, Yuan et al., 2019, Cui et al., 2020, Luo et al., 2020, Liu et al., 2020, Sun et al., 2020). For instance, in one of the studies, a combination of D18 polymeric donor and Y6 SM acceptor could lead to an excellent OSC's performance with 18.22% efficiency, which was the highest-performing single-junction OSCs reported to date based on binary photoactive layer (Liu et al., 2020). Despite of the lower efficiency performance, other material combinations

for photoactive layer have also been studied and started to gain popularity in OSCs' field. For example, all-small-molecule OSCs utilizing SM donor and acceptor had recently achieved an efficiency of over 14-15% as reported by Zhou *et al.*, Hu *et al.* and Qin *et al.* (Zhou *et al.*, 2019, Hu *et al.*, 2020, Qin *et al.*, 2020a). On the contrary, much lower performance was obtained in all-polymer OSCs with efficiency around 9-10% as reported by Liu *et al.* and Wu *et al.* (Liu *et al.*, 2019b, Wu *et al.*, 2019).

It was obvious that the use of polymeric donor and SM acceptor benefited device performance the most, particularly when molecular structure of donor and acceptor materials were designed meticulously. Yet, their efficiency performances were still lower than other inorganic PV technologies. For example, the highest efficiency recorded for monocrystalline silicon, polycrystalline silicon, CIGS and CdTe solar cells were 27.6%, 23.3%, 23.4% and 22.1%, respectively (Philipps and Warmuth, 2020, National Renewable Energy Laboratory, 2020). This implies the need to explore strategies for further improvement in OSCs' efficiency to achieve comparable performance with other inorganic-based solar cells. To date, three main strategies have been applied to enhance OSCs' performance, including material design, morphology control and device engineering. Nonetheless, before going into each strategy in depth, it is crucial to first understand the basic concepts of OSCs (e.g., development progress, operating principles, device structures, etc).

2.2 Development of OSCs

The earliest OSCs were discovered in 1958 where D. Kearns and M. Calvin fabricated the first Schottky-junction OSCs using magnesium phthalocyanine as the photoactive layer (Kearns and Calvin, 1958). Even though PV effect was detected, the energy conversion efficiency was still extremely low because of the limitation of single-layered photoactive layer configuration. For almost 30 years, the development of OSCs remained relatively stagnant and the conversion efficiency was relatively low with the highest to be 0.7% in 1978 (Morel et al., 1978). In 1986, C. W. Tang introduced the concept of *p-n* junction in OSCs, where two organic layers consisting of a *p*-type hole-transporting layer (phthalocyanine derivative) and a *n*-type electron-transporting layer (perylene derivative) were used (Tang, 1986). Tang succeeded in achieving 1% efficiency, which was a milestone in the field of OSCs. This eventually led to the birth of bilayer heterojunction or biplanar photoactive layer configuration in OSCs.

In 1992, Sariciftci *et al.* discovered the evidence of photoinduced ultrafast charge transfer in a time regime of picoseconds between poly(phenylenevinylene) derivative (MEH-PPV) and fullerene (C₆₀) (Sariciftci et al., 1992). On that account, few deductions were made stating that since the charge transfer process was on the order of magnitude several times faster than any other competing process, then a highly efficient charge generation process (nearly 100%) in OSCs could be achieved. Based on those observations, Yu *et al.* fabricated the first ever bulk heterojunction (BHJ) OSCs in 1995 (Yu et al., 1995). Yu *et al.* managed to boost the efficiency to 2.9% by blending MEH-PPV donor and fullerene acceptor as the photoactive layer. Since then, several novel

photoactive materials had been designed, introduced and investigated, which resulted in the rapid development progress of BHJ OSCs throughout the years. To date, the most eminent donor materials are derived from PBDB-T polymer donors (Qian et al., 2012), such as PBDB-T-2F or PM6 (Zhang et al., 2015) and PBDB-T-2Cl or PM7 (Zhang et al., 2018b). Meanwhile, the most used acceptor materials are derived from ITIC SM acceptors (Lin et al., 2015), such as IT-M (Li et al., 2016) and IT-4F (Zhao et al., 2017b). SM acceptors derived from BTP-4F or Y6 (Yuan et al., 2019), namely BTP-4Cl-BO or BTP-eC11 (Cui et al., 2020), BTP-eC9 (Cui et al., 2020) and BTP-2F-ThCl (Luo et al., 2020) are currently dominating the OSCs' field due to their high efficiency performances beyond 15%. Consequently, the current efficiency performance of BHJ OSCs has surpassed 15-18% boundary (Xu et al., 2019, Yuan et al., 2019, Cui et al., 2020, Luo et al., 2020, Liu et al., 2020, Sun et al., 2020). If any, the complete chemical names for the aforementioned organic materials are being listed in "List of Chemical Names".

2.3 Operating Principles of OSCs

The main operating principles of OSCs can be divided into several key processes as shown in **Figure 2.1**: i) exciton generation, ii) exciton diffusion, iii) exciton dissociation, iv) generation of charge transfer exciton (CTE), v) free charge carrier generation and vi) transport of free charge carrier to electrodes for collection (Gunes et al., 2007, Cheng et al., 2009, Schlenker and Thompson, 2011, Facchetti, 2013, Huang and Deng, 2014, Kang et al., 2016).

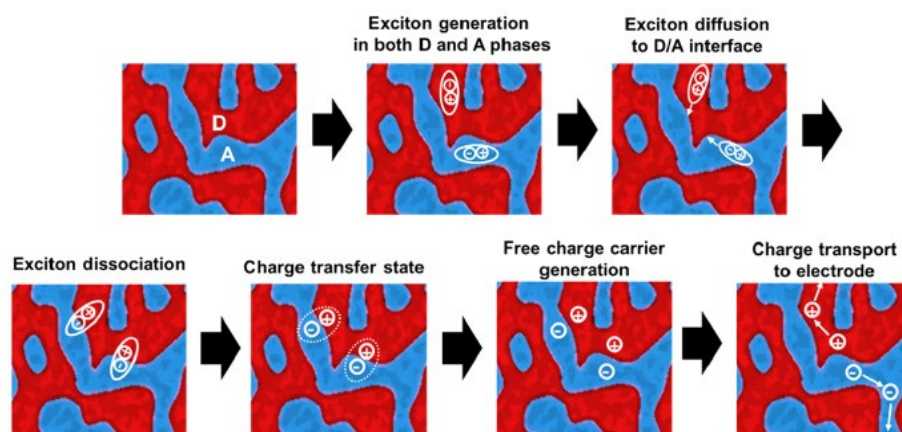


Figure 2.1 Key processes in OSCs (Kang et al., 2016). The blue area in the figure represents acceptor (A) and the red area represents donor (D). Both D and A are the constituents of the photoactive layer in OSCs and blended to form BHJ photoactive layer configuration.

2.3.1 Exciton generation

Absorption of light by photoactive organic materials (mostly donor materials of the photoactive layer) generates extra energy for the excitation of electron from highest occupied molecular orbital (HOMO) to lowest unoccupied molecular orbital (LUMO) energy level. However, only light with photon energies equal to or greater than the bandgap of the photoactive organic materials can be absorbed to knock the electron loose. This process is analogous to the excitation of electron from valence to conduction band in a typical inorganic semiconductor.

Following the excitation of electron to LUMO energy level, electron vacancy or hole is formed in the HOMO energy level and will always co-exist with the excited photogenerated electron. Due to this phenomenon, electron-hole pair is formed during absorption of light. The electron-hole pair is often termed as Frenkel exciton in organic semiconductors and Wannier-Mott exciton in

inorganic semiconductors (Brebels et al., 2017). The main distinguishing feature between them lies in their binding energies. While Wannier-Mott exciton in inorganic semiconductors is weakly bounded by Coulombic forces, Frenkel exciton is the complete opposite as it is tightly bounded by strong Coulombic forces, resulting in a high binding energy (E_b) in the range of 0.3-1.0 eV (Brebels et al., 2017).

2.3.2 Exciton diffusion

Frenkel exciton then diffuses into the D/A interface via random hopping. During this process, exciton often decays or recombines due to the short exciton diffusion length of ~10-20 nm in addition to the short exciton lifetime of ~1 ns in organic materials (Hoppe and Sariciftci, 2004, Brabec et al., 2010). Since its discovery in 1995 (Yu et al., 1995), BHJ photoactive layer configuration (as shown in **Figure 2.1**) has been utilized to overcome those issues by ensuring that exciton can be generated within its diffusion length from the D/A interface, so that the recombination of exciton via radiative or non-radiative pathway can be minimized.

2.3.3 Exciton dissociation

Exciton dissociation process takes place after Frenkel exciton has made it to the D/A interface. As Frenkel exciton is strongly bounded by Coulombic forces with E_b of ~0.3-1.0 eV (Brebels et al., 2017), efficient exciton dissociation entirely depends on the D/A interface. D/A interface presents a way to overcome the high E_b because of the strong internal electric field created by the gap in energy levels between donor and acceptor materials at the interface. This strong

electric field is sufficient to be the driving force to dissociate exciton into free charge carriers of electron and hole.

2.3.4 Generation of CTE and free charge carrier

Separated charges of electron and hole are formed upon the dissociation of Frenkel exciton. Electron is now found in the LUMO energy level of acceptor materials, while hole is in the HOMO energy level of donor materials. Although separated, charges are still found near the D/A interface, which indicate that both electron and hole are still in a close distance with one another. Therefore, there are strong Coulombic interaction existing between electron and hole near the D/A interface. The electron-hole pair found near the D/A interface after dissociation is referred as CTE. In this process, CTE will eventually decay, either through the recombination of separated charges or the reactions with surrounding neutral ground-state molecules. The former pathway is a major loss mechanism that hinders OSCs from having high efficiency, while the latter pathway leads to the generation of free charge carrier.

2.3.5 Charge transport to electrodes

Separated free charge carriers are then transported to electrodes for collection before they decay or recombine. Thus, it is important to ensure that photoactive materials have high charge carrier mobility to transport electron and hole effectively. Furthermore, it is crucial to ensure that electrodes can collect electron and hole effectively through the formation of Ohmic contact. With the presence of driving force, both hole and electron are transported via random hopping between molecules, where hole is transported effectively in the donor

materials to reach a higher work function (WF) electrode (or anode) and electron in acceptor materials to a lower WF electrode (or cathode). The driving forces include: i) internal electric field formed from the difference in energy levels between donor and acceptor materials at the D/A interface and ii) external electric field created via the use of electrodes with different WF. When the electrodes are connected to an external circuit, electrical current will be generated.

2.4 Photoactive Layer Configurations in OSCs

Photoactive layer as the main constituent of OSCs plays a critical role in OSCs as it directly affects the generation, diffusion and dissociation of exciton, plus the generation and transport of free charge carrier. Hence, any modifications made on the photoactive layer configuration will impact OSCs' performance greatly. Over the past few decades, photoactive layer configuration in OSCs had evolved from single-layered Schottky-junction and bilayer heterojunction to BHJ. To date, BHJ configuration has dominated OSCs' market and has been widely preferred over its predecessors (Schottky-junction and bilayer heterojunction) due to the remarkable performance it can offer (Xu et al., 2019, Yuan et al., 2019, Cui et al., 2020, Luo et al., 2020, Liu et al., 2020, Sun et al., 2020). Both advantages and limitations of the different configurations are being discussed below.

2.4.1 Single-layered Schottky-junction configuration

In the earliest form, OSCs consist of only a thermally evaporated *p*-type donor as the photoactive layer. This photoactive layer is placed between two metal electrodes with varying WF as illustrated in **Figure 2.2a**. Based on characteristics, Schottky-junction OSCs tend to produce sensible voltage but with very low photocurrent (Coakley and McGehee, 2004). The main reason behind this is due to the characteristic nature of short exciton diffusion length (~10-20 nm), where only those excitons generated within 20 nm from the depletion region can be dissociated (Hoppe and Sariciftci, 2004, Brabec et al., 2010). In Schottky-junction OSCs, the depletion region with thickness *W* provides a driving force for exciton dissociation process and is typically formed due to the Schottky contact existing between metal and semiconductor (as shown in **Figure 2.2b**) (Hoppe and Sariciftci, 2004). In other words, the depletion region is basically the only region where exciton will dissociate, thereby, making Schottky-junction OSCs to be exciton diffusion limited as most excitons will decay or recombine before even reaching this region. Consequently, a low charge carrier generation or photocurrent is often achieved in this configuration even though a substantial amount of sunlight can be potentially absorbed, leading to poor device performance. Studies shown that the performance of Schottky-junction OSCs remained relatively low for more than 20 years, with the highest to be 0.7% in 1978 as reported by Morel *et al.* (Morel et al., 1978). Such limitations have pushed the development of bilayer heterojunction configuration utilizing *n*-type acceptor and *p*-type donor as the photoactive layer.

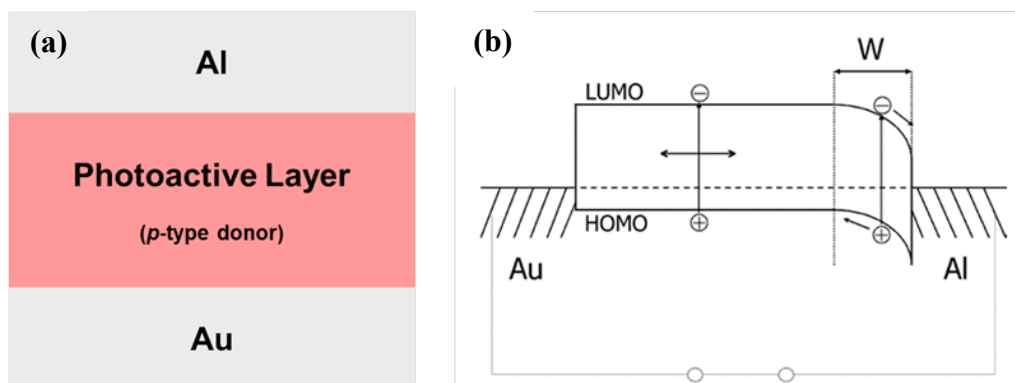


Figure 2.2 (a) Thermally evaporated photoactive layer (*p*-type donor) being sandwiched between two metal electrodes, one with higher WF (gold, Au) and another with lower WF (aluminium, Al). (b) Schematic of energy level diagram in Schottky-junction OSCs, where Schottky contact was formed with length W near the Al contact (Hoppe and Sariciftci, 2004). The negative sign represents electron's movement towards cathode (Al), whereas the positive sign represents hole's movement towards anode (Au).

2.4.2 Bilayer heterojunction configuration

Bilayer heterojunction photoactive layer configuration was first developed in 1986 by Tang to overcome the limitations of Schottky-junction configuration (Tang, 1986). In bilayer heterojunction OSCs, photoactive layer consisting of a *p*-type hole-transporting layer and a *n*-type electron-transporting layer, is placed between two metal electrodes with varying WF as illustrated in **Figure 2.3a**. At that time, Tang used phthalocyanine derivative for hole transport and perylene derivative for electron transport to fabricate OSCs with 1% efficiency and stated that the performance improvement was attributed to the enhanced exciton dissociation at the interface (Tang, 1986).

In bilayer heterojunction OSCs, exciton dissociation and charge carrier generation happen at the D/A interface, which is the planar interface formed when donor and acceptor materials are stacked together (Hoppe and Sariciftci, 2004). At the D/A interface, the gap in HOMO and LUMO energy level between donor and acceptor materials creates an electric field that prompts the effective exciton dissociation process (Huang and Deng, 2014). Moreover, bilayer heterojunction OSCs have monomolecular charge transport as depicted in **Figure 2.3b**, which promotes an effective charge separation at the interface with lower chance of recombination (Coakley and McGehee, 2004, Hoppe and Sariciftci, 2004). All these characteristics are the main contributors for better overall device performances of bilayer heterojunction OSCs over Schottky-junction OSCs.

Nevertheless, due to its short diffusion length and lifetime (Hoppe and Sariciftci, 2004, Brabec et al., 2010), exciton will still decay before reaching the D/A interface, rendering this device to be exciton diffusion limited. Small interfacial area of the D/A interface for exciton dissociation is also one of the limitations that restricts the performance of bilayer heterojunction OSCs (Cheng et al., 2009, McDowell et al., 2018, Zhang et al., 2018a). Device stability is lacking as well, mainly due to the interfacial erosion issues during fabrication of bilayer devices (Cheng et al., 2009). These conditions are the main culprits that limit the performance of bilayer heterojunction OSCs and consequently, lead to the development of BHJ OSCs.

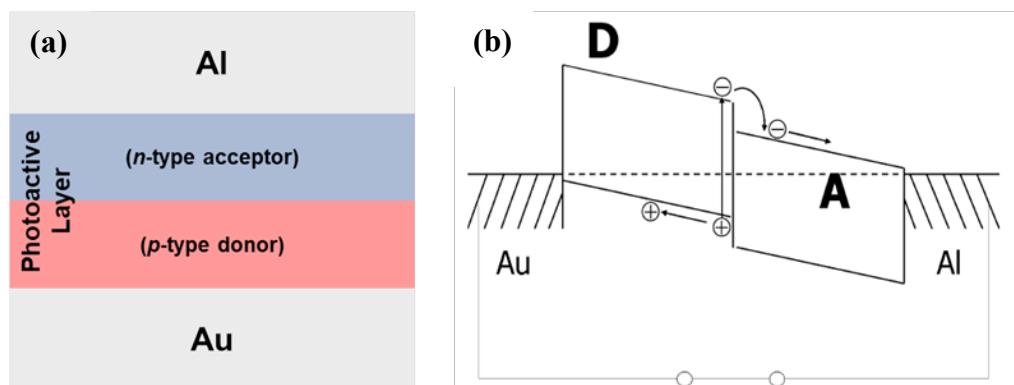


Figure 2.3 (a) Photoactive layer consisting of n -type acceptor and p -type donor, placed between two metal electrodes, one with higher WF (gold, Au) and another with lower WF (aluminium, Al). (b) Schematic of energy level diagram in bilayer heterojunction OSCs, where donor (D) contacts Au electrode and acceptor (A) contacts Al electrode (Hoppe and Sariciftci, 2004). The negative sign represents electron's movement towards cathode (Al), whereas the positive sign represents hole's movement towards anode (Au).

2.4.3 BHJ configuration

BHJ photoactive layer configuration was first invented in 1995 by Yu *et al.* to overcome the limitation of its predecessors (Schottky-junction and bilayer heterojunction configurations) (Yu *et al.*, 1995). In BHJ OSCs, the photoactive layer is made by blending p -type donor and n -type acceptor for hole and electron transport, respectively, and is usually placed between two metal electrodes with varying WF as illustrated in **Figure 2.4a**. **Figure 2.4b** shows the schematic diagram of energy level in BHJ OSCs.

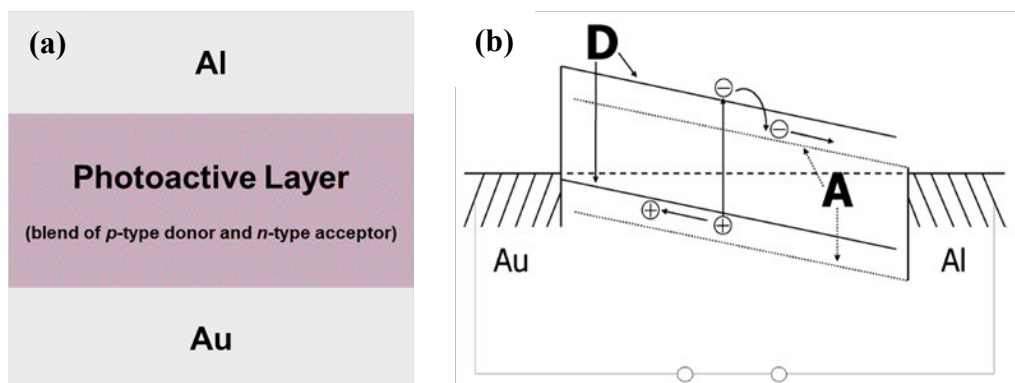


Figure 2.4 (a) Photoactive blend layer consisting of *n*-type acceptor and *p*-type donor, positioned between two metal electrodes, one with higher WF (gold, Au) and another with lower WF (aluminium, Al). (b) Schematic of energy level diagram in BHJ OSCs, where donor (D) contacts Au electrode and acceptor (A) contacts Al electrode (Hoppe and Sariciftci, 2004). The negative sign represents electron's movement towards cathode (Al), whereas the positive sign represents hole's movement towards anode (Au).

In BHJ OSCs, nanoscale interpenetrating networks of donor and acceptor domains are created via the blending of *n*-type acceptor and *p*-type donor (Hoppe and Sariciftci, 2004, Yang et al., 2005). Such morphology reduces the distance that exciton needs to travel, thus ensuring that majority of excitons can diffuse to the D/A interface for further dissociation before they decay or recombine. Large interfacial area of the D/A interface which is of greater magnitude than their predecessors is formed as well (Hoppe and Sariciftci, 2004, Yang et al., 2005). The large D/A interfacial area provides enough D/A interfaces across the photoactive layer, allowing exciton dissociation to happen anywhere across the film. Due to these characteristics, BHJ OSCs can promote not only a more effective and efficient exciton diffusion and dissociation, but also better charge generation and transport when compared with their predecessors. With such desirable features, BHJ configuration has dominated the OSCs' field as the go-

to photoactive layer configuration. In fact, most high-performing OSCs known to date are developed based on this photoactive layer configuration (Xu et al., 2019, Yuan et al., 2019, Cui et al., 2020, Luo et al., 2020, Liu et al., 2020, Sun et al., 2020). For instance, ground-breaking studies based on PBDB-T-2F:Y6 as reported by Yuan *et al.* utilized a BHJ photoactive layer configuration to obtain 15.7% efficiency performance (Yuan et al., 2019). It is important to note that those works were the first single-junction binary OSCs to reach 15% performance.

2.5 Structures of OSCs

Although BHJ photoactive layer can create effective exciton dissociation and charge carrier generation, it can still result in low performance when the interface between electrode and photoactive layer is being neglected. Due to this constrain, interfacial layer material is normally introduced in BHJ OSCs to act as an interface between the electrode and the photoactive layer. Interfacial layer is, therefore, another important constituent of OSCs apart from electrode and photoactive layer. This means that OSCs are generally comprised of three distinct layers (photoactive layer, interfacial layer and electrode). Those three components (photoactive layer, interfacial layer and electrode) can be arranged differently to form two different device structures, termed as conventional and inverted structures.

In conventional OSCs (as depicted in **Figure 2.5a**), the glass substrate (for rigid OSCs) or flexible substrate (for flexible OSCs) is typically coated with a thin layer of high WF ITO that functions as transparent bottom anode. The hole-transporting layer (HTL) or anode interfacial layer is deposited onto the ITO substrate. HTL is a selective layer with suitable energy level to block electron and promote hole extraction towards the anode and a classic HTL choice for conventional OSCs is PEDOT:PSS (Yin et al., 2016). PEDOT:PSS is usually employed to reduce the surface roughness of the underlying ITO layer so that a smoother and evenly distributed photoactive layer can be produced (Brebels et al., 2017). Though superior as HTL, PEDOT:PSS is highly hydrophilic and acidic in nature, which may cause harm to the underlying layer (Huang and Deng, 2014, Zeng et al., 2015, Yin et al., 2016), thus rendering it to be highly unsuitable for inverted OSCs. The photoactive layer is subsequently deposited on top of the HTL. In most cases, a blend between donor and acceptor materials (BHJ photoactive layer) made up the photoactive layer. Following the successful deposition, ETL or cathode interfacial layer will be deposited on top of the photoactive layer. ETL is a selective layer with suitable energy level to block hole and promote electron extraction towards the cathode (Yin et al., 2016). There is a wide-ranging of material options for ETL but recently, 2,9-bis[3-(dimethyloxidoamino)propyl]anthra[2,1,9-def:6,5,10-d'e'f]diisoquinoline-1,3,8,10(2H,9H)-tetrone (**PDINO**) and poly(9,9-bis(3'-(N,N-dimethyl)-N-ethylammonium-propyl-2,7-fluorene)-alt-2,7-(9,9-dioctylfluorene))dibromide (**PFN-Br**) are utilized mostly for conventional OSCs. Both PDINO and PFN-Br are alcohol-/water- soluble materials that give not only high electron mobility, excellent conductivity and good solubility but also good photochemical stability

(Nielsen et al., 2015). At last, low WF metal, functioning as cathode is deposited on top of the ETL. With this conventional structure, free-moving electrons are forced to move towards the top electrode (cathode or lower WF electrode), whereas free-moving holes moved towards the bottom electrode (anode or higher WF electrode) (as illustrated in **Figure 2.5c**).

Inverted OSCs (as shown in **Figure 2.5b**) can also make use of ITO-coated glass substrate as the transparent bottom electrode. Yet, the top electrode must be substituted with materials having higher WF than ITO. As a result, ITO electrode in inverted OSCs functions as cathode for collecting electron, while the top electrode serves as the anode for collecting hole. This implies that the movements of free-moving electron and hole are reversed in inverted OSCs (as illustrated in **Figure 2.5d**). Based on the same concept, ETL and HTL are still utilized as the interfacial layer between electrode and photoactive layer to improve OSCs' performance by providing a suitable charge transport direction for the free charge carriers. On the whole, molybdenum oxide (MoO_3) as HTL and ZnO as ETL are the popular choice for inverted OSCs. MoO_3 is often used in inverted OSCs due to its good ambient stability and non-acidic nature, while solution-processed ZnO is used due to its high transparency in the visible light region and good electron affinity (Yin et al., 2014).

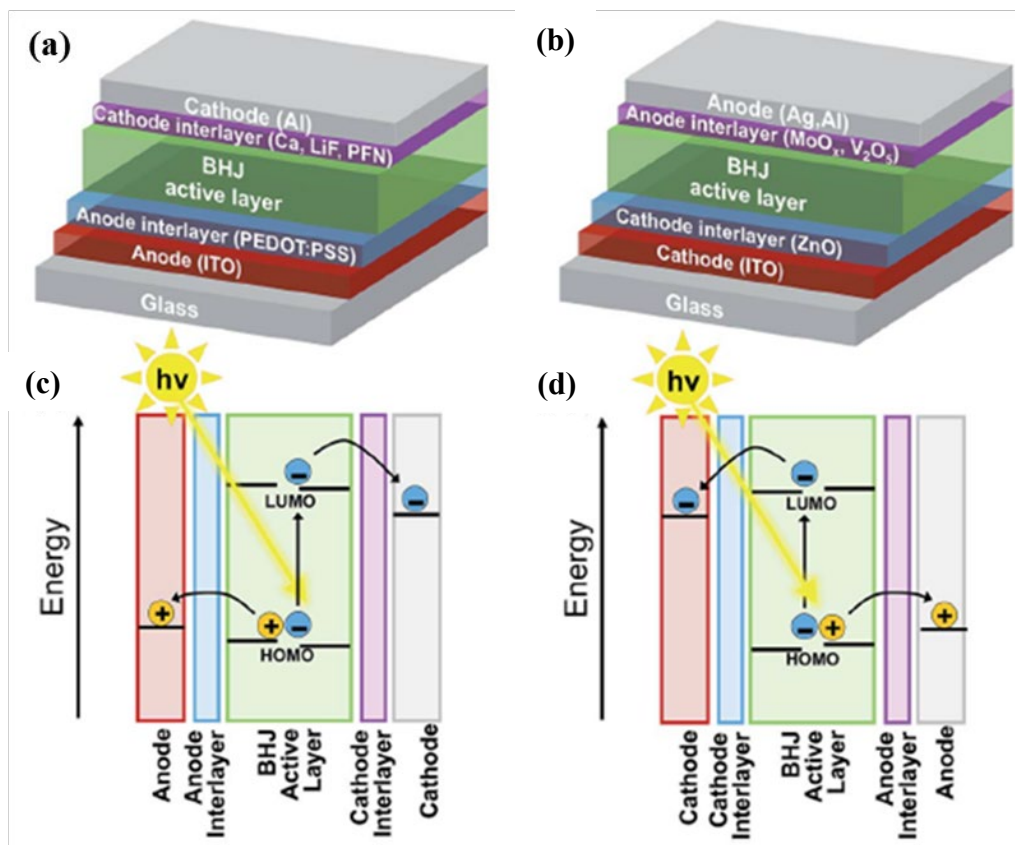


Figure 2.5 General structures of (a) conventional and (b) inverted OSCs (McAfee et al., 2015). Schematic of energy level diagram for (c) conventional OSCs and (d) inverted OSCs, where it shows electron's and hole's movements upon illumination (McAfee et al., 2015). The negative sign represents electron's movement, whereas the positive sign represents hole's movement.

2.6 Fabrication of OSCs

In order to fabricate OSCs, the three main components (photoactive layer, interfacial layer and electrode) are normally prepared and deposited through layer-by-layer approach. To date, there are several preparation and deposition techniques for the fabrication of OSCs, yet the choice of techniques highly depends on material characteristics. Both preparation and deposition techniques

for the fabrication of OSCs, along with their compatibilities with different materials (polymeric, SM, metal and inorganic materials) are discussed below.

2.6.1 Preparation techniques

In general, two commonly used preparation techniques for the fabrication of OSCs are vacuum evaporation and solution-processing techniques (Gunes et al., 2007). In vacuum evaporation technique, materials in solid or powder form can be utilized directly without processing. Those materials are normally coated onto the substrate in a high-vacuum chamber with pressure less than 10^{-5} mbar (Gunes et al., 2007). On the contrary, solution-processing technique usually involves the dissolution of materials in an appropriate processing solvent (e.g., non-polar or polar organic solvent). Those solutions are then deposited onto the substrate via printing or coating technologies (Hoppe and Sariciftci, 2004, Brabec, 2004).

Typically, polymeric materials are more suitable to be prepared through solution-processing technique rather than vacuum evaporation technique. This is because vacuum evaporation requires high-temperature processing while polymers easily decompose under high temperature and have extremely large molar mass for evaporation (Gunes et al., 2007). Thus, vacuum evaporation technique is highly preferable for SM, metal or inorganic materials as they are thermally more stable (Gunes et al., 2007). Nevertheless, some SM or inorganic materials can also be prepared via solution-processing technique as their solubilities in the processing solvent do not raise any concern (Zhang et al., 2017). Both preparation techniques have been utilized for the fabrication of

OSCs, but whenever possible, solution-processing technique is preferred as it has greater opportunity for large-scale manufacturing due to the ease of fabrication that saves energy, cost and time. Typically, state-of-the-art OSCs incorporate BHJ photoactive layer that is processed via solution-processing technique, interfacial layers that are fabricated using either solution-processing technique (e.g., PEDOT:PSS, PDINO, ZnO) or vacuum evaporation technique (e.g., MoO₃) and metal electrodes that are processed via vacuum evaporation technique (e.g., Al) (Xu et al., 2019, Yuan et al., 2019, Cui et al., 2020, Luo et al., 2020, Liu et al., 2020, Sun et al., 2020).

2.6.2 Deposition techniques

After the preparation of materials using vacuum evaporation or solution-processing techniques, they are deposited layer-by-layer onto the substrate to form conventional or inverted OSCs. Materials that are prepared through vacuum evaporation technique can be directly deposited onto the substrate. Meanwhile, materials prepared using solution-processing technique are typically deposited onto the substrate using printing or coating technologies.

Printing and coating techniques are both methods employed to deposit solution-processed materials to form a thin-film. By definition, printing is an approach in which the ink layer is transplanted from a stamp to a substrate by a reversing action, while coating is a process in which ink is transferred to the substrate by either pouring, painting, spraying or casting (Krebs, 2009). Thus, printing technique is a necessary tool for ensuring a high-volume productivity and significant cost reduction of PV technology, while coating technique is

mostly utilized for small-scale study such as laboratory study (Brabec, 2004). In current state, OSCs are still in the development stage requiring small-scale laboratory studies. Hence, coating technology remains as the more popular technique to date for the deposition of solution-processed materials in OSCs.

An example of coating technology is spin coating, which is a zero-dimensional coating technique that allows the formation of uniform films throughout the surface (coating without a pattern) (Krebs, 2009, Ge et al., 2014, Carle et al., 2017). Spin coating is an easy and simple lab-scale deposition method, where film properties (e.g., thickness and morphology) can be controlled effectively by manipulating the operating conditions (e.g., rotational speed, diffusivity and volatility) (Krebs, 2009). Generally, spin coating can be operated via these simple mechanisms: i) application of solution on top of the flat substrate, ii) variation in rotational speed of the disc causing the disc to spin, iii) spinning of the disc induces acceleration of the substrate, iv) liquid on top of the substrate spreads out evenly due to the centrifugal force resulted from the accelerating substrate and v) evaporation and drying of liquid throughout its uniform spreading, resulting in the formation of homogeneous film with minimal defect concentration (Krebs, 2009). **Figure 2.6** illustrates the spin coating process.

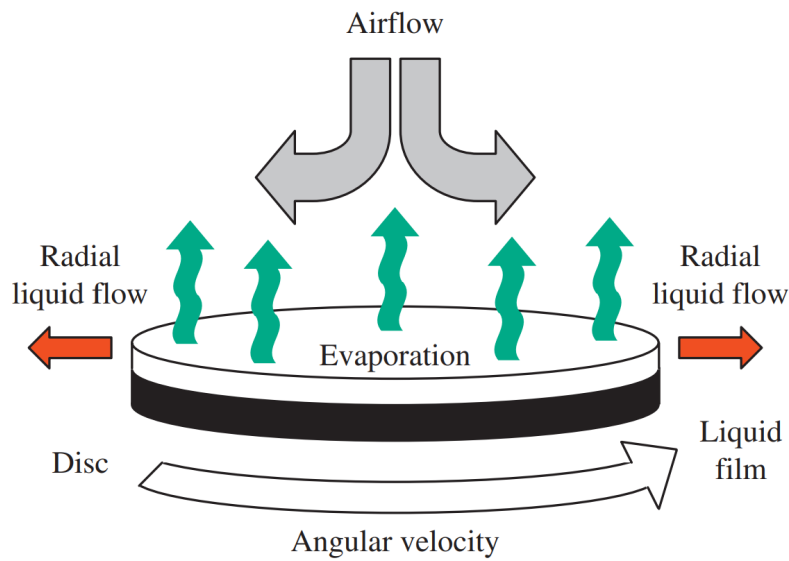


Figure 2.6 Illustration of spin coating process (Krebs, 2009).

As of now, spin coating is considered as the more superior technique for the deposition of solution-processed materials due to the minimal development of other printing and coating technologies. High-performing OSCs as reported by Cui *et al.*, Luo *et al.* and Liu *et al.* for example, still made use of spin coating method to deposit solution-processable materials (Cui *et al.*, 2020, Luo *et al.*, 2020, Liu *et al.*, 2020). However, spin coating is unfavourable for large-scale operation as it has larger solution volume loss (most of the solution applied on the substrate is ejected away during spinning) (Krebs, 2009). Therefore, the development of other printing and coating technologies that are compatible for roll-to-roll productions (e.g., inkjet printing, screen printing, knife-over-edge coating, slot-die coating, etc), will be crucial in the near future to support large-area and large-scale manufacturing of OSCs. In the past few years, some studies had adopted such printing and coating technologies, compatible for large-area OSCs fabrication. For instance, Corzo *et al.* adopted inkjet printing to deposit photoactive layer, where a device performance of $\sim 6\%$ was obtained in 2 cm^2

device (Corzo et al., 2019). Though the resulting device performance was still considerably low as compared with those processed with spin coating method, it still had potentials to initiate future studies on large-area OSCs fabricated using printing technologies.

2.7 Key Performance Parameters in OSCs

The performance of OSCs is analysed based on several key parameters that are inter-correlated to one another. These parameters are open circuit voltage (V_{oc}), short circuit current (J_{sc}), fill factor (FF), series and shunt resistances, external quantum efficiency (EQE) and most importantly, power conversion efficiency (PCE). OSCs' performance can be evaluated based on their PCEs to determine the effectiveness in converting solar irradiation to electrical energy. Nonetheless, it is also important to understand other key performance parameters of OSCs as they affect the PCE of OSCs significantly. The key performance parameters of OSCs are discussed below.

2.7.1 Open circuit voltage (V_{oc})

Open circuit voltage or abbreviated as V_{oc} , is expressed as the maximum cell voltage provided by a solar cell under no current condition ($J = 0$) (Heeger, 2014). V_{oc} is typically measured in volt (V) and mainly affected by the cell's electric field. Earlier studies shown that V_{oc} had a strong linear correlation with the difference in LUMO and HOMO energy level of acceptor and donor

materials when blended together (Brabec et al., 2001, Scharber et al., 2006, McDowell et al., 2018). It is represented with the empirical equation as follow:

$$e \cdot V_{oc} = (|E_{HOMO(D)}| - |E_{LUMO(A)}|) - 0.3 \quad (1)$$

where V_{oc} [V] is the open circuit voltage, E [eV] is the energy level (HOMO or LUMO), e is the elementary charge and 0.3 is an empirical number denoting the LUMO-LUMO offset between donor and acceptor materials. The relationship between V_{oc} and the energy level of donor and acceptor materials is also depicted in **Figure 2.7**.

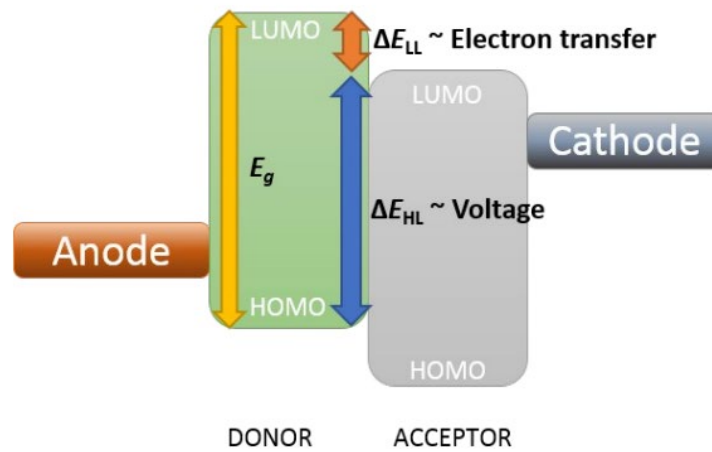


Figure 2.7 Schematic of energy level diagram of BHJ OSCs (omitting interfacial layer, such as HTL and ETL) (Brebels et al., 2017). Optical bandgap, E_g is the difference between HOMO and LUMO energy level of donor material as it is mostly responsible for light absorption. ΔE_{LL} is the LUMO-LUMO offset between donor and acceptor materials. ΔE_{HL} is the difference between HOMO and LUMO energy level of donor and acceptor materials, respectively.

Theoretically, it is desirable to have high V_{oc} performances in OSCs. High V_{oc} values can be obtained by maximizing the energy level difference between donor and acceptor materials, such as by using a donor material with low-lying HOMO and/or acceptor material with high-lying LUMO. For instance, Zhang *et al.* designed a polymer donor called PBDB-T-2F with low-lying HOMO of 5.45 eV, which was beneficial for high V_{oc} performance in OSCs (Zhang et al., 2015). However, increasing HOMO_(D)-LUMO_(A) offset will cause a smaller LUMO-LUMO offset between donor and acceptor materials, which is responsible for exciton dissociation process. Hence, in return to lower energy loss and higher V_{oc} , having large HOMO_(D)-LUMO_(A) offset can result in a lower J_{sc} value due to the less efficient exciton dissociation process. Based on the rule of thumb, LUMO-LUMO offset should not be less than 0.3 eV to guarantee sufficient driving force for electron transfer so that efficient exciton dissociation process can occur at the interface (Scharber et al., 2006, Facchetti, 2013, Menke et al., 2018).

Aside from energy level, V_{oc} were also reported to be affected by the WF of electrodes to a certain extent because the difference in WF provided external electric field to the cell (Brabec, 2004). Moreover, it was reported by Perez *et al.* that V_{oc} could also be influenced by the morphology and molecular structure of photoactive layer (Perez et al., 2009).

2.7.2 Short circuit current (J_{sc})

Short circuit current or abbreviated as J_{sc} , is typically measured in milliamperes per square centimetre (mA cm^{-2}) and defined as the current that

flows in the cell when there is no external resistance present ($V = 0$) (Heeger, 2014). The electron movement throughout the cell upon illumination induces this current flow, which correlates to the amount of free charge carrier generated. Thus, the theoretical upper limit of J_{sc} can be attained by increasing the number of free charge carrier generated, such as by improving the light absorption performance of the photoactive layer and/or optimizing the photoactive layer's morphology (Huang and Deng, 2014).

A widely accepted method to improve photoactive layer's morphology is through the utilization of BHJ configuration, where it creates a percolative donor and acceptor domains to promote efficient generation, diffusion and dissociation of exciton, as well as generation and transport of free charge carrier. Further improvements in BHJ morphology can also be conducted to maximize the J_{sc} values for better OSCs' performance. For instance, by varying processing conditions of the BHJ photoactive layer, such as by adjusting the D:A ratio and the concentration of solid in solvent, choosing suitable processing solvent, adding chemical additives or utilizing post-production treatment (thermal annealing and solvent treatment). Through the optimization of these parameters, excessive or large-scale phase segregations of donor and acceptor domains that are detrimental to device performance can be prevented, which helps to boost the J_{sc} performance. For example, Yuan *et al.* utilized a high-performing PBDB-T-2F:Y6 photoactive blend layer and investigated the effect of D:A ratio, additives ratio and annealing treatment to device performance (Yuan et al., 2019). As reported, a slight change of D:A ratio from 1:1 to 1:1.2 could increase the J_{sc} values from 25.25 to 25.32 mA cm⁻². Varying additives ratio could slightly tune the J_{sc} values as well. Varying annealing treatment seemed to be the most

effective approach to improve J_{sc} values as non-annealed device only exhibited J_{sc} of 24.31 mA cm⁻² while those annealed at 110°C exhibited J_{sc} of 25.32 mA cm⁻². Those findings explained the role of processing condition in tuning photoactive layer's morphology for better J_{sc} performances.

Another efficient way to improve J_{sc} is by narrowing the E_g of donor materials in the photoactive layer to allow more sunlight to be absorbed (improved light absorption performance). E_g of donor materials can be reduced by raising HOMO energy level and/or lowering LUMO energy level of donor materials. However, raising HOMO energy level of donor materials will consequently lead to a smaller HOMO_(D)-LUMO_(A) offset, which in turn lowers the V_{oc} performance to a certain extent (see **Figure 2.7** for clearer illustrations). Lowering LUMO energy level of donor materials will also result in a smaller LUMO-LUMO offset between donor and acceptor materials, which limits exciton dissociation process at the D/A interface (see **Figure 2.7** for clearer illustrations). In this case, there is a certain extent where the donor material's LUMO energy level can be reduced. Based on the rule of thumb, the LUMO of donor must be higher than that of the acceptor and the difference between those LUMOs should not be less than 0.3 eV for energetically favourable electron transfer (Scharber et al., 2006, Facchetti, 2013, Menke et al., 2018).

As discussed, a trade-off between favourable electron transfer (via tuning LUMO-LUMO offset of donor and acceptor materials), high J_{sc} (via narrowing or reducing E_g of donor materials) and high V_{oc} (via tuning HOMO_(D)-LUMO_(A) offset) needs to be determined. Finding this trade-off, however, has remained a great challenge as simultaneous enhancement in all these parameters is nearly

impossible, thus limiting the PCE of OSCs. The relationships between PCE and those parameters are summarized in **Figure 2.8**.

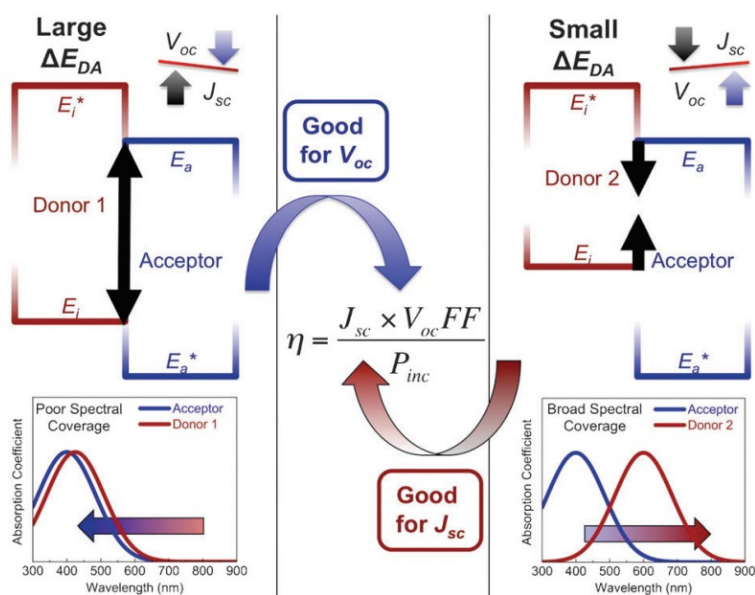


Figure 2.8 The relationship of electron transfer, V_{oc} and J_{sc} to PCE (Schlenker and Thompson, 2011). Two hypothetical donors (D1 and D2) are introduced with the same LUMO energy level but different HOMO energy level. D2 has a smaller E_g compared to D1 due to its high-lying HOMO. Other parameters are kept constant, including HOMO and LUMO energy level of acceptor. With this, LUMO-LUMO offset responsible for electron transfer is kept constant. D1 has a low energy loss (high V_{oc}) but its large E_g results to a poor absorption of light (low J_{sc}), while D2 has a broad spectral coverage for absorption due to its narrow E_g (high J_{sc}) but with a higher energy loss (low V_{oc}).

2.7.3 Fill factor (FF)

Fill factor or abbreviated as FF , measures the quality of a solar cell by comparing the actual maximum power output ($V_{max} \times J_{max}$) to theoretical maximum power output ($V_{oc} \times J_{sc}$) (Facchetti, 2013, Ge et al., 2014, Heeger, 2014), which is represented by the equation below:

$$FF = (V_{\max} \cdot J_{\max}) / (V_{oc} \cdot J_{sc}) \quad (2)$$

where FF is the fill factor, V_{\max} [V] is the maximum voltage generated, V_{oc} [V] is the open circuit voltage, J_{\max} [mA cm^{-2}] is the maximum current generated and J_{sc} [mA cm^{-2}] is the short circuit current. The ratio of these parameters can be illustrated in a typical current density vs voltage (J - V) characteristic curve as displayed in **Figure 2.9**.

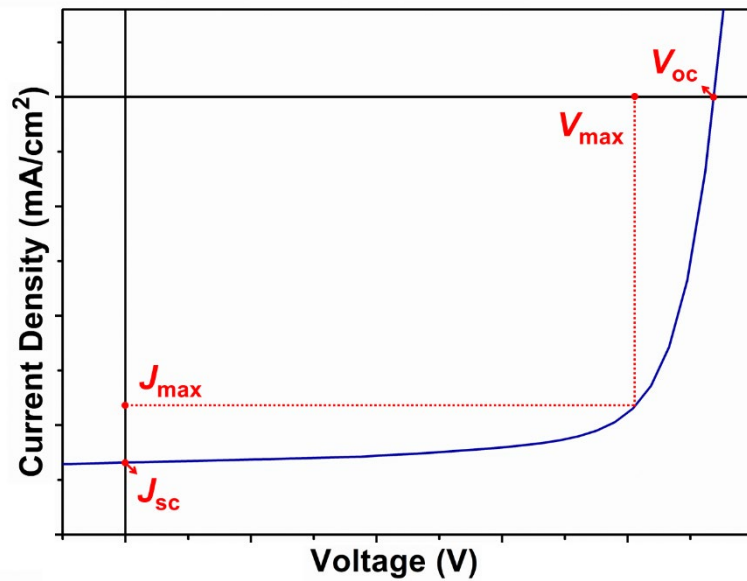


Figure 2.9 Typical current density vs voltage (J - V) curve in OSCs under illumination. The area of curve enclosed by V_{\max} and J_{\max} represents the actual maximum power output, while that enclosed by V_{oc} and J_{sc} represents the theoretical maximum power output. The ratio of actual power output to theoretical power output gives FF .

FF is a ratio from 0 to 1 as the actual maximum power output ($V_{\max} \times J_{\max}$) is always smaller than the theoretical maximum power output ($V_{oc} \times J_{sc}$). But in most cases, FF is often expressed in percentage form (%) from 0-100% range. Theoretically, it is desirable to have high FF performances in OSCs. High FF values are achieved in OSCs when free charge carriers are successfully

swept-out to their respective electrodes before recombination takes place (Gunes et al., 2007, Huang and Deng, 2014, Heeger, 2014). Hence, it is important for OSCs to have good charge carrier mobility and low charge recombination to ensure the charge carriers are successfully transported and extracted to the electrodes for higher FF performances. An approach to accomplish this is by having a slow photoactive layer growth rate, which can be achieved through longer solidification time of the photoactive layer. Li *et al.* proved this, where a slower growth rate was found to promote desirable photoactive layer morphology for improving hole mobility to acquire higher FF (Li et al., 2005).

2.7.4 Series and shunt resistances

Series and shunt resistances measured in ohm (Ω), strongly influence the FF performances in OSCs (Yip and Jen, 2012). Hence, it is vital to understand the concept behind series and shunt resistances in OSCs to improve performance. Series resistance (R_s) is normally governed by the conductivity of electrodes and organic materials and the contact resistance between them, whereas shunt resistance (R_{sh}) is determined by the quality of the photoactive layer (Yip and Jen, 2012). Thus, R_s is related to materials and contact engineering, while R_{sh} depends on the current leakage in the photoactive layer through pinholes, traps or recombination (Liao et al., 2010).

In normal circumstances, it is highly desirable to have OSCs with small R_s to escalate the forward current and large R_{sh} to prevent loss of charge carriers in the photoactive layer. One strategy to increase R_{sh} was conducted by Li *et al.*, where a suitably thick photoactive layer was used to minimize pinholes and

microcracks (Li et al., 2005). Furthermore, Li *et al.* also studied the degree of polymer self-organization in the photoactive layer by controlling the drying rate of the photoactive layer film. In the study, photoactive layer growth rate was controlled by varying the time taken for the wet film to solidify – longer solidification time gave slower growth rate. In this case, Li *et al.* found that slower growth rate was more desirable to reduce R_s as compared to fast growth rate (Li et al., 2005). Thus, simple strategies such as opting for thicker photoactive layer or controlling photoactive layer growth rate can be taken into consideration to reduce R_s and increase R_{sh} values.

2.7.5 External quantum efficiency (EQE)

EQE quantifies the number of electrons accumulated at the cathode given a specific number of incident photons at a specific wavelength during light irradiation (Huang and Deng, 2014, Ge et al., 2014). EQE is defined in the equation below:

$$EQE = [(1240 \cdot J)/(\lambda \cdot P_{in})] \quad (3)$$

where EQE [%] is the external quantum efficiency, J [mA cm^{-2}] is the current density, P_{in} [mW cm^{-2}] is the incident photon's power and λ [nm] is the wavelength of the incident photons. Take note that 1240 is a constant with a unit of mW nm mA^{-1} , simplified from Planck constant, speed of light in a vacuum and elementary charge.

A high EQE characterizes the ability of OSCs to generate and collect electrons effectively after being irradiated with light. Therefore, high EQE values are preferable in OSCs for achieving high energy conversion efficiencies. Referring to the equation, EQE and J_{sc} performances are related, which means that higher EQE in OSCs can be achieved by improving the J_{sc} performance. As mentioned previously, optimization of photoactive layer's morphology is one of the strategies that can boost J_{sc} and EQE performances simultaneously.

2.7.6 Power conversion efficiency (PCE)

Power conversion efficiency or abbreviated as PCE, measures how efficient an OSC can convert sunlight into electricity. It is a measure of the ratio between power output and power input, which can be represented by the following equation:

$$PCE = (V_{oc} \cdot J_{sc} \cdot FF) / P_{in} \quad (4)$$

where PCE [%] is the power conversion efficiency, V_{oc} [V] is the open circuit voltage, J_{sc} [mA cm^{-2}] is the short circuit current, FF [%] is the fill factor and P_{in} [mW cm^{-2}] is the incident photon's power. The three important constituent parameters of PCE (V_{oc} , J_{sc} and FF) can be extracted from a standard J - V curve as shown in **Figure 2.9**.

Conventionally, high PCE is desirable as an indication for high-performing OSCs. It is particularly important for OSCs to have high PCE if commercialization is to be realized. Higher PCE in OSCs can be attained by simultaneously improving the V_{oc} , J_{sc} and FF values, for example, by opting for

narrow E_g donor materials to absorb light effectively for higher J_{sc} , proper tuning of the energy level of donor and acceptor materials for higher V_{oc} , selecting materials with high charge carrier mobility to enhance J_{sc} and FF , and/or optimizing photoactive layer's morphology with desirable phase separation to simultaneously improve V_{oc} , J_{sc} and FF values. On a side note, morphology optimization may enhance V_{oc} by reducing recombination losses, but only to the extent pinned by the HOMO_(D)-LUMO_(A) offset.

2.8 Performance Enhancement Strategies in OSCs

Three main approaches have been used to enhance OSCs' performance, particularly in terms of their PCE values. This includes material design, morphology control and device engineering. Material design as the name suggests, is a strategy to develop novel organic material via judicial design of molecular structure, such as the addition of specific atom into the molecular structure, the rearrangement of molecular structure, etc. This strategy is normally employed to synthesize novel high-performing photoactive layer (Cui et al., 2020, Liu et al., 2020, Luo et al., 2020, Qin et al., 2020a, Sun et al., 2020) and/or interfacial layer materials (Zhang et al., 2014, Peng et al., 2018, Li et al., 2020). However, studies about material design on the photoactive layer are more commonly found due to their role in boosting OSCs performance. Detailed discussion about material design strategy used on the photoactive layer can be found in the next sub-section.

Morphology control, on the other hand is a strategy that alters the morphological properties of a surface. This is conducted via modification of processing conditions that include D:A blend ratio, concentration of solid in solvent, choice of processing solvent, additives addition and/or post-production treatment (annealing and solvent treatment). In OSCs, morphology control via modification of those processing conditions can be used on solution-processed layers such as photoactive and interfacial layers to optimize device performance (Zhang et al., 2014, Peng et al., 2018, Cui et al., 2020, Liu et al., 2020, Luo et al., 2020, Qin et al., 2020a, Sun et al., 2020). Detailed discussion on morphology control strategy can be found in the next sub-section.

Lastly, device engineering is a strategy that mainly alters the pristine properties of interfacial layer, photoactive layer and/or electrode to improve the overall device performance. Here, the pristine properties include optical, electrical, mechanical and morphological properties. Several methods can be opted to achieve such desirable effect. For instance, doping of photoactive layer could induce significant change in morphological, optical and/or electrical properties (Chen et al., 2016). Similarly, doping of solution-processed electrode (e.g., PH1000) could alter the mechanical properties of pristine electrode for flexible device application (Peng et al., 2019). Other method such as the deposition of an additional layer on top of the interfacial layer could also be conducted to modify the electrical and morphological properties of pristine interfacial layer (Borse et al., 2018). Detailed discussion on device engineering strategy can be found in the next sub-section.

All three strategies are strongly related to one another. In fact, it is impossible to obtain an optimum device performance with only material design, morphology control or device engineering strategy. For example, novel material synthesized for photoactive layer may need further tuning in terms of processing condition to optimize its surface morphology, thus, incorporating morphology control strategy as well. Incorporating ternary photoactive layer as device engineering strategy may drastically enhance device performance, provided that there is a proper tuning of processing condition (e.g., D:A blend ratio, concentration of solid in processing solvent, etc), combining the use of device engineering and morphology control strategies. Some researchers even manage to incorporate the three performance enhancement strategies into their work to obtain the optimum device performance. A literature published by Chen *et al.* is a good example of it (Chen et al., 2020). In his work, Chen *et al.* managed to design and synthesize a novel donor material named ECTBD using material design strategy. It was then added into the PBDB-T-2F:Y6 photoactive layer system to form a ternary photoactive layer. The film's morphology was tuned via optimizing the processing condition to control the final film's morphology. As a result, an optimum device performance of 16.51% with improved J_{sc} and FF was achieved in devices based on PM6:ECTBD:Y6 photoactive layer. Those studies incorporated all material design, morphology control and device engineering strategies on the photoactive layer, explaining the role of each strategy and how it could support the other strategies to obtain the optimum device performance.

Just like Chen's work, other studies that incorporated more than one performance enhancement strategy can be found frequently. In this case, the main research highlight should be the key determining factor to distinguish which performance enhancement strategy is used. For instance, even though Chen's work includes all three performance enhancement strategies, its research highlight still lies clearly on the synthesis of novel ECTBD donor via material design strategy.

2.8.1 Material design

Studies about material design on the photoactive layer are more commonly found as compared to interfacial layer. In fact, most efforts in OSCs have been made towards synthesizing novel donor and acceptor materials for the photoactive layer to obtain high-performing OSCs (Xu et al., 2019, Wang et al., 2019b, Yuan et al., 2019, Luo et al., 2020, Cui et al., 2020, Sun et al., 2020). This strategy is proven to be successful as by 2020, the PCE of single-junction BHJ OSCs had reached the 15-18% range (Xu et al., 2019, Yuan et al., 2019, Cui et al., 2020, Luo et al., 2020, Liu et al., 2020, Sun et al., 2020). The most revolutionary work was conducted by Yuan *et al.* in 2019, where Yuan *et al.* developed a novel BTP-based acceptor called Y6 to boost the performance of OSCs beyond 15% (Yuan et al., 2019). Yuan *et al.* shifted the research direction from ITIC-based SM acceptors to BTP-based SM acceptors and the catalyst to further studies of BTP-based SM acceptors. For instance, BTP-eC9 and BTP-eC11 developed by Cui *et al.* in 2020 (Cui et al., 2020), or BTP-2F-ThCl developed by Luo *et al.* in 2020 (Luo et al., 2020) were both derived from Y6 SM acceptors.

The design of novel donor and acceptor materials is focused primarily on their molecular structures. They can be designed via main-chain engineering (engineering on the backbone of organic materials as displayed in **Figure 2.10**) and/or side-chain engineering (engineering on the side chain and substituent components attached to the backbone of organic materials as shown in **Figure 2.10**) (Zhang and Li, 2015, Xiao et al., 2017).

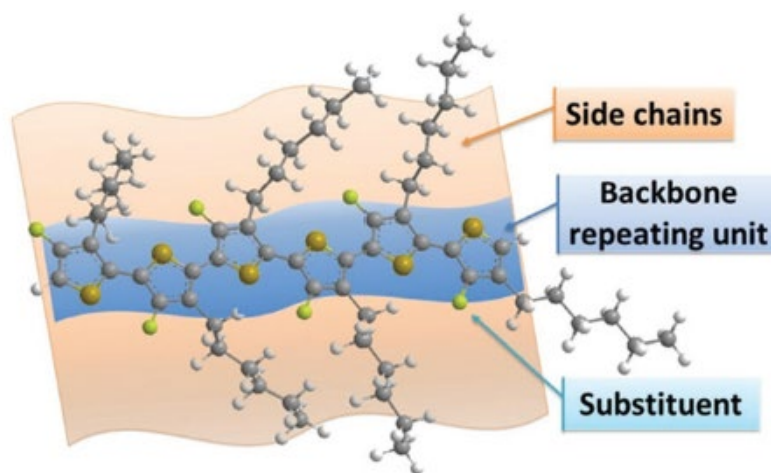


Figure 2.10 Typical molecular structure of organic materials, composed of backbone, side chain and substituent components (Zhou et al., 2012).

An example of main-chain engineering is the copolymerization of donor and acceptor moieties into one system (D-A copolymerization) to allow fine tuning of energy level, such that desirable HOMO and LUMO energy level can be achieved (Li, 2012, Zhang and Li, 2015, Xiao et al., 2017). For instance, Bang *et al.* conducted the copolymerization of D-A alternating unit from three monomers of benzodithiophene and terthiophene as donor unit and *N*-alkylthieno[3,4-*c*]pyrrole-4,6-dione as acceptor unit (Bang et al., 2017). The resulting polymer showed a low-lying HOMO of 5.56 eV and a narrow E_g of 1.84 eV. Recent study conducted by Sun *et al.* also demonstrated similar findings,

where the copolymerization of bithienyl benzodithiophene donor unit and monoalkoxy-substituted bifluoroquinoxaline acceptor unit resulted in low-lying HOMO of 5.47 eV and E_g of 1.92 eV in PBQ10 polymeric donor (Sun et al., 2020). Both studies explained the effectiveness of material design via D-A copolymerization to tune the energy level of the materials (e.g., HOMO, LUMO and E_g) through redistribution of frontier molecular orbitals.

On the other hand, there are two approaches to tune the molecular structure via side-chain engineering, which is through the utilization of flexible side chains and/or substituents (Li, 2012, Zhang and Li, 2015, Xiao et al., 2017). Wang *et al.* studied the effect of various side chain in their novel polymeric donor (Wang et al., 2013). It was found that polymer donor with alkylfuranlyl side chain group gave the best performance, providing a low bandgap of 1.77 eV, improved solubility in common processing solvent, low-lying HOMO of 5.40 eV and higher hole mobility. As reported by Liu *et al.*, the incorporation of side chain group could also effectively tune the energy level of organic materials (Liu et al., 2019d). In another research, the incorporation of methyl side chain in ITIC could tune the LUMO of the acceptor without causing too much steric hindrance for intermolecular packing (Li et al., 2016). Thus, efficient charge separation could still be achieved even when donor and acceptor had a lower LUMO-LUMO offset.

The utilization of substituent attached to the main backbone of organic materials could also be considered. For instance, Xiao *et al.* recently explained the role of electron-withdrawing substituent and electron-donating substituent in tuning the energy level of polymeric donor (Xiao et al., 2017). Based on the

study, incorporation of electron-withdrawing substituent could lower the HOMO energy level, while electron-donating substituent could increase the LUMO energy level. Zhao *et al.* also studied the influence of substituent in organic materials, in which fluorine was introduced as electron-withdrawing substituent in the polymer donor (Zhao *et al.*, 2017b). Zhao *et al.* found that the incorporation of fluorine could result in down-shifting of both HOMO and LUMO energy level with a relatively lower-lying HOMO (5.40 eV) compared to the non-fluorinated counterparts. All those studies suggested that an ideal choice of side chain and/or substituent could have a profound effect in tuning material's energy level, improving solubility properties and influencing aggregation properties, which were all crucial for better photovoltaic performance.

Overall, with proper design consideration of the main chain and side chain, organic materials can be engineered in terms of their molecular structures to function favourably as donor and acceptor in the photoactive layer for high-performing BHJ OSCs.

2.8.2 Morphology control

Even though excellent photoactive layer and/or interfacial layer can be synthesized through careful material design, it will still be impossible for BHJ OSCs to obtain an optimum PCE without the optimization of surface morphology. In OSCs, morphology control of the photoactive layer is particularly crucial and important to raise device performance by promoting a desirable phase separation between donor and acceptor materials. Therefore,

high-performing BHJ OSCs are typically achieved through combined strategies of material design and morphology control of the photoactive layer. In fact, both strategies are always utilized together to realize high-performing BHJ OSCs beyond 15% efficiency (Xu et al., 2019, Yuan et al., 2019, Cui et al., 2020, Luo et al., 2020, Liu et al., 2020, Sun et al., 2020).

The morphology of photoactive layer can be controlled and optimized by varying its processing conditions from preparation up to deposition conditions. These include D:A blend ratio, concentration of solid in solvent, choice of processing solvent, additives addition and post-production treatment. Optimal D:A blend ratio and concentration of solid in solvent are crucial requirements to achieve favourable nanoscale phase-separated morphology of donor and acceptor domains in BHJ OSCs. This is usually determined using trial-and-error method during experiments, where the effects of different D:A ratio and concentrations on OSCs' performance are being investigated. For example, Liu *et al.* showed the significant effect of varying D:A ratio on photovoltaic performance, where an optimum device performance could be obtained when judicial D:A ratio was made (Liu et al., 2019d). In this case, D:A ratio of 1:1 was the most suitable to promote favourable phase-separated morphology, thereby optimum device performance of 13.28% was obtained in PBDB-T:IDTCN-O - based device.

Good choice of processing solvent to dissolve donor and acceptor materials is also essential to control the final photoactive layer's morphology. Previous literatures had indeed shown that a sound choice of processing solvent could promote a desirable phase separation in the photoactive layer (Yang et al.,

2004). The choice of solvent is normally made based on these criteria: i) solvent should be able to dissolve donor and acceptor materials, ii) solvent should not form complex with donor and acceptor materials, iii) solvent should have a low boiling point and iv) solvent should promote phase separation in the photoactive layer (Zhang et al., 2017, McDowell and Bazan, 2017, McDowell et al., 2018). Fulfilling the aforementioned criteria are chloroform (CF) and chlorobenzene (CB), which are the two most widely used solvents to process photoactive layer.

Addition of solvent additive to the photoactive layer solution is also crucial to optimize the final photoactive layer's morphology. Studies had shown that additives could induce a desirable photoactive layer's morphology by affecting the degree of phase separation and the molecular orientation of donor and acceptor domains (He et al., 2018). The type of additive is normally chosen based on the fact that additive should be partly miscible in the processing solvent but is free to solvate donor, acceptor, neither or both (McDowell et al., 2018). Among the available choices, 1,8-diodooctane (DIO) and 1-chloronaphthalene (CN) are two commonly used additives for photoactive blend layer. Zhou *et al.* studied the effects of adding a series of brominated compounds into DIO to function as binary additives (Zhou et al., 2017). Those binary additives displayed positive effects on the absorption performance, charge transport and film morphology, which brought about enhancement in photovoltaic performance.

Post-production treatment is another technique used to engineer the final photoactive layer's morphology, so that insufficient or excessive phase separation can be prevented. Post-production treatment can be conducted either through solvent treatment (Li et al., 2011, Nam et al., 2012, Liu et al., 2012, Sun

et al., 2015) or thermal annealing (Li et al., 2005, Zhang et al., 2012, Jagadamma et al., 2017). In solvent treatment, photoactive blend films are exposed to a certain solvent, either in vapour or liquid form to tailor the films' morphology (Li et al., 2011). Meanwhile, photoactive blend films are subjected to heat for a short duration in thermal annealing treatment to tailor the films' morphology through further migration and crystallization of molecules (Jorgensen et al., 2008). Previous literatures had shown that both post-treatment techniques could alter the phase separation and crystallization degree in the photoactive layer (Nam et al., 2012, Zhang et al., 2012). As a result, a desirable phase-separated photoactive layer's morphology could be achieved through employing post-production treatment. Yuan *et al.* also utilized annealing treatment to optimize PBDB-T-2F:Y6 blend morphology (Yuan et al., 2019). In fact, annealing treatment seemed to be the most effective strategy in this work to improve device performance in terms of J_{sc} . A boost in J_{sc} value was observed from 24.31 to 25.32 mA cm⁻² when non-annealed device was compared to that annealed at 110°C. One of the reasons contributing to the increment was the smoother photoactive layer's morphology with evenly distributed and uniform nanoscale phase separation between donor and acceptor domains.

In short, optimizing all the aforementioned processing conditions can result in the optimization of photoactive layer's morphology with desirable nanoscale phase separation between donor and acceptor domains. This consequently promotes better photovoltaic performances in BHJ OSCs. The control of morphology via optimization of processing conditions (e.g., concentration of solid in solvent, choice of processing solvent and post-production treatment) not only applies to photoactive layer, but also to solution-

processed interfacial layers like PEDOT:PSS, PDINO and ZnO to control their final film morphologies.

2.8.3 Device engineering

Device engineering gains lesser attention as compared to other performance enhancement strategies, even when it plays an equally pivotal role in enhancing OSCs' performance. In general, device engineering can be conducted via modification of interfacial layer (Zheng et al., 2018, Xiong et al., 2019), photoactive layer (Zhou et al., 2018, Liu et al., 2019a) or electrode layer (Fan et al., 2016, Shin et al., 2018, Song et al., 2020b) to alter their pristine properties and consequently, improve the overall device performances.

In OSCs, interfacial layers are utilized to improve photovoltaic performance by solving the charge extraction and mobility issues (Yip and Jen, 2012, Zeng et al., 2015, Yin et al., 2016). The use of interfacial layer is exceptionally crucial for non-fullerene -based OSCs as non-fullerene acceptor is often associated with an up-shifted LUMO ($\sim 3.7-4.0$ eV) that leads to poor electron extraction (Zhao et al., 2017a, Zhu et al., 2018). In this case, interfacial layer such as ETL is employed to tune the WF of cathode to better match the LUMO energy level of such non-fullerene acceptor, so that issues regarding poor electron extraction in non-fullerene -based OSCs can be solved. Apart from its WF tuning ability, interfacial layer can also improve OSCs' performance through several other mechanisms and functions (Yip and Jen, 2012, Zeng et al., 2015, Yin et al., 2016). It can be used to promote Ohmic contact at the electrode/photoactive layer interface to enhance charge extraction, transport and

collection. It can be utilized to alter charge selectivity by providing energy barrier that blocks electron and hole from moving towards the wrong electrode. It can also be employed to alter the morphology of the photoactive layer to promote efficient generation, diffusion and dissociation of exciton, as well as generation and transport of free charge carrier. And lastly, it can also be applied to modulate optical field in the photoactive layer to improve light absorption. Overall, this suggests the importance of interfacial layer in OSCs to improve device performance, particularly when a judicious choice of interfacial layers (including ETL and HTL) is made. The choice is typically made based on material's properties (e.g., conductivity, solubility, wettability, etc) and suitability with different OSCs' structures (conventional or inverted).

Improvement in device performance can be further made by employing interfacial layer modification or interface engineering strategy. This strategy focuses on improving the pristine properties of interfacial layer to function more effectively as interface between electrode and photoactive layer. This can be done either via doping of materials into the interfacial layer solution (Liao et al., 2013, Li et al., 2017a, Borse et al., 2018) or additional deposition of materials on top of the previously deposited interfacial film to form second interfacial layer (Lee et al., 2014, Borse et al., 2018). The main difference is that the former is conducted in solution preparation stage, whereas the latter in solution deposition stage. An example of the former strategy was conducted by Zheng *et al.*, where Zheng *et al.* applied interface engineering strategy on PEDOT:PSS HTL by introducing WO_x nanoparticles in the HTL to boost the efficiency performance of PBDB-T-2F:IT-4F -based device from 13.29% to 14.57% (Zheng et al., 2018). An example of the latter strategy was conducted by Borse

et al., where Borse *et al.* opted for interface engineering strategy by depositing barium hydroxide ($\text{Ba}(\text{OH})_2$) layer on top of the ZnO film to smoothen ZnO morphology and to promote better interfacial contact between ETL and the photoactive layer (Borse *et al.*, 2018). Consequently, photovoltaic performance of such inverted device was increased from 7.12% to 8.54%. Despite which strategy was implemented, those results shown the simplicity and viability of interface engineering strategy to improve device performance for the realization of high-performing OSCs.

Among different classes of interfacial layer, sol-gel ZnO is one of the most widely used interfacial layer in inverted OSCs due to its low cost, high stability, excellent optical transparency and non-toxic nature (Sun *et al.*, 2011, Ma *et al.*, 2012, Lee *et al.*, 2014, Nian *et al.*, 2015, Liu *et al.*, 2016, Jung *et al.*, 2018). In spite of its advantages, sol-gel ZnO often suffers from high surface roughness and poor hydrophobicity, which subsequently impedes charge extraction processes and device performances (Liao *et al.*, 2013, Borse *et al.*, 2018). Due to this, interface engineering on sol-gel ZnO is essential to be conducted to subdue the limitations of ZnO film functionally, so that high-performing inverted OSCs can be obtained. This opens up opportunities to conduct interface engineering study on sol-gel ZnO.

Apart from interfacial layer, OSCs also contain photoactive layer which acts as the primary layer in OSCs. Conceptually, photoactive layer plays a crucial role in determining OSCs' performance because a slight change in terms of material's choice or even configuration for the photoactive layer can result in a significant difference in device performance. This is expected as photoactive

layer is highly affecting the generation, diffusion and dissociation processes of exciton, as well as generation and transport processes of free charge carrier. Over the years, intense works on photoactive layer have been done from modification of photoactive layer configuration to material design for the synthesis of novel organic donor and/or acceptor materials. By 2020, the performance of single-junction BHJ OSCs had reached the 15-18% range (Xu et al., 2019, Yuan et al., 2019, Cui et al., 2020, Luo et al., 2020, Liu et al., 2020, Sun et al., 2020).

Further work on photoactive layer can be made by employing photoactive layer modification or active layer engineering strategy. This strategy involves the creation of ternary blend system to improve photon harvesting capability and/or regulate surface morphology of the photoactive layer, while at the same time, maintain the simplicity of single-junction device architecture. In ternary photoactive layer system, additional material is being introduced into the host binary blend that consist of one donor and one acceptor materials, paired based on their energy level offset to create driving force for efficient exciton dissociation. Typically, the additional material is chosen with consideration of absorption performance, energy level and morphological compatibility with the host binary blend. The material added may act as a dopant (addition < 10%) or even additional donor or acceptor material (addition \geq 10%). For instance, Chen *et al.* doped graphitic carbon nitride into PTB7-Th:PC₇₁BM photoactive blend layer to improve the conductivity and charge transport properties of photoactive layer (Chen et al., 2016). As a result, performance increment from 8.39% to 9.20% was observed, which was mainly attributed to the improved J_{sc} and FF .

Another study reported by Chang *et al.* added ITCT as 2nd acceptor into PBDB-T-SF:Y6 host binary blend to realize the simultaneous enhancement in J_{sc} , V_{oc} and FF performances, thus boosting the PCE from 15.18% to 16.14% (Chang *et al.*, 2019). Similarly, Gao *et al.* employed 2nd acceptor called IT-4F into J71:T6Me host binary blend to enhance photon harvesting range of the photoactive layer for higher J_{sc} performances in ternary device (Gao *et al.*, 2019). Liu *et al.* also introduced IXIC-4Cl acceptor into the host PBDB-T-2Cl:ITC-2Cl binary blend to realize the improvement in J_{sc} and FF values due to improved optical and morphological properties of the pristine binary layer (Liu *et al.*, 2019a). Another experiment reported by An *et al.* added J71 as 2nd donor material in PBDB-T-2F:Br-ITIC host binary blend to improve photon harvesting range and regulate phase separation in the photoactive layer (An *et al.*, 2019). As a result, performance enhancement from 12.63% to 14.13% was obtained.

Conclusively, this explains the potential of active layer engineering strategy to improve device performance for the realization of high-performing OSCs. Nonetheless, it is important to note that this strategy is sometimes challenging due to the complex morphological blend of the photoactive layer upon addition (e.g., incorporation of additional material may lead to unfavourable charge transport due to large-scale phase separation). Deep charge traps are also high likely to occur, making it even more challenging to adopt ternary photoactive layer system. Therefore, the compatibility of materials used (in terms of absorption profile, morphological feature and energy level) for active layer engineering strategy are extremely vital to be considered in order to enhance absorption capability, promote desirable phase separation degree and avoid charge traps in the photoactive layer. Over the past years, studies and

experimental trials employing active layer engineering strategy had been conducted with the main aim of enhancing device performance via altering the pristine properties of photoactive layer. However, as of now, no desirable performance improvements were observed on those experimental studies. The detailed performance parameters regarding those experiments are presented in “Appendix B: Other Experimental Work”.

Apart from interfacial layer and photoactive layer, OSCs also contain electrode layer, which is the last constituent layer of OSCs responsible for charge collection. In OSCs, electrodes play equally crucial roles with the other constituent layers in determining device performance, not only in terms of photovoltaic performance but also in terms of mechanical stability (Ramachandran et al., 2015, Cheng and Zhan, 2016, Li et al., 2018). However, despite their roles, studies on electrode are still lacking as compared to those about photoactive layer or interfacial layer. Thus, it is particularly essential to pay close attention towards the development of electrodes, specifically for the development of flexible transparent electrodes (FTEs) to realize the future applications of OSCs in next-generation flexible and wearable electronics (Li et al., 2018, Qin et al., 2020b). Ideally, excellent FTEs should possess high optical transparency, excellent conductivity, low sheet resistance and superior mechanical flexibility and stability (Li et al., 2018). An example of electrode possessing most of those desirable traits is conventional ITO electrode, causing it to be widely used in rigid OSCs as transparent bottom electrode. However, brittle properties of ITO often limit its mechanical flexibility (Li et al., 2018, Qin et al., 2020b). In other words, upon mechanical deformation, ITO tends to crack and subsequently leads to decrease in conductivity and increase in sheet

resistance. This factor has impeded the utilization of ITO electrode in flexible OSCs.

Over the years, several ITO alternatives have been developed for flexible OSCs, and one of them is PEDOT:PSS (PH1000) electrode (Ouyang, 2013, Thomas et al., 2014, Kim et al., 2015, Song et al., 2018). PEDOT:PSS electrode is considered as a promising ITO alternative as it can be used not only for rigid device applications but also for flexible device applications. It possesses exceptional intrinsic flexibility, high optical transparency, low surface roughness, excellent solution-processability and superior thermal stability (Li et al., 2018, Qin et al., 2020b). Despite all that, pristine PEDOT:PSS electrode still suffers from poor photovoltaic performance due to its inherent weaknesses. To overcome those weaknesses, electrode layer modification or electrode engineering strategy on pristine PEDOT:PSS electrode is needed. This strategy focuses on improving the pristine properties of PEDOT:PSS electrode (e.g., optical, electrical, morphological and mechanical properties) to function more effectively as efficient FTEs in flexible OSCs. This can be done either via doping treatment using organic compounds (Vosgueritchian et al., 2012, Ouyang, 2013, Thomas et al., 2014, Peng et al., 2019) or surface post-treatment using acid (Yeon et al., 2015, Kim et al., 2015, Song et al., 2018, Song et al., 2020b). The main difference is that the former is conducted in solution preparation stage, whereas the latter in solution deposition stage. An example of doping treatment was conducted by Vosgueritchian *et al.*, where Vosgueritchian *et al.* applied electrode engineering strategy on PEDOT:PSS FTEs by introducing Zonyl as a fluorosurfactant to improve the conductivity, morphology and optical transparency of pristine PEDOT:PSS electrode (Vosgueritchian et al., 2012). An

example of surface post-treatment was conducted by Song *et al.*, where Song *et al.* developed a gentle acid post-treatment method at room temperature to improve the optical, electrical and morphological properties of PEDOT:PSS electrode (Song et al., 2018). Through this approach, the conductivity of PEDOT:PSS could be significantly improved to 2860 S cm^{-1} and the morphology in terms of surface roughness and phase separation could be optimized. As a result, the first high-performing flexible OSCs with efficiency beyond 10% was obtained at that time.

Recently, Peng *et al.* also reported that a combination of doping and acid treatment could simultaneously enhance PEDOT:PSS properties such as transparency, conductivity and mechanical flexibility, resulting in the realization of high-performing flexible OSCs with over 12% efficiency (Peng et al., 2019). Even so, not many electrode engineering studies on PEDOT:PSS are directed towards these aspects. This presented a research opportunity to engineer high-performing PEDOT:PSS electrodes with improved conductivity as well as enhanced adhesion ability via doping and acid treatment, so that the performance and mechanical stability of flexible OSCs could be enhanced.

2.9 Summary

Organic solar cells or OSCs have been developed over the years due to their promising potentials as substitutes for conventional silicon solar cells. Yet, issues regarding efficiency and stability of OSCs still need to be overcome to obtain comparable device performance against mature silicon-based solar cells.

These issues remain as great challenges, which consequently shifting the research focus of OSCs towards the development of efficient and stable OSCs.

Throughout the development of OSCs, three main strategies have been utilized to improve OSCs' performance, namely material design (e.g., design and synthesis of novel organic material for photoactive layer), morphology control (e.g., morphology control of photoactive layer through post-production treatment) and device engineering (e.g., interface, active layer or electrode engineering). Thus far, material design and morphology control of the photoactive layer have been the dominating approaches to improve OSCs' performance. Yet, device engineering gains lesser attention even though it plays an equally pivotal role to enhance OSCs' performance. In fact, as mentioned earlier, previous studies shown that simple device engineering strategy, such as by doping or addition of additional material, is an effective approach to improve the overall device performance. This presents an opportunity to delve into the areas of device engineering, specifically on novel interface and electrode engineering strategies that have not been done to boost the overall device performance.

Chapter 3. Methodology

3.1 Introduction

The experimental work conducted for Chapter 4 (interface engineering), Chapter 5 (electrode engineering) and Chapter 6 (application of electrode engineering) are being elaborated comprehensively in this chapter. This methodology chapter includes details regarding the materials and instrumentations used, device fabrication procedures and device characterization methods.

3.2 Materials

All materials used in this study were acquired from the manufacturers listed in **Table 1.1** to **1.6** below. If any, specifications of the materials are also included for reference. Unless otherwise specified, all the materials listed below were used directly without any further purifications.

Table 1.1 List of substrates and their corresponding information.

Material Name	Specification	Manufacturer
Glass	Thickness: 1.1 mm Sheet resistance: n/a	Wuhu Token Sciences Co., Ltd.
Polyethylene terephthalate (PET)	Thickness: < 0.2 mm Sheet resistance: n/a	South China Xiangcheng Technology Co., Ltd.
ITO-coated glass	Thickness: 1.1 mm Sheet resistance: $\leq 15 \Omega \text{ sq}^{-1}$	Wuhu Token Sciences Co., Ltd.
ITO-coated PET	Thickness: < 0.2 mm Sheet resistance: $\leq 15 \Omega \text{ sq}^{-1}$	South China Xiangcheng Technology Co., Ltd.

Table 1.2 List of photoactive materials and their corresponding information.

Material Name	Specification	Manufacturer
PBDB-T	n/a	Solarmer Materials, Inc.
PBDB-T-2F	n/a	Solarmer Materials, Inc.
IT-M	n/a	Solarmer Materials, Inc.
BTP-4F or Y6	n/a	Solarmer Materials, Inc.

* Complete chemical names for organic materials are listed in “List of Chemical Names”

Table 1.3 List of ETL and HTL materials and their corresponding information.

Material Name	Specification	Manufacturer
Zinc acetate	Purity: 97.5%	J&K Scientific, Ltd.
PBD	Purity: > 99.0%	Xi'an Polymer Light Technology Corp.
PDINO	n/a	Solarmer Materials, Inc.
MoO ₃ powder	Purity: 99.999%	Alfa Aesar
PEDOT:PSS	Clevios P VP AI 4083 1.3-1.7% solid content	Heraeus

Table 1.4 List of solvents and their corresponding information.

Material Name	Specification	Manufacturer
Ethanolamine	Purity: 99.5%	J&K Scientific, Ltd.
2-Methoxyethanol	Purity: 99.0%	J&K Scientific, Ltd.
CB	Purity: 99.8%	Sigma-Aldrich, Inc.
Methanol	Purity: 99.8%	Sigma-Aldrich, Inc.
CF	Purity: 99.9%	Sinopharm Chemical Reagent Co., Ltd.
MSA	Purity: 99.0%	J&K Scientific, Ltd.
Ethanol	Purity: 99.9%	Sinopharm Chemical Reagent Co., Ltd.
Acetone	Purity: 99.9%	Sinopharm Chemical Reagent Co., Ltd.
Isopropanol	Purity: 99.9%	Sinopharm Chemical Reagent Co., Ltd.

Table 1.5 List of additives/dopants and their corresponding information.

Material Name	Specification	Manufacturer
DIO additives	Purity: 98.0%	Sigma-Aldrich, Inc.
CN additives	Purity: > 97.0%	Tokyo Chemical Industry Co., Ltd.
Ethylene glycol	Purity: > 99.0%	Aladdin Biochemical Technology Co., Ltd.
Xylitol	Purity: 98.0%	Aladdin Biochemical Technology Co., Ltd.
Dulcitol	Purity: 98.0%	Aladdin Biochemical Technology Co., Ltd.

Table 1.6 List of electrode materials and their corresponding information.

Material Name	Specification	Manufacturer
Calcium (Ca metal)	Purity: 99.5%	Alfa Aesar
Aluminium (Al metal)	Purity: 99.999%	Alfa Aesar
Silver (Ag metal)	Purity: 99.999%	Zhongjin Research New Material Technology Co., Ltd.
PEDOT:PSS	Clevios PH1000 1.0-1.3% solid content	Heraeus

3.3 Instruments

All instrumentations or experimental equipment used in this study were acquired from the manufacturers listed in **Table 1.7**. In addition, the purpose of each instrument used is discussed in **Table 1.8**.

Table 1.7 List of instrumentations and their corresponding information.

Instrument Name	Model	Manufacturer
X-ray photoelectron spectrometer	AXIS Ultra DLD	Kratos Analytical, Ltd.
Ultraviolet photoelectron spectrometer	AXIS Ultra DLD	Kratos Analytical, Ltd.
UV-vis spectrophotometer	LAMBDA 950	PerkinElmer, Inc.
Energy dispersive X-ray spectrometer	Verios G4 UC	Thermo Fisher Scientific, Inc.
Transmission electron microscopy	Talos™ F200X	Thermo Fisher Scientific, Inc.
Atomic force microscopy	Dimension 3100	Veeco Instruments, Inc.
Contact angle measurement system	OCA 25	DataPhysics Instruments GmbH
Surface profiler	Dektak 150	Veeco Instruments, Inc.
Adhesion force measurement system	DCAT21	Ningbo Jinmao Import and Export Co., Ltd.
4-Point probes measurement system	CRESBOX	Napson Corp.
<i>J-V</i> measurement (solar simulator)	Oriel Sol3A	Newport Corporation
<i>J-V</i> measurement (digital source)	Keithley 2440	Tektronix, Inc.
Quantum efficiency measurement system	QE-R	Enli Technology Co., Ltd.
Ultrasonic cleanser	SK8200H	Kudos Ultrasonic Instrument Co., Ltd.
UV-ozone box	BZS250GF-TC	Huiwo Technology Co., Ltd.
Spin coater	SPIN-1200D	Midas System Co., Ltd.
Heating plate (with magnetic stirrer)	C-MAG HS 7	IKA® Works
Vacuum deposition and glove box	n/a	M. Braun Inertgas-Systeme GmbH

Table 1.8 Function of instrumentations used.

Instrument Name	Function
X-ray photoelectron spectrometer	Analyse compositions and elemental states of films
Ultraviolet photoelectron spectrometer	Measure energy level and work function of materials
UV-vis spectrophotometer	Characterize transmittance, absorption and reflectance performances
Energy dispersive X-ray spectrometer	Analyse elemental distribution in film
Transmission electron microscopy	Characterize surface morphological features of film
Atomic force microscopy	Characterize surface morphological features of film
Contact angle measurement system	Characterize surface wettability of film
Surface profiler	Measure film's thickness
Adhesion force measurement system	Measure adhesion force between two materials
4-Point probes measurement system	Measure square resistance of materials
<i>J-V</i> measurement (solar simulator)	Characterize photovoltaic performances
<i>J-V</i> measurement (digital source)	Characterize photovoltaic performances
Quantum efficiency measurement system	Measure quantum efficiencies
Ultrasonic cleanser	Clean the surface of substrates
UV-ozone box	Enhance surface properties to ensure uniform deposition on substrates
Spin coater	Deposit solution to form thin-film
Heating plate (with magnetic stirrer)	Thermal annealing of film
Vacuum deposition and glove box	Provide inert environment for device fabrication and electrode deposition

3.4 Device Fabrications

Generally, devices are fabricated through layer-by-layer preparation and deposition techniques (Wang et al., 2013, Ouyang et al., 2015, Ai et al., 2016, Lei et al., 2018, Peng et al., 2018, Song et al., 2018, Fan et al., 2019, Peng et al., 2019, Fanady et al., 2020, Song et al., 2020a, Song et al., 2020b). The general device arrangement is as follow: electrode, interfacial layer, photoactive layer, interfacial layer and electrode. Prior to deposition, materials are being prepared either in solid or solution form. In our lab, solution-processable materials are deposited using spin coating method, while solid materials are deposited via vacuum evaporation method (Wang et al., 2013, Ouyang et al., 2015, Ai et al.,

2016, Lei et al., 2018, Peng et al., 2018, Song et al., 2018, Fan et al., 2019, Peng et al., 2019, Fanady et al., 2020, Song et al., 2020a, Song et al., 2020b). Several examples of solution-processable materials are PDINO (Zhang et al., 2014) and sol-gel ZnO (Sun et al., 2011), which are used as interfacial layer. Examples of solid materials are Ag and Al metal (Chen et al., 2019), which act as electrode. A more detailed fabrication procedure will be discussed in the following subsection.

In this study, all organic PV devices were fabricated in batches, where a maximum of 16 independent devices could be fabricated at once. Several experimental trials were conducted as well to confirm data reproducibility and reliability.

3.4.1 Fabrication procedures for interface engineering study

In interface engineering study, inverted OSCs with configuration of glass/ITO/ZnO/with or without PBD/PBDB-T:IT-M/MoO₃/Ag were fabricated to study the effect of PBD addition as interfacial modifier to device performance. ITO-coated glass substrates (1.5×1.5 cm), received from the aforementioned manufacturer, were directly cleaned under sequential sonification for 20 minutes each in detergent, deionized water, acetone and isopropanol (Wang et al., 2013). Prior to fabrication, the pre-cleaned substrates were dried with nitrogen (N₂) stream and further treated with UV-ozone for about 25 minutes, similar to the previous literatures (Wang et al., 2013).

Sol-gel ZnO was utilized in this study as the solution-processed ETL, where it was prepared similar to the previously published literatures (Sun et al., 2011). The 0.5 M ZnO precursor solution was made by dissolving 100.9 mg zinc acetate in 33.5 μ L ethanolamine and 1 mL 2-methoxyethanol. The corresponding precursor solution was stirred without heat for a minimum of 2 hours before depositing onto the substrates. The ZnO precursor solution was deposited onto the ITO substrates using spin coating technique at 4000 rpm for 60 seconds (film thickness: \sim 30 nm), followed by subsequent thermal annealing at 150°C for 30 minutes. The substrates were then transferred into a N₂-filled glove box for further deposition of other layers (e.g., PBD, photoactive layer, etc). This meant that up until this point, all experiments were conducted in an ambient environment.

PBD was incorporated in this study as the 2nd solution-processed ETL to modify and improve the properties of sol-gel ZnO ETL. This technique formed the hybrid electron-transporting bilayer consisting of PBD and ZnO layer. PBD solution was prepared by mixing PBD in methanol solvent with varying concentration from 0.5-5.0 mg mL⁻¹. This solution was stirred overnight without heat before its application onto ZnO film. PBD solution was deposited on top of the ZnO film with different spin coating speed and annealing condition. Under optimal conditions, PBD was spin-coated at 1000 rpm for 60 seconds (film thickness: \sim 10 nm) and annealed under vacuum for 15 minutes.

Photoactive blend layer, consisting of PBDB-T polymeric donor and IT-M SM acceptor was prepared similarly to the published literatures (Li et al., 2016, Peng et al., 2018). In this case, PBDB-T and IT-M (D:A = 1:1 by weight) was

dissolved in 20 mg mL⁻¹ CB (total solid concentration). The corresponding solution was stirred overnight at 45°C before usage. About 1 hour before deposition, 0.7 vol% of DIO as additive was added into the solution. The photoactive layer (PBDB-T:IT-M) was deposited on top of the ZnO or ZnO/PBD film at 1900 rpm for 60 seconds to obtain film thickness of ~100 nm. It was then annealed at 120°C for 10 minutes. At last, 8 nm MoO₃ as HTL and 100 nm Ag as electrode were thermally evaporated onto the photoactive layer in a vacuum chamber with base pressure of ~5×10⁻⁶ mbar or ~5×10⁻⁴ Pa (Peng et al., 2018, Song et al., 2018). MoO₃ and Ag were deposited through a shadow mask with an effective area of 3.8 mm², as illustrated in **Figure 3.1**.

The deposition of material in vacuum chamber was conducted in two-step processes of pre-deposition and deposition stage (Wang et al., 2013, Ouyang et al., 2015, Ai et al., 2016, Lei et al., 2018, Peng et al., 2018, Song et al., 2018, Fan et al., 2019, Peng et al., 2019, Fanady et al., 2020, Song et al., 2020a, Song et al., 2020b). In the pre-deposition stage, large baffle under the shadow mask was closed for pre-steaming process. This process was conducted to account for the unstable evaporation rate and presence of trace impurities. The baffle could be opened for deposition stage when the evaporation rate was stable. The typical deposition rate should be in the range of 0.2-1.5 Å s⁻¹. The thickness of material deposited could be observed and controlled in the deposition controller. It was important to note that within the first 10 nm of deposition, the deposition rate should be well-controlled and slow to prevent adverse effect of high temperature metal vapour on the photoactive layer. After exceeding 10 nm, the deposition rate could be increased by adjusting the power.

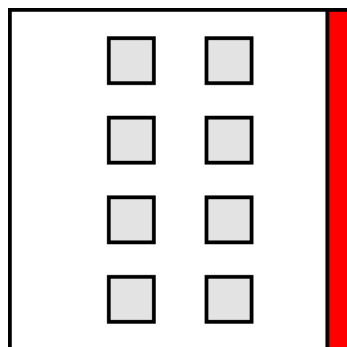


Figure 3.1 Shadow mask used for the deposition of MoO₃ and Ag. The shadow mask has 8 square holes with precise active area of 3.8 mm² each. The red region represents ITO electrode and the grey region represents MoO₃ and Ag electrode.

3.4.2 Fabrication procedures for electrode engineering study

In electrode engineering study, conventional OSCs with configuration of PEDOT:PSS (PH1000)/PEDOT:PSS (hereinafter termed as 4083)/PBDB-T-2F:Y6/PDINO/Al were fabricated on PET plastic substrates for flexible OSCs application. Electrode engineering was conducted on PEDOT:PSS (PH1000) as ITO alternatives to modify its properties for future high-performing flexible OSCs. In this study, OSCs based on PET/ITO, PET/PEDOT:PSS, PET/modified PEDOT:PSS (hereinafter referred as D-PEDOT:PSS) and glass/ITO substrates were all fabricated for comparison purposes. All substrates (1.5×1.5 cm), obtained from the aforementioned manufacturers, were cleansed with the same procedures as the previous section 3.4.1.

PEDOT:PSS (PH1000) functioned as electrode in this study, where it was fabricated using spin coating technique, similar to earlier literatures (Song et al., 2018, Peng et al., 2019). Prior to its deposition, 5.0 wt% of polyhydroxy compound was added as a dopant into the PEDOT:PSS aqueous solution.

Different polyhydroxy compounds (ethylene glycol, xylitol and dulcitol) were investigated to obtain the best dopant choice for PEDOT:PSS FTEs. The subsequent mixture was then deposited onto the PET plastic substrates at 1800 rpm for 60 seconds, followed by thermal annealing at 90°C for 20 minutes. MSA was utilized afterwards for the post-treatment of doped PEDOT:PSS films. In this case, MSA treatment procedures were similar to the previous reported literatures (Fan et al., 2016, Song et al., 2018), in which films were dipped into the MSA solution for about 10 minutes before being rinsed in deionized water and ethanol. The MSA-treated films were then annealed at 90°C for 20 minutes to form a dry D-PEDOT:PSS electrode (film thickness: ~60 nm).

PEDOT:PSS (4083), or in short abbreviated as 4083 was utilized in this study as HTL, where it was deposited on top of the ITO, pristine PEDOT:PSS or D-PEDOT:PSS FTEs. A method similar to other published literatures was employed for the preparation and deposition of 4083 solution (Song et al., 2018, Peng et al., 2019). In this case, prior to its deposition, 4083 solution was first filtered through a 0.45 μm syringe filter. It was followed by spin coating at 2600 rpm for 60 seconds (film thickness: ~30 nm) and annealing at 90°C for 20 minutes. The resulting substrates were transferred into a N₂-filled glove box for further deposition of other layers (e.g., photoactive layer, PDINO, etc). This meant that up until this step, all experiments were conducted in an ambient environment.

Photoactive blend layer, consisting of PBDB-T-2F polymeric donor and Y6 SM acceptor was prepared similarly to the published literatures (Yuan et al., 2019). In this case, PBDB-T-2F and Y6 (D:A = 1:1.2 by weight) was dissolved

in 16 mg mL^{-1} CF (total solid concentration). The corresponding solution was stirred for about 5-6 hours at a temperature below 40°C before usage. About 1 hour before deposition, 0.5 vol% of CN as additive was added into the solution. The photoactive layer (PBDB-T-2F:Y6) was then spin-coated on top of the HTL at 2700 rpm for 60 seconds (film thickness: $\sim 110 \text{ nm}$), followed by thermal annealing at 110°C for 10 minutes.

PDINO was incorporated in this study as ETL, where it was prepared by dissolving PDINO in methanol solvent with concentration of 1.5 mg mL^{-1} (Peng et al., 2019). It was deposited on top of the photoactive layer at 3000 rpm for 60 seconds (film thickness: $\sim 8 \text{ nm}$) without annealing treatment. At last, 100 nm Al as electrode was thermally evaporated onto the ETL in a vacuum chamber with base pressure of $\sim 5 \times 10^{-6} \text{ mbar}$ or $\sim 5 \times 10^{-4} \text{ Pa}$ (Peng et al., 2018, Song et al., 2018). The deposition technique is similar to the previous section 3.4.1. Al was deposited through a shadow mask with an effective area of 4.0 mm^2 , as illustrated in **Figure 3.2**.

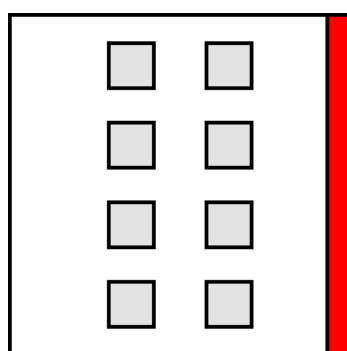


Figure 3.2 Shadow mask used for the deposition of Al. The shadow mask has 8 square holes with precise active area of 4.0 mm^2 each. The red region represents ITO electrode and the grey region represents Al electrode.

3.4.3 Fabrication procedures for application of electrode engineering study

In this study, foldable-flexible semi-transparent OSCs (FST-OSCs) with conventional configuration of PET/D-PEDOT:PSS/4083/PBDB-T-2F:Y6/PDINO/Ag were fabricated. All layers were fabricated similarly to the previous section 3.4.2, but the main difference arose from the choice of metal electrodes where Ag was employed as the electrode instead of Al. Different thicknesses of Ag electrode were investigated to optimize the performance of FST-OSCs for greenhouse applications.

3.5 Device Characterizations

3.5.1 J - V measurement

Upon completion of device fabrication, organic photovoltaic devices were directly tested for their photovoltaic performances. The test is conducted under the same international standard to allow a valid comparison between OSCs fabricated by different research groups around the world (Rostalski and Meissner, 2000). Normally, a standard light source with light intensity of 100 mW cm^{-2} is used with light filter to simulate AM1.5G spectrum (Rostalski and Meissner, 2000).

In this study, the test was performed in N_2 -filled glove box without device encapsulation using J - V measurement system, consisting of digital source-measure meter (Keithley 2440, Tektronix) and AM1.5G solar simulator

(Oriel Sol3A, Newport). Light intensity was calibrated at 100 mW cm^{-2} using a certified reference silicon standard cell (SRC-2020 with KG5 filter) obtained from Enli Technology Co., Ltd and the calibration report was traceable to NREL. Photovoltaic performances of devices (e.g., current density, voltage, fill factor and efficiency) were measured by connecting the two electrodes (bottom and top electrodes) through an outer loop. Data were collected and automatically recorded every time measurement was made. Those data could be plotted into current density vs voltage curve to obtain the typical $J-V$ characteristic curve. All measurements performed were similar to the earlier literatures published by Prof. Ziyi Ge's group (Ouyang et al., 2015, Ai et al., 2016, Lei et al., 2018, Song et al., 2018, Fan et al., 2019, Peng et al., 2019).



Figure 3.3 AM1.5G solar simulator (*left*) and digital source-measure meter (*right*).

3.5.2 EQE measurement

Upon completion of device fabrication, organic photovoltaic devices were directly tested for their quantum efficiency performances. The measurement performed was similar to the earlier literatures published by Prof. Ziyi Ge's group (Fanady et al., 2020, Song et al., 2020a, Song et al., 2020b). The test was performed in N_2 -filled glove box without device encapsulation using

quantum efficiency measurement system (QE-R, Enli Technology) with 75 W xenon lamp source, of which light intensity was calibrated using a reference silicon probe (RC-S103011-G) obtained from Enli Technology Co., Ltd. Upon measurement, EQE performances of devices were generated and plotted into EQE and/or integrated J_{sc} vs wavelength curves.



Figure 3.4 Quantum efficiency measurement system.

3.5.3 X-ray photoelectron spectroscopy (XPS) and ultraviolet photoelectron spectroscopy (UPS) measurement

Glass or PET substrates (1.5×1.5 cm) were cleansed similarly in ultrasonic cleanser using detergent, deionized water, acetone and isopropanol. Substrates were then dried with N₂ stream and further treated with UV-ozone before usage. Solution to be tested was deposited afterwards using the same fabrication procedures and conditions. For instance, if XPS and UPS studies were to be conducted on ZnO ETL, deposition of ZnO solution should be done at 4000 rpm for 60 seconds and annealed at 150°C for 30 minutes. After deposition and drying of film, substrates were carefully cut into a 0.5×0.5 cm testing sample for measurement in AXIS Ultra DLD XPS/UPS spectrometer (Kratos Analytical). Data were collected and plotted to form the typical XPS and

UPS spectra. All measurements performed were similar to the previous literatures published by Prof. Ziyi Ge's group (Song et al., 2018, Fan et al., 2019, Peng et al., 2019).

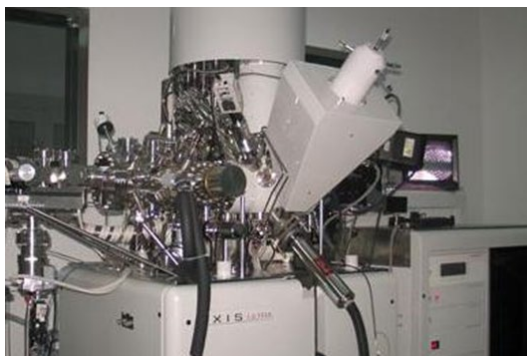


Figure 3.5 XPS/UPS spectrometer.

3.5.4 UV-visible (UV-vis) measurement

Glass or PET substrates (1.5×1.5 cm) were cleansed similarly in ultrasonic cleanser using detergent, deionized water, acetone and isopropanol. Substrates were then dried with N₂ stream and further treated with UV-ozone before usage. Solution to be tested was deposited afterwards using the same fabrication procedures and conditions. For instance, to evaluate the transmissivity of ZnO ETL, ZnO solution should be deposited on the substrates at 4000 rpm for 60 seconds and annealed at 150°C for 30 minutes. After deposition and drying of film, samples were transferred for measurement in LAMBDA 950 spectrometer (PerkinElmer). Data were collected and plotted to form transmittance spectra. Aside from transmittance, LAMBDA 950 spectrometer can also measure reflectance and absorption performances. All measurements performed were similar to the previous literatures published by

Prof. Ziyi Ge's group (Lei et al., 2018, Song et al., 2018, Fan et al., 2019, Peng et al., 2019).



Figure 3.6 UV-vis spectrophotometer.

3.5.5 Energy dispersive x-ray spectroscopy (EDS) measurement

Quartz glass substrates (1.5×1.5 cm) were utilized for EDS measurement. The substrates were cleansed similarly in ultrasonic cleanser using detergent, deionized water, acetone and isopropanol. Substrates were then dried with N_2 stream and further treated with UV-ozone before usage. Solution to be tested was deposited afterwards using the same fabrication procedures and conditions. In this case, as-cast PEDOT:PSS and D-PEDOT:PSS solutions were deposited onto the quartz substrates to form thin-film. After deposition and drying of film, samples were then transferred for measurement in Verios G4 UC spectrometer (Thermo Fisher). Upon measuring, EDS images of tested films were generated. All measurements performed were similar to the previous literatures published by Prof. Ziyi Ge's group (Song et al., 2020b).

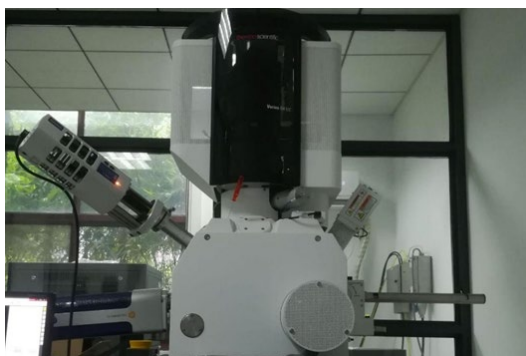


Figure 3.7 EDS spectrometer.

3.5.6 Transmission electron microscopy (TEM) measurement

Glass substrates (1.5×1.5 cm) were cleansed similarly in ultrasonic cleanser using detergent, deionized water, acetone and isopropanol. Substrates were then dried with N₂ stream and further treated with UV-ozone before usage. For as-cast PEDOT:PSS, solution was directly dropped onto the copper mesh and then dried through annealing process. For D-PEDOT:PSS, solution was deposited onto the glass substrates using the same fabrication procedures and conditions. After deposition and drying of film, the substrate was soaked in deionized water. Acid treatment destroys hydrogen bond between substrate and D-PEDOT:PSS which result to the separation of film. Those separated films are then attached to the copper mesh. Copper mesh samples were then transferred for measurement in Talos F200X (Thermo Fisher). Upon measuring, TEM images of tested films were generated. All measurements performed were similar to the previous literatures published by Prof. Ziyi Ge's group (Lei et al., 2018, Song et al., 2018).



Figure 3.8 TEM microscopy.

3.5.7 Atomic force microscopy (AFM) measurement

Glass substrates (1.5×1.5 cm) were cleansed similarly in ultrasonic cleanser using detergent, deionized water, acetone and isopropanol. Substrates were then dried with N₂ stream and further treated with UV-ozone before usage. Solution to be tested was deposited afterwards using the same fabrication procedures and conditions. After deposition and drying of film, samples were then transferred for measurement in Dimension 3100 (Veeco Instruments). Upon measuring, AFM images of tested films were generated. All measurements performed were similar to the previous literatures published by Prof. Ziyi Ge's group (Ai et al., 2016, Lei et al., 2018, Song et al., 2018, Fan et al., 2019).

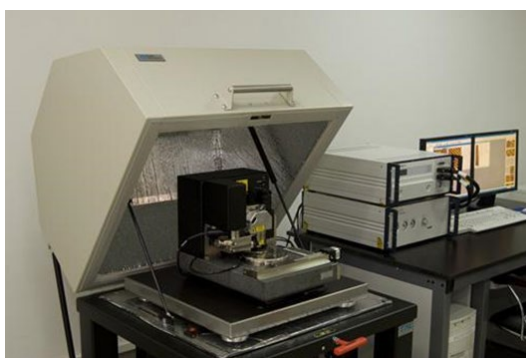


Figure 3.9 AFM microscopy.

3.5.8 Contact angle measurement

Glass substrates (1.5×1.5 cm) were cleansed similarly in ultrasonic cleanser using detergent, deionized water, acetone and isopropanol. Substrates were then dried with N₂ stream and further treated with UV-ozone before usage. ZnO and ZnO/PBD were prepared and deposited onto the substrates using the same fabrication procedures and conditions. After deposition and drying of film, samples were then transferred for contact angle measurement in OCA 25 (DataPhysics Instruments). In contact angle measurement system, droplet of deionized water was being dropped onto the substrates containing ZnO and ZnO/PBD films. Images of the droplet wetting the film's surface were captured by the equipment and the contact angle could be measured from it. All measurements performed were similar to the previous literatures published by Prof. Ziyi Ge's group (Ai et al., 2016, Song et al., 2018).

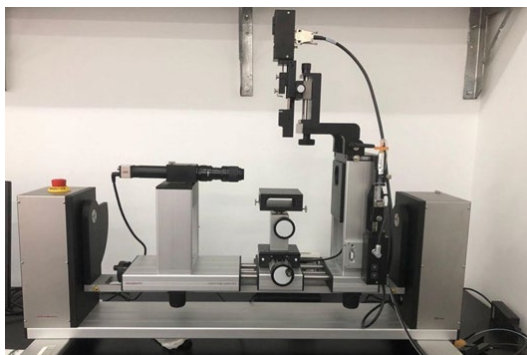


Figure 3.10 Contact angle measurement system.

3.5.9 Surface thickness measurement

Glass substrates (1.5×1.5 cm) were cleansed similarly in ultrasonic cleanser using detergent, deionized water, acetone and isopropanol. Substrates

were then dried with N₂ stream and further treated with UV-ozone before usage. Solution to be tested was deposited afterwards using the same fabrication procedures and conditions. After deposition and drying of film, the thickness of film (e.g., electrode, photoactive layer and interfacial layer) could be measured individually using Dektak 150 surface profiler (Veeco Instruments). All measurements performed were similar to the previous literatures published by Prof. Ziyi Ge's group (Ouyang et al., 2015, Peng et al., 2019).



Figure 3.11 Surface profiler.

3.5.10 Adhesion force measurement

PET substrates (1.5×1.5 cm) were cleansed similarly in ultrasonic cleanser using detergent, deionized water, acetone and isopropanol. Substrates were then dried with N₂ stream and further treated with UV-ozone before usage. As-cast PEDOT:PSS and D-PEDOT:PSS solutions were prepared using the same fabrication procedures and conditions. Both solutions and substrates were transferred for adhesion force measurement in DCAT21, where the adhesiveness of as-cast PEDOT:PSS and D-PEDOT:PSS to PET plastic substrates could be determined. All measurements performed were similar to the previous literatures published by Prof. Ziyi Ge's group (Fan et al., 2019, Peng et al., 2019).



Figure 3.12 Adhesion force measurement system.

3.5.11 Square resistance (R_{sq}) measurement

Glass substrates (1.5×1.5 cm) were cleansed similarly in ultrasonic cleanser using detergent, deionized water, acetone and isopropanol. Substrates were then dried with N_2 stream and further treated with UV-ozone before usage. Solution to be tested was deposited afterwards using the same fabrication procedures and conditions. In this case, as-cast PEDOT:PSS and D-PEDOT:PSS solutions were deposited onto the glass substrates. After deposition and drying of film, samples were transferred for 4-point probes measurement in CRESBOX (Napson). R_{sq} values were recorded. All measurements performed were similar to the previous literatures published by Prof. Ziyi Ge's group (Fan et al., 2019).



Figure 3.13 4-Point probes measurement system.

3.5.12 Colour coordinates

Colour coordinates could be determined using “CIE1931 Chromaticity Coordinate Calculation” program, similar to other studies (Xie et al., 2018). The program automatically calculates the colour coordinates based on photovoltaic performance data.

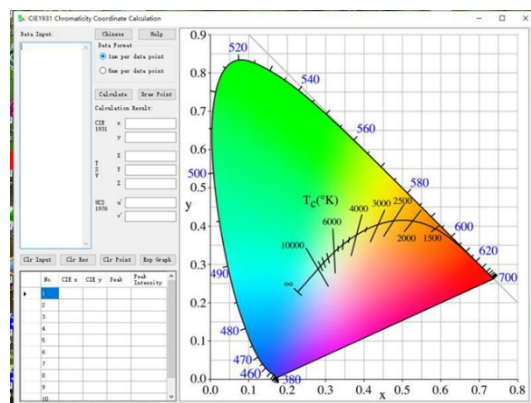


Figure 3.14 CIE1931 chromaticity coordinate program.

3.5.13 Flexibility and mechanical stability measurement

The flexibility and mechanical stability of devices were evaluated through simple bending and folding test. The test was performed in N₂-filled glove box without device encapsulation. For bending test, devices were placed on a cylindrical surface with a radius of about 3.0 mm. Meanwhile, devices were folded in folding test. Devices then underwent a specific number of repeated bending/folding before re-measurement of the device performance. This was conducted to observe the change in device performance upon extreme mechanical deformation. All measurements were conducted similarly as the

previous literatures published by Prof. Ziyi Ge's group (Song et al., 2018, Fan et al., 2019, Peng et al., 2019).

3.5.14 Plants growth

Glass beakers were utilized as containers to grow mung beans. Cottons were soaked in water before being placed inside a glass beaker. Three mung beans were prepared for the study of plants under dark, direct sunlight and direct sunlight with FST-OSCs. Hence, each beaker with soaked cotton housed one mung bean for growth observation. For dark environment, plant was placed inside a cardboard, where no light could pass through. For sunlight environment, plant was placed directly under sun. Meanwhile, for sunlight environment with FST-OSCs, plant was placed under the sun, but the lid of beaker was partially covered with FST-OSCs. Observations were made over a period of 9 days with regular watering of plants every day. The changes in plants growth in terms of length, branch sturdiness and hypertrophic leaves were being recorded and analysed. Note that the tests were performed to qualitatively observe the changes in plants growth, which were conducted similarly as previous studies (Liu et al., 2019c).

3.5.15 WF calculation

WF, φ [eV] can be calculated from UPS curve, which is represented in the following equation (Borse et al., 2018):

$$\varphi = h\nu - (E_{\text{cutoff (BE)}} - E_{\text{onset}}) \quad (5)$$

where $h\nu$ [eV] is the incident photon energy of He I (21.22 eV), $E_{\text{cutoff (BE)}}$ [eV] is the high binding energy determined by linear extrapolation to zero at the yield of secondary electrons and E_{onset} [eV] is the onset relative to the Fermi level (E_{Fermi}) of Au (0 eV). WF can also be represented in terms of kinetic energy, resulting in the simplification of equation to $\phi = E_{\text{cutoff (KE)}} - E_{\text{onset}}$. In this study, Fermi level of Au had been set to 0 eV prior to measurement, thus, the E_{cutoff} values obtained from UPS curve (based on kinetic energy) corresponded directly to the WF of electrode.

3.5.16 Conductivity calculation (interfacial layer)

The electrical conductivity of interfacial layer, δ [S m⁻¹] is quantified based on the following equation (Nian et al., 2015):

$$\delta = G_o \cdot (d_o/S) \quad (6)$$

where G_o [A V⁻¹] is the conductance obtained from the slope in J - V curve, d_o [m] is the thickness of interfacial layer film (in this study, ZnO with ~30 nm and ZnO/PBD with ~40 nm) and S [m²] is the device active area (in this study, 0.038 cm²).

3.5.17 Conductivity calculation (electrode)

The electrical conductivity of electrode, σ [S cm⁻¹] is normally quantified based on the following relationship (Meng et al., 2015):

$$\sigma = 1/(R_{\text{sq}} \cdot d_o) \quad (7)$$

where R_{sq} [$\Omega \text{ sq}^{-1}$] is the square resistance of electrode film and d_o [cm] is the thickness of electrode film (in this study, D-PEDOT:PSS with ~60 nm).

3.5.18 Exciton dissociation efficiency calculation

Exciton dissociation efficiency or probability, $P(E,T)$ [%] can be estimated using the following equation (Peng et al., 2018):

$$P(E, T) = J_{ph}/J_{sat} \quad (8)$$

where J_{ph} [mA cm^{-2}] is the photocurrent density equal to J_{sc} at short circuit condition and J_{sat} [mA cm^{-2}] is the saturated photocurrent density or the values of J_{ph} when $V_{eff} \geq 2 \text{ V}$. J_{ph} is obtained from $J_L - J_D$, where J_L is the current density under light irradiation and J_D is the current density under dark condition. Meanwhile, V_{eff} is defined by $V_o - V$, where V_o is the value of voltage when $J_{ph} = 0$ and V is the applied voltage.

3.5.19 Charge mobility calculation

Charge mobility, μ [$\text{m}^2 \text{ V}^{-1} \text{ s}^{-1}$] is estimated using space-charge limited current (SCLC) technique by fitting dark current density (J_D) and voltage (V) into the following equation (Peng et al., 2018):

$$J_D = (9/8) \cdot \epsilon_o \cdot \epsilon_r \cdot \mu \cdot (V^2/L^3) \quad (9)$$

where ϵ_o is the permittivity of free space constant, ϵ_r is the relative dielectric constant of the photoactive layer (typically 3), L is the thickness of the

photoactive layer and V is the difference between applied and built-in voltage.

All parameters are in standard unit.

3.5.20 Figure of merit (FoM) calculation

FoM is a dimensionless number, defined as the ratio of direct current conductivity (σ_{dc}) to optical conductivity (σ_{op}), which can also be presented as (Vosgueritchian et al., 2012):

$$\text{FoM} = 188.5 / [R_{sq} (T_{(\lambda)}^{-0.5} - 1)] \quad (10)$$

where R_{sq} [$\Omega \text{ sq}^{-1}$] is the square resistance of electrode and $T_{(\lambda)}$ [%] is the transmittance of electrode measured at $\lambda = 550 \text{ nm}$.

3.5.21 Average visible transmittance (AVT) calculation

AVT [%] is calculated by incorporating both human luminosity and transmittance performance. It is calculated using the following equation (Traverse et al., 2017):

$$\text{AVT} = (\int T_{(\lambda)} \cdot P_{(\lambda)} \cdot S_{(\lambda)} d\lambda) / (\int P_{(\lambda)} \cdot S_{(\lambda)} d\lambda) \quad (11)$$

where $T_{(\lambda)}$ is the transmittance curve in the visible light region (370-740 nm), $P_{(\lambda)}$ is the photopic response curve of human eyes and $S_{(\lambda)}$ is the solar spectrum (AM1.5G). It is important to note that AVT is calculated without taking into consideration the transmissivity of PET substrates.

Chapter 4. Performance Enhancement via Interface Engineering Strategy

4.1 Summary

In this chapter, enhancement of OSCs' performance was achieved through interface modification or interface engineering strategy. Interface engineering on sol-gel ZnO ETL was conducted by introducing additional oxadiazole-based electron-transporting materials, PBD between ZnO ETL and photoactive layer. The significance of incorporating PBD on ZnO was demonstrated by investigating the change in optical, electrical and morphological properties of pristine ZnO ETL. Herein, the utilization of PBD could improve ZnO film's conductivity, which was favourable for better charge transport ability. As compared to ZnO ETL, ZnO/PBD ETL had lower work function to facilitate more efficient electron extraction from the photoactive layer. Moreover, PBD could smoothen the ZnO film's morphology and improve hydrophobicity of the surface to provide uniform and intimate interfacial contact between ETL and the photoactive layer. As a result, through this interface engineering strategy, inverted OSCs based on PBDB-T:IT-M photoactive layer exhibited ~7% enhancement in PCE from 10.8% (ZnO-based device) to 11.6% (optimized ZnO/PBD-based device). Overall, this chapter highlights interface engineering strategy as an approach to improve photovoltaic performance for the realization of high-performing OSCs.

4.2 Introduction

A judicious choice of interfacial layers, including ETL and HTL is essential in OSCs to optimize device performance. The choice is typically made based on material's properties (e.g., conductivity, solubility, wettability, etc) and suitability with different OSCs' structures (conventional or inverted). For the case of inverted OSCs, MoO₃ is mostly utilized as the HTL due to its excellent transparency, robustness and stability to promote abundant and efficient hole extraction. On the contrary, the role of ETL in inverted OSCs is more prominent to minimize the large contact barrier existing between WF of ITO bottom electrode and LUMO energy level of acceptor material, so that efficient electron extraction can be achieved. Hence, studies of interfacial layer in inverted OSCs are generally centred on the development of ETL. Till date, several classes of ETL including *n*-type metal oxides (Sun et al., 2011), conjugated polyelectrolytes (CPEs) (Seo et al., 2011), alcohol-/water- soluble materials (He et al., 2012, Zhang et al., 2014, Fan and Zhu, 2016, Sun et al., 2017) and self-assembled dipole monolayers (SADMs) (Ma et al., 2010) have been explored; each with varying mechanisms and functions such as by tuning WF of the electrode, altering charge selectivity and etc. Among them, sol-gel ZnO first pioneered in 2004, is one of the best choices for solution-processed *n*-type metal oxides due to low cost, high stability, excellent optical transparency and non-toxic nature (Shirakawa et al., 2004). Furthermore, sol-gel ZnO demonstrates a promising capability to extract and transport electron while effectively block hole, making it a great candidate to be used as ETL in inverted OSCs. Once deposited as thin-film, conventional sol-gel ZnO is often post-treated with high-temperature annealing (~150-200°C) to promote the formation of crystalline

ZnO and reduce high density defect that may deteriorate OSCs' performance (Sun et al., 2011). Despite this effort, sol-gel ZnO still suffers from high surface roughness and its hydrophilic nature limits its interfacial contact with the organic photoactive layer (Liao et al., 2013, Borse et al., 2018). These conditions subsequently lead to poor electron extraction and device performance in inverted OSCs. On that account, interface modification or interface engineering on sol-gel ZnO is conducted to subdue the limitations of ZnO film functionally, so that high-performing inverted OSCs can be acquired.

To date, interface engineering on sol-gel ZnO has been studied through the doping of organic materials into ZnO (Liao et al., 2013, Li et al., 2017a, Borse et al., 2018) or the deposition of organic or inorganic materials as second interfacial layer on top of ZnO film (Lee et al., 2014, Borse et al., 2018). Both methods can impede surface trap and defect in sol-gel ZnO, provide better interfacial contact with the photoactive layer, alter the WF of the electrode, improve the conductivity of sol-gel ZnO and suppress recombination loss which are all beneficial for the improvement of photovoltaic performance. For example, Li *et al.* used sol-gel ZnO doped with ethylenediaminetetraacetic acid (EDTA) organic chelating agent to improve the PCE of inverted OSCs from 11.1% to 12.1% (Li et al., 2017a). On the other hand, Borse *et al.* introduced barium hydroxide (Ba(OH)₂) layer deposited on top of the ZnO film to smoothen its morphology and promote better interfacial contact with the photoactive layer, resulting in PCE increment from 7.12% to 8.54% (Borse et al., 2018).

Herein, PBD was introduced on top of the previously deposited ZnO film to modify its properties. This oxadiazole-based SM material was first used by Adachi in 1989 as ETL in bilayer organic light emitting diodes (OLEDs) (Adachi et al., 1989). And even up to now, it is still considered as one of the most used ETLs in OLEDs mainly due to its good electron affinity and mobility as well as outstanding charge injection ability (Kulkarni et al., 2004). Even though PBD is frequently used in OLEDs as electron-transporting materials, its applications in other areas of optoelectronic devices are still limited (Li et al., 2004, Sommer et al., 2009, Lee et al., 2011). Recently, PBD was discovered to function effectively as a buffer layer in thin-film transistors (TFTs) as it could tune the energy level alignment for improving charge extraction in TFTs (Shan and Kim, 2018). Yet, no studies were reported regarding the use of PBD in OSCs. In light of its advantages, PBD was incorporated for the first time in OSCs as second interfacial layer on top of ZnO to modify ZnO film's properties. The introduction of PBD on ZnO film was a promising strategy as it could improve the electrical and morphological properties of sol-gel ZnO film. Furthermore, PBD layer could further tune the WF of the electrode to better match the LUMO energy level of acceptor material. All those features allowed ZnO/PBD interlayer to function effectively as ETL in inverted OSCs.

4.3 Results and Discussions

4.3.1 Elemental states

The change in elemental states of sol-gel ZnO film upon deposition of PBD layer was studied by comparing the XPS spectra of modified ZnO/PBD film (chemical structures of PBD depicted in **Figure 4.1a**) and pristine ZnO film. The overall XPS survey spectra of those two films are presented in **Figure 4.1b**. Based on **Figure 4.1b**, both films showed similar XPS survey spectra with notable peaks of Zn 2p, O 1s, N 1s and C 1s. Among those peaks, the most distinct change could be seen from the enhancement and broadening of N peak due to the introduction of PBD layer as depicted in **Figure 4.1b, inset**. To support this statement, high-resolution N 1s peak of ZnO/PBD film was deconvoluted into its constituents shown in **Figure 4.1c**. In **Figure 4.1c**, a slight increment of N peak at 400.0 eV was observed, which was attributed to the presence of N-C double bond found in PBD molecules (Lee et al., 2014). The broadening of N peak was also noticed, which was caused by the occurrence of additional peak at 398.5 eV. In this case, the peak at lower E_b (398.5 eV) was ascribed to the interaction between N atoms of PBD and Zn atoms of ZnO found on the ZnO/PBD interfaces (Lee et al., 2014).

Figure 4.1d illustrates the C 1s survey spectra of ZnO/PBD film to further testify the presence of PBD on top of ZnO film. In this case, three constituent peaks were found at 284.8, 285.8 and 288.7 eV. Those peaks were ascribed to the presence of C-C, C=C, C-H, C-O and C=N bond (Wang et al., 2017b, Wang et al., 2019a), which were all present in PBD molecules. In short,

all of the results confirmed that PBD was successfully deposited on top of the ZnO film to function as a hybrid electron-transporting bilayer.

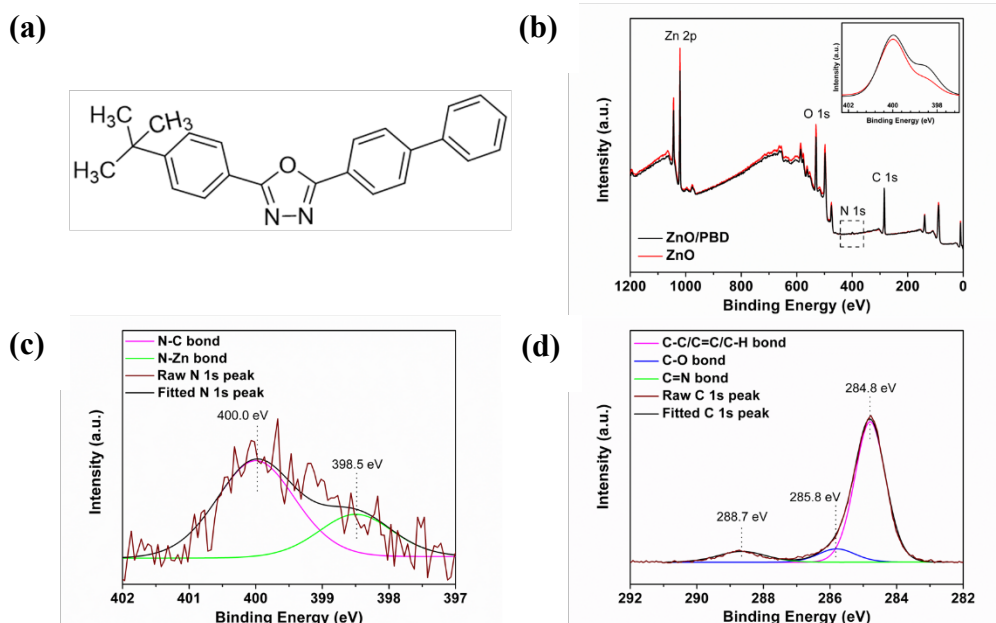


Figure 4.1 (a) Chemical structures of PBD electron-transporting materials. (b) XPS survey spectra of ZnO and ZnO/PBD on glass/ITO substrates; inset shows the enlarged N 1s spectra. The deconvoluted high-resolution (c) N 1s and (d) C 1s peaks of ZnO/PBD deposited on glass/ITO substrates.

The change in elemental states upon PBD deposition was further investigated by comparing the positions and shapes of Zn 2p and O 1s peaks of ZnO and ZnO/PBD films. The high-resolution Zn 2p and O 1s XPS spectra are shown in **Figure 4.2a** and **4.2b**, respectively. Two major peaks of $2p_{3/2}$ at lower E_b and $2p_{1/2}$ at higher E_b were obtained in **Figure 4.2a**, confirming the presence of ZnO phase formation in ZnO and ZnO/PBD films (Borse et al., 2018). Both $2p_{1/2}$ and $2p_{3/2}$ peaks looked identical with a slight shift in $2p_{3/2}$ peak from 1021.6 to 1021.5 eV upon deposition of PBD on ZnO film. This indicated that the incorporation of PBD had minimal influence on the Zn-O bond formation in ZnO

film. This was further supported from O 1s XPS survey of **Figure 4.2b**, where it shown similar peaks' position before and after the deposition of PBD. In here, the constant peak's position at higher E_b was attributed to O atoms in ZnO matrix, which was in agreement to the previous findings (Sun et al., 2011, Liao et al., 2013). Meanwhile, the peak at lower E_b corresponding to oxygen-deficient components was slightly shifted (Sun et al., 2011, Liao et al., 2013). The relative magnitude for this oxygen-deficient peak was calculated to be 51.28% for pristine ZnO film and 51.22% for ZnO/PBD film, implying that the number of oxygen-deficient components remained relatively constant even after PBD deposition. This meant that the incorporation of PBD could not induce significant reduction in surface traps and defects in ZnO film. Thus, the potential enhancement in device performance using ZnO/PBD ETL should not be related to the impediment of surface traps and defects. All in all, it was clear that through XPS studies, the introduction of PBD did not cause any notable effect on the elemental states of ZnO film.

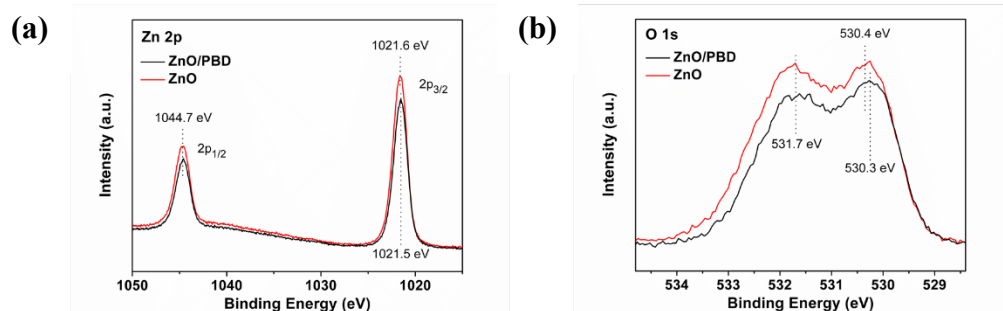


Figure 4.2 High-resolution (a) Zn 2p and (b) O 1s peaks of ZnO and ZnO/PBD deposited on glass/ITO substrates.

4.3.2 Work function

The role of PBD in tuning the WF of ITO cathode in inverted OSCs was studied using UPS measurements on ZnO- and ZnO/PBD- modified ITO surfaces. The UPS spectra of ZnO- and ZnO/PBD- modified ITO cathodes are portrayed in **Figure 4.3**. The detailed calculation method regarding how WF can be determined is being discussed in Chapter 3 (Methodology).

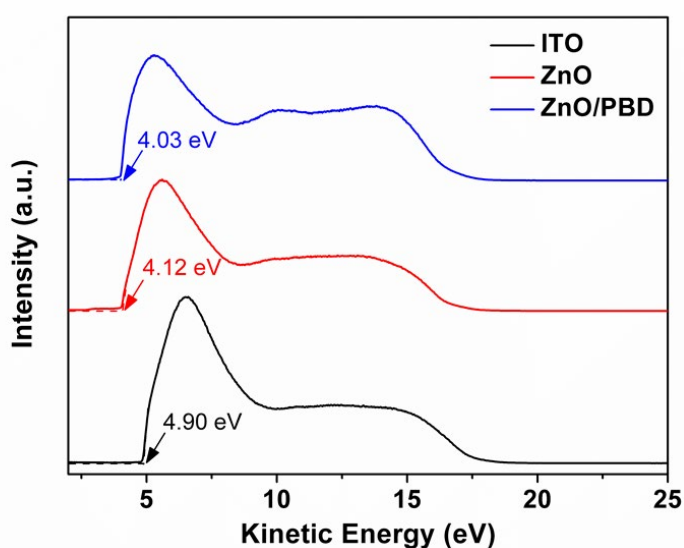


Figure 4.3 UPS spectra of ZnO- and ZnO/PBD- modified ITO cathodes as compared to bare ITO cathode.

Based on **Figure 4.3**, the WF of ZnO- and ZnO/PBD- modified ITO cathodes were determined to be 4.12 and 4.03 eV, while the WF of bare ITO cathode was 4.90 eV. It was obvious that the use of interfacial layers (ZnO and ZnO/PBD) could effectively modify the WF of bare ITO cathode. In comparison to ZnO-modified ITO cathode (4.12 eV), ZnO/PBD-modified ITO cathode showed a lower WF of 4.03 eV, which was relatively closer to LUMO energy level of IT-M acceptor (3.98 eV) (Li et al., 2016). This highly suggested that

additional PBD layer in ZnO/PBD interlayer could further tune the WF of ITO cathode by creating a better energy level alignment with the LUMO energy level of IT-M acceptor. On the one hand, this could promote Ohmic contact for efficient electron extraction and on the other hand, such WF modification might strengthen cell's built-in field beneficial for boosting photovoltaic performance.

4.3.3 Optical properties

Considering that both ZnO and ZnO/PBD films functioned as ETL in inverted OSCs, the transmittance performance of these films will be a crucial factor when evaluating optical properties. On this account, UV-vis transmittance of ZnO/PBD film was examined and compared to the pristine ZnO film.

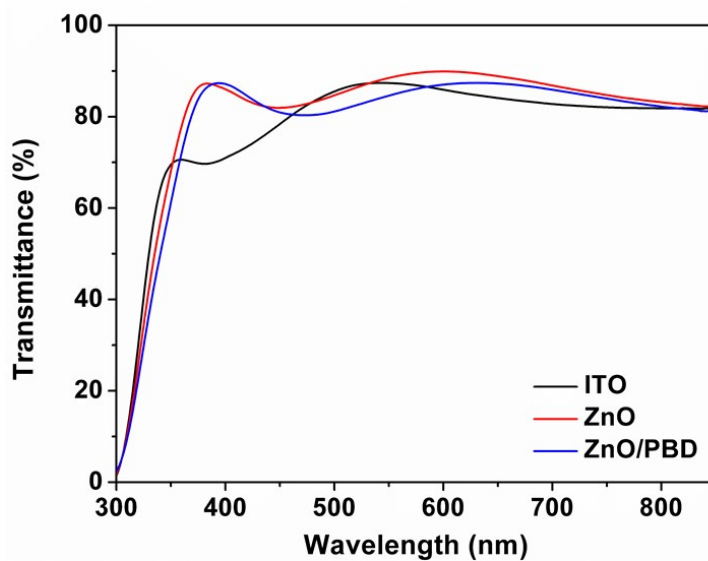


Figure 4.4 Transmittance spectra of ZnO and ZnO/PBD deposited on glass/ITO substrates as compared to bare glass/ITO.

As depicted in **Figure 4.4**, the transmittance spectra for both films showed comparable performance with a slight red-shifting in peak from ~382 nm (ZnO) to ~394 nm (ZnO/PBD), which could be due to the optical effect induced by additional PBD layer. It was observed that the ZnO/PBD film had lower transmissivity in the higher wavelength region ($\lambda > 440$ nm), most likely due to the absorption originated from PBD layer. Regardless of this, both films still displayed comparable and excellent transmissivity above 80% on a broad wavelength range from 360-850 nm and even higher than that of ITO. This implied that both films could function effectively as ETL in inverted OSCs due to their good transparency properties. In addition, it was also evident that the slight change in optical properties was not the main reason for performance improvement in devices based on ZnO/PBD ETL.

4.3.4 Electrical properties

The change in electrical properties of ZnO film upon PBD deposition was studied by analysing the electrical conductivity of the film. Devices with configuration of ITO/ZnO/Al and ITO/ZnO/PBD/Al were fabricated to compare the conductivity of the two films and the results were plotted into the J - V curve shown in **Figure 4.5**. The electrical conductivity of a film is calculated using **Equation 6**, as discussed in Chapter 3 (Methodology).

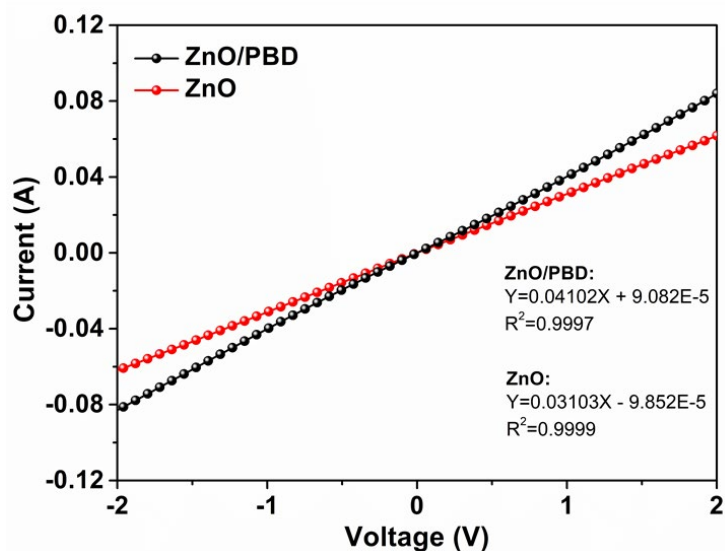


Figure 4.5 Electrical conductivity of ZnO and ZnO/PBD interlayer.

As portrayed in **Figure 4.5**, the trend on the J - V curve for both films revealed a linear fitted relationship between current and voltage, indicating that both interfacial layers were able to form Ohmic contact with the electrodes. Meanwhile, slopes in the J - V curve were correlated with the electrical conductivity. Based on the relationship portrayed in **Equation 6**, the conductivity of ZnO film was determined to be $2.45 \times 10^{-4} \text{ S m}^{-1}$ and raised by $\sim 76\%$ to $4.32 \times 10^{-4} \text{ S m}^{-1}$ through the utilization of PBD on ZnO. The higher conductivity of ZnO/PBD film suggested that ZnO/PBD had a lower contact resistance favourable for promoting better charge transport processes in OSCs.

4.3.5 Morphological properties

The morphological features of ZnO and ZnO/PBD films were studied by analysing the AFM height and phase images shown in **Figure 4.6** below.

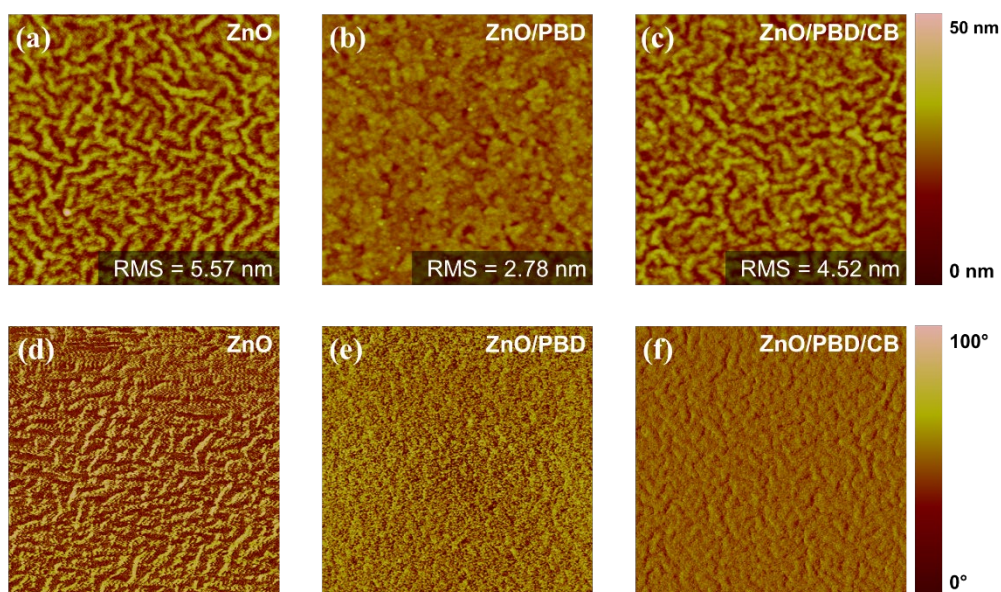


Figure 4.6 AFM ($5 \times 5 \mu\text{m}$) height and phase images of **(a, d)** ZnO, **(b, e)** ZnO/PBD and **(c, f)** ZnO/PBD/CB deposited on glass/ITO substrates.

It was observed from the height (**Figure 4.6a**) and phase images (**Figure 4.6d**) that the pristine ZnO film exhibited a rough surface morphology with root-mean-square (RMS) roughness of 5.57 nm. The RMS roughness of ZnO film was toned down significantly to 2.78 nm when PBD was deposited on top of the ZnO film (**Figure 4.6b** and **4.6e**), proving the ability of PBD to smoothen the ZnO film's morphology significantly.

CB as the processing solvent of photoactive layer was deposited on top of the ZnO/PBD film to simulate the actual inverted OSCs when photoactive blend layer of PBDB-T:IT-M in CB was deposited on top of the ETL. As shown in **Figure 4.6c** and **4.6f**, CB deposition could alter the surface morphology of ZnO/PBD film by partially removing PBD molecules from ZnO/PBD film. Partial removal of PBD was first speculated as the CB deposition on ZnO/PBD film did not raise the surface roughness back to 5.57 nm, which was the RMS

value for pristine ZnO film. This was later confirmed by the overall XPS survey spectra presented in **Figure 4.7a**, which compared ZnO/PBD/CB film to ZnO/PBD film. It was observed from **Figure 4.7a** that both films depicted similar peaks' position in the N 1s region, but with slightly lower spectral intensities for ZnO/PBD/CB film. Therefore, confirming the presence of PBD molecules upon CB deposition. In addition, high-resolution N 1s peak of ZnO/PBD/CB film as displayed in **Figure 4.7b**, also testified the presence of PBD even after CB deposition.

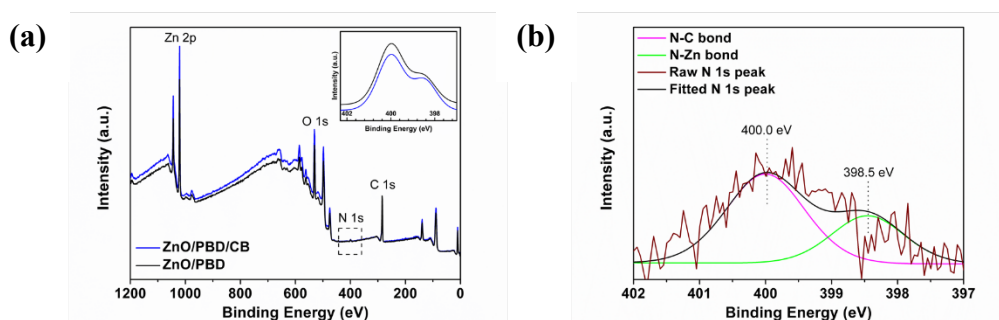


Figure 4.7 (a) XPS survey spectra of ZnO/PBD and ZnO/PBD/CB on glass/ITO substrates; inset shows the enlarged N 1s spectra. **(b)** High-resolution N 1s peak of ZnO/PBD/CB deposited on glass/ITO substrates.

Due to this unique characteristic, the surface roughness of ZnO/PBD film upon CB deposition was increased to 4.52 nm. This explained that CB solvent of the photoactive layer could become the key factor in optimizing the morphology of ZnO/PBD film by regulating its surface roughness via partial removal of PBD molecules. Such optimized morphology of ZnO/PBD film could provide uniform contact with the PBDB-T:IT-M photoactive layer, which was beneficial for better charge extraction and transport in OSCs.

The change in hydrophobicity of ZnO film upon PBD deposition was also investigated through contact angle measurement with deionized water shown in **Figure 4.8**. Similar to previous studies (Liao et al., 2013, Borse et al., 2018), the pristine ZnO film showed a small contact angle of 27° , indicating its hydrophilic nature. Interestingly, the contact angle was improved to 47° when PBD was deposited on top of the ZnO film, suggesting a better hydrophobicity of ZnO/PBD ETL as compared to the pristine ZnO ETL. In here, a more hydrophobic surface is desirable for ETL in inverted OSCs as it can promote a more intimate contact with the organic photoactive layer for better charge extraction and transport in OSCs.

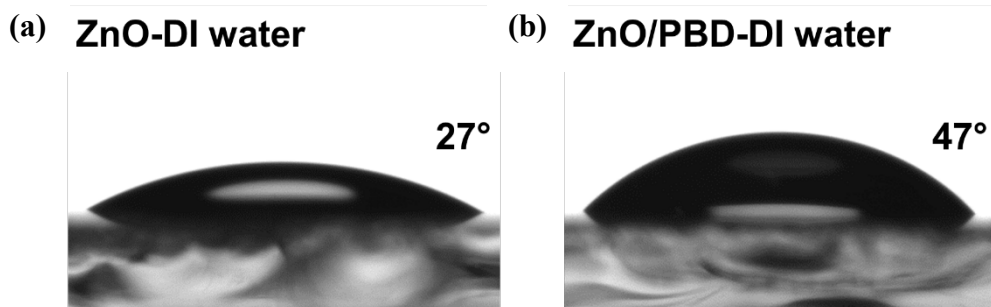


Figure 4.8 Contact angle images when deionized water was dripped onto the (a) ITO/ZnO and (b) ITO/ZnO/PBD substrates. The inset number is the contact angle.

4.3.6 Photovoltaic performances

To evaluate the usage of ZnO/PBD hybrid electron-transporting bilayer in organic photovoltaics, inverted devices with configuration of ITO/ZnO/PBD/PBDB-T:IT-M/MoO₃/Ag were fabricated as illustrated in **Figure 4.9a**. Comparative studies between pristine ZnO and ZnO/PBD interlayers are also needed, thereby, inverted devices with configuration of

ITO/ZnO/PBDB-T:IT-M/MoO₃/Ag were also fabricated. The corresponding energy level of these materials are all shown in **Figure 4.9b**, and the detailed procedures to fabricate such inverted OSCs can be found in Chapter 3 (Methodology).

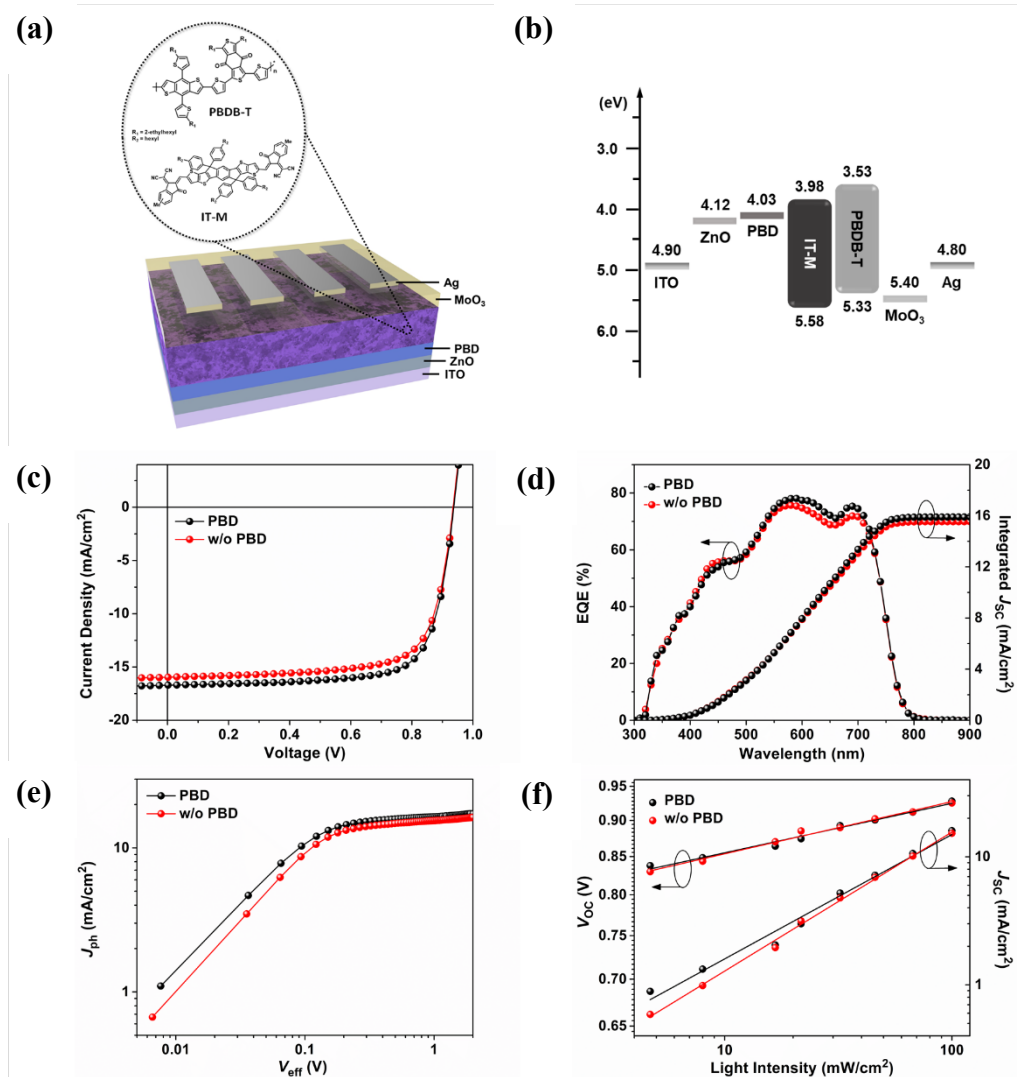


Figure 4.9 (a) Device structure of inverted OSCs with ZnO/PBD ETL; inset shows the chemical structures of PBDB-T donor and IT-M acceptor. (b) Energy levels of materials used in the OSCs. (c) J - V characteristics under standard AM1.5G illumination with 100 mW cm⁻² light intensity, (d) EQE spectra, (e) J_{ph} versus V_{eff} curve and (f) J_{sc} and V_{oc} light intensity dependence curve of devices with or without optimized PBD interlayer.

The J - V characteristics of inverted OSCs incorporating ZnO and optimized ZnO/PBD interlayers are depicted in **Figure 4.9c**. Meanwhile, the detailed photovoltaic parameters of OSCs with ZnO and optimized ZnO/PBD interlayers are listed in **Table 2.1**. The optimization of PBD layer in terms of its processing condition was also conducted to achieve the optimal OSCs' performance. The optimization of PBD layer on ZnO film is summarized in **Table 2.2** to **2.4**, where the effects of concentration, thickness and post-processing treatment on photovoltaic performance are being explored. It is important to note that all photovoltaic performances were measured under standard AM1.5G illumination with 100 mW cm^{-2} light intensity in N_2 -filled glovebox without encapsulation.

Table 2.1 Detailed photovoltaic parameters of inverted OSCs with ZnO and optimized ZnO/PBD interlayer.

Devices	V_{oc} [V]	J_{sc} [mA cm^{-2}]	FF [%]	PCE_{max} (avg.) ^a [%]
ZnO	0.935	15.9	72.8	10.8 (10.7)
ZnO/PBD	0.937	16.7	74.1	11.6 (11.3)

^a Average PCE was obtained from 8 independent devices

Table 2.2 Optimization of PBD interlayer on ZnO film in terms of PBD concentration.

Concentration [mg mL^{-1}]	V_{oc} [V]	J_{sc} [mA cm^{-2}]	FF [%]	PCE_{max} (avg.) ^a [%]
0.5	0.929	16.5	71.8	11.0 (10.7)
1.0	0.937	16.7	74.1	11.6 (11.3)
2.0	0.930	16.1	72.7	10.9 (10.6)
5.0	0.924	16.0	72.4	10.7 (10.4)

^a Average PCE was obtained from 8 independent devices

Table 2.3 Optimization of PBD interlayer on ZnO film in terms of PBD film thickness.

Thickness ^b [nm]	V_{oc} [V]	J_{sc} [mA cm ⁻²]	FF [%]	PCE _{max} (avg.) ^a [%]
~10	0.937	16.7	74.1	11.6 (11.3)
~7	0.939	16.1	75.2	11.4 (11.0)
~5	0.940	15.7	74.3	11.0 (10.8)

^a Average PCE was obtained from 8 independent devices

^b PBD thicknesses were modified by varying the spin coating speed for PBD deposition and were measured by averaging 5 different data points chosen at random

Table 2.4 Optimization of PBD interlayer on ZnO film in terms of post-processing annealing treatment.

Annealing T. [°C]	V_{oc} [V]	J_{sc} [mA cm ⁻²]	FF [%]	PCE _{max} (avg.) ^a [%]
non-annealed	0.937	16.7	74.1	11.6 (11.3)
50	0.910	16.4	72.3	10.8 (10.7)
75	0.914	16.1	72.7	10.7 (10.5)

^a Average PCE was obtained from 8 independent devices

As compared to pristine ZnO interlayer, the devices based on ZnO/PBD interlayer exhibited slightly higher PCE of 11.6% with J_{sc} of 16.7 mA cm⁻², V_{oc} of 0.937 V and FF of 74.1%. In contrast, reference devices based on ZnO interlayer only displayed a PCE of 10.8% with J_{sc} of 15.9 mA cm⁻², V_{oc} of 0.935 V and FF of 72.8%. The results indicated that the interfacial modification of ZnO film using PBD could improve the device performance through the simultaneous enhancement in J_{sc} and FF . Such enhancement of device performance was mostly attributed to the desirable features of bilayer ZnO/PBD ETL. As discussed previously, the better WF tuning ability, desirable film morphology and higher film conductivity of ZnO/PBD were the key factors to promote better charge extraction and transport processes in OSCs, which consequently improve J_{sc} and FF values.

EQE spectra of devices based on ZnO and ZnO/PBD interlayers were analysed to confirm the increment in J_{sc} . The EQE spectra shown in **Figure 4.9d** displayed a wide photo-response range from 300 to 800 nm. The photo-response peak found in 550-650 nm was ascribed to the absorption of PBDB-T donor, while the peak found in 650-750 nm was contributed by the absorption of IT-M acceptor. The absorption profiles of PBDB-T donor, IT-M acceptor and PBDB-T:IT-M blend film are shown in **Figure 4.10**. Devices based on ZnO/PBD interlayer had higher EQE performance in the wavelength region above 480 nm as compared to those based on ZnO interlayer, supporting the fact that ZnO/PBD-based device had a higher J_{sc} than ZnO-based device. Moreover, the integrated J_{sc} values measured from EQE curves were calculated to be 15.5 and 15.9 mA cm⁻² for devices based on ZnO and ZnO/PBD interlayers, agreeing well with the J_{sc} values measured from J - V curves (within 5% deviation range). The difference in J_{sc} values was normally attributed to the small spectral mismatch of the solar simulator's spectrum with the AM1.5G spectrum (Schilinsky et al., 2002).

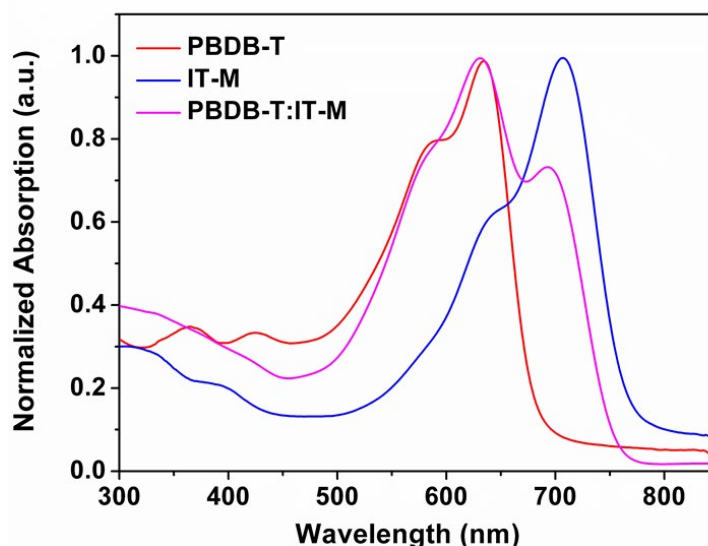


Figure 4.10 Absorption profiles of PBDB-T, IT-M and PBDB-T:IT-M blend film.

A plot of J_{ph} versus V_{eff} is shown in **Figure 4.9e** to compare the exciton dissociation efficiency of fabricated devices. The method used to quantify exciton dissociation efficiency is being discussed in Chapter 3 (Methodology). Based on J_{ph} versus V_{eff} curve, the J_{sat} values were determined to be 16.3 mA cm^{-2} for ZnO-based device and 17.1 mA cm^{-2} for ZnO/PBD-based device. Under short circuit conditions, the J_{ph}/J_{sat} ratio of devices based on ZnO and ZnO/PBD interlayers were calculated to be 97.5% and 97.7%, indicating that both devices had comparable exciton dissociation efficiency and that the performance improvement in ZnO/PBD-based device was not governed by exciton dissociation processes in the photoactive layer.

Non-geminate recombination mechanisms of devices based on ZnO and ZnO/PBD interlayers were investigated to understand the reasons behind improved photovoltaic performance. Bimolecular recombination was first analysed by investigating the dependence of J_{sc} on light intensity (P). Theoretically, the relationship between J_{sc} and P can be expressed as $J_{sc} \propto P^\alpha$, where α is the exponential factor denoting the degree of bimolecular recombination (Luo et al., 2018). When α is close to 1, there is a negligible bimolecular recombination (Luo et al., 2018). As shown in the J_{sc} versus P plot in **Figure 4.9f**, the slopes of 1.09 and 0.97 were obtained for devices based on ZnO and ZnO/PBD interlayers, respectively. The slope closer to 1 indicated that ZnO/PBD-based device had a relatively negligible bimolecular recombination.

Non-geminate recombination mechanisms were further studied in terms of trap-assisted recombination by analysing the dependence of V_{oc} on P . Theoretically, the slope of V_{oc} versus P curve in **Figure 4.9f** is equal to nkT/q , where n is the ideality factor, k is the Boltzmann's constant, T is the temperature and q is the elementary charge (Ie et al., 2018). In normal circumstances, the slope is found between $1 kT/q$ and $2 kT/q$ for trap-assisted recombination to occur. Slope closer to $1 kT/q$ indicates pure domination of bimolecular recombination, whereas slope closer to $2 kT/q$ stipulates domination of trap-assisted recombination (Ie et al., 2018). Devices based on ZnO interlayer showed a slope of $1.40 kT/q$, indicating the occurrence of trap-assisted recombination. In contrast, devices based on ZnO/PBD interlayer showed a smaller slope of $1.32 kT/q$, implying the suppression of trap-assisted recombination via the use of ZnO/PBD interlayer. Overall, studies on charge recombination proved that ZnO/PBD-based device had negligible bimolecular recombination and

suppressed trap-assisted recombination, implying that charges could be efficiently extracted and transported to the electrodes when ZnO/PBD hybrid interlayer was utilized. Hence, it was evident that in this study, charge recombination processes were one of the key principles governing the increase in photovoltaic performance (J_{sc} and FF) of ZnO/PBD-based device.

Charge transport properties of devices based on ZnO and ZnO/PBD interlayers were investigated using SCLC technique as discussed in Chapter 3 (Methodology). Electron-only devices with structure of ITO/ZnO/with or without PBD/PBDB-T:IT-M/Ca/Al were fabricated to compare the charge transport in ZnO and ZnO/PBD interlayers in terms of electron mobilities. From the typical $J^{1/2}$ - V curves shown in **Figure 4.11**, the electron mobility was calculated to be $1.67 \times 10^{-4} \text{ cm}^2 \text{ V}^{-1} \text{ s}^{-1}$ for ZnO-based device and $2.14 \times 10^{-4} \text{ cm}^2 \text{ V}^{-1} \text{ s}^{-1}$ for ZnO/PBD-based device. The improvement in electron mobility depicted a better charge transport ability in ZnO/PBD interlayer, mainly caused by the higher conductivity of the hybrid interlayer. Along with suppressed recombination, the good charge transport ability in ZnO/PBD interlayer governed the enhancement in photovoltaic performance (J_{sc} and FF) of ZnO/PBD-based device.

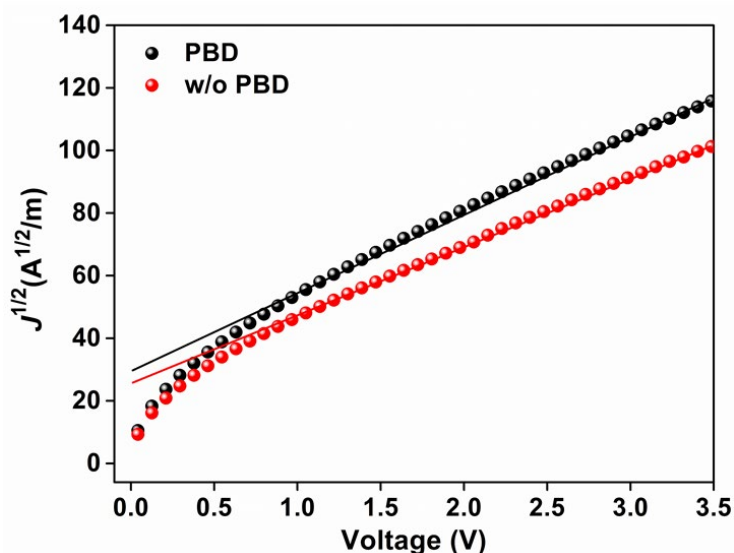


Figure 4.11 Electron mobility of devices with or without optimized PBD interlayer, measured using SCLC method.

All in all, the use of ZnO/PBD hybrid interlayer was proven to be effective in improving OSCs' performance by subduing the limitations of pristine ZnO. For instance, the creation of better energy level alignment to improve electron extraction to the cathode, the improvement in conductivity to improve charge mobility and the optimization of morphology to allow uniform and intimate contact with the photoactive layer. All these features were the key factors that significantly affect charge extraction and transport processes in OSCs. Due to these, charge recombination could be reduced effectively, while charge transport could be increased effectively. As discussed in Chapter 2 (Literature Review), reduced charge recombination and enhanced charge transport could result in higher J_{sc} and FF performances, which was in accordance with the current findings. Herein, interface engineering strategy could increase the J_{sc} and FF values from 15.9 mA cm^{-2} and 72.8% to 16.7 mA cm^{-2} and 74.1% , yielding to $\sim 7\%$ performance increment to 11.6% .

4.4 Conclusion

In conclusion, interfacial modification of ZnO film was conducted successfully by introducing additional oxadiazole-based electron-transporting materials known as PBD on top of the ZnO film to function as a hybrid electron-transporting bilayer. Through this bilayer strategy, inverted devices based on PBDB-T:IT-M photoactive layer demonstrated ~7% increment in the photovoltaic performance from 10.8% (ZnO-based device) to 11.6% (ZnO/PBD-based device). The enhancement in efficiency of ZnO/PBD-based device was due to the simultaneous increase in J_{sc} and FF values, mainly governed by the improvement in charge transport ability and suppression of charge recombination processes. Herein, the engineered ZnO/PBD interlayer could provide more efficient electron extraction as evidenced from its better WF reduction to match LUMO of IT-M acceptor and at the same time, able to facilitate uniform and intimate contact with the photoactive layer. Moreover, ZnO/PBD interlayer had better interlayer conductivity compared to pristine ZnO interlayer. All those superior features of ZnO/PBD hybrid interlayer had crucial influences on the charge extraction, transport and recombination processes in OSCs, which were conducive for the enhancement in photovoltaic performance of ZnO/PBD-based device. Overall, this study demonstrated that PBD could be used effectively for interfacial modification of ZnO to boost OSCs' performance by forming hybrid interlayer that could circumvent the inherent weaknesses of sol-gel ZnO (e.g., poor interfacial contact). Thus, interface engineering is proven to be a powerful strategy to enhance OSCs' performance in addition to material design and morphology control.

Chapter 5. Performance Enhancement via Electrode Engineering Strategy

5.1 Summary

In this chapter, enhancement of OSCs' performance was achieved via electrode engineering strategy. Electrode engineering on PEDOT:PSS FTEs was conducted by utilizing polyhydroxy compound dopant and gentle acid post-treatment method, specifically xylitol dopant and MSA treatment. The significance of those strategies on PEDOT:PSS FTEs was demonstrated by investigating the changes in optical, electrical, morphological and mechanical properties of pristine PEDOT:PSS FTEs. Herein, the utilization of xylitol doping and MSA treatment could induce better interconnected PEDOT:PSS morphology with favourable phase separation, which was conducive for enhancing electrode's conductivity to 2032 S cm^{-1} . In addition, such strategy could also provide electrode a stronger adhesion ability with the PET substrate, which was known to be effective for improving the mechanical stability of electrodes. With electrode engineering strategy, conventional flexible OSCs based on MSA-treated xylitol-doped PEDOT:PSS FTEs and PBDB-T-2F:Y6 photoactive layer demonstrated an excellent PCE of 14.2% with remarkable mechanical robustness against bending and folding, maintaining over 89% and 76% of the original PCE even after 1000 bending and folding cycles. In short, this chapter highlights electrode engineering strategy as an approach to improve both photovoltaic performance and mechanical stability for the realization of high-performing flexible OSCs based on PEDOT:PSS FTEs.

5.2 Introduction

Several factors have impeded the utilization of ITO electrode in flexible OSCs (Li et al., 2018, Qin et al., 2020b). As a result, several ITO alternatives have been explored for their potential as FTEs in flexible OSCs, which include silver nanowires (Ag NWs) (Song et al., 2013, Guo et al., 2013, Seo et al., 2017, Dong et al., 2019), conducting polymers (Kim et al., 2014, Fan et al., 2016, Song et al., 2018, Fan et al., 2019), carbon-based materials (graphene and carbon nanotubes) (Salvatierra et al., 2013, Park et al., 2014a, Konios et al., 2015, Shin et al., 2018) and many more (Park et al., 2014b, Ou et al., 2016). Among them, PEDOT:PSS as transparent conducting polymer shows the most promising potential for cost-effective flexible devices owing to its exceptional intrinsic flexibility, high optical transparency, low surface roughness, excellent solution-processability and superior thermal stability (Li et al., 2018, Qin et al., 2020b). Despite that, PEDOT:PSS suffers from low conductivity which may substantially restrain its application as electrode in flexible OSCs (Zhang et al., 2013, Meng et al., 2015).

Typically, the conductivity of PEDOT:PSS can be tuned by modifying the PEDOT to PSS ratio (Qin et al., 2020b). For instance, PEDOT:PSS that is normally used for HTL applications has a ratio of 1:6 (PEDOT to PSS ratio in Clevios P VP 4083), while for electrode applications, a ratio as low as 1:2.5 (PEDOT to PSS ratio in Clevios PH1000) is widely preferred. Though by comparison, PEDOT:PSS (PH1000) is more conductive than PEDOT:PSS (4083), but its pristine conductivity ($\sim 0.3 \text{ S cm}^{-1}$) is still significantly low for practical application as FTEs in flexible OSCs (Mengistie et al., 2014). On that

account, electrode modification or electrode engineering on PEDOT:PSS (PH1000) is conducted to subdue the limitations of pristine PEDOT:PSS functionally, so that high-performing FTEs for flexible OSCs can be obtained.

To date, electrode engineering on PEDOT:PSS FTEs can be conducted through doping treatment using organic compounds (Vosgueritchian et al., 2012, Ouyang, 2013, Thomas et al., 2014, Peng et al., 2019) and/or surface post-treatment using acid (Yeon et al., 2015, Kim et al., 2015, Song et al., 2018, Song et al., 2020b). Both methods can improve the optical, electrical and morphological properties of pristine PEDOT:PSS films, which contribute to improved FTEs' conductivity. Some recent studies also mentioned that the combination of doping and surface treatment could simultaneously increase the mechanical flexibility and conductivity of PEDOT:PSS FTEs. For instance, Song *et al.* proved that D-sorbitol doping and eco-friendly citric acid treatment could enhance PEDOT:PSS properties as FTEs such as transparency, conductivity and mechanical flexibility, which subsequently resulted in the realization of high-performing flexible OSCs with PCE of over 14% (Song et al., 2020b). However, not many studies on PEDOT:PSS are directed towards this aspect. This has therefore, driven the current work to engineer a high-performing PEDOT:PSS electrode with improved conductivity as well as enhanced adhesion ability to improve performance and mechanical stability.

Herein, two constructive approaches were utilized to enhance PEDOT:PSS performance as FTEs. A range of polyhydroxy compounds that differed based on their alkyl chain length were initially investigated as dopant and xylitol compound appeared to show the best effect in terms of square

resistance, R_{sq} and conductivity, σ . In addition to doping treatment, MSA was also used as surface post-treatment method at room temperature. Through these approaches, the optical, electrical and morphological properties of pristine PEDOT:PSS FTEs could be engineered and improved. Most importantly, such doping and acid treatment could provide electrode a stronger adhesion ability with the PET substrate, which were conducive for boosting mechanical stability of FTEs against extreme mechanical deformation (bending and folding). All those features allowed MSA-treated xylitol-doped PEDOT:PSS or D-PEDOT:PSS to function effectively as FTEs in high-performing flexible OSCs.

5.3 Results and Discussions

5.3.1 Preliminary doping selection

A range of polyhydroxy compounds was preliminarily studied as dopant for modifying the pristine properties of PEDOT:PSS FTEs. Three polyhydroxy compounds as depicted in **Figure 5.1**, namely ethylene glycol, xylitol and dulcitol were doped into PEDOT:PSS aqueous solution and the corresponding solutions were subsequently deposited as thin-films.

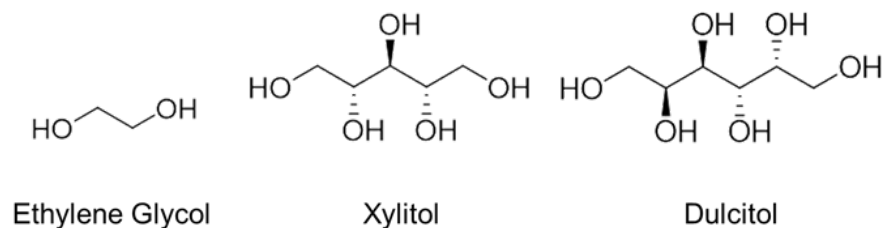


Figure 5.1 Chemical structures of polyhydroxy compounds – ethylene glycol, xylitol dan dulcitol.

The variation of R_{sq} and σ of those doped films were investigated as summarized in **Figure 5.2**. Generally, it is highly desirable for FTEs to have high conductivity and low square resistance to promote efficient electrodes' performance. From **Figure 5.2**, it was obvious that PEDOT:PSS films doped with xylitol yielded the highest conductivity of 1350 S cm^{-1} and lowest square resistance of $78 \text{ } \Omega \text{ sq}^{-1}$, making xylitol to be the best dopant candidates for PEDOT:PSS FTEs among the three available polyhydroxy compounds.

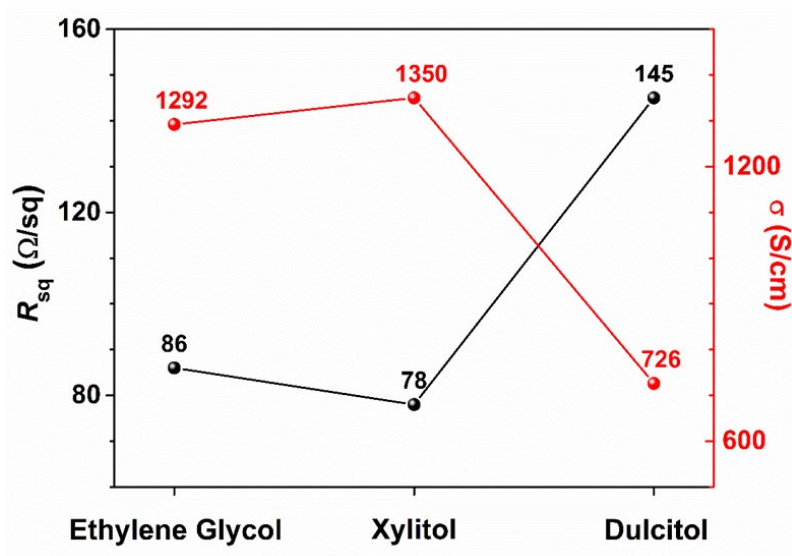


Figure 5.2 Comparison of R_{sq} and σ of PEDOT:PSS films (thickness: $\sim 90 \text{ nm}$) doped with various polyhydroxy compounds.

5.3.2 Bonding properties

The role of xylitol doping in enhancing PEDOT:PSS FTEs performance was first studied by evaluating the potential chemical interaction and bonding between electrodes and substrates. The xylitol-doped PEDOT:PSS films could induce strong intermolecular forces with the substrates, particularly when flexible PET plastic substrates were used. The intermolecular forces present were hydrogen bond and van der Waals bond, formed primarily from the interactions between hydroxylated surface of xylitol components in PEDOT:PSS and carbonyl group of PET substrates. The schematic illustrations of hydrogen bond and van der Waals bond effects on the substrate/electrode interfaces are displayed in **Figure 5.3**.

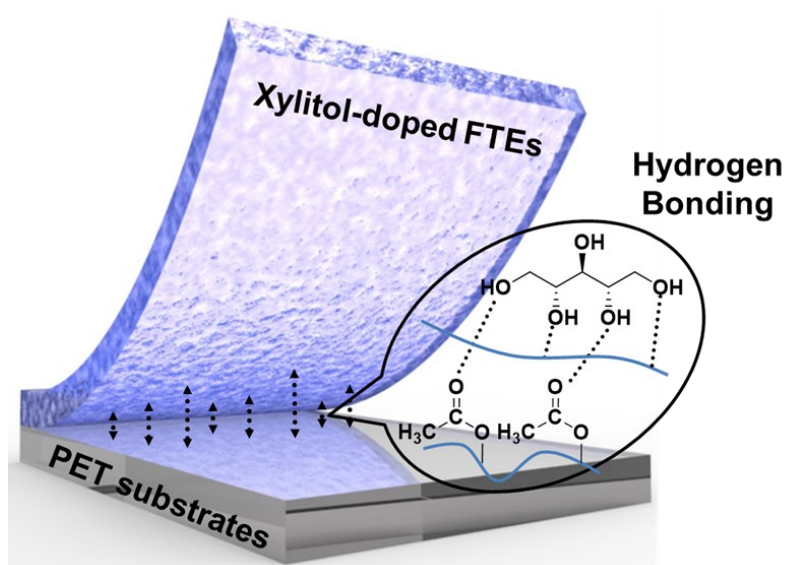


Figure 5.3 The schematic diagram of hydrogen bond and van der Waals bond effects on the substrate/electrode interfaces.

The chemical interaction and bonding occurring at the substrate/electrode interfaces were then quantified by measuring the adhesive force of pristine and xylitol-doped PEDOT:PSS solutions using high sensitivity micro electro-mechanical balance, as shown in **Figure 5.4**. The as-cast or pristine PEDOT:PSS solution had a relatively low adhesion force of 0.217 mN. Interestingly, the adhesion force was improved by almost 48% to 0.321 mN upon the addition of 5.0 wt% xylitol dopant. The improved adhesion force in xylitol-doped PEDOT:PSS FTEs was indicative of the presence of strong bonding interaction (hydrogen bond and van der Waals bond) at the substrate/electrode interfaces, which was in accordance with the previous hypothesis. Such strong bonding interaction at the interface could provide FTEs a stronger adhesion ability with the substrates, which was highly beneficial for bending and folding applications of flexible OSCs. Furthermore, intramolecular and/or intermolecular hydrogen bonds between xylitol molecules in PEDOT:PSS FTEs might further enhance electrodes' mechanical stability against bending and folding deformation. Thus, simple strategies such as xylitol doping on PEDOT:PSS could present a new opportunity for the realization of high-performing FTEs with good mechanical properties.

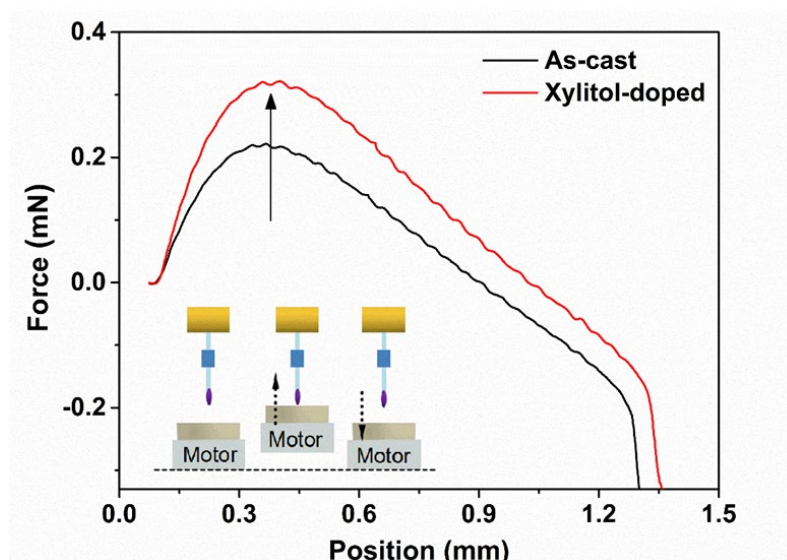


Figure 5.4 Adhesive force of as-cast PEDOT:PSS solution and PEDOT:PSS solution doped with xylitol; inset shows the process schematic for adhesion force measurement.

5.3.3 Optical properties

In conjunction with xylitol doping, MSA treatment was also used as the post-processing treatment for PEDOT:PSS film. Combination of xylitol doping and MSA treatment could further improve the overall FTEs' performance, not only in terms of mechanical stability but in terms of optical, electrical and morphological properties as well.

The optical properties of D-PEDOT:PSS were analysed using UV-vis spectroscopy. **Figure 5.5a** compares the transmittance and reflectance spectra of PET/D-PEDOT:PSS with PET/ITO and glass/ITO. Meanwhile, the transmittance spectra of PET/as-cast PEDOT:PSS as compared to PET/D-PEDOT:PSS is presented in **Figure 5.5b**. Among the fabricated FTEs, PET/ITO film displayed the lowest transparency below 80% across the entire 300-850 nm region. Even without considering its inherent physical properties of being rigid,

bulky and fragile, such low transmittance in the major absorbing region makes it unsuitable to use ITO for preparing highly efficient flexible OSCs.

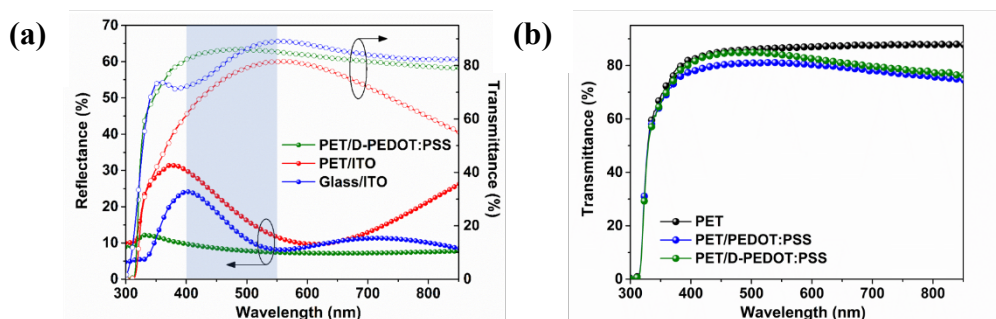


Figure 5.5 (a) Transmittance and reflectance spectra of glass/ITO, PET/ITO and PET/D-PEDOT:PSS. (b) Comparison of transmittance spectra of as-cast PEDOT:PSS and D-PEDOT:PSS films deposited on PET plastic substrates as compared to bare PET.

As-cast PEDOT:PSS as ITO alternatives could improve the transmittance performance across the 300-850 nm region as depicted in **Figure 5.5b**. Further improvement in transmissivity could be achieved when PEDOT:PSS was subjected to xylitol micro-doping and MSA treatment, where PET/D-PEDOT:PSS film could exhibit a more stable transmittance performance with an overall transmittance of $\sim 80\%$ across 350-850 nm region. This caused PET/D-PEDOT:PSS to have a comparable optical transparency to glass/ITO as displayed in **Figure 5.5a**. Notably, PET/D-PEDOT:PSS even showed superior transparency over glass/ITO in the wavelength region of 360-500 nm where its transmissivity almost reached 90%. Furthermore, as depicted in **Figure 5.5a**, PET/D-PEDOT:PSS had a low reflectance below 15% across the entire wavelength region (300-850 nm). This was considerably lower than the reflectance of glass/ITO that could reach up to 25%. Both high transmissivity and low reflectivity of D-PEDOT:PSS on PET plastic substrate enabled most of

the incident lights to pass through for photoactive layer absorption, proving its exceptional potential as alternative ITO electrodes. Its superb transparency in the visible light region (370-740 nm) also created a greater opportunity for usage in semi-transparent devices in the near future.

5.3.4 Electrical properties

The electrical properties of D-PEDOT:PSS FTEs were investigated by studying their R_{sq} , σ and FoM values. The relationships between each parameter and the methods used to quantify each parameter are being discussed in Chapter 3 (Methodology). The results are summarized in **Table 3.1**. Other data for conventional acid-treated PEDOT:PSS FTEs are also listed for comparison.

Table 3.1 R_{sq} , σ and FoM values of D-PEDOT:PSS films when compared with different acid-treated PEDOT:PSS films.

Treatment	R_{sq} [$\Omega \text{ sq}^{-1}$]	σ [S cm^{-1}]	d_o [nm]	FoM
Sulphuric acid (98 wt%)	67	2714	55	72
Nitric acid (68 wt%)	88	1748	65	64
Xylitol + MSA (99 wt%)	82	2032	60	78

It can be deduced from **Table 3.1** and **Equation 7** that R_{sq} and σ values are inversely correlated, where small R_{sq} values correspond to high σ values. Based on previous literatures, pristine PEDOT:PSS FTEs shown an extremely low σ of approximately 0.3 S cm^{-1} , rendering their usage as FTEs unpractical in flexible OSCs (Mengistie et al., 2014).

Combined xylitol and MSA treatment can solve those issues, by improving both the R_{sq} and σ values. The R_{sq} and σ values of D-PEDOT:PSS FTEs were measured to be $82 \Omega \text{ sq}^{-1}$ and 2032 S cm^{-1} respectively, as illustrated in **Table 3.1**. Those values were even comparable to other acid-treated PEDOT:PSS FTEs. Besides that, FoM is an important performance metric for estimating the performance of FTEs. It is particularly desirable to have an FoM value of over 35, as it is the minimum benchmark for commercial viability of FTEs (Vosgueritchian et al., 2012). Using **Equation 10**, the FoM value of D-PEDOT:PSS FTEs was calculated to be 78, which was the highest when compared to other acid treatment methods (sulphuric acid with 72 and nitric acid with 64). The FoM results strongly proved the functionality of D-PEDOT:PSS FTEs in flexible OSCs.

5.3.5 Morphological properties

The morphological features of D-PEDOT:PSS were compared to the as-cast and xylitol-doped PEDOT:PSS through TEM analysis shown in **Figure 5.6**. **Figure 5.6a** depicts the TEM results for films based on as-cast, xylitol-doped and xylitol-doped MSA-treated PEDOT:PSS. While **Figure 5.6b** presents the morphology illustrations for films based on as-cast, xylitol-doped and xylitol-doped MSA-treated PEDOT:PSS. The possible ionic and hydrogen bonding interactions in as-cast, xylitol-doped and xylitol-doped MSA-treated PEDOT:PSS films are illustrated in **Figure 5.6c** to explain the reason of morphological change upon doping and acid treatment.

As depicted in **Figure 5.6a** and **5.6b**, the as-cast PEDOT:PSS films exhibited coiled structures and poor phase separations between PEDOT and PSS with no obvious aggregations. On the other hand, good phase separations were observed in the xylitol-doped films with more fibre-like interconnected PEDOT chains. The phase separations were further enhanced through incorporation of xylitol doping and MSA treatment in D-PEDOT:PSS films, where continuous and well-distributed PEDOT domains were observed. The enhanced phase separation was caused by the disappearance of Coulombic interactions or ionic bonding between PEDOT and PSS chains through two main mechanisms as illustrated in **Figure 5.6c**. First was through the hydrogen bond interactions between xylitol components and PSS components. Second was through the interactions between H^+ of MSA solution with PSS^- to form neutral PSSH chains. The disappearance of Coulombic interactions also caused the conformational change of PEDOT chains from coil to extended-coil or linear nanofibrils structure, which reduced the energy barrier width for inter-chain and inter-domain charge hopping along PEDOT chains. The structural rearrangement of PEDOT increased the crystallinity order in D-PEDOT:PSS films to facilitate efficient intra- and inter-chain charge transport.

Moreover, the morphological features of D-PEDOT:PSS were probed using AFM. EDS and XPS analyses were also performed on D-PEDOT:PSS FTEs to provide more insights on the changes in surface components, particularly S compositions. The results were then compared to those of as-cast or pristine PEDOT:PSS as shown in **Figure 5.7**.

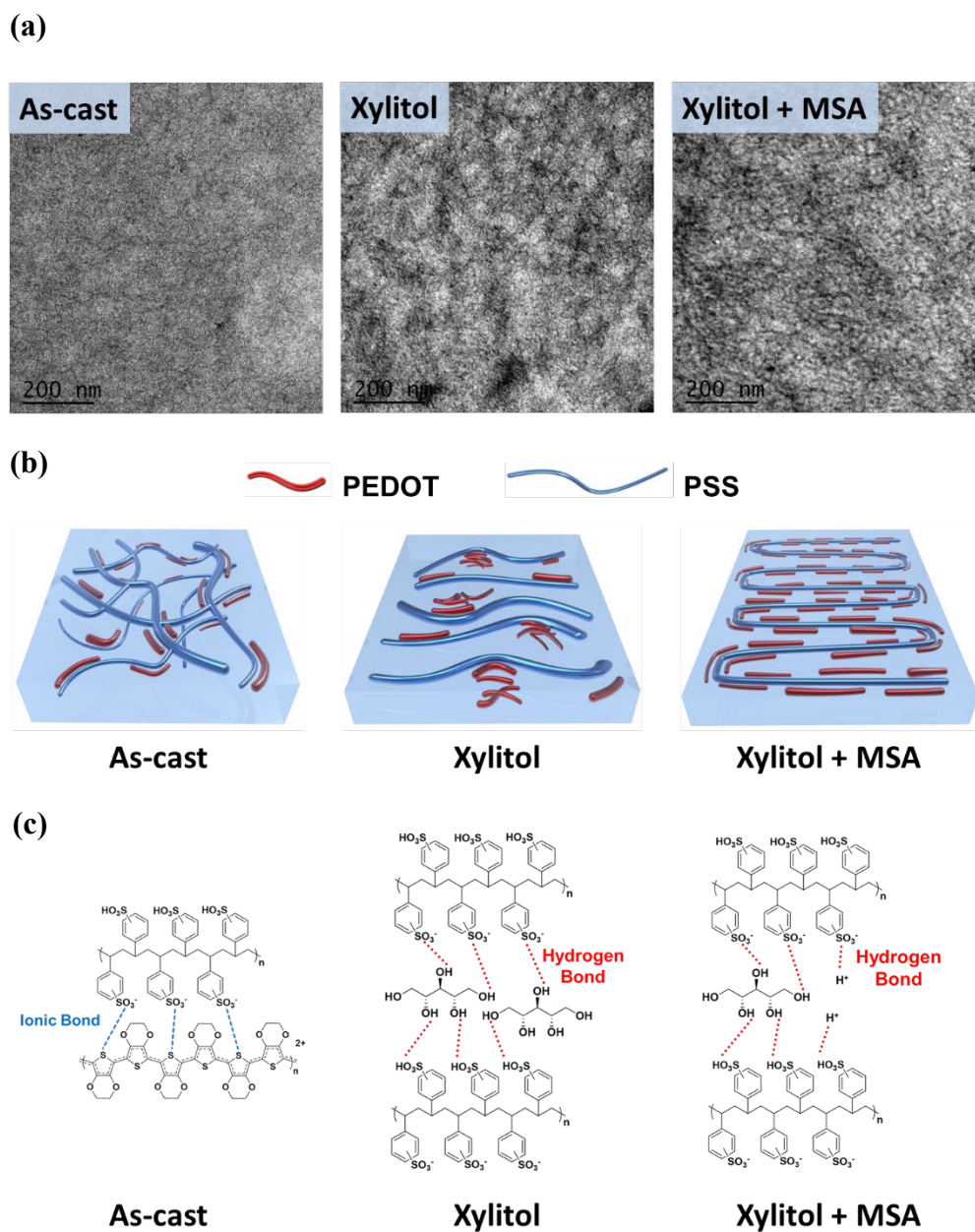


Figure 5.6 (a) TEM images of the as-cast, xylitol-doped and xylitol-doped MSA-treated PEDOT:PSS films fabricated on PET plastic substrates. (b) The schematic diagram of morphology of the as-cast, xylitol-doped and xylitol-doped MSA-treated PEDOT:PSS films. (c) The schematic diagram of ionic and hydrogen bonding in as-cast, xylitol-doped and xylitol-doped MSA-treated PEDOT:PSS films.

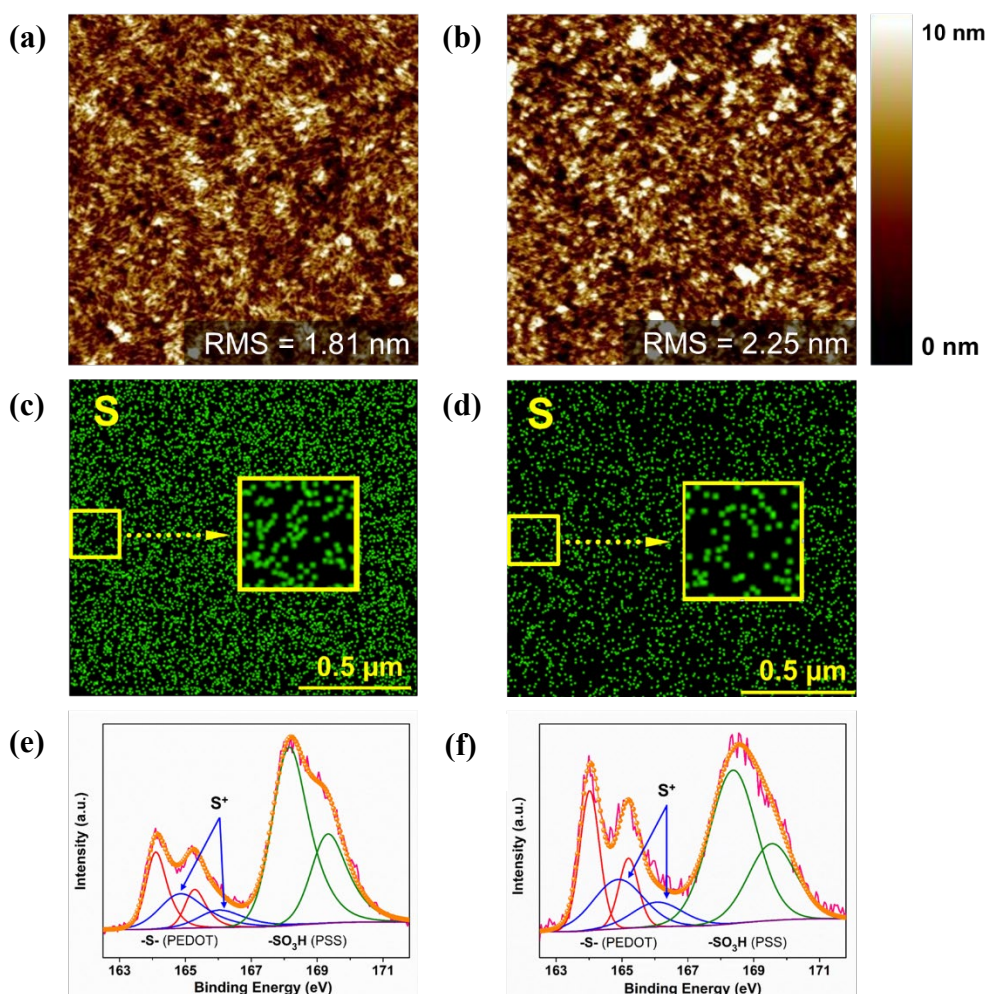


Figure 5.7 AFM ($2 \times 2 \mu\text{m}$) height images of **(a)** as-cast PEDOT:PSS and **(b)** D-PEDOT:PSS films. EDS elemental mapping showing the distribution of S element in **(c)** as-cast PEDOT:PSS and **(d)** D-PEDOT:PSS films. Fitted S 2p XPS spectra of **(e)** as-cast PEDOT:PSS and **(f)** D-PEDOT:PSS films.

Figure 5.7a and **5.7b** compare the AFM images of the as-cast PEDOT:PSS and D-PEDOT:PSS, respectively. The as-cast film displayed a relatively smooth surface with RMS roughness of 1.81 nm. However, the as-cast film suffered from poor phase separation, where disconnected PEDOT-rich grains (corresponded to the bright positive region of AFM images) were observed. After combined treatment, D-PEDOT:PSS film exhibited a slightly rougher surface with RMS of 2.25 nm. It also displayed continuous and well-

distributed PEDOT-rich grains with more uniform phase separation than the as-cast film. The enhanced phase separation in D-PEDOT:PSS was essentially caused by xylitol doping and MSA treatment, where both promoted the disappearance of Coulombic interactions between PEDOT and PSS chains through hydrogen bond interactions and interactions between H^+ and PSS^- , respectively. These findings were in fact, in accordance with the previous TEM analysis. Thus, it could be concluded that D-PEDOT:PSS films had better interconnected morphology with favourable phase separation and structural rearrangement when compared to the pristine PEDOT:PSS films. The morphological features of D-PEDOT:PSS FTEs were favourable for improving electrodes' conductivity.

EDS elemental analysis of S elements in as-cast PEDOT:PSS and D-PEDOT:PSS FTEs were conducted, as shown in **Figure 5.7c** and **5.7d** respectively. The bright positive region corresponded to the S elemental distribution on the film. The as-cast film displayed a higher density of S atoms as compared to the modified film (**Figure 5.7c, inset** and **5.7d, inset**). In other words, a more concentrated S component was found in the pristine PEDOT:PSS film, whereas a significant drop in S components was observed in the D-PEDOT:PSS film.

To further evaluate this finding, XPS analysis was conducted on the pristine film and the film with xylitol doping and MSA treatment. As shown in **Figure 5.7e**, there were two major XPS peaks observed in the low E_b region (163-166 eV) and in the high E_b region (167-171 eV). The peaks between 163-166 eV were attributed to the S 2p band of thiophene ring in PEDOT, while those found at higher E_b were originated from the S 2p band of the sulfonate moieties in PSS. Similar peaks' location after xylitol doping and MSA treatment were observed as shown in **Figure 5.7f**. However, there was a substantial drop in the S 2p XPS intensity ratio of PEDOT to PSS, demonstrating the removal of some PSS chains from PEDOT:PSS matrix. Those removals were caused by the disappearance of Coulombic interactions between PEDOT and PSS chains, induced by xylitol doping and MSA treatment. Such removal would eventually lower down the S elemental concentration in D-PEDOT:PSS films, which was in accordance with the aforementioned EDS findings. This indicated that xylitol doping and MSA treatment could significantly modify the surface components of pristine PEDOT:PSS film to yield a more desirable FTEs' morphology.

5.3.6 Mechanical stability

Mechanical stability of D-PEDOT:PSS FTEs against extreme mechanical deformation was analysed by studying the variation of R_{sq} during bending and folding test. Additionally, it was also compared to the as-cast PEDOT:PSS FTEs. The results are summarized in **Figure 5.8**.

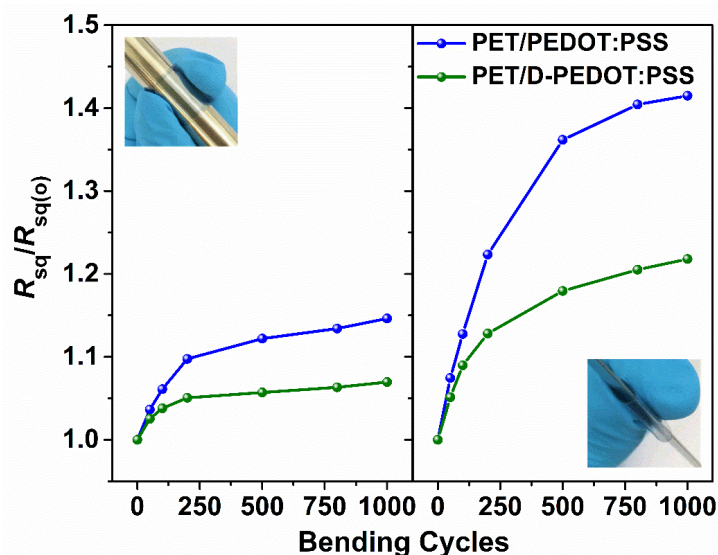


Figure 5.8 $R_{sq}/R_{sq(o)}$ of PET/D-PEDOT:PSS and PET/PEDOT:PSS (control samples) as a function of bending cycles; insets show the images of bending and folding test conducted using cylinder and ruler, respectively.

$R_{sq}/R_{sq(o)}$ value estimates the extent of the change in square resistance of electrodes upon bending/folding test. Samples were subjected to a cylinder for bending test (**Figure 5.8, inset**), where it underwent 1000 bending cycles. The folding test was conducted similarly (**Figure 5.8, inset**). It was noticed that both FTEs exhibited low R_{sq} change ($R_{sq}/R_{sq(o)} < 1.15$) even after 1000 bending cycles, indicating their robustness against bending. Yet, strong adhesion induced by xylitol in PET/D-PEDOT:PSS resulted in a rather excellent bending performance where its R_{sq} was increased by only less than 5% after 1000 bending cycles. On the contrary, as-cast PET/PEDOT:PSS demonstrated larger deviation of more than 10% after 1000 bending cycles. The deviation became even greater when as-cast PET/PEDOT:PSS was subjected to small-radius folding test, in which the R_{sq} value was raised considerably by over 40% after 1000 folding cycles. Xylitol doping on D-PEDOT:PSS FTEs could reduce this effect greatly

by enhancing the adhesiveness of electrodes to the substrates. Thus, after 1000 folding cycles, the deviation in R_{sq} of PET/D-PEDOT:PSS still remained in the 20% range. This suggested that interface interactions between electrodes and substrates could be an efficient way to boost the mechanical stability of FTEs against bending and folding.

Based on the aforementioned findings, incorporation of both xylitol doping and MSA treatment could improve the performance of as-cast PEDOT:PSS FTEs in terms of better optical properties (transmittance and reflectance), excellent electrical properties (conductivity, square resistance and FoM), more favourable morphological features with uniform phase separation and stronger adhesion ability (better mechanical robustness against bending and folding). All these characteristics allowed D-PEDOT:PSS to be used as alternative ITO electrodes for flexible device applications, such as flexible OSCs.

5.3.7 Photovoltaic performances

D-PEDOT:PSS FTEs were used in flexible organic photovoltaic devices to evaluate their photovoltaic performances. Photoactive layer based on PBDB-T-2F donor and Y6 acceptor (chemical structures depicted in **Figure 5.9a**) was selected due to its high efficiency performance. Flexible OSCs based on D-PEDOT:PSS FTEs were then fabricated with configuration of PET/D-PEDOT:PSS FTE/4083/PBDB-T-2F:Y6/PDINO/Al as displayed in **Figure 5.9b**. Flexible OSCs based on glass/ITO and PET/ITO electrodes were also fabricated for comparison with those based on PET/D-PEDOT:PSS electrodes. The detailed procedures to fabricate such OSCs is included in Chapter 3

(Methodology). The J - V characteristics of rigid (glass/ITO) and flexible (PET/D-PEDOT:PSS) devices are depicted in **Figure 5.9c**. Meanwhile, the detailed photovoltaic parameters of OSCs based on glass/ITO, PET/ITO and PET/D-PEDOT:PSS electrodes are listed in **Table 3.2**. All photovoltaic performances were measured under standard AM1.5G illumination with 100 mW cm^{-2} light intensity in N_2 -filled glovebox without encapsulation.

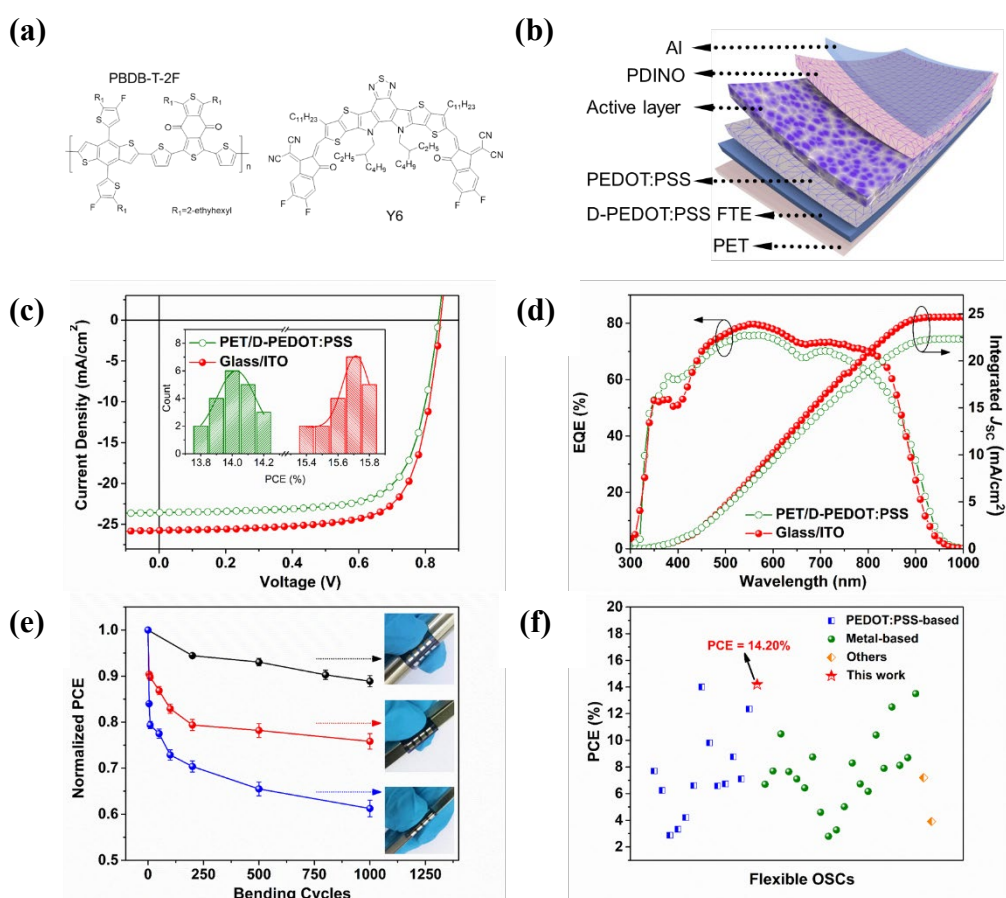


Figure 5.9 (a) Chemical structures of PBDB-T-2F donor and Y6 acceptor. (b) Device structure of flexible OSCs incorporating D-PEDOT:PSS FTEs. (c) J - V characteristics and (d) EQE spectra of devices based on PET/D-PEDOT:PSS and glass/ITO. (e) Normalized PCE of flexible OSCs based on D-PEDOT:PSS FTEs after subjected to bending (black), mid-device folding or folding between Al electrodes (red) and folding on top of the Al electrodes (blue). (f) Recent scatter plot report for PCE values of flexible OSCs with different FTEs; all data are listed in "Appendix A".

Table 3.2 Detailed photovoltaic parameters of rigid and flexible OSCs based on D-PEDOT:PSS and ITO electrodes.

Devices	V_{oc} [V]	J_{sc} [mA cm ⁻²]	FF [%]	PCE_{max} (avg.) ^a [%]
Glass/ITO	0.846	25.8	72.6	15.8 (14.6)
PET/D-PEDOT:PSS	0.840	23.6	71.7	14.2 (13.7)
PET/ITO	0.829	18.9	68.3	10.7 (10.5)

^a Average PCE was obtained from over 20 independent devices

Rigid OSCs based on glass/ITO exhibited a high efficiency of 15.8% with J_{sc} of 25.8 mA cm⁻², V_{oc} of 0.846 V and FF of 72.6%, which were comparable to previous studies (Yuan et al., 2019). When those ITOs were utilized on flexible PET substrates, a notably low PCE of 10.7% was achieved mainly ascribed to the significantly low FF (68.3%) and J_{sc} (18.9 mA cm⁻²). This discrepancy normally was caused by the low-quality sputtering of ITO on PET plastic substrates, limiting the optical transparency and conductivity of PET/ITO electrodes (Song et al., 2018). Hence, significantly lower J_{sc} and FF were observed when comparing glass/ITO to PET/ITO. By using D-PEDOT:PSS as an ITO alternative, the flexible device yielded an excellent PCE of 14.2% with J_{sc} of 23.6 mA cm⁻², V_{oc} of 0.840 V and FF of 71.7%, which was one of the highest-performing flexible OSCs reported to date. For reference purposes, the PCE values of all fabricated flexible OSCs in the recent years are summarized in **Figure 5.9f** and **Table A.1** to **A.3** of “Appendix A: Supporting Information”.

As compared to rigid ITO-based OSCs, flexible OSCs based on D-PEDOT:PSS FTEs showed a slightly lower PCE, mainly attributed to the drop in J_{sc} value from 25.8 to 23.6 mA cm⁻² due to better optical transparency of ITO in the longer wavelength region. To support this, EQE of the two devices were

measured as displayed in **Figure 5.9d**. The integrated J_{sc} values measured from EQE curves matched well with the J_{sc} values measured from $J-V$ curves (within 5% deviation range). The difference in J_{sc} values was mainly caused by the small spectral mismatch of the solar simulator's spectrum with the AM1.5G spectrum (Schilinsky et al., 2002). It could be observed clearly that when $\lambda > 450$ nm, rigid ITO-based device dominated over the flexible D-PEDOT:PSS device, resulting in higher J_{sc} . Nonetheless, flexible D-PEDOT:PSS device showed superiority in the wavelength region between 350-450 nm, which was due to the higher transparency characteristics of D-PEDOT:PSS FTEs. Although there was a slight decrease in PCE of flexible devices, the 14.2% performance of flexible OSCs based on D-PEDOT:PSS unfolded an encouraging opportunity to produce high-efficiency flexible OSCs.

The mechanical stability of flexible devices based on D-PEDOT:PSS FTEs were investigated by studying the change in PCE during bending and folding test. **Figure 5.9e** displays the results when the device was subjected to bending (black), mid-device folding or folding between Al electrodes (red) and folding on top of the Al electrodes (blue). Flexible OSCs based on D-PEDOT:PSS FTEs showed good performance stability against bending where it retained ~89% of the original PCE value after 1000 bending cycles. However, when Al top electrodes folding were performed, the device showed a significant drop in PCE in the first 100 cycles, maintaining only ~73% of the original PCE value. This PCE further dropped by ~61% after 1000 folding cycles, suggesting poor stability against Al top electrodes folding. Interestingly, the deterioration of PCE upon folding was minimized when folding was not performed on top of the Al electrodes (mid-device folding). In fact, for the same 100 cycles, the PCE

still remained relatively close to ~83% and after 1000 folding cycles, the device even maintained a remarkable ~76% of the original PCE value. This superior characteristic was primarily due to the enhanced adhesion ability of D-PEDOT:PSS electrodes with the PET plastic substrates, which prevented the rapid increase in square resistance (**Figure 5.8**) and consequently the significant drop in PCE upon mid-device folding (**Figure 5.9e**). This was not the case with Al top electrodes folding as the presence of Al electrodes might influence device stability.

All in all, the use of xylitol doping and MSA treatment on PEDOT:PSS FTEs was proven to be an effective approach for obtaining high-performing flexible OSCs. Using those strategies, flexible OSCs based on D-PEDOT:PSS could exhibit an excellent PCE of 14.2% with J_{sc} of 23.6 mA cm⁻², V_{oc} of 0.840 V and FF of 71.7%, which were one of the highest-performing flexible OSCs reported to date. There were several factors that contributed to such high photovoltaic performances, ranging from optical, electrical, morphological to mechanical aspects. For instance, electrode engineering on PEDOT:PSS FTEs via xylitol doping and MSA treatment could improve the transmissivity of pristine PEDOT:PSS film on PET plastic substrate to function effectively as transparent electrodes with comparable optical transparency to glass/ITO. It could significantly raise the conductivity of pristine PEDOT:PSS film, which was the key feature of high-performing FTEs. It could promote a more favourable morphological feature with uniform phase separation which helped to improve conductivity performance. Most importantly, electrode engineering on PEDOT:PSS FTEs could modify the mechanical properties of pristine PEDOT:PSS FTEs by providing stronger adhesion ability to the PET substrate

to yield better mechanical robustness against deformation. As a result, flexible OSCs based on D-PEDOT:PSS FTEs could undergo significant bending and folding test, where it retained ~89% and ~76% of the original PCE values after 1000 bending and folding cycles, respectively. All those findings proved the importance of electrode engineering strategy to realize high-performing flexible OSCs based on PEDOT:PSS FTEs.

5.4 Conclusion

In conclusion, electrode modification of PEDOT:PSS film was conducted successfully in this study by introducing polyhydroxy compound doping and MSA treatment. The range of polyhydroxy compounds were initially investigated and among them, xylitol appeared to be the most feasible, in terms of both conductivity and square resistance. For that reason, MSA-treated xylitol-doped PEDOT:PSS (or D-PEDOT:PSS) FTEs with excellent transparency, low reflectivity and high conductivity were obtained. Xylitol doping and MSA treatment could also induce better interconnected morphology with favourable phase separation and structural rearrangement as compared to the pristine PEDOT:PSS FTEs, which were conducive for improved electrodes' conductivity. Most importantly, such doping and acid treatment could provide D-PEDOT:PSS a stronger adhesion ability with the PET substrate, due to the presence of strong bonding interactions at PET/D-PEDOT:PSS interface. This interface interactions were proven to be effective in boosting the mechanical stability of FTEs against bending and folding, where the change in R_{sq} was still

below 5% and 20% after 1000 bending and folding cycles. Through this electrode engineering strategy, conventional flexible devices based on PBDB-T-2F:Y6 photoactive layer and D-PEDOT:PSS FTEs demonstrated an excellent PCE of 14.2% with J_{sc} of 23.6 mA cm⁻², V_{oc} of 0.840 V and FF of 71.7%. It was worth noting that due to the excellent mechanical stability of D-PEDOT:PSS FTEs, those flexible OSCs could display remarkable mechanical robustness against bending and folding, maintaining over 89% and 76% of the original PCE even after 1000 bending and folding cycles. Overall, this chapter demonstrated that xylitol doping and MSA treatment could be used effectively for electrode modification of PEDOT:PSS to improve OSCs' performance in terms of photovoltaic performance and mechanical stability. Hence, electrode engineering is proven to be a convincing strategy to obtain high-performing flexible OSCs in addition to material design and morphology control.

Chapter 6. Application of Flexible Semi-Transparent OSCs Achieved Through Electrode Engineering Strategy

6.1 Summary

In this chapter, the potential application of device engineering, specifically electrode engineering strategy was studied and demonstrated as a continuation of work from Chapter 5. The desirable mechanical and optical properties of D-PEDOT:PSS as induced by xylitol doping and MSA treatment created opportunities for its usage in flexible semi-transparent devices. In here, FST-OSCs were fabricated using D-PEDOT:PSS FTEs and PBDB-T-2F:Y6 photoactive layer. The desirable optical properties of D-PEDOT:PSS FTEs in the visible light region and PBDB-T-2F:Y6 photoactive layer in the near-infrared region facilitated the fabrication of FST-OSCs with over 10% efficiency and 21% AVT. Those FST-OSCs also displayed excellent mechanical stability against bending and folding, where over 80% of the initial efficiency could be maintained even after 1000 folding cycles. The potential of such FST-OSCs was demonstrated by incorporating them as part of the roof in the simulated greenhouse. Parallel comparisons between plants grown under direct sunlight with FST-OSCs roof and those under direct sunlight yielded remarkably similar results in terms of branch sturdiness and hypertrophic leaves. Overall, this chapter proves the significance of electrode engineering strategy in realizing high-performing FST-OSCs based on PEDOT:PSS FTEs for practical greenhouse applications, where visible light can be utilized for plants growth and infrared light for power generation.

6.2 Introduction

Previous chapters have shown the importance of both interface and electrode engineering strategy in enhancing OSCs' performance. Electrode engineering strategy is particularly effective as it can improve OSCs' performance, in terms of both photovoltaic performance and mechanical stability (Ramachandran et al., 2015, Cheng and Zhan, 2016, Li et al., 2018). On that account, high-performing flexible OSCs with good mechanical stability (high bending resistance) can be fabricated for future applications in next-generation flexible and wearable electronics.

The extent of their applications continues when OSCs have additional desirable optical properties, which enable the realization of high-performing flexible semi-transparent OSCs (Chang et al., 2018, Li et al., 2018, Dai and Zhan, 2018). For instance, D-PEDOT:PSS FTEs as studied in the previous chapter, possess remarkable mechanical (high bending resistance) and optical (high transmissivity and low reflectivity in the visible light region) properties as induced by xylitol doping and MSA treatment, which provide great opportunity for usage in foldable-flexible semi-transparent OSCs or abbreviated as FST-OSCs. In addition, photoactive layer based on PBDB-T-2F:Y6 exhibits optical properties that are advantageous for FST-OSCs applications, as it can readily absorb solar irradiation in the near-infrared to infrared region while being partially transparent in the visible light region. These two features are particularly favourable for agricultural applications (e.g., common greenhouse) as sunlight in the visible light region can be predominantly transmitted for plants growth. In fact, solar irradiation located in the visible light region (370-740 nm)

is mostly responsible for photosynthesis process in plant growth (Singhal et al., 1999). Thus, FST-OSCs for photovoltaic and photosynthesis applications can be realized (Chang et al., 2018).

Displaying such potentials, the development of FST-OSCs based on binary photoactive layer still lagged behind (Li et al., 2015, Liu et al., 2015, Jinno et al., 2017, Park et al., 2018). To date, the highest reported PCE for FST-OSCs with AVT of over 20% was just over 10% (Liu et al., 2019c). Therefore, further attentions should be focused on the development of FST-OSCs due to their promising capabilities as power-generating windows/roofs in building-integrated photovoltaics and photovoltaic vehicles (e.g., future foldable roofs in multi-functioned self-powered greenhouse). This driven the current work on high-performing FST-OSCs based on D-PEDOT:PSS FTEs and PBDB-T-2F:Y6 photoactive layer.

Herein, PEDOT:PSS FTEs that were previously engineered through xylitol doping and MSA treatment were used for the fabrication of FST-OSCs. The future practical application of high-performing FST-OSCs achieved through electrode engineering strategy, was being demonstrated by incorporating them as part of the roof in simulated greenhouse. Due to the preferable optical properties of the photoactive layer and D-PEDOT:PSS FTEs, FST-OSCs with 10.5% PCE and 21.0% AVT were obtained, which represented one of the highest-performing semi-transparent OSCs based on flexible substrates reported to date. Furthermore, FST-OSCs also displayed remarkable mechanical stability and robustness against folding, maintaining over 80% of the original PCE even after 1000 folding cycles. This was due to the enhanced FTEs' adhesion ability

with the substrates as induced by xylitol doping in D-PEDOT:PSS. Hence, FST-OSCs based on D-PEDOT:PSS created opportunities to be utilized as foldable roofs for greenhouse. In fact, plants grown under direct sunlight and FST-OSCs shown comparable growth rate, which unveiled the use of FST-OSCs beyond photovoltaic as solar irradiation could be selectively absorbed and transmitted by FST-OSCs for power generation and plant growth, respectively.

6.3 Results and Discussions

6.3.1 FST-OSCs

Foldable-flexible semi-transparent devices based on D-PEDOT:PSS FTEs and PBDB-T-2F:Y6 photoactive layer were studied as both (electrode and photoactive layer) had optical transparency that allowed visible light to pass through. **Figure 6.1** summarizes the findings regarding optical properties of D-PEDOT:PSS FTEs and PBDB-T-2F:Y6 photoactive layer. D-PEDOT:PSS FTEs, as shown in **Figure 6.1a**, displayed high optical transparency and minimal reflectivity, particularly in the visible light region. On the other hand, PBDB-T-2F:Y6 photoactive layer, as shown in **Figure 6.1b**, exhibited partial transparency in the visible light region while being responsive in the near-infrared region. The high optical transparency in the 400-550 nm region (as highlighted in both figures) was particularly beneficial as this was the most concentrated region for two key pigments of plants (chlorophylls and carotenoids) to absorb light for photosynthesis process (Singhal et al., 1999). Such features encouraged the utilization of D-PEDOT:PSS FTEs and PBDB-T-2F:Y6 photoactive layer in

realizing high-performing FST-OSCs for both photovoltaic and photosynthesis applications.

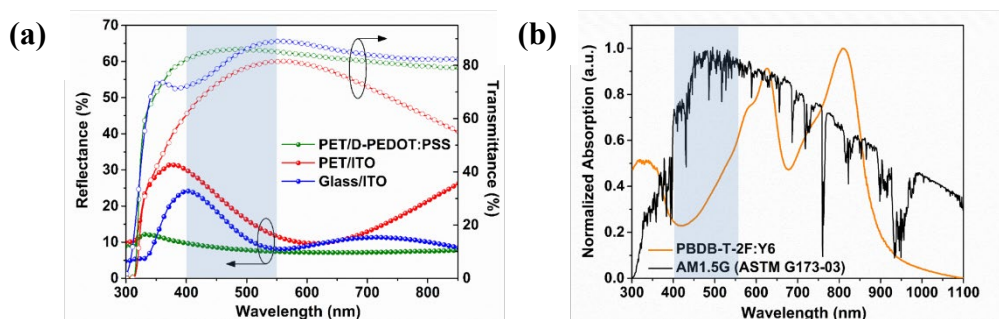


Figure 6.1 (a) Optical properties of D-PEDOT:PSS fabricated on PET substrates. (b) Optical properties of PBDB-T-2F:Y6 photoactive layer film. The blue highlighted region (400-550 nm) denotes the most concentrated region for two key pigments of plants to absorb light for photosynthesis.

6.3.2 Photovoltaic performances

FST-OSCs based on D-PEDOT:PSS FTEs were fabricated with the configuration of PET/D-PEDOT:PSS FTE/4083/PBDB-T-2F:Y6/PDINO/Ag. The device architecture was similar to the flexible OSCs fabricated and studied in Chapter 5. The main difference between them was the replacement of Al top electrode with ultrathin semi-transparent Ag electrode with thickness between 10-20 nm. The photoactive layer based on PBDB-T-2F donor and Y6 acceptor was selected as well due to its high efficiency performance and remarkable transparency in the visible light region. Detailed procedures for the fabrication of such FST-OSCs can be found in Chapter 3 (Methodology).

The schematic of FST-OSCs installed as part of the roof on the multi-functioned self-powered greenhouse is shown in **Figure 6.2a**. The improved mechanical stability induced by interface bonding interaction between electrodes and substrates also allowed FST-OSCs installed on roof to be folded. The schematic illustration of FST-OSCs when folded is depicted in **Figure 6.2b**.

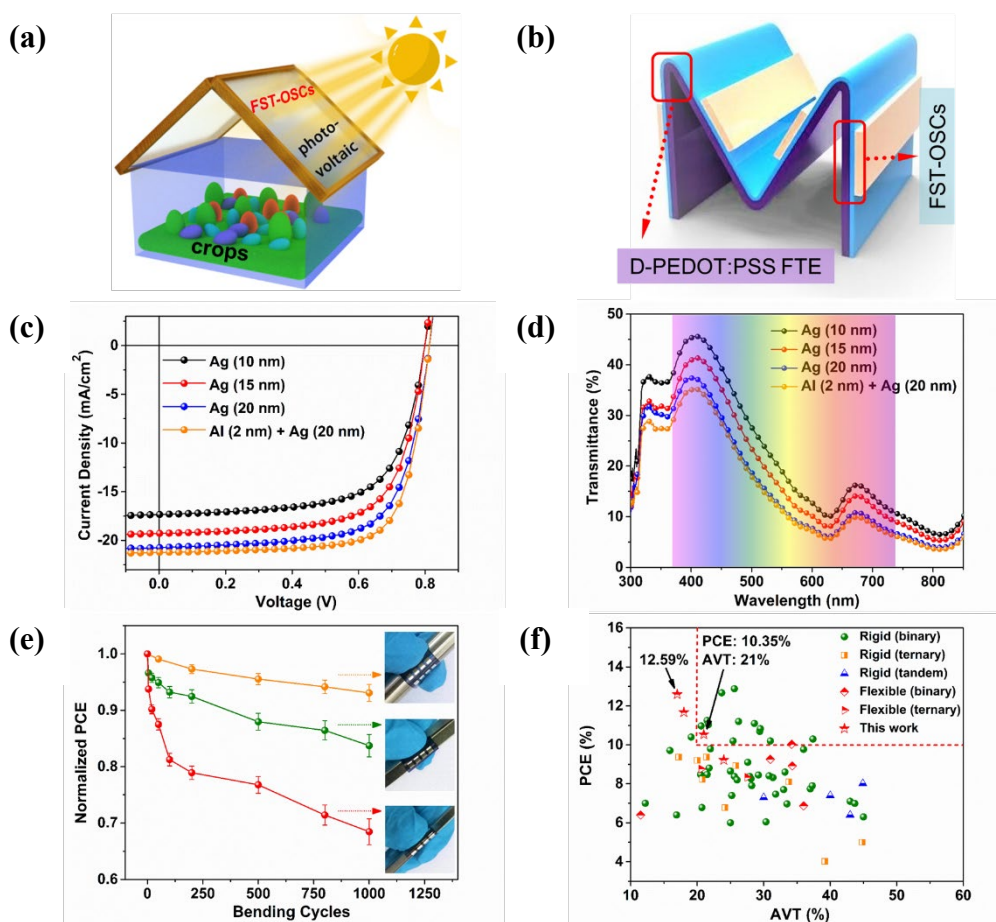


Figure 6.2 (a) An installation of FST-OSCs as roofs in greenhouse. (b) Folding schematic diagram of FST-OSCs (folding between top Ag electrodes). (c) Typical $J-V$ characteristics and (d) transmittance spectra of foldable-flexible semi-transparent devices. (e) Normalized PCE of FST-OSCs based on D-PEDOT:PSS FTEs after subjected to bending (orange), mid-device folding or folding between Ag electrodes (green) and folding on top of the Ag electrodes (red). (f) Recent scatter plot report for PCE and AVT values of semi-transparent OSCs; all data are listed in “Appendix A”.

Figure 6.2c shows the J - V characteristics of FST-OSCs with different Ag thicknesses as the cathode. For comparison, flexible semi-transparent device based on Al (2 nm) and Ag (20 nm) electrodes was also fabricated. The detailed photovoltaic parameters of all devices fabricated are listed in **Table 4.1**. It is important to note that all photovoltaic performances were measured under standard AM1.5G illumination with 100 mW cm^{-2} light intensity in N_2 -filled glovebox without encapsulation.

Table 4.1 Detailed photovoltaic parameters of FST-OSCs based on D-PEDOT:PSS with different cathode thicknesses.

Cathode	V_{oc} [V]	J_{sc} [mA cm ⁻²]	FF [%]	PCE_{max} (avg.) ^a [%]	AVT [%]	Colour Coordinates [x, y]
Ag (10 nm)	0.798	17.3	66.6	9.22 (9.01)	24.0	(0.243, 0.246)
Ag (15 nm)	0.800	19.3	68.4	10.5 (10.3)	21.0	(0.237, 0.235)
Ag (20 nm)	0.812	20.7	69.3	11.7 (11.4)	18.0	(0.231, 0.223)
Al (2 nm) + Ag (20 nm)	0.810	21.2	73.0	12.6 (12.4)	17.0	(0.229, 0.221)

^a Average PCE was obtained from over 20 independent devices

Generally, all fabricated FST-OSCs could demonstrate excellent photovoltaic properties as shown in **Figure 6.2c** and **Table 4.1**. All FST-OSCs showed excellent transmittance performance across the visible light region (370-740 nm), as depicted in **Figure 6.2d**. At 400 nm region in particular, the transmissivity of FST-OSCs could reach up to over 45%, which was crucial for greenhouse applications. In addition, all FST-OSCs exhibited low reflectivity in the 400-550 nm region as depicted in **Figure 6.3**. This 400-550 nm region is the key region responsible for plant photosynthesis process (Singhal et al., 1999), proving the potential of electrode engineering in obtaining high-performing FST-OSCs for roof and window applications in greenhouse.

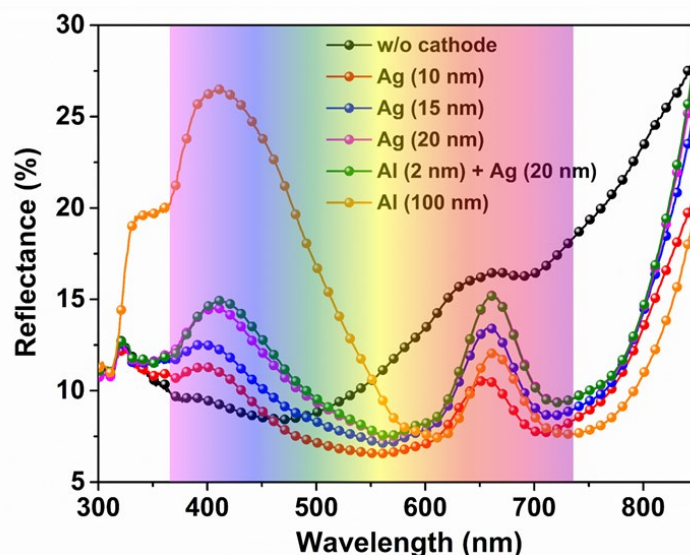


Figure 6.3 Reflectance spectra of semi-transparent devices based on PET/D-PEDOT:PSS.

Among the fabricated devices, FST-OSCs based on Al and Ag electrodes exhibited the highest photovoltaic performance with PCE of 12.6%, J_{sc} of 21.2 mA cm⁻², V_{oc} of 0.810 V and FF of 73.0%. When those Al electrodes were removed, the performance of FST-OSCs was slightly reduced to 11.7% mainly due to the drop in J_{sc} and FF values. The tapering of Ag electrodes from 20 to 10 nm affected the device performance to a certain extent as well. For instance, reducing Ag thicknesses from 20 to 10 nm could lower the device performance from 11.7% to 9.22%, primarily due to the significant drop in J_{sc} and FF values from 20.7 mA cm⁻² and 69.3% to 17.3 mA cm⁻² and 66.6%, respectively. Apart from photovoltaic performance, AVT is another key performance criterion to be considered in FST-OSCs. The relationship between AVT and photovoltaic performance was investigated by varying the thickness of Ag electrodes linearly from 10 to 20 nm. As depicted in **Table 4.1**, the thickness of Ag electrodes played a significant role in photovoltaic and AVT performances. When the thickness of Ag tapered, both J_{sc} and PCE would decrease while AVT would

increase. This was expected as the thinner Ag film could reflect less light back to the photoactive layer for re-absorption, thereby reducing the J_{sc} and PCE values. While thinner Ag film also meant that more light could be transmitted through the device, allowing FST-OSCs to have higher AVT and better visible light transparency for greenhouse applications. Therefore, a trade-off between photovoltaic and AVT performances in FST-OSCs needs to be considered.

Herein, the best device was obtained by considering both photovoltaic and AVT performances. FST-OSCs based on 15 nm Ag electrode showed high AVT of over 20%, which was the commercial minimum light transmission requirement for semi-transparent devices. Furthermore, it exhibited good photovoltaic performances with PCE of 10.5%, J_{sc} of 19.3 mA cm⁻², V_{oc} of 0.800 V and FF of 68.4%. To the best of our knowledge, the current 10.5% device performance represented one of the highest-performing semi-transparent OSCs based on flexible substrates with AVT higher than 20%. For reference purposes, the PCE and AVT values of all fabricated semi-transparent OSCs based on rigid and flexible substrates in the recent years are summarized in **Figure 6.2f** and **Table A.4 to A.6** of “Appendix A: Supporting Information”. It can be observed that the efficiency of semi-transparent OSCs exceeding 10% and AVT greater than 20% are rarely reported.

The mechanical stability of FST-OSCs for bending and folding purposes is another crucial performance criterion to be considered along with photovoltaic and AVT performances. The mechanical stability of the best device (FST-OSC based on 15 nm Ag electrode) against repetitive harsh deformation was investigated by analysing the change in PCE during bending and folding test.

Figure 6.2e illustrates the results when the device was subjected to bending (orange), mid-device folding or folding between Ag electrodes (green) and folding on top of the Ag electrodes (red). FST-OSCs based on D-PEDOT:PSS FTEs showed good performance stability against bending where it retained ~93% of the original PCE value after 1000 bending cycles. However, when Ag top electrodes folding were performed, the device showed a significant drop in PCE in the first 100 cycles, maintaining only ~80% of the original PCE value. This PCE further dropped by ~68% after 1000 folding cycles, suggesting poor stability against Ag top electrodes folding. Interestingly, the deterioration of PCE upon folding was minimized when folding was not performed on top of the Ag electrodes (mid-device folding). In fact, for the same 100 cycles, the PCE still remained relatively close to the original PCE value (~93%) and after 1000 folding cycles, the device even maintained a remarkable ~84% of the original PCE value. This superior characteristic was primarily due to the enhanced adhesion ability of D-PEDOT:PSS FTEs with the PET plastic substrates, which prevented the significant drop in PCE upon mid-device folding (**Figure 6.2e**). That was not the case with Ag top electrodes folding as the presence of Ag electrodes might influence device stability.

The last performance criterion for FST-OSCs is colour properties or colour characteristics. Colour characteristics of FST-OSCs were studied as the consideration of human perception of colour is critical for practical applications. **Table 4.1** and **Figure 6.4a** show the colour coordinates (x, y) of FST-OSCs with different cathode thicknesses in the CIE 1931xyY chromaticity diagram, in which the colour coordinates (x, y) are calculated from the transmission spectra of FST-OSCs shown in **Figure 6.2d**. The corresponding coordinates for devices

based on 10 nm Ag, 15 nm Ag, 20 nm Ag and 2 nm Al with 20 nm Ag cathodes were (0.243, 0.246), (0.237, 0.235), (0.231, 0.223) and (0.229, 0.221), respectively. Moreover, digital photographs as shown in **Figure 6.4b** were taken with green leaves covered by the FST-OSCs based on 15 nm Ag as the best device. The FST-OSCs displayed good transparency colour perception, appearing bluish in colour. The photos demonstrated that FST-OSCs had appealing colour appearances and excellent visible light transparency, which were important for windows/roofs application in greenhouse.

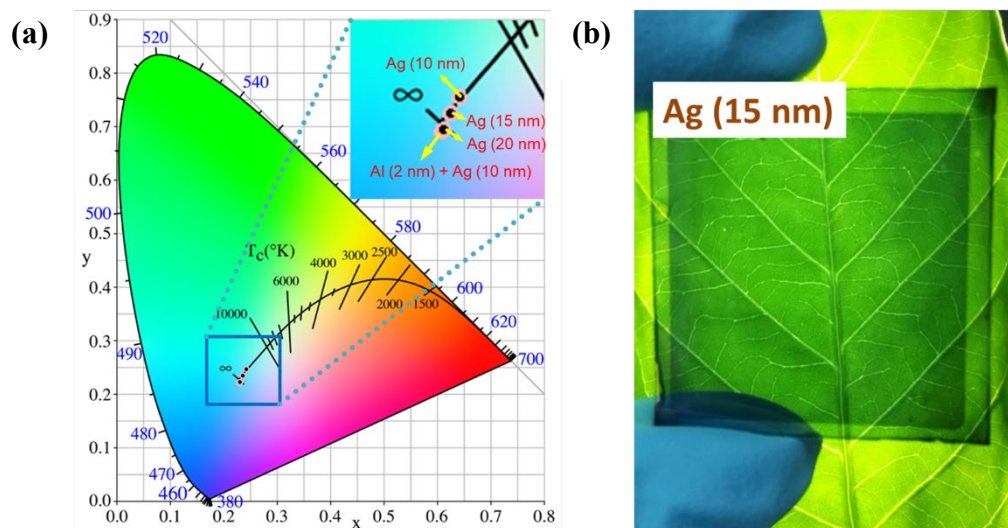


Figure 6.4 (a) Representation of the colour coordinates of fabricated FST-OSCs on a CIE 1931xyY chromaticity diagram. **(b)** Digital photographs taken with green leaves covered with FST-OSCs.

6.3.3 Application of FST-OSCs

The potential of FST-OSCs for practical application was evaluated by simulating the greenhouse environment using FST-OSCs as part of the roof. Plant growth was monitored for 9 days under three different environments of

dark, sunlight without FST-OSCs and sunlight with FST-OSCs as part of the roof. The changes in plant growth are summarized in **Figure 6.5**.

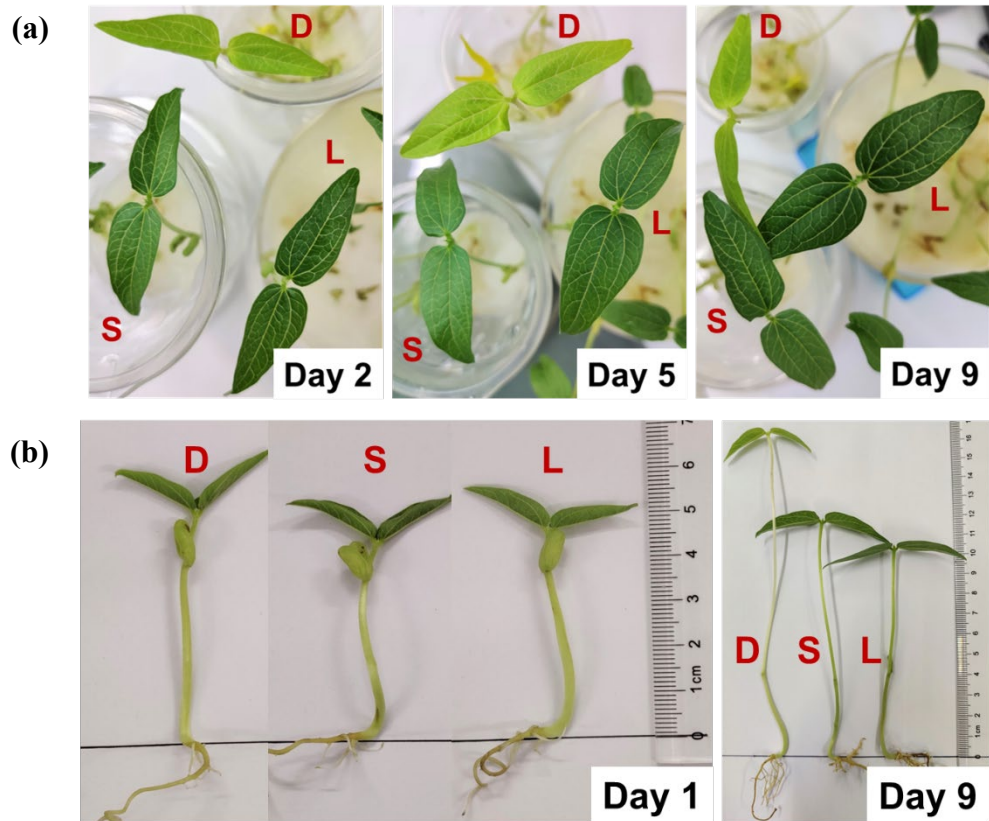


Figure 6.5 (a) Optical photograph of mung bean leaves changing in 9 days under direct sunlight (L), direct sunlight with FST-OSCs roof (S) and dark (D). **(b)** Optical photograph of mung beans, showing the stems length changing in 9 days under direct sunlight (L), direct sunlight with FST-OSCs roof (S) and dark (D).

Distinct differences were observed in terms of colour, height and branch sturdiness as shown in **Figure 6.5**. Plants grown under dark had chlorophyll deficiency in their leaves due to their inability to photosynthesize, hence, had lighter green colour as compared to others (**Figure 6.5a**). Furthermore, since photosynthesis supplied plants with nutrients for growth, the inability to photosynthesize caused plants grown under dark to have slender stems and

smaller leaves (**Figure 6.5b**). On the contrary, plants grown under FST-OSCs were comparable to those grown under sunlight, as visible light could be transmitted through FST-OSCs to promote photosynthesis in plants for growth. As a result, plants grown under FST-OSCs had comparable branch sturdiness and hypertrophic leaves. The changes in plant growth demonstrated that FST-OSCs in the simulated greenhouse environment could achieve commercial minimum PCE (over 10%) while ensuring sufficient sunlight transmitted for plants growth.

All in all, the utilization of xylitol doping and MSA treatment on PEDOT:PSS FTEs was proven not only effective for obtaining high-performing flexible OSCs, but also for high-performing FST-OSCs. This was due to the remarkable visible light transparency D-PEDOT:PSS could offer as FTEs. Using that strategy, best FST-OSCs (15 nm Ag electrode) based on D-PEDOT:PSS could exhibit PCE of 10.5% and AVT of 21.0% with J_{sc} of 19.3 mA cm⁻², V_{oc} of 0.800 V and FF of 68.4%. It is worth noting that this performance is one of the highest-performing semi-transparent OSCs based on flexible substrates with AVT higher than 20% reported to date. Moreover, electrode engineering strategy on PEDOT:PSS FTEs could promote better mechanical stability in FST-OSCs. As a result, FST-OSCs based on D-PEDOT:PSS FTEs could undergo significant bending and folding test, where they retained ~93% and ~84% of the original PCE values after 1000 bending and folding cycles, respectively. All those features contributed to the implementation of FST-OSCs based on D-PEDOT:PSS FTEs as windows/roofs for greenhouse applications. Studies on plant growth were conducted to prove the potential of such FST-OSCs in greenhouse application. Plants grown under FST-OSCs in the simulated

greenhouse environment showed comparable growth tendencies in terms of branch sturdiness and hypertrophic leaves to those grown under direct sunlight, as visible light could be transmitted through FST-OSCs to promote photosynthesis in plants for growth. This strongly proved that electrode engineering strategy could produce high-performing FST-OSCs for both photovoltaic and photosynthesis applications (e.g., simultaneously generate power and promote growth of crops in greenhouse).

6.4 Conclusion

Electrode modification on PEDOT:PSS film via xylitol doping and MSA treatment could promote desirable visible light transparency and mechanical stability in OSCs, which were highly favourable for the fabrication of high-performing FST-OSCs. Due to those strategies, best device performance with PCE of 10.5% (J_{sc} of 19.3 mA cm⁻², V_{oc} of 0.800 V, FF of 68.4% and AVT of 21.0%) was attained for FST-OSCs based on D-PEDOT:PSS FTEs and PBDB-T-2F:Y6 photoactive layer. The PCE of 10.5% with AVT of 21.0% in this work represented one of the best-performing semi-transparent OSCs based on flexible substrates. Apart from that, electrode engineering strategy on PEDOT:PSS FTEs could display remarkable mechanical stability and robustness against bending and folding (particularly mid-device folding), where over 80% of the initial efficiency could still be maintained even after 1000 folding cycles. Both transparency and mechanical stability features created opportunities for the utilization of FST-OSCs as windows/roofs in greenhouse. Studies on plant

growth were conducted to prove the potential of such FST-OSCs for greenhouse application. The plants showed comparable growth rate under FST-OSCs to those grown under sunlight, proving the usage of FST-OSCs beyond photovoltaic as solar irradiation could be selectively absorbed (infrared light) and transmitted (visible light) by FST-OSCs for power generation and plant growth, respectively. This highlighted the propitious potential of FST-OSCs based on PEDOT:PSS electrodes in generating power and promoting plant growth for future multi-functional self-powered greenhouse.

Chapter 7. Conclusion and Future Work

7.1 Conclusion

In conclusion, this study explores the prospects of OSCs as renewable source of energy to replace non-renewable fossil fuels to meet the ever-increasing global energy demand. Two device engineering strategies, namely interface and electrode engineering were utilized and proven to be effective methods for obtaining high-performing OSCs in addition to material design and morphology control strategies. Both device engineering strategies could enhance device performance by improving the optical, electrical, morphological and/or mechanical properties of pristine interfacial layer and electrode layer. Moreover, potential applications of high-performing OSCs achieved via electrode engineering strategy were demonstrated.

7.1.1 Interface engineering strategy

Interface engineering on sol-gel ZnO ETL was performed via additional deposition of PBD layer. This technique enabled the formation of hybrid electron-transporting bilayer consisting of PBD and ZnO layer. The significance of that strategy was investigated on inverted OSCs based on PBDB-T:IT-M photoactive layer, where ~7% increment in photovoltaic performance from 10.8% (ZnO-based device) to 11.6% (ZnO/PBD-based device) was observed. The performance enhancement in ZnO/PBD-based device was largely attributed to the simultaneous increase in J_{sc} and FF values, mainly governed by the improvement in charge transport ability and suppression of charge

recombination processes. In terms of optical properties, the utilization of PBD did not significantly affect ETL's transparency. In fact, both ZnO and ZnO/PBD interlayer showed comparable optical performances. In terms of electrical properties, the utilization of PBD could improve pristine ZnO film's conductivity by ~76%, which were conducive for improved charge transport ability. In terms of morphological properties, the utilization of PBD could smoothen the ZnO film's morphology and improve hydrophobicity of the surface to facilitate uniform and intimate contact with the photoactive layer. Furthermore, PBD could tune the WF of the ITO electrode to better match the LUMO energy level of IT-M acceptor for more efficient electron extraction from the photoactive layer.

7.1.2 Electrode engineering strategy

Electrode engineering on PEDOT:PSS FTEs was performed via xylitol doping and MSA treatment. As a result, high-performing D-PEDOT:PSS FTEs with remarkable mechanical robustness against bending and folding were obtained. The effectiveness of xylitol doping and MSA treatment was investigated on conventional flexible OSCs based on PBDB-T-2F:Y6 photoactive layer, where an excellent photovoltaic performance of 14.2% with remarkable mechanical robustness against bending and folding was observed. In terms of optical properties, xylitol doping and MSA treatment on PEDOT:PSS FTEs could slightly improve FTEs' transparency. In terms of electrical properties, xylitol doping and MSA treatment could significantly boost FTEs' conductivity from non-conductive film to film with 2032 S cm^{-1} conductivity. In terms of morphological properties, xylitol doping and MSA treatment could

induce better interconnected PEDOT:PSS morphology with favourable phase separation and structural rearrangement as compared to the pristine PEDOT:PSS FTEs, which was beneficial for improving electrodes' conductivity. In terms of mechanical properties, the utilization of xylitol doping and MSA treatment could provide electrode a stronger adhesion ability with the PET substrate, due to the presence of strong bonding interactions at PET/D-PEDOT:PSS interface. Those interface interactions were proven to be effective in boosting the mechanical stability of FTEs against bending and folding, where the change in R_{sq} was still below 5% and 20% after 1000 bending and folding cycles.

7.1.3 Application of electrode engineering strategy

Electrode modification of PEDOT:PSS film via xylitol doping and MSA treatment could promote desirable visible light transparency and mechanical stability in OSCs, which were highly favourable for the fabrication of high-performing FST-OSCs. Subsequently, best device performance with PCE of 10.5% and AVT of 21.0% was attained for FST-OSCs based on D-PEDOT:PSS FTEs and PBDB-T-2F:Y6 photoactive layer. Such FST-OSCs could display remarkable mechanical stability and robustness against bending and folding, where over 80% of the initial efficiency could still be maintained even after 1000 folding cycles. The desirable mechanical and optical properties of D-PEDOT:PSS as induced by xylitol doping and MSA treatment created opportunities for usage as foldable windows/roofs in greenhouse. Thus, studies on plant growth in simulated greenhouse environment were conducted to validate the potential of such FST-OSCs. In a simulated greenhouse environment, plants grown under direct sunlight with FST-OSCs roof and those under direct

sunlight yielded remarkably similar results in terms of branch sturdiness and hypertrophic leaves. This implied the significance of electrode engineering strategy in realizing high-performing FST-OSCs based on PEDOT:PSS FTEs for practical greenhouse applications, where visible light could be utilized for plants growth and infrared light for power generation.

7.2 Future Work

In recent years, the performance of OSCs has increased from time to time. Not only rigid OSCs, both flexible and semi-transparent OSCs have also undergone significant development. It is believed that with the efforts of researchers in various field, novel and better-performing photoactive layer materials will soon arise. By then, it is the role of device engineering to further maximize the efficiency of OSCs to reach a performance comparable to silicon-based solar cells. Future work on device engineering can be carried out based on two aspects, future improvement of the current study and potential opportunities in the current OSCs market:

- i) The current work shown the potentials of PBD as OLED-based interfacial modifier in OSCs. Further studies about PBD in OSCs are worth investigating for other ETL systems in conventional or inverted OSCs. It would be best to conduct those studies on devices based on high-performing photoactive layer to further contribute towards the development of PCE, reaching 20% boundary.

- ii) Though PBD could raise ZnO conductivity by $\sim 76\%$, it still could not induce significant reduction in surface traps and defects in ZnO film. Hence, more attentions should be focused on the study of other potential materials for interfacial modification of ZnO ETL in inverted OSCs to maximize and optimize the effectiveness of interface engineering strategy.
- iii) Application of interface engineering strategy is worth discussing for future work. This can be done by applying interface engineering strategy to fabricate high-performing semi-transparent OSCs and/or flexible OSCs. For example, in the case of semi-transparent OSCs, the current PBDB-T:IT-M photoactive layer needs to be substituted with another photoactive layer that is responsive in the near-infrared region and transparent in the visible light region. Combining such photoactive layer with highly transparent ZnO/PBD interlayer, can result in the fabrication of high-performing inverted semi-transparent OSCs. The potential of such device can then be studied for window, roof, vehicle and/or greenhouse applications. However, it is worth noting that not all photoactive layer system is compatible with ZnO/PBD interlayer, in a way that interface engineering can bring about desirable performance enhancement effect.
- iv) Xylitol doping and MSA treatment were proven to be effective methods in obtaining high-performing PEDOT:PSS FTEs for flexible OSCs and foldable-flexible semi-transparent OSCs. Extensive studies incorporating D-PEDOT:PSS FTEs on flexible tandem OSCs or even

flexible semi-transparent tandem OSCs are worth the efforts to drive the development of OSCs towards commercialization.

- v) Future studies can be made by combining interface and electrode engineering strategies into one OSCs system. Though possible, it will still be extremely challenging due to material compatibility issues in OSCs. In fact, studies combining several device engineering strategies were never found till date. Take the current work as an example, ZnO ETL as mentioned previously, requires high-temperature annealing to minimize defect sites, while PET substrate is highly sensitive to high-temperature processing. This means that PET/D-PEDOT:PSS/ZnO/PBD configuration, which combines interface engineering strategy on ZnO and electrode engineering strategy on PEDOT:PSS may not be the most feasible and desirable combination. Solution to incorporate D-PEDOT:PSS FTEs on glass substrates may be presented, and still, compatibility issues may arise when ZnO ETL (normally used in inverted device architecture) is deposited on top of the D-PEDOT:PSS FTEs (normally used in conventional device architecture). Overall, this explains the challenges of combining more than one device engineering strategies into one OSCs system.
- vi) Under normal circumstances, single-junction OSCs most likely to suffer from low J_{sc} (due to narrow absorption spectra) and low V_{oc} (due to large photovoltaic loss) (Ameri et al., 2013, Lian et al., 2014). Due to this issue, tandem devices have been developed to improve the photovoltaic performance by simultaneously tackling absorption and loss (e.g., thermalization loss of high energy photon or transmission loss of low

energy photon) issues found in single-junction devices (Che et al., 2018, Meng et al., 2018). In tandem OSCs, two sub-cells with complementing absorption performances, are stacked together and connected by a highly transparent and conductive interconnecting layer (Ameri et al., 2013). The interconnecting layer typically consists of ETL and HTL pair that provide Ohmic contact with the sub-cells to act as charge extraction and recombination zones (Ameri et al., 2013). For instance, interconnecting layer combining *n*-type metal oxide like ZnO and *p*-type polymer like PEDOT:PSS may become a good choice in tandem OSCs to result in efficiency performance beyond 17% as reported by Meng *et al.* (Meng et al., 2018). There is also a case where conductive layer is utilized between ETL and HTL pair, which brings about the potential of introduction of conductive PBD layer in tandem devices. Thus, the incorporation of PBD into tandem OSCs to modify ZnO-based interconnecting layer is worth researching in the future as it will be a crucial layer to connect two sub-cells in tandem devices.

- vii) Another device engineering approach, namely active layer engineering is a promising alternative due to its attractiveness in boosting device performance by improving the photon harvesting capability and/or regulating the morphology of photoactive layer, while at the same time maintaining the simplicity of single-junction device architecture. In active layer engineering, additional material is added into the host donor and acceptor to form ternary photoactive layer system. The material can be dopant or even additional donor or acceptor material. This strategy has been proven to be very effective as several literatures shown rapid

increment in efficiency performance upon addition of third material. For instance, Chang *et al.* reported performance improvement from 15.18% to 16.14% (Chang et al., 2019), An *et al.* reported performance improvement from 12.63% to 14.13% (An et al., 2019) and many more (Chen et al., 2016, Gao et al., 2019). Therefore, this strategy can be an attractive option that is worth studying for the realization of high-performing OSCs.

Bibliography

ADACHI, C., TSUTSUI, T. & SAITO, S. 1989. Organic electroluminescent device having a hole conductor as an emitting layer. *Applied Physics Letters*, 55, 1489-1491.

AI, L., OUYANG, X., LIU, Z., PENG, R., MI, D., KAKIMOTO, M. A. & GE, Z. 2016. Multi-channel interface dipole of hyperbranched polymers with quasi-immovable hydron to modification of cathode interface for high-efficiency polymer solar cells. *Progress in Photovoltaics: Research and Applications*, 24, 1044-1054.

AMERI, T., LI, N. & BRABEC, C. J. 2013. Highly efficient organic tandem solar cells: a follow up review. *Energy & Environmental Science*, 6, 2390-2413.

AN, Q., WANG, J. & ZHANG, F. 2019. Ternary polymer solar cells with alloyed donor achieving 14.13% efficiency and 78.4% fill factor. *Nano Energy*, 60, 768-774.

BAGHER, A. M. 2014. Comparison of organic solar cells and inorganic solar cells. *International Journal of Sustainable and Green Energy*, 3, 53-58.

BAI, Y., ZHAO, C., CHEN, X., ZHANG, S., ZHANG, S., HAYAT, T., ALSAEDI, A., TAN, Z., HOU, J. & LI, Y. 2019. Interfacial engineering and optical coupling for multicolored semitransparent inverted organic photovoltaics with a record efficiency of over 12%. *Journal of Materials Chemistry A*, 7, 15887-15894.

BANG, S. M., KANG, S., LEE, Y. S., LIM, B., HEO, H., LEE, J., LEE, Y. & NA, S. I. 2017. A novel random terpolymer for high-efficiency bulk-heterojunction polymer solar cells. *RSC Advances*, 7, 1975-1980.

BATTAGLIA, C., CUEVAS, A. & DE WOLF, S. 2016. High-efficiency crystalline silicon solar cells: status and perspectives. *Energy & Environmental Science*, 9, 1552-1576.

- BORSE, K., SHARMA, R., GUPTA, D. & YELLA, A. 2018. Interface engineering through electron transport layer modification for high efficiency organic solar cells. *RSC Advances*, 8, 5984-5991.
- BRABEC, C. J. 2004. Organic photovoltaics: technology and market. *Solar Energy Materials and Solar Cells*, 83, 273-292.
- BRABEC, C. J., CRAVINO, A., MEISSNER, D., SARICIFTCI, N. S., FROMHERZ, T., RISPENS, M. T., SANCHEZ, L. & HUMMELEN, J. C. 2001. Origin of the open circuit voltage of plastic solar cells. *Advanced Functional Materials*, 11, 374-380.
- BRABEC, C. J., GOWRISANKER, S., HALLS, J. J. M., LAIRD, D., JIA, S. & WILLIAMS, S. P. 2010. Polymer-fullerene bulk heterojunction solar cells. *Advanced Materials*, 22, 3839-3856.
- BREBELS, J., MANCA, J. V., LUTSEN, L., VANDERZANDE, D. & MAES, W. 2017. High dielectric constant conjugated materials for organic photovoltaics. *Journal of Materials Chemistry A*, 5, 24037-24050.
- BRITISH PETROLEUM 2019. BP energy outlook 2019 edition. British Petroleum.
- CARLE, J. E., HELGESEN, M., HAGEMANN, O., HOSEL, M., HECKLER, I. M., BUNDGAARD, E., GEVORGYAN, S. A., SONDERGAARD, R. R., JORGENSEN, M., GARCIA VALVERDE, R., CHAOUKI ALMAGRO, S., VILLAREJO, J. A. & KREBS, F. C. 2017. Overcoming the scaling lag for polymer solar cells. *Joule*, 1, 274-289.
- CHANG, C. Y., HUANG, W. K., CHANG, Y. C., LEE, K. T. & SIAO, H. Y. 2015. High-performance flexible tandem polymer solar cell employing a novel cross-linked conductive fullerene as an electron transport layer. *Chemistry of Materials*, 27, 1869-1875.
- CHANG, C. Y., ZUO, L., YIP, H. L., LI, C. Z., LI, Y., HSU, C. S., CHENG, Y. J., CHEN, H. & JEN, A. K. Y. 2014. Highly efficient polymer tandem cells and semitransparent cells for solar energy. *Advanced Energy Materials*, 4, 1301645.

CHANG, S. Y., CHENG, P., LI, G. & YANG, Y. 2018. Transparent polymer photovoltaics for solar energy harvesting and beyond. *Joule*, 2, 1039-1054.

CHANG, Y., LAU, T. K., PAN, M. A., LU, X., YAN, H. & ZHAN, C. 2019. The synergy of host-guest nonfullerene acceptors enables 16%-efficiency polymer solar cells with increased open-circuit voltage and fill-factor. *Materials Horizons*, 6, 2094-2102.

CHAPIN, D. M., FULLER, C. S. & PEARSON, G. L. 1954. A new silicon p-n junction photocell for converting solar radiation into electrical power. *Journal of Applied Physics*, 25, 676-677.

CHE, X., LI, Y., QU, Y. & FORREST, S. R. 2018. High fabrication yield organic tandem photovoltaics combining vacuum- and solution-processed subcells with 15% efficiency. *Nature Energy*, 3, 422-427.

CHEN, C. C., DOU, L., GAO, J., CHANG, W. H., LI, G. & YANG, Y. 2013. High-performance semi-transparent polymer solar cells possessing tandem structures. *Energy & Environmental Science*, 6, 2714-2720.

CHEN, J., LI, G., ZHU, Q., GUO, X., FAN, Q., MA, W. & ZHANG, M. 2019. Highly efficient near-infrared and semitransparent polymer solar cells based on an ultra-narrow bandgap nonfullerene acceptor. *Journal of Materials Chemistry A*, 7, 3745-3751.

CHEN, K. S., SALINAS, J. F., YIP, H. L., HUO, L., HOU, J. & JEN, A. K. Y. 2012. Semi-transparent polymer solar cells with 6% PCE, 25% average visible transmittance and a color rendering index close to 100 for power generating window applications. *Energy & Environmental Science*, 5, 9551-9557.

CHEN, S., YAN, T., FANADY, B., SONG, W., GE, J., WEI, Q., PENG, R., CHEN, G., ZOU, Y. & GE, Z. 2020. High efficiency ternary organic solar cells enabled by compatible dual-donor strategy with planar conjugated structures. *Science China Chemistry*, 63, 917-923.

CHEN, S., YAO, H., HU, B., ZHANG, G., ARUNAGIRI, L., MA, L. K., HUANG, J., ZHANG, J., ZHU, Z., BAI, F., MA, W. & YAN, H. 2018. A nonfullerene semitransparent tandem organic solar cell with 10.5% power conversion efficiency. *Advanced Energy Materials*, 8, 1800529.

CHEN, X., LIU, Q., WU, Q., DU, P., ZHU, J., DAI, S. & YANG, S. 2016. Incorporating graphitic carbon nitride (g-C₃N₄) quantum dots into bulk-heterojunction polymer solar cells leads to efficiency enhancement. *Advanced Functional Materials*, 26, 1719-1728.

CHENG, P., LI, G., ZHAN, X. & YANG, Y. 2018. Next-generation organic photovoltaics based on non-fullerene acceptors. *Nature Photonics*, 12, 131-142.

CHENG, P. & ZHAN, X. 2016. Stability of organic solar cells: challenges and strategies. *Chemical Society Reviews*, 45, 2544-2582.

CHENG, Y. J., YANG, S. H. & HSU, C. S. 2009. Synthesis of conjugated polymers for organic solar cell applications. *Chemical Reviews*, 109, 5868-5923.

COAKLEY, K. M. & MCGEHEE, M. D. 2004. Conjugated polymer photovoltaic cells. *Chemistry of Materials*, 16, 4533-4542.

CORZO, D., ALMASABI, K., BIHAR, E., MACPHEE, S., ROSAS-VILLALVA, D., GASPARINI, N., INAL, S. & BARAN, D. 2019. Digital inkjet printing of high-efficiency large-area nonfullerene organic solar cells. *Advanced Materials Technologies*, 4, 1900040.

CUI, Y., YANG, C., YAO, H., ZHU, J., WANG, Y., JIA, G., GAO, F. & HOU, J. 2017. Efficient semitransparent organic solar cells with tunable color enabled by an ultralow-bandgap nonfullerene acceptor. *Advanced Materials*, 29, 1703080.

CUI, Y., YAO, H., ZHANG, J., XIAN, K., ZHANG, T., HONG, L., WANG, Y., XU, Y., MA, K., AN, C., HE, C., WEI, Z., GAO, F. & HOU, J. 2020. Single-junction organic photovoltaic cells with approaching 18% efficiency. *Advanced Materials*, 32, 1908205.

CZOLK, J., LANDERER, D., KOPPITZ, M., NASS, D. & COLSMANN, A. 2016. Highly efficient, mechanically flexible, semi-transparent organic solar cells doctor bladed from non-halogenated solvents. *Advanced Materials Technologies*, 1, 1600184.

DAI, S. & ZHAN, X. 2018. Nonfullerene acceptors for semitransparent organic solar cells. *Advanced Energy Materials*, 8, 1800002.

DONG, X., SHI, P., SUN, L., LI, J., QIN, F., XIONG, S., LIU, T., JIANG, X. & ZHOU, Y. 2019. Flexible nonfullerene organic solar cells based on embedded silver nanowires with an efficiency up to 11.6%. *Journal of Materials Chemistry A*, 7, 1989-1995.

DU, X., LI, X., LIN, H., ZHOU, L., ZHENG, C. & TAO, S. 2019. High performance opaque and semi-transparent organic solar cells with good tolerance to film thickness realized by a unique solid additive. *Journal of Materials Chemistry A*, 7, 7437-7450.

FACCHETTI, A. 2013. Polymer donor-polymer acceptor (all-polymer) solar cells. *Materials Today*, 16, 123-132.

FAN, H. & ZHU, X. 2016. High-performance inverted polymer solar cells with zirconium acetylacetonate buffer layers. *ACS Applied Materials & Interfaces*, 8, 33856-33862.

FAN, X., SONG, W., LEI, T., XU, B., YAN, F., WANG, N., CUI, H. & GE, Z. 2019. High-efficiency robust organic solar cells using transfer-printed PEDOT:PSS electrodes through interface bonding engineering. *Materials Chemistry Frontiers*, 3, 901-908.

FAN, X., XU, B., LIU, S., CUI, C., WANG, J. & YAN, F. 2016. Transfer-printed PEDOT:PSS electrodes using mild acids for high conductivity and improved stability with application to flexible organic solar cells. *ACS Applied Materials & Interfaces*, 8, 14029-14036.

FANADY, B., SONG, W., PENG, R., WU, T. & GE, Z. 2020. Efficiency enhancement of organic solar cells enabled by interface engineering of sol-gel zinc oxide with an oxadiazole-based material. *Organic Electronics*, 76, 105483.

FOUR PEAKS TECHNOLOGIES. 2011. *Early history of solar* [Online]. Scottsdale: Four Peaks Technologies, Inc. Available: http://solarcellcentral.com/history_page.html [Accessed 17 May 2020].

GAO, J., MING, R., AN, Q., MA, X., ZHANG, M., MIAO, J., WANG, J., YANG, C. & ZHANG, F. 2019. Ternary organic solar cells with J71 as donor and alloyed acceptors exhibiting 13.16% efficiency. *Nano Energy*, 63, 103888.

GE, Z., CHEN, S., PENG, R. & ISLAM, A. 2014. Research progress and manufacturing techniques for large-area polymer solar cells. In: HUANG, H. & HUANG, J. (eds.) *Organic and Hybrid Solar Cells*. Cham: Springer International Publishing.

GUNES, S., NEUGEBAUER, H. & SARICIFTCI, N. S. 2007. Conjugated polymer-based organic solar cells. *Chemical Reviews*, 107, 1324-1338.

GUO, F., ZHU, X., FORBERICH, K., KRANTZ, J., STUBHAN, T., SALINAS, M., HALIK, M., SPALLEK, S., BUTZ, B., SPIECKER, E., AMERI, T., LI, N., KUBIS, P., GULDI, D. M., MATT, G. J. & BRABEC, C. J. 2013. ITO-free and fully solution-processed semitransparent organic solar cells with high fill factors. *Advanced Energy Materials*, 3, 1062-1067.

HE, D., ZHAO, F., XIN, J., RECH, J. J., WEI, Z., MA, W., YOU, W., LI, B., JIANG, L., LI, Y. & WANG, C. 2018. A fused ring electron acceptor with decacyclic core enables over 13.5% efficiency for organic solar cells. *Advanced Energy Materials*, 8, 1802050.

HE, Z., ZHONG, C., SU, S., XU, M., WU, H. & CAO, Y. 2012. Enhanced power-conversion efficiency in polymer solar cells using an inverted device structure. *Nature Photonics*, 6, 591-595.

HEEGER, A. J. 2014. 25th Anniversary article: bulk heterojunction solar cells: understanding the mechanism of operation. *Advanced Materials*, 26, 10-28.

HOPPE, H. & SARICIFTCI, N. S. 2004. Organic solar cells: an overview. *Journal of Materials Research*, 19, 1924-1945.

HU, D., YANG, Q., CHEN, H., WOBLEN, F., LE CORRE, V. M., SINGH, R., LIU, T., MA, R., TANG, H., KOSTER, L. J. A., DUAN, T., YAN, H., KAN, Z., XIAO, Z. & LU, S. 2020. 15.34% Efficiency all-small-molecule organic solar cells with an improved fill factor enabled by a fullerene additive. *Energy & Environmental Science*, 13, 2134-2141.

HUAI, Z., WANG, L., SUN, Y., FAN, R., HUANG, S., ZHAO, X., LI, X., FU, G. & YANG, S. 2018. High-efficiency and stable organic solar cells enabled by dual cathode buffer layers. *ACS Applied Materials & Interfaces*, 10, 5682-5692.

HUANG, H. & DENG, W. 2014. Introduction to organic solar cells. In: HUANG, H. & HUANG, J. (eds.) *Organic and Hybrid Solar Cells*. Cham: Springer International Publishing.

HUANG, J., LI, C. Z., CHUEH, C. C., LIU, S. Q., YU, J. S. & JEN, A. K. Y. 2015. 10.4% power conversion efficiency of ITO-free organic photovoltaics through enhanced light trapping configuration. *Advanced Energy Materials*, 5, 1500406.

IE, Y., MORIKAWA, K., ZAJACZKOWSKI, W., PISULA, W., KOTADIYA, N. B., WETZELAER, G. J. A. H., BLOM, P. W. M. & ASO, Y. 2018. Enhanced photovoltaic performance of amorphous donor-acceptor copolymers based on fluorine-substituted benzodioxocyclohexene-annulated thiophene. *Advanced Energy Materials*, 8, 1702506.

IPCC 2015. Climate change 2014: synthesis report. In: CORE WRITING TEAM, PACHAURI, R. K. & MEYER, L. (eds.). Switzerland: IPCC.

JAGADAMMA, L. K., SAJJAD, M. T., SAVIKHIN, V., TONEY, M. F. & SAMUEL, I. D. W. 2017. Correlating photovoltaic properties of a PTB7-Th:PC71BM

blend to photophysics and microstructure as a function of thermal annealing. *Journal of Materials Chemistry A*, 5, 14646-14657.

JEON, I., CUI, K., CHIBA, T., ANISIMOV, A., NASIBULIN, A. G., KAUPPINEN, E. I., MARUYAMA, S. & MATSUO, Y. 2015. Direct and dry deposited single-walled carbon nanotube films doped with MoO_x as electron-blocking transparent electrodes for flexible organic solar cells. *Journal of the American Chemical Society*, 137, 7982-7985.

JIA, B., DAI, S., KE, Z., YAN, C., MA, W. & ZHAN, X. 2018. Breaking 10% efficiency in semitransparent solar cells with fused-undecacyclic electron acceptor. *Chemistry of Materials*, 30, 239-245.

JIANG, Z., FUKUDA, K., XU, X., PARK, S., INOUE, D., JIN, H., SAITO, M., OSAKA, I., TAKIMIYA, K. & SOMEYA, T. 2018. Reverse-offset printed ultrathin Ag mesh for robust conformal transparent electrodes for high-performance organic photovoltaics. *Advanced Materials*, 30, 1707526.

JINNO, H., FUKUDA, K., XU, X., PARK, S., SUZUKI, Y., KOIZUMI, M., YOKOTA, T., OSAKA, I., TAKIMIYA, K. & SOMEYA, T. 2017. Stretchable and waterproof elastomer-coated organic photovoltaics for washable electronic textile applications. *Nature Energy*, 2, 780-785.

JORGENSEN, M., NORRMAN, K. & KREBS, F. C. 2008. Stability/degradation of polymer solar cells. *Solar Energy Materials and Solar Cells*, 92, 686-714.

JUNG, S., LEE, J., SEO, J., KIM, U., CHOI, Y. & PARK, H. 2018. Development of annealing-free, solution-processable inverted organic solar cells with N-doped graphene electrodes using zinc oxide nanoparticles. *Nano Letters*, 18, 1337-1343.

KALTENBRUNNER, M., WHITE, M. S., GLOWACKI, E. D., SEKITANI, T., SOMEYA, T., SARICIFTCI, N. S. & BAUER, S. 2012. Ultrathin and lightweight organic solar cells with high flexibility. *Nature Communications*, 3, 770.

KANG, H., JUNG, S., JEONG, S., KIM, G. & LEE, K. 2015. Polymer-metal hybrid transparent electrodes for flexible electronics. *Nature Communications*, 6, 6503.

KANG, H., LEE, W., OH, J., KIM, T., LEE, C. & KIM, B. J. 2016. From fullerene-polymer to all-polymer solar cells: the importance of molecular packing, orientation, and morphology control. *Accounts of Chemical Research*, 49, 2424-2434.

KEARNS, D. & CALVIN, M. 1958. Photovoltaic effect and photoconductivity in laminated organic systems. *The Journal of Chemical Physics*, 29, 950-951.

KIM, N., KANG, H., LEE, J. H., KEE, S., LEE, S. H. & LEE, K. 2015. Highly conductive all-plastic electrodes fabricated using a novel chemically controlled transfer-printing method. *Advanced Materials*, 27, 2317-2323.

KIM, N., KEE, S., LEE, S. H., LEE, B. H., KAHNG, Y. H., JO, Y. R., KIM, B. J. & LEE, K. 2014. Highly conductive PEDOT:PSS nanofibrils induced by solution-processed crystallization. *Advanced Materials*, 26, 2268-2272.

KIM, W., KIM, S., KANG, I., JUNG, M. S., KIM, S. J., KIM, J. K., CHO, S. M., KIM, J. H. & PARK, J. H. 2016. Hybrid silver mesh electrode for ITO-free flexible polymer solar cells with good mechanical stability. *Chemistry Sustainability Energy Materials*, 9, 1042-1049.

KONIOS, D., PETRIDIS, C., KAKAVELAKIS, G., SYGLETU, M., SAVVA, K., STRATAKIS, E. & KYMAKIS, E. 2015. Reduced graphene oxide micromesh electrodes for large area, flexible, organic photovoltaic devices. *Advanced Functional Materials*, 25, 2213-2221.

KREBS, F. C. 2009. Fabrication and processing of polymer solar cells: a review of printing and coating techniques. *Solar Energy Materials and Solar Cells*, 93, 394-412.

KULKARNI, A. P., TONZOLA, C. J., BABEL, A. & JENEKHE, S. A. 2004. Electron transport materials for organic light-emitting diodes. *Chemistry of Materials*, 16, 4556-4573.

LEE, B. R., JUNG, E. D., NAM, Y. S., JUNG, M., PARK, J. S., LEE, S., CHOI, H., KO, S. J., SHIN, N. R., KIM, Y. K., KIM, S. O., KIM, J. Y., SHIN, H. J., CHO, S. & SONG, M. H. 2014. Amine-based polar solvent treatment for highly efficient inverted polymer solar cells. *Advanced Materials*, 26, 494-500.

LEE, D. H., SHIN, H. C., CHAE, H. & CHO, S. M. 2011. Selective metal transfer and its application to patterned multicolor organic light-emitting diodes. *Advanced Materials*, 23, 1851-1854.

LEE, T. D. & EBONG, A. U. 2017. A review of thin film solar cell technologies and challenges. *Renewable and Sustainable Energy Reviews*, 70, 1286-1297.

LEI, T., PENG, R., FAN, X., WEI, Q., LIU, Z., GUAN, Q., SONG, W., HONG, L., HUANG, J., YANG, R. & GE, Z. 2018. Highly efficient non-fullerene organic solar cells using 4,8-bis((2-ethylhexyl)oxy)benzo[1,2-b:4,5-b']dithiophene-based polymers as additives. *Macromolecules*, 51, 4032-4039.

LEI, T., PENG, R., HUANG, L., SONG, W., YAN, T., ZHU, L. & GE, Z. 2019. 13.5% flexible organic solar cells achieved by robust composite ITO/PEDOT:PSS electrodes. *Materials Today Energy*, 14, 100334.

LI, F., CHEN, Z., WEI, W., CAO, H., GONG, Q., TENG, F., QIAN, L. & WANG, Y. 2004. Blue-light-emitting organic electroluminescence via exciplex emission based on a fluorene derivative. *Journal of Physics D: Applied Physics*, 37, 1613-1616.

LI, G., SHROTRIYA, V., HUANG, J., YAO, Y., MORIARTY, T., EMERY, K. & YANG, Y. 2005. High-efficiency solution processable polymer photovoltaic cells by self-organization of polymer blends. *Nature Materials*, 4, 864-868.

LI, G., ZHU, R. & YANG, Y. 2012a. Polymer solar cells. *Nature Photonics*, 6, 153-161.

- LI, H., TANG, H., LI, L., XU, W., ZHAO, X. & YANG, X. 2011. Solvent-soaking treatment induced morphology evolution in P3HT/PCBM composite films. *Journal of Materials Chemistry*, 21, 6563-6568.
- LI, S., YE, L., ZHAO, W., ZHANG, S., MUKHERJEE, S., ADE, H. & HOU, J. 2016. Energy-level modulation of small-molecule electron acceptors to achieve over 12% efficiency in polymer solar cells. *Advanced Materials*, 28, 9423-9429.
- LI, X., LIU, X., ZHANG, W., WANG, H. & FANG, J. 2017a. Fullerene-free organic solar cells with efficiency over 12% based on EDTA-ZnO hybrid cathode interlayer. *Chemistry of Materials*, 29, 4176-4180.
- LI, X., MENG, H., SHEN, F., SU, D., HUO, S., SHAN, J., HUANG, J. & ZHAN, C. 2019. Semitransparent fullerene-free polymer solar cell with 44% AVT and 7% efficiency based on a new chlorinated small molecule acceptor. *Dyes and Pigments*, 166, 196-202.
- LI, Y. 2012b. Molecular design of photovoltaic materials for polymer solar cells: toward suitable electronic energy levels and broad absorption. *Accounts of Chemical Research*, 45, 723-733.
- LI, Y., LIN, J. D., CHE, X., QU, Y., LIU, F., LIAO, L. S. & FORREST, S. R. 2017b. High efficiency near-infrared and semitransparent non-fullerene acceptor organic photovoltaic cells. *Journal of the American Chemical Society*, 139, 17114-17119.
- LI, Y., SONG, W., YAN, T., XIAO, J., HAN, Y., CHEN, S., PENG, R., ZHANG, J. & GE, Z. 2020. Enhanced efficiency of organic solar cells via Si-based non-conjugated small-molecule electrolyte as cathode interlayer. *Organic Electronics*, 85, 105863.
- LI, Y., XU, G., CUI, C. & LI, Y. 2018. Flexible and semitransparent organic solar cells. *Advanced Energy Materials*, 8, 1701791.

- LI, Z., QIN, F., LIU, T., GE, R., MENG, W., TONG, J., XIONG, S. & ZHOU, Y. 2015. Optical properties and conductivity of PEDOT:PSS films treated by polyethylenimine solution for organic solar cells. *Organic Electronics*, 21, 144-148.
- LIAN, J., YUAN, Y., PENG, E. & HUANG, J. 2014. Interfacial layers in organic solar cells. In: HUANG, H. & HUANG, J. (eds.) *Organic and Hybrid Solar Cells*. Cham: Springer International Publishing.
- LIAO, K. S., YAMBEM, S. D., HALDAR, A., ALLEY, N. J. & CURRAN, S. A. 2010. Designs and architectures for the next generation of organic solar cells. *Energies*, 3, 1212-1250.
- LIAO, S. H., JHUO, H. J., CHENG, Y. S. & CHEN, S. A. 2013. Fullerene derivative-doped zinc oxide nanofilm as the cathode of inverted polymer solar cells with low-bandgap polymer (PTB7-Th) for high performance. *Advanced Materials*, 25, 4766-4771.
- LIN, Y., WANG, J., ZHANG, Z. G., BAI, H., LI, Y., ZHU, D. & ZHAN, X. 2015. An electron acceptor challenging fullerenes for efficient polymer solar cells. *Advanced Materials*, 27, 1170-1174.
- LIU, F., ZHOU, Z., ZHANG, C., ZHANG, J., HU, Q., VERGOTE, T., LIU, F., RUSSELL, T. P. & ZHU, X. 2017b. Efficient semitransparent solar cells with high NIR responsiveness enabled by a small-bandgap electron acceptor. *Advanced Materials*, 29, 1606574.
- LIU, J., CHEN, S., QIAN, D., GAUTAM, B., YANG, G., ZHAO, J., BERGQVIST, J., ZHANG, F., MA, W., ADE, H., INGANAS, O., GUNDOGDU, K., GAO, F. & YAN, H. 2016. Fast charge separation in a non-fullerene organic solar cell with a small driving force. *Nature Energy*, 1, 16089.
- LIU, J., YAO, Y., XIAO, S. & GU, X. 2018. Review of status developments of high-efficiency crystalline silicon solar cells. *Journal of Physics D: Applied Physics*, 51, 123001.

LIU, Q., JIANG, Y., JIN, K., QIN, J., XU, J., LI, W., XIONG, J., LIU, J., XIAO, Z., SUN, K., YANG, S., ZHANG, X. & DING, L. 2020. 18% Efficiency organic solar cells. *Science Bulletin*, 65, 272-275.

LIU, Q., TOUDERT, J., CIAMMARUCHI, L., MARTINEZ-DENEGRI, G. & MARTORELL, J. 2017a. High open-circuit voltage and short-circuit current flexible polymer solar cells using ternary blends and ultrathin Ag-based transparent electrodes. *Journal of Materials Chemistry A*, 5, 25476-25484.

LIU, T., LUO, Z., CHEN, Y., YANG, T., XIAO, Y., ZHANG, G., MA, R., LU, X., ZHAN, C., ZHANG, M., YANG, C., LI, Y., YAO, J. & YAN, H. 2019a. A nonfullerene acceptor with a 1000 nm absorption edge enables ternary organic solar cells with improved optical and morphological properties and efficiencies over 15%. *Energy & Environmental Science*, 12, 2529-2536.

LIU, X., LI, X., ZHENG, N., GU, C., WANG, L., FANG, J. & YANG, C. 2019b. Insight into the efficiency and stability of all-polymer solar cells based on two 2D-conjugated polymer donors: achieving high fill factor of 78%. *ACS Applied Materials & Interfaces*, 11, 43433-43440.

LIU, X., WEN, W. & BAZAN, G. C. 2012. Post-deposition treatment of an arylated-carbazole conjugated polymer for solar cell fabrication. *Advanced Materials*, 24, 4505-4510.

LIU, Y., CHENG, P., LI, T., WANG, R., LI, Y., CHANG, S. Y., ZHU, Y., CHENG, H. W., WEI, K. H., ZHAN, X., SUN, B. & YANG, Y. 2019c. Unraveling sunlight by transparent organic semiconductors toward photovoltaic and photosynthesis. *ACS Nano*, 13, 1071-1077.

LIU, Y., LI, M., YANG, J., XUE, W., FENG, S., SONG, J., TANG, Z., MA, W. & BO, Z. 2019d. High-efficiency as-cast organic solar cells based on acceptors with steric hindrance induced planar terminal group. *Advanced Energy Materials*, 9, 1901280.

- LIU, Z., YOU, P., LIU, S. & YAN, F. 2015. Neutral-color semitransparent organic solar cells with all-graphene electrodes. *ACS Nano*, 9, 12026-12034.
- LU, S., LIN, J., LIU, K., YUE, S., REN, K., TAN, F., WANG, Z., JIN, P., QU, S. & WANG, Z. 2017. Large area flexible polymer solar cells with high efficiency enabled by imprinted Ag grid and modified buffer layer. *Acta Materialia*, 130, 208-214.
- LUO, M., ZHAO, C., YUAN, J., HAI, J., CAI, F., HU, Y., PENG, H., BAI, Y., TAN, Z. & ZOU, Y. 2019. Semitransparent solar cells with over 12% efficiency based on a new low bandgap fluorinated small molecule acceptor. *Materials Chemistry Frontiers*, 3, 2483-2490.
- LUO, Z., LI, G., GAO, W., WU, K., ZHANG, Z. G., QIU, B., BIN, H., XUE, L., LIU, F., LI, Y. & YANG, C. 2018. A universal nonfullerene electron acceptor matching with different band-gap polymer donors for high-performance polymer solar cells. *Journal of Materials Chemistry A*, 6, 6874-6881.
- LUO, Z., MA, R., LIU, T., YU, J., XIAO, Y., SUN, R., XIE, G., YUAN, J., CHEN, Y., CHEN, K., CHAI, G., SUN, H., MIN, J., ZHANG, J., ZOU, Y., YANG, C., LU, X., GAO, F. & YAN, H. 2020. Fine-tuning energy levels via asymmetric end groups enables polymer solar cells with efficiencies over 17%. *Joule*, 4, 1-12.
- MA, H., YIP, H. L., HUANG, F. & JEN, A. K. Y. 2010. Interface engineering for organic electronics. *Advanced Functional Materials*, 20, 1371-1388.
- MA, X., XIAO, Z. AN, Q., ZHANG, M., HU, Z., WANG, J., DING, L. & ZHANG, F. 2018. Simultaneously improved efficiency and average visible transmittance of semitransparent polymer solar cells with two ultra-narrow bandgap nonfullerene acceptors. *Journal of Materials Chemistry A*, 6, 21485-21492.
- MA, Z., TANG, Z., WANG, E., ANDERSSON, M. R., INGANAS, O. & ZHANG, F. 2012. Influences of surface roughness of ZnO electron transport layer on the photovoltaic performance of organic inverted solar cells. *The Journal of Physical Chemistry C*, 116, 24462-24468.

- MCAFEE, S. M., TOPPLE, J. M., HILL, I. G. & WELCH, G. C. 2015. Key components to the recent performance increases of solution processed non-fullerene small molecule acceptors. *Journal of Materials Chemistry A*, 3, 16393-16408.
- MCDOWELL, C., ABDELSAMIE, M., TONEY, M. F. & BAZAN, G. C. 2018. Solvent additives: key morphology-directing agents for solution-processed organic solar cells. *Advanced Materials*, 30, 1707114.
- MCDOWELL, C. & BAZAN, G. C. 2017. Organic solar cells processed from green solvents. *Current Opinion in Green and Sustainable Chemistry*, 5, 49-54.
- MENG, L., ZHANG, Y., WAN, X., LI, C., ZHANG, X., WANG, Y., KE, X., XIAO, Z., DING, L., XIA, R., YIP, H. L., CAO, Y. & CHEN, Y. 2018. Organic and solution-processed tandem solar cells with 17.3% efficiency. *Science*, 361, 1094-1098.
- MENG, W., GE, R., LI, Z., TONG, J., LIU, T., ZHAO, Q., XIONG, S., JIANG, F., MAO, L. & ZHOU, Y. 2015. Conductivity enhancement of PEDOT:PSS films via phosphoric acid treatment for flexible all-plastic solar cells. *ACS Applied Materials & Interfaces*, 7, 14089-14094.
- MENGISTIE, D. A., IBRAHEM, M. A., WANG, P. C. & CHU, C. W. 2014. Highly conductive PEDOT:PSS treated with formic acid for ITO-free polymer solar cells. *ACS Applied Materials & Interfaces*, 6, 2292-2299.
- MENKE, S. M., RAN, N. A., BAZAN, G. C. & FRIEND, R. H. 2018. Understanding energy loss in organic solar cells: toward a new efficiency regime. *Joule*, 2, 25-35.
- MOREL, D. L., GHOSH, A. K., FENG, T., STOGRYN, E. L., PURWIN, P. E., SHAW, R. F. & FISHMAN, C. 1978. High-efficiency organic solar cells. *Applied Physics Letters*, 32, 495-497.
- NAM, S., JANG, J., CHA, H., HWANG, J., AN, T. K., PARK, S. & PARK, C. E. 2012. Effects of direct solvent exposure on the nanoscale morphologies and electrical characteristics of PCBM-based transistors and photovoltaics. *Journal of Materials Chemistry*, 22, 5543-5549.

NATIONAL RENEWABLE ENERGY LABORATORY 2020. Best research-cell efficiency chart.

NIAN, L., ZHANG, W., ZHU, N., LIU, L., XIE, Z., WU, H., WURTHNER, F. & MA, Y. 2015. Photoconductive cathode interlayer for highly efficient inverted polymer solar cells. *Journal of the American Chemical Society*, 137, 6995-6998.

NIELSEN, C. B., HOLLIDAY, S., CHEN, H. Y., CRYER, S. J. & MCCULLOCH, I. 2015. Non-fullerene electron acceptors for use in organic solar cells. *Accounts of Chemical Research*, 48, 2803-2812.

OU, Q. D., XIE, H. J., CHEN, J. D., ZHOU, L., LI, Y. Q. & TANG, J. X. 2016. Enhanced light harvesting in flexible polymer solar cells: synergistic simulation of a plasmonic meta-mirror and a transparent silver mesowire electrode. *Journal of Materials Chemistry A*, 4, 18952-18962.

OUYANG, J. 2013. "Secondary doping" methods to significantly enhance the conductivity of PEDOT:PSS for its application as transparent electrode of optoelectronic devices. *Displays*, 34, 423-436.

OUYANG, X., PENG, R., AI, L., ZHANG, X. & GE, Z. 2015. Efficient polymer solar cells employing a non-conjugated small-molecule electrolyte. *Nature Photonics*, 9, 520-524.

PARK, H., CHANG, S., ZHOU, X., KONG, J., PALACIOS, T. & GRADECAK, S. 2014a. Flexible graphene electrode-based organic photovoltaics with record-high efficiency. *Nano Letters*, 14, 5148-5154.

PARK, J. H., LEE, D. Y., KIM, Y. H., KIM, J. K., LEE, J. H., PARK, J. H., LEE, T. W. & CHO, J. H. 2014b. Flexible and transparent metallic grid electrodes prepared by evaporative assembly. *ACS Applied Materials & Interfaces*, 6, 12380-12387.

PARK, S., HEO, S. W., LEE, W., INOUE, D., JIANG, Z., YU, K., JINNO, H., HASHIZUME, D., SEKINO, M., YOKOTA, T., FUKUDA, K., TAJIMA, K. &

SOMEYA, T. 2018. Self-powered ultra-flexible electronics via nano-grating-patterned organic photovoltaics. *Nature*, 561, 516-521.

PENG, R., LIU, Z., GUAN, Q., HONG, L., SONG, W., WEI, Q., GAO, P., HUANG, J., FAN, X., WANG, M. & GE, Z. 2018. Highly efficient non-fullerene polymer solar cells enabled by novel non-conjugated small-molecule cathode interlayers. *Journal of Materials Chemistry A*, 6, 6327-6334.

PENG, R., SONG, W., YAN, T., FANADY, B., LI, Y., ZHAN, Q. & GE, Z. 2019. Interface bonding engineering of a transparent conductive electrode towards highly efficient and mechanically flexible ITO-free organic solar cells. *Journal of Materials Chemistry A*, 7, 11460-11467.

PEREZ, M. D., BOREK, C., FORREST, S. R. & THOMPSON, M. E. 2009. Molecular and morphological influences on the open circuit voltages of organic photovoltaic devices. *Journal of the American Chemical Society*, 131, 9281-9286.

PHILIPPS, S. & WARMUTH, W. 2020. Photovoltaics report. Freiburg: Fraunhofer Institute for Solar Energy System.

QIAN, D., YE, L., ZHANG, M., LIANG, Y., LI, L., HUANG, Y., GUO, X., ZHANG, S., TAN, Z. A. & HOU, J. 2012. Design, application, and morphology study of a new photovoltaic polymer with strong aggregation in solution state. *Macromolecules*, 45, 9611-9617.

QIN, J., AN, C., ZHANG, J., MA, K., YANG, Y., ZHANG, T., LI, S., XIAN, K., CUI, Y., TANG, Y., MA, W., YAO, H., ZHANG, S., XU, B., HE, C. & HOU, J. 2020a. 15.3% Efficiency all-small-molecule organic solar cells enabled by symmetric phenyl substitution. *Science China Materials*, 63, 1142-1150.

QIN, J., LAN, L., CHEN, S., HUANG, F., SHI, H., CHEN, W., XIA, H., SUN, K. & YANG, C. 2020b. Recent progress in flexible and stretchable organic solar cells. *Advanced Functional Materials*, 30, 2002529.

RAMACHANDRAN, R., MANI, V., CHEN, S. M., KUMAR, G. P. G., GAJENDRAN, P., DEVI, N. B. & DEVASENATHIPATHY, R. 2015. Recent progress in electrode fabrication materials and various insights in solar cells: review. *International Journal of Electrochemical Science*, 10, 3301-3318.

RAUT, K. H., CHOPDE, H. N. & DESHMUKH, D. W. 2018. A review on comparative studies of diverse generation in solar cell. *International Journal of Electrical Engineering and Ethics*, 1, 1-9.

ROSER, M., RITCHIE, H. & ORTIZ-OSPINA, E. 2020. *World population growth* [Online]. OurWorldInData.org. Available: <https://ourworldindata.org/world-population-growth> [Accessed 17 May 2020].

ROSTALSKI, J. & MEISSNER, D. 2000. Monochromatic versus solar efficiencies of organic solar cells. *Solar Energy Materials and Solar Cells*, 61, 87-95.

SALVATIERRA, R. V., CAVA, C. E., ROMAN, L. S. & ZARBIN, A. J. G. 2013. ITO-free and flexible organic photovoltaic device based on high transparent and conductive polyaniline/carbon nanotube thin films. *Advanced Functional Materials*, 23, 1490-1499.

SANO, T., INABA, S. & VOHRA, V. 2019. Ternary active layers for neutral color semitransparent organic solar cells with PCEs over 4%. *ACS Applied Energy Materials*, 2, 2534-2540.

SARICIFTCI, N. S., SMILOWITZ, L., HEEGER, A. J. & WUDL, F. 1992. Photoinduced electron transfer from a conducting polymer to buckminsterfullerene. *Science*, 258, 1474-1476.

SCHARBER, M. C., MUHLBACHER, D., KOPPE, M., DENK, P., WALDAUF, C., HEEGER, A. J. & BRABEC, C. J. 2006. Design rules for donors in bulk-heterojunction solar cells towards 10% energy-conversion efficiency. *Advanced Materials*, 18, 789-794.

SCHILINSKY, P., WALDAUF, C. & BRABEC, C. J. 2002. Recombination and loss analysis in polythiophene based bulk heterojunction photodetectors. *Applied Physics Letters*, 81, 3885-3887.

SCHLENKER, C. W. & THOMPSON, M. E. 2011. The molecular nature of photovoltage losses in organic solar cells. *Chemical Communications*, 47, 3702-3716.

SEO, J. H., GUTACKER, A., SUN, Y., WU, H., HUANG, F., CAO, Y., SCHERF, U., HEEGER, A. J. & BAZAN, G. C. 2011. Improved high-efficiency organic solar cells via incorporation of a conjugated polyelectrolyte interlayer. *Journal of the American Chemical Society*, 133, 8416-8419.

SEO, J. H., HWANG, I., UM, H. D., LEE, S., LEE, K., PARK, J., SHIN, H., KWON, T. H., KANG, S. J. & SEO, K. 2017. Cold isostatic-pressured silver nanowire electrodes for flexible organic solar cells via room-temperature processes. *Advanced Materials*, 29, 1701479.

SEO, J. H., UM, H. D., SHUKLA, A., HWANG, I., PARK, J., KANG, Y. C., KIM, C. S., SONG, M. & SEO, K. 2015. Low-temperature solution-processed flexible organic solar cells with PFN/AgNWs cathode. *Nano Energy*, 16, 122-129.

SHAN, F. & KIM, S. J. 2018. Tailoring threshold voltage in indium-zinc-oxide thin-film transistors by inserting a 2-(4-biphenyl)-5-(4-tert-butylphenyl)-1,3,4-oxadiazole buffer layer. *Physica Status Solidi (a)*, 215, 1700869.

SHI, H., XIA, R., SUN, C., XIAO, J., WU, Z., HUANG, F., YIP, H. L. & CAO, Y. 2017. Synergic interface and optical engineering for high-performance semitransparent polymer solar cells. *Advanced Energy Materials*, 7, 1701121.

SHIN, D. H., SEO, S. W., KIM, J. M., LEE, H. S. & CHOI, S. H. 2018. Graphene transparent conductive electrodes doped with graphene quantum dots-mixed silver nanowires for highly-flexible organic solar cells. *Journal of Alloys and Compounds*, 744, 1-6.

SHIRAKAWA, T., UMEDA, T., HASHIMOTO, Y., FUJII, A. & YOSHINO, K. 2004. Effect of ZnO layer on characteristics of conducting polymer/C60 photovoltaic cell. *Journal of Physics D: Applied Physics*, 37, 847-850.

SILVA, W. J. D., KIM, H. P., YUSOFF, A. R. B. M. & JANG, J. 2013. Transparent flexible organic solar cells with 6.87% efficiency manufactured by an all-solution process. *Nanoscale*, 5, 9324-9329.

SINGHAL, G. S., RENGER, G., SOPORY, S. K., IRRGANG, K. D. & GOVINDJEE 1999. *Concepts in photobiology: photosynthesis and photomorphogenesis*, Springer Netherlands.

SISTA, S., HONG, Z., CHEN, L. M. & YANG, Y. 2011. Tandem polymer photovoltaic cells-current status, challenges and future outlook. *Energy & Environmental Science*, 4, 1606-1620.

SOMMER, J. R., FARLEY, R. T., GRAHAM, K. R., YANG, Y., REYNOLDS, J. R., XUE, J. & SCHANZE, K. S. 2009. Efficient near-infrared polymer and organic light-emitting diodes based on electrophosphorescence from (tetraphenyltetranaphtho[2,3]porphyrin)platinum(II). *ACS Applied Materials & Interfaces*, 1, 274-278.

SONG, M., YOU, D. S., LIM, K., PARK, S., JUNG, S., KIM, C. S., KIM, D. H., KIM, D. G., KIM, J. K., PARK, J., KANG, Y. C., HEO, J., JIN, S. H., PARK, J. H. & KANG, J. W. 2013. Highly efficient and bendable organic solar cells with solution-processed silver nanowire electrodes. *Advanced Functional Materials*, 23, 4177-4184.

SONG, W., FAN, X., XU, B., YAN, F., CUI, H., WEI, Q., PENG, R., HONG, L., HUANG, J. & GE, Z. 2018. All-solution-processed metal-oxide-free flexible organic solar cells with over 10% efficiency. *Advanced Materials*, 30, 1800075.

SONG, W., FANADY, B., PENG, R., HONG, L., WU, L., ZHANG, W., YAN, T., WU, T., CHEN, S. & GE, Z. 2020a. Foldable semitransparent organic solar cells for photovoltaic and photosynthesis. *Advanced Energy Materials*, 10, 2000136.

SONG, W., PENG, R., HUANG, L., LIU, C., FANADY, B., LEI, T., HONG, L., GE, J., FACCHETTI, A. & GE, Z. 2020b. Over 14% efficiency folding-flexible ITO-free organic solar cells enabled by eco-friendly acid-processed electrodes. *iScience*, 23, 100981.

SU, W., FAN, Q., GUO, X., WU, J., ZHANG, M. & LI, Y. 2019. Efficient as-cast semi-transparent organic solar cells with efficiency over 9% and a high average visible transmittance of 27.6%. *Physical Chemistry Chemical Physics*, 21, 10660-10666.

SUN, C., PAN, F., QIU, B., QIN, S., CHEN, S., SHANG, Z., MENG, L., YANG, C. & LI, Y. 2020. D-A copolymer donor based on bithienyl benzodithiophene D-unit and monoalkoxy bifluoroquinoxaline A-unit for high-performance polymer solar cells. *Chemistry of Materials*, 32, 3254-3261.

SUN, C., WU, Z., HU, Z., XIAO, J., ZHAO, W., LI, H. W., LI, Q. Y., TSANG, S. W., XU, Y. X., ZHANG, K., YIP, H. L., HOU, J., HUANG, F. & CAO, Y. 2017. Interface design for high-efficiency non-fullerene polymer solar cells. *Energy & Environmental Science*, 10, 1784-1791.

SUN, G., SHAHID, M., FEI, Z., XU, S., EISNER, F. D., ANTHOPOLOUS, T. D., MCLACHLAN, M. A. & HEENEY, M. 2019. Highly-efficient semi-transparent organic solar cells utilising non-fullerene acceptors with optimised multilayer MoO₃/Ag/MoO₃ electrodes. *Materials Chemistry Frontiers*, 3, 450-455.

SUN, Q., ZHANG, F., WANG, J., AN, Q., ZHAO, C., LI, L., TENG, F. & HU, B. 2015. A two-step strategy to clarify the roles of a solution processed PFN interfacial layer in highly efficient polymer solar cells. *Journal of Materials Chemistry A*, 3, 18432-18441.

SUN, Y., SEO, J. H., TAKACS, C. J., SEIFTER, J. & HEEGER, A. J. 2011. Inverted polymer solar cells integrated with a low-temperature-annealed sol-gel-derived ZnO film as an electron transport layer. *Advanced Materials*, 23, 1679-1683.

TANG, C. W. 1986. Two-layer organic photovoltaic cell. *Applied Physics Letters*, 48, 183-185.

THOMAS, J. P., ZHAO, L., MCGILLIVRAY, D. & LEUNG, K. T. 2014. High-efficiency hybrid solar cells by nanostructural modification in PEDOT:PSS with co-solvent addition. *Journal of Materials Chemistry A*, 2, 2383-2389.

TRAVERSE, C. J., PANDEY, R., BARR, M. C. & LUNT, R. R. 2017. Emergence of highly transparent photovoltaics for distributed applications. *Nature Energy*, 2, 849-860.

U.S. DEPARTMENT OF ENERGY. 2002. *The history of solar* [Online]. Office of Energy Efficiency & Renewable Energy. Available: https://www1.eere.energy.gov/solar/pdfs/solar_timeline.pdf [Accessed 17 May 2020].

UPAMA, M. B., MAHMUD, M. A., CONIBEER, G. & UDDIN, A. 2020. Trendsetters in high-efficiency organic solar cells: toward 20% power conversion efficiency. *Solar RRL*, 4, 1900342.

UPAMA, M. B., WRIGHT, M., ELUMALAI, N. K., MAHMUD, M. A., WANG, D., XU, C. & UDDIN, A. 2017. High-efficiency semitransparent organic solar cells with non-fullerene acceptor for window application. *ACS Photonics*, 4, 2327-2334.

VOSGUERITCHIAN, M., LIPOMI, D. J. & BAO, Z. 2012. Highly conductive and transparent PEDOT:PSS films with a fluorosurfactant for stretchable and flexible transparent electrodes. *Advanced Functional Materials*, 22, 421-428.

WANG, H., WANG, D., TIAN, L., LI, H., WANG, P., OU, N., WANG, X. & YANG, J. 2019a. Graphene-like porous ZnO/graphene oxide nanosheets for high-performance acetone vapor detection. *Molecules*, 24, 522.

WANG, J., FEI, F., LUO, Q., NIE, S., WU, N., CHEN, X., SU, W., LI, Y. & MA, C. Q. 2017a. Modification of the highly conductive PEDOT:PSS layer for use in silver nanogrid electrodes for flexible inverted polymer solar cells. *ACS Applied Materials & Interfaces*, 9, 7834-7842.

- WANG, M., HAN, J., HU, Y. & GUO, R. 2017b. Mesoporous C, N-codoped TiO₂ hybrid shells with enhanced visible light photocatalytic performance. *RSC Advances*, 7, 15513-15520.
- WANG, T., SUN, R., XU, S., GUO, J., WANG, W., GUO, J., JIAO, X., WANG, J., JIA, S., ZHU, X., LI, Y. & MIN, J. 2019b. A wide-bandgap D-A copolymer donor based on a chlorine substituted acceptor unit for high performance polymer solar cells. *Journal of Materials Chemistry A*, 7, 14070-14078.
- WANG, W., YAN, C., LAU, T. K., WANG, J., LIU, K., FAN, Y., LU, X. & ZHAN, X. 2017c. Fused hexacyclic nonfullerene acceptor with strong near-infrared absorption for semitransparent organic solar cells with 9.77% efficiency. *Advanced Materials*, 29, 1701308.
- WANG, Y., LIU, Y., CHEN, S., PENG, R. & GE, Z. 2013. Significant enhancement of polymer solar cell performance via side-chain engineering and simple solvent treatment. *Chemistry of Materials*, 25, 3196-3204.
- WORFOLK, B. J., ANDREWS, S. C., PARK, S., REINSPACH, J., LIU, N., TONEY, M. F., MANNSFELD, S. C. B. & BAO, Z. 2015. Ultrahigh electrical conductivity in solution-sheared polymeric transparent films. *Proceedings of the National Academy of Sciences USA*, 112, 14138-14143.
- WU, J., MENG, Y., GUO, X., ZHU, L., LIU, F. & ZHANG, M. 2019. All-polymer solar cells based on a novel narrow-bandgap polymer acceptor with power conversion efficiency over 10%. *Journal of Materials Chemistry A*, 7, 16190-16196.
- XIA, R., BRABEC, C. J., YIP, H. L. & CAO, Y. 2019. High-throughput optical screening for efficient semitransparent organic solar cells. *Joule*, 3, 2241-2254.
- XIAO, S., ZHANG, Q. & YOU, W. 2017. Molecular engineering of conjugated polymers for solar cells: an updated report. *Advanced Materials*, 29, 1601391.

- XIE, Y., HUO, L., FAN, B., FU, H., CAI, Y., ZHANG, L., LI, Z., WANG, Y., MA, W., CHEN, Y. & SUN, Y. 2018. High-performance semitransparent ternary organic solar cells. *Advanced Functional Materials*, 28, 1800627.
- XIONG, S., HU, L., HU, L., SUN, L., QIN, F., LIU, X., FAHLMAN, M. & ZHOU, Y. 2019. 12.5% Flexible nonfullerene solar cells by passivating the chemical interaction between the active layer and polymer interfacial layer. *Advanced Materials*, 31, 1806616.
- XU, G., SHEN, L., CUI, C., WEN, S., XUE, R., CHEN, W., CHEN, H., ZHANG, J., LI, H., LI, Y. & LI, Y. 2017. High-performance colorful semitransparent polymer solar cells with ultrathin hybrid-metal electrodes and fine-tuned dielectric mirrors. *Advanced Functional Materials*, 27, 1605908.
- XU, X., FENG, K., BI, Z., MA, W., ZHANG, G. & PENG, Q. 2019. Single-junction polymer solar cells with 16.35% efficiency enabled by a platinum(II) complexation strategy. *Advanced Materials*, 31, 1901872.
- YAN, C., BARLOW, S., WANG, Z., YAN, H., JEN, A. K. Y., MARDER, S. R. & ZHAN, X. 2018. Non-fullerene acceptors for organic solar cells. *Nature Reviews Materials*, 3, 18003.
- YAN, T., SONG, W., HUANG, J., PENG, R., HUANG, L. & GE, Z. 2019. 16.67% rigid and 14.06% flexible organic solar cells enabled by ternary heterojunction strategy. *Advanced Materials*, 31, 1902210.
- YANG, F., SHTEIN, M. & FORREST, S. R. 2005. Controlled growth of a molecular bulk heterojunction photovoltaic cell. *Nature Materials*, 4, 37-41.
- YANG, L., ZHANG, T., ZHOU, H., PRICE, S. C., WILEY, B. J. & YOU, W. 2011. Solution-processed flexible polymer solar cells with silver nanowire electrodes. *ACS Applied Materials & Interfaces*, 3, 4075-4084.
- YANG, X., HU, X., WANG, Q., XIONG, J., YANG, H., MENG, X., TAN, L., CHEN, L. & CHEN, Y. 2017. Large-scale stretchable semiembedded copper nanowire

transparent conductive films by an electrospinning template. *ACS Applied Materials & Interfaces*, 9, 26468-26475.

YANG, X., VAN DUREN, J. K. J., JANSSEN, R. A. J., MICHELS, M. A. J. & LOOS, J. 2004. Morphology and thermal stability of the active layer in poly(p-phenylenevinylene)/methanofullerene plastic photovoltaic devices. *Macromolecules*, 37, 2151-2158.

YAO, M., LI, T., LONG, Y., SHEN, P., WANG, G., LI, C., LIU, J., GUO, W., WANG, Y., SHEN, L. & ZHAN, X. 2020. Color and transparency-switchable semitransparent polymer solar cells towards smart windows. *Science Bulletin*, 65, 217-224.

YEON, C., YUN, S. J., KIM, J. & LIM, J. W. 2015. PEDOT:PSS films with greatly enhanced conductivity via nitric acid treatment at room temperature and their application as Pt/TCO-free counter electrodes in dye-sensitized solar cells. *Advanced Electronic Materials*, 1, 1500121.

YIN, Z., CHEN, S. & ZHENG, Q. 2014. Inverted organic solar cells (OSCs). In: HUANG, H. & HUANG, J. (eds.) *Organic and Hybrid Solar Cells*. Cham: Springer International Publishing.

YIN, Z., WEI, J. & ZHENG, Q. 2016. Interfacial materials for organic solar cells: recent advances and perspectives. *Advanced Science*, 3, 1500362.

YIP, H. L. & JEN, A. K. Y. 2012. Recent advances in solution-processed interfacial materials for efficient and stable polymer solar cells. *Energy & Environmental Science*, 5, 5994-6011.

YOU, H., ZHANG, J., ZHANG, Z., ZHANG, C., LIN, Z., CHANG, J., HAN, G., ZHANG, J., LU, G. & HAO, Y. 2017. Low temperature aqueous solution-processed ZnO and polyethylenimine ethoxylated cathode buffer bilayer for high performance flexible inverted organic solar cells. *Energies*, 10, 494.

- YU, G., GAO, J., HUMMELEN, J. C., WUDL, F. & HEEGER, A. J. 1995. Polymer photovoltaic cells: enhanced efficiencies via a network of internal donor-acceptor heterojunctions. *Science*, 270, 1789-1791.
- YU, Z., LI, L., ZHANG, Q., WEILI, H. & PEI, Q. 2011. Silver nanowire-polymer composite electrodes for efficient polymer solar cells. *Advanced Materials*, 23, 4453-4457.
- YUAN, J., ZHANG, Y., ZHOU, L., ZHANG, G., YIP, H. L., LAU, T. K., LU, X., ZHU, C., PENG, H., JOHNSON, P. A., LECLERC, M., CAO, Y., ULANSKI, J., LI, Y. & ZOU, Y. 2019. Single-junction organic solar cell with over 15% efficiency using fused-ring acceptor with electron-deficient core. *Joule*, 3, 1140-1151.
- YUSOFF, A. R. B. M., LEE, S. J., SHNEIDER, F. K., SILVA, W. J. D. & JANG, J. 2014. High-performance semitransparent tandem solar cell of 8.02% conversion efficiency with solution-processed graphene mesh and laminated Ag nanowire top electrodes. *Advanced Energy Materials*, 4, 1301989.
- ZENG, H., ZHU, X., LIANG, Y. & GUO, X. 2015. Interfacial layer engineering for performance enhancement in polymer solar cells. *Polymers*, 7, 333-372.
- ZHANG, F., ZHUO, Z., ZHANG, J., WANG, X., XU, X., WANG, Z., XIN, Y., WANG, J., WANG, J., TANG, W., XU, Z. & WANG, Y. 2012. Influence of PC60BM or PC70BM as electron acceptor on the performance of polymer solar cells. *Solar Energy Materials and Solar Cells*, 97, 71-77.
- ZHANG, H., WANG, C., LI, X., JING, J., SUN, Y. & LIU, Y. 2017. The effect of processing conditions on performance of small-molecule organic solar cells. *Solar Energy*, 157, 71-80.
- ZHANG, J., KAN, B., PEARSON, A. J., PARNELL, A. J., COOPER, J. F. K., LIU, X. K., CONAGHAN, P. J., HOPPER, T. R., WU, Y., WAN, X., GAO, F., GREENHAM, N. C., BAKULIN, A. A., CHEN, Y. & FRIEND, R. H. 2018a. Efficient non-fullerene organic solar cells employing sequentially deposited donor-acceptor layers. *Journal of Materials Chemistry A*, 6, 18225-18233.

- ZHANG, J., XU, G., TAO, F., ZENG, G., ZHANG, M., YANG, Y., LI, Y. & LI, Y. 2019. Highly efficient semitransparent organic solar cells with color rendering index approaching 100. *Advanced Materials*, 31, 1807159.
- ZHANG, M., GUO, X., MA, W., ADE, H. & HOU, J. 2015. A large-bandgap conjugated polymer for versatile photovoltaic applications with high performance. *Advanced Materials*, 27, 4655-4660.
- ZHANG, S., QIN, Y., ZHU, J. & HOU, J. 2018b. Over 14% efficiency in polymer solar cells enabled by a chlorinated polymer donor. *Advanced Materials*, 30, 1800868.
- ZHANG, W., ZHAO, B., HE, Z., ZHAO, X., WANG, H., YANG, S., WU, H. & CAO, Y. 2013. High-efficiency ITO-free polymer solar cells using highly conductive PEDOT:PSS/surfactant bilayer transparent anodes. *Energy & Environmental Science*, 6, 1956-1964.
- ZHANG, Z. & LI, Y. 2015. Side-chain engineering of high-efficiency conjugated polymer photovoltaic materials. *Science China Chemistry*, 58, 192-209.
- ZHANG, Z., QI, B., JIN, Z., CHI, D., QI, Z., LI, Y. & WANG, J. 2014. Perylene diimides: a thickness-insensitive cathode interlayer for high performance polymer solar cells. *Energy & Environmental Science*, 7, 1966-1973.
- ZHANG, Z. & WANG, J. 2012. Structures and properties of conjugated donor-acceptor copolymers for solar cell applications. *Journal of Materials Chemistry*, 22, 4178-4187.
- ZHAO, F., DAI, S., WU, Y., ZHANG, Q., WANG, J., JIANG, L., LING, Q., WEI, Z., MA, W., YOU, W., WANG, C. & ZHAN, X. 2017a. Single-junction binary-blend nonfullerene polymer solar cells with 12.1% efficiency. *Advanced Materials*, 29, 1700144.
- ZHAO, G., KIM, S. M., LEE, S. G., BAE, T. S., MUN, C. W., LEE, S., YU, H., LEE, G. H., LEE, H. S., SONG, M. & YUN, J. 2016. Bendable solar cells from stable,

flexible, and transparent conducting electrodes fabricated using a nitrogen-doped ultrathin copper film. *Advanced Functional Materials*, 26, 4180-4191.

ZHAO, G., SONG, M., CHUNG, H. S., KIM, S. M., LEE, S. G., BAE, J. S., BAE, T. S., KIM, D., LEE, G. H., HAN, S. Z., LEE, H. S., CHOI, E. A. & YUN, J. 2017c. Optical transmittance enhancement of flexible copper film electrodes with a wetting layer for organic solar cells. *ACS Applied Materials & Interfaces*, 9, 38695-38705.

ZHAO, G., WANG, W., BAE, T. S., LEE, S. G., MUN, C., LEE, S., YU, H., LEE, G. H., SONG, M. & YUN, J. 2015. Stable ultrathin partially oxidized copper film electrode for highly efficient flexible solar cells. *Nature Communications*, 6, 8830.

ZHAO, W., LI, S., YAO, H., ZHANG, S., ZHANG, Y., YANG, B. & HOU, J. 2017b. Molecular optimization enables over 13% efficiency in organic solar cells. *Journal of the American Chemical Society*, 139, 7148-7151.

ZHENG, Z., HU, Q., ZHANG, S., ZHANG, D., WANG, J., XIE, S., WANG, R., QIN, Y., LI, W., HONG, L., LIANG, N., LIU, F., ZHANG, Y., WEI, Z., TANG, Z., RUSSELL, T. P., HOU, J. & ZHOU, H. 2018. A highly efficient non-fullerene organic solar cell with a fill factor over 0.80 enabled by a fine-tuned hole-transporting layer. *Advanced Materials*, 30, 1801801.

ZHOU, H., YANG, L. & YOU, W. 2012. Rational design of high performance conjugated polymers for organic solar cells. *Macromolecules*, 45, 607-632.

ZHOU, L., LIN, H., CHEN, X., DU, X., ZHENG, C., TAO, S. & ZHANG, X. 2017. Novel brominated compounds using in binary additives based organic solar cells to achieve high efficiency over 10.3%. *Organic Electronics*, 50, 507-514.

ZHOU, R., JIANG, Z., YANG, C., YU, J., FENG, J., ADIL, M. A., DENG, D., ZOU, W., ZHANG, J., LU, K., MA, W., GAO, F. & WEI, Z. 2019. All-small-molecule organic solar cells with over 14% efficiency by optimizing hierarchical morphologies. *Nature Communications*, 10, 5393.

ZHOU, Z., XU, S., SONG, J., JIN, Y., YUE, Q., QIAN, Y., LIU, F., ZHANG, F. & ZHU, X. 2018. High-efficiency small-molecule ternary solar cells with a hierarchical morphology enabled by synergizing fullerene and non-fullerene acceptors. *Nature Energy*, 3, 952-959.

ZHU, J., KE, Z., ZHANG, Q., WANG, J., DAI, S., WU, Y., XU, Y., LIN, Y., MA, W., YOU, W. & ZHAN, X. 2018. Naphthodithiophene-based nonfullerene acceptor for high-performance organic photovoltaics: effect of extended conjugation. *Advanced Materials*, 30, 1704713.

Appendix A: Supporting Information

Table A.1 Comparison of PCE values of flexible OSCs with different PEDOT:PSS-based FTEs.

FTEs	Photoactive Layer	PCE [%]	Reference
PEDOT:PSS	PTB7-Th:PC ₇₁ BM	7.70	(Kim et al., 2015)
PEDOT:PSS	PBDTT-S-TT:PC ₇₁ BM	6.42	(Fan et al., 2016)
PEDOT:PSS	P3HT:PCBM	2.87	(Worfolk et al., 2015)
PEDOT:PSS	P3HT:ICBA	3.33	(Meng et al., 2015)
PEDOT:PSS	P3HT:PCBM	4.20	(Kaltenbrunner et al., 2012)
PEDOT:PSS	PfBT4T-2OD:PC ₆₁ BM:PC ₇₁ BM	6.60	(Czolk et al., 2016)
PEDOT:PSS	PBDB-T-2F:Y6:PC ₇₁ BM	14.1	(Yan et al., 2019)
PEDOT:PSS/Ag island	PTB7-Th:PC ₇₁ BM	9.90	(Kang et al., 2015)
PEDOT:PSS/Ag grid	PTB7-Th:PC ₇₁ BM	6.58	(Wang et al., 2017a)
PEDOT:PSS/Ag mesh	PTB7:PC ₇₁ BM	6.73	(Kim et al., 2016)
Ag-mesh/PEDOT:PSS	PBDB-T:PTB7-Th:IHIC	8.76	(Zhang et al., 2019)
Graphene/PEDOT:PSS	PTB7:PC ₇₁ BM	7.10	(Park et al., 2014a)
PEDOT:PSS	PBDB-T-2Cl:IT-4F	12.4	(Peng et al., 2019)
D-PEDOT:PSS	PBDB-T-2F:Y6	14.2	This Work

Table A.2 Comparison of PCE values of flexible OSCs with different metal-based FTEs.

FTEs	Photoactive Layer	PCE [%]	Reference
ZnO/Cu(N1) 8.0 nm/ZnO	PTB7:PC ₇₁ BM	6.70	(Zhao et al., 2016)
ZnO/Cu 9.5 nm on Cu(O)/ZnO	PTB7:PC ₇₁ BM	7.29	(Zhao et al., 2017c)
TiO ₂ /ZnO/Ag/ZnO	PBDB-T:ITIC:PC ₇₁ BM	10.5	(Liu et al., 2017a)
ZnO/Cu (O=5%) 7 nm/ZnO	PTB7-Th:PC ₇₁ BM	7.65	(Zhao et al., 2015)
ZnO/Cu(N1) 6.5 nm/ZnO	PTB7:PC ₇₁ BM	7.10	(Zhao et al., 2016)
Ag grid	PTB7-Th:PC ₇₁ BM	6.43	(Lu et al., 2017)
Ag NW	PTB7-Th:PC ₇₁ BM	8.75	(Seo et al., 2017)
Cu NW	PTB7-Th:PC ₇₁ BM	4.60	(Yang et al., 2017)
Ag NWs	PBnDT-DTffBT:PC ₇₁ BM	2.80	(Yang et al., 2011)
Ag NWs	P3HT:PC ₇₁ BM	3.28	(Yu et al., 2011)
Ag NWs	PTB7-F20:PC ₇₁ BM	5.02	(Song et al., 2013)
Ag Mesh	PTzNTz:PC ₇₁ BM	8.30	(Jiang et al., 2018)
Ag Mesh	PTB7:PC ₇₁ BM	6.73	(Kim et al., 2016)
Ag NWs	PTB7:PC ₇₁ BM	6.17	(Seo et al., 2015)
Ultrathin Ag	PBDTT-F-TT:PC ₇₁ BM	10.4	(Huang et al., 2015)
ITO	PNTz4T: PC ₇₁ BM	7.90	(Jinno et al., 2017)
ITO	PTB7-Th:IEICO-4F	12.5	(Xiong et al., 2019)
ITO	PTB7:PC ₇₁ BM	8.12	(You et al., 2017)
ITO	PSBTBT:PC ₇₁ BM/P3HT:ICBA	8.70	(Chang et al., 2015)
ITO	PBDB-T-2F:Y6	13.5	(Lei et al., 2019)

Table A.3 Comparison of PCE values of flexible OSCs with different carbon-based FTEs.

FTEs	Photoactive Layer	PCE [%]	Reference
Graphene	PTB7:PC ₇₁ BM	7.10	(Park et al., 2014a)
Carbon nanotube	PTB7:PC ₇₁ BM	3.91	(Jeon et al., 2015)

Table A.4 Summaries of PCE and AVT values of recently reported rigid ST-OSCs – *Part I*.

Classifications	Photoactive Layer	PCE [%]	AVT [%]	Reference
Binary	PTB7:PC ₇₁ BM	6.40	16.9	(Xu et al., 2017)
Binary	PTB7-Th:PC ₇₁ BM	7.00	12.2	(Xu et al., 2017)
Binary	PTB7-Th:IEICO-4Cl	6.97	33.5	(Cui et al., 2017)
Binary	PTB7-Th:IEICO-4Cl	7.47	31.8	(Cui et al., 2017)
Binary	PTB7-Th:IEICO-4Cl	7.91	28.2	(Cui et al., 2017)
Binary	PTB7-Th:IEICO-4Cl	8.38	25.6	(Cui et al., 2017)
Binary	PTB7-Th:BT-CIC	7.10	43.0	(Li et al., 2017b)
Binary	PTB7-Th:BT-CIC	7.70	33.0	(Li et al., 2017b)
Binary	PTB7-Th:BT-CIC	8.20	26.0	(Li et al., 2017b)
Binary	PTB7-Th:ATT-2	6.30	45.0	(Liu et al., 2017b)
Binary	PTB7-Th:ATT-2	7.74	37.0	(Liu et al., 2017b)
Binary	PBDTTT-C-T:PC ₇₁ BM	6.22	21.3	(Chen et al., 2012)
Binary	PTB7-Th:PC ₇₁ BM	6.78	20.7	(Shi et al., 2017)
Binary	PTB7-Th:PC ₇₁ BM	6.05	30.4	(Shi et al., 2017)
Binary	PBDB-T:ITIC	7.40	25.2	(Upama et al., 2017)
Binary	PTB7-Th:IHIC	9.77	36.0	(Wang et al., 2017c)
Binary	PTB7-Th:IUIC	10.2	31.0	(Jia et al., 2018)
Binary	PFBDB-T:C8-ITIC	10.4	19.1	(Sun et al., 2019)
Binary	PFBDB-T:C8-ITIC	9.80	22.0	(Sun et al., 2019)
Binary	PBFTT:IT-4Cl	7.90	37.3	(Su et al., 2019)
Binary	PBFTT:IT-4Cl	8.60	33.2	(Su et al., 2019)
Binary	PBFTT:IT-4Cl	9.10	27.6	(Su et al., 2019)
Binary	J71:IHIC	8.26	28.1	(Zhang et al., 2019)
Binary	J71:IHIC	8.48	21.5	(Zhang et al., 2019)
Binary	PTB7-Th:IHIC	8.38	27.9	(Zhang et al., 2019)
Binary	PTB7-Th:IHIC	8.48	20.5	(Zhang et al., 2019)
Binary	PTB7-Th:IEICO-4F	10.7	29.4	(Xia et al., 2019)
Binary	PTB7-Th:IEICO-4F	11.0	20.6	(Xia et al., 2019)
Binary	PTB7-Th:IEICO-4F	10.8	29.5	(Xia et al., 2019)
Binary	PTB7-Th:IEICO-4F	11.3	21.5	(Xia et al., 2019)
Binary	PTB7-Th:PC ₇₁ BM	8.45	29.2	(Xia et al., 2019)

Table A.5 Summaries of PCE and AVT values of recently reported rigid ST-OSCs – *Part 2*.

Classifications	Photoactive Layer	PCE [%]	AVT [%]	Reference
Binary	PTB7-Th:PC ₇₁ BM	8.81	21.8	(Xia et al., 2019)
Binary	PTB7-Th:PC ₇₁ BM	8.32	31.4	(Xia et al., 2019)
Binary	PTB7-Th:PC ₇₁ BM	8.65	25.0	(Xia et al., 2019)
Binary	PTB7-Th:PC ₇₁ BM	8.41	30.8	(Du et al., 2019)
Binary	PTB7-Th:PC ₇₁ BM	9.71	15.9	(Du et al., 2019)
Binary	PBDB-T-2F:Y14	12.7	23.7	(Luo et al., 2019)
Binary	PBDB-T-2F:ITIC-4F	11.2	26.2	(Bai et al., 2019)
Binary	PBDB-T-2F:Y6	12.9	25.6	(Bai et al., 2019)
Binary	J101:ZITI	11.0	21.7	(Wang et al., 2019b)
Binary	PTB7-Th:ACS8	11.1	28.6	(Chen et al., 2019)
Binary	PTB7-Th:FOIC	10.2	25.4	(Yao et al., 2020)
Binary	PBDB-T-2F:ID-4Cl	6.99	43.7	(Li et al., 2019)
Ternary	PBT1-S:PTB7-Th:PC ₇₁ BM	9.20	20.0	(Xie et al., 2018)
Ternary	PBT1-S:PTB7-Th:PC ₇₁ BM	8.10	33.8	(Xie et al., 2018)
Ternary	PBT1-S:PTB7-Th:PC ₇₁ BM	5.00	44.8	(Xie et al., 2018)
Ternary	PTB7-Th:CO ₈ DFIC:IEICO-4F	6.78	24.2	(Ma et al., 2018)
Ternary	PTB7-Th:CO ₈ DFIC:IEICO-4F	8.23	20.8	(Ma et al., 2018)
Ternary	PTB7-Th:CO ₈ DFIC:IEICO-4F	9.37	17.2	(Ma et al., 2018)
Ternary	J71:PTB7-Th:IHIC	8.93	25.8	(Zhang et al., 2019)
Ternary	J71:PTB7-Th:IHIC	9.37	21.4	(Zhang et al., 2019)
Ternary	PCDTBT:PC ₇₁ BM:ITIC	4.02	39.2	(Sano et al., 2019)
Tandem	PIDT-phanQ:PC ₇₁ BM PIDT-phanQ:PC ₆₁ BM	7.40	40.0	(Chang et al., 2014)
Tandem	PBDTT-FDPP-C ₁₂ :PC ₆₁ BM PBDTT-SeDPP:PCBM	6.40	43.0	(Chen et al., 2013)
Tandem	PBDTT-FDPP-C ₁₂ :PC ₆₁ BM PBDTT-SeDPP:PCBM	7.30	30.0	(Chen et al., 2013)
Tandem	PSEHTT:ICBA PBDTT-DPP: PC ₇₁ BM	8.02	44.9	(Yusoff et al., 2014)
Tandem	P3TEA:FTTB-PDI ₄ PTB7-Th:IEICS-4F	10.5	20.0	(Chen et al., 2018)

Table A.6 Summaries of PCE and AVT values of recently reported flexible ST-OSCs.

Classifications	Photoactive Layer	PCE [%]	AVT [%]	Reference
Binary	PTB7-Th:PC ₇₁ BM	6.40	11.5	(Xu et al., 2017)
Binary	PSEHTT:ICBA	6.87	36.0	(Silva et al., 2013)
Binary	PTB7-Th:IEICO-4F	10.0	34.2	(Liu et al., 2019c)
Binary	PTB7-Th:FOIC	9.26	31.0	(Liu et al., 2019c)
Binary	PTB7-Th:F8IC	8.92	34.3	(Liu et al., 2019c)
Binary	PBDB-T-2F:Y6	9.22	24.0	This Work
Binary	PBDB-T-2F:Y6	10.5	21.0	This Work
Binary	PBDB-T-2F:Y6	11.7	18.0	This Work
Binary	PBDB-T-2F:Y6	12.6	17.0	This Work
Ternary	PBDB-T:PTB7-Th:IHIC	8.33	27.5	(Zhang et al., 2019)
Ternary	PBDB-T:PTB7-Th:IHIC	8.76	20.6	(Zhang et al., 2019)

Appendix B: Other Experimental Work

Table B.1 Raw data of conventional PBDB-T:IT-M -based OSCs.

Configuration : ITO PEDOT:PSS PBDB-T : IT-M PDINO Al Addition : none				
Devices No.	V_{oc} [V]	J_{sc} [mA cm⁻²]	FF [%]	PCE [%]
1	0.928	16.1	71.7	10.7
2	0.931	16.4	71.8	10.9
3	0.930	16.4	70.9	10.8
4	0.929	16.3	71.0	10.7
5	0.930	16.4	70.8	10.8
6	0.926	16.3	71.1	10.7
7	0.928	16.6	71.2	11.0
8	0.932	16.3	72.0	11.0
9	0.931	16.3	71.9	10.9
Avg.	0.930	16.3	71.4	10.8

*** Photoactive layer parameters:**

- PBDB-T : IT-M ratio (1:1)
- Total 20 mg mL⁻¹ in CB
- 0.7% DIO
- Spin-coated at 2150 rpm and annealed at 120°C for 10 minutes

*** HTL parameters:**

- Spin-coated at 3000 rpm and annealed at 150°C for 15 minutes

*** ETL parameters:**

- Spin-coated at 3000 rpm without annealing

Table B.2 Raw data of conventional PBDB-T:IT-M:PBI-Por -based OSCs (1% addition).

Configuration : ITO PEDOT:PSS PBDB-T : IT-M : PBI-Por PDINO Al Addition : 1% PBI-Por				
Devices No.	V_{oc} [V]	J_{sc} [mA cm⁻²]	FF [%]	PCE [%]
1	0.916	14.7	66.6	8.94
2	0.918	15.8	68.7	9.95
3	0.915	14.8	65.1	8.84
4	0.913	15.0	65.0	8.92
5	0.913	15.0	65.7	8.98
6	0.915	15.0	64.2	8.80
7	0.912	15.1	65.2	8.99
8	0.913	15.0	64.3	8.83
9	0.913	15.3	63.5	8.88
Avg.	0.914	15.1	65.4	9.02

*** Photoactive layer parameters:**

- PBDB-T : IT-M : PBI-Por ratio (1:0.99:0.01)
- Total 20 mg mL⁻¹ in CB
- 0.7% DIO
- Spin-coated at 2150 rpm and annealed at 120°C for 10 minutes

*** HTL parameters:**

- Spin-coated at 3000 rpm and annealed at 150°C for 15 minutes

*** ETL parameters:**

- Spin-coated at 3000 rpm without annealing

Table B.3 Raw data of conventional PBDB-T:IT-M:PBI-Por -based OSCs (5% addition).

Configuration : ITO PEDOT:PSS PBDB-T : IT-M : PBI-Por PDINO Al				
Addition : 5% PBI-Por				
Devices No.	V_{oc} [V]	J_{sc} [mA cm ⁻²]	FF [%]	PCE [%]
1	0.895	15.5	67.1	9.30
2	0.892	15.4	66.9	9.19
3	0.889	15.6	66.4	9.22
4	0.890	15.4	66.8	9.16
5	0.895	15.3	67.8	9.26
6	0.894	15.3	67.8	9.30
7	0.869	14.7	62.5	7.99
8	0.868	15.0	62.9	8.18
9	0.864	14.8	63.0	8.05
Avg.	0.884	15.2	65.7	8.85

* Photoactive layer parameters:				
- PBDB-T : IT-M : PBI-Por ratio (1:0.95:0.05)				
- Total 20 mg mL ⁻¹ in CB				
- 0.7% DIO				
- Spin-coated at 2150 rpm and annealed at 120°C for 10 minutes				
* HTL parameters:				
- Spin-coated at 3000 rpm and annealed at 150°C for 15 minutes				
* ETL parameters:				
- Spin-coated at 3000 rpm without annealing				

Table B.4 Summary of conventional PBDB-T:IT-M:PBI-Por -based OSCs.

Devices	V_{oc} [V]	J_{sc} [mA cm ⁻²]	FF [%]	PCE_{max} (avg.)^a [%]
0%	0.932	16.3	72.0	11.0 (10.8)
1%	0.918	15.8	68.7	9.95 (9.02)
5%	0.895	15.5	67.1	9.30 (8.85)

^a Average PCE was obtained from 9 independent devices

Table B.5 Raw data of conventional PBDB-T:IT-M:PBD -based OSCs (1% dopant).

Configuration : ITO PEDOT:PSS PBDB-T : IT-M : PBD PDINO Al Addition : 1% PBD as dopant				
Devices No.	V_{oc} [V]	J_{sc} [mA cm ⁻²]	FF [%]	PCE [%]
1	0.945	15.9	71.1	10.7
2	0.942	16.2	70.2	10.7
3	0.938	16.0	70.3	10.6
4	0.941	16.2	70.4	10.8
5	0.937	16.1	70.6	10.6
6	0.938	16.3	69.9	10.7
7	0.939	16.0	68.9	10.4
8	0.934	16.4	69.1	10.6
9	0.933	16.2	69.6	10.6
Avg.	0.939	16.1	70.0	10.6

* Photoactive layer parameters: <ul style="list-style-type: none"> - PBDB-T : IT-M : PBD ratio (1:1:0.01) - Total 20 mg mL⁻¹ in CB - 0.7% DIO - Spin-coated at 2150 rpm and annealed at 120°C for 10 minutes 				
* HTL parameters: <ul style="list-style-type: none"> - Spin-coated at 3000 rpm and annealed at 150°C for 15 minutes 				
* ETL parameters: <ul style="list-style-type: none"> - Spin-coated at 3000 rpm without annealing 				

Table B.6 Summary of conventional PBDB-T:IT-M:PBD -based OSCs.

Devices	V_{oc} [V]	J_{sc} [mA cm ⁻²]	FF [%]	PCE_{max} (avg.)^a [%]
0%	0.932	16.3	72.0	11.0 (10.8)
1% dopant	0.945	15.9	71.1	10.7 (10.6)

^a Average PCE was obtained from 9 independent devices

Table B.7 Raw data of inverted PBDB-T:IT-M -based OSCs.

Configuration : ITO ZnO PBDB-T : IT-M MoO ₃ Ag				
Addition : none				
Devices No.	V_{oc} [V]	J_{sc} [mA cm⁻²]	FF [%]	PCE [%]
1	0.933	15.6	74.4	10.8
2	0.933	15.4	73.2	10.5
3	0.932	15.5	73.7	10.7
4	0.929	15.7	73.1	10.7
5	0.936	15.8	71.8	10.6
6	0.933	15.9	71.3	10.6
7	0.931	15.9	71.6	10.6
8	0.936	15.8	72.3	10.7
9	0.933	15.7	71.9	10.5
Avg.	0.933	15.7	72.6	10.6

*** Photoactive layer parameters:**

- PBDB-T : IT-M ratio (1:1)
- Total 20 mg mL⁻¹ in CB
- 0.7% DIO
- Spin-coated at 1900 rpm and annealed at 120°C for 10 minutes

*** HTL parameters:**

- Thickness of 10 nm

*** ETL parameters:**

- 0.5 M ZnO precursor solution
- Spin-coated at 4000 rpm and annealed at 150°C for 30 minutes

Table B.8 Raw data of inverted PBDB-T:IT-M:TFT-CN -based OSCs (1% addition).

Configuration : ITO ZnO PBDB-T : IT-M : TFT-CN MoO ₃ Ag Addition : 1% TFT-CN				
Devices No.	V_{oc} [V]	J_{sc} [mA cm⁻²]	FF [%]	PCE [%]
1	0.851	6.76	48.3	2.78
2	0.847	6.95	47.3	2.79
3	0.848	5.52	48.5	2.27
4	0.853	6.04	49.1	2.53
5	0.851	5.86	48.9	2.44
6	0.855	5.85	47.5	2.38
7	0.856	6.28	48.3	2.60
8	0.848	5.92	48.8	2.45
9	0.849	5.72	48.7	2.36
Avg.	0.851	6.10	48.4	2.51

*** Photoactive layer parameters:**

- PBDB-T : IT-M : TFT-CN ratio (1:0.99:0.01)
- Total 20 mg mL⁻¹ in CB
- 0.7% DIO
- Spin-coated at 1900 rpm and annealed at 120°C for 10 minutes

*** HTL parameters:**

- Thickness of 10 nm

*** ETL parameters:**

- 0.5 M ZnO precursor solution
- Spin-coated at 4000 rpm and annealed at 150°C for 30 minutes

Table B.9 Raw data of inverted PBDB-T:IT-M:TFT-CN -based OSCs (6% addition).

Configuration : ITO ZnO PBDB-T : IT-M : TFT-CN MoO ₃ Ag Addition : 6% TFT-CN				
Devices No.	V_{oc} [V]	J_{sc} [mA cm⁻²]	FF [%]	PCE [%]
1	0.616	1.65	42.0	0.426
2	0.610	1.72	41.8	0.438
3	0.611	1.58	41.5	0.401
4	0.613	1.65	41.5	0.420
5	0.609	1.58	41.2	0.396
6	0.616	1.56	42.1	0.406
7	0.613	1.60	41.7	0.408
8	0.620	1.67	42.1	0.436
9	0.626	1.74	42.4	0.462
Avg.	0.615	1.64	41.8	0.422

*** Photoactive layer parameters:**

- PBDB-T : IT-M : TFT-CN ratio (1:0.94:0.06)
- Total 20 mg mL⁻¹ in CB
- 0.7% DIO
- Spin-coated at 1900 rpm and annealed at 120°C for 10 minutes

*** HTL parameters:**

- Thickness of 10 nm

*** ETL parameters:**

- 0.5 M ZnO precursor solution
- Spin-coated at 4000 rpm and annealed at 150°C for 30 minutes

Table B.10 Raw data of inverted PBDB-T:IT-M:TFT-CN -based OSCs (1% dopant).

Configuration : ITO ZnO PBDB-T : IT-M : TFT-CN MoO ₃ Ag Addition : 1% TFT-CN as dopant				
Devices No.	V_{oc} [V]	J_{sc} [mA cm⁻²]	FF [%]	PCE [%]
1	0.830	4.39	46.3	1.69
2	0.833	4.42	46.3	1.70
3	0.835	4.61	47.4	1.82
4	0.822	4.32	48.3	1.72
5	0.828	4.58	46.0	1.75
6	0.837	4.52	48.1	1.82
7	0.859	4.51	49.0	1.90
8	0.850	4.49	49.6	1.89
9	0.853	4.70	49.1	1.97
Avg.	0.839	4.50	47.8	1.81

*** Photoactive layer parameters:**

- PBDB-T : IT-M : TFT-CN ratio (1:1:0.01)
- Total 20 mg mL⁻¹ in CB
- 0.7% DIO
- Spin-coated at 1900 rpm and annealed at 120°C for 10 minutes

*** HTL parameters:**

- Thickness of 10 nm

*** ETL parameters:**

- 0.5 M ZnO precursor solution
- Spin-coated at 4000 rpm and annealed at 150°C for 30 minutes

Table B.11 Raw data of inverted PBDB-T:IT-M:TFT-CN -based OSCs (6% dopant).

Configuration : ITO ZnO PBDB-T : IT-M : TFT-CN MoO ₃ Ag				
Addition : 6% TFT-CN as dopant				
Devices No.	V_{oc} [V]	J_{sc} [mA cm ⁻²]	FF [%]	PCE [%]
1	0.625	2.01	43.8	0.551
2	0.626	2.12	44.1	0.587
3	0.636	2.13	43.5	0.591
4	0.644	2.15	44.0	0.611
5	0.624	2.07	43.7	0.563
6	0.627	1.99	43.2	0.539
7	0.640	2.02	44.4	0.574
8	0.633	1.97	44.0	0.549
9	0.645	2.10	44.2	0.596
Avg.	0.633	2.06	43.9	0.573

* Photoactive layer parameters:				
- PBDB-T : IT-M : TFT-CN ratio (1:1:0.06)				
- Total 20 mg mL ⁻¹ in CB				
- 0.7% DIO				
- Spin-coated at 1900 rpm and annealed at 120°C for 10 minutes				
* HTL parameters:				
- Thickness of 10 nm				
* ETL parameters:				
- 0.5 M ZnO precursor solution				
- Spin-coated at 4000 rpm and annealed at 150°C for 30 minutes				

Table B.12 Summary of inverted PBDB-T:IT-M:TFT-CN -based OSCs.

Devices	V_{oc} [V]	J_{sc} [mA cm ⁻²]	FF [%]	PCE_{max} (avg.)^a [%]
0%	0.933	15.6	74.4	10.8 (10.6)
1%	0.847	6.95	47.3	2.79 (2.51)
6%	0.626	1.74	42.4	0.462 (0.422)
1% dopant	0.853	4.70	49.1	1.97 (1.81)
6% dopant	0.644	2.15	44.0	0.611 (0.573)

^a Average PCE was obtained from 9 independent devices

Table B.13 Raw data of conventional PBDB-T-2F:IT-4F -based OSCs.

Configuration : ITO PEDOT:PSS PBDB-T-2F : IT-4F PDINO Al				
Addition : none				
Devices No.	V_{oc} [V]	J_{sc} [mA cm⁻²]	FF [%]	PCE [%]
1	0.866	20.8	75.2	13.5
2	0.865	20.0	74.9	12.9
3	0.868	19.7	75.4	12.9
4	0.863	20.2	75.1	13.1
5	0.871	19.8	74.5	12.9
6	0.860	19.8	75.4	12.8
7	0.864	20.9	74.9	13.5
8	0.866	19.7	75.2	12.9
9	0.855	21.2	73.9	13.4
Avg.	0.864	20.3	74.8	13.1

*** Photoactive layer parameters:**

- PBDB-T-2F : IT-4F ratio (1:1)
- Total 20 mg mL⁻¹ in CB
- 0.7% DIO
- Spin-coated at 1800 rpm and annealed at 100°C for 10 minutes

*** HTL parameters:**

- Spin-coated at 3000 rpm and annealed at 150°C for 15 minutes

*** ETL parameters:**

- Spin-coated at 3000 rpm without annealing

Table B.14 Raw data of conventional PBDB-T-2F:IT-4F:PBD -based OSCs (1% dopant).

Configuration : ITO PEDOT:PSS PBDB-T-2F : IT-4F : PBD PDINO Al Addition : 1% PBD as dopant					
Devices No.	V_{oc} [V]	J_{sc} [mA cm ⁻²]	FF [%]	PCE [%]	
1	0.855	18.5	72.7	11.5	
2	0.846	18.8	72.5	11.6	
3	0.848	18.9	71.2	11.4	
4	0.851	18.1	73.4	11.3	
5	0.845	18.3	73.5	11.4	
6	0.849	18.3	73.4	11.4	
7	0.844	18.6	73.5	11.5	
8	0.848	18.1	72.7	11.1	
9	0.846	18.1	73.7	11.3	
Avg.	0.848	18.4	73.0	11.4	

* Photoactive layer parameters: <ul style="list-style-type: none"> - PBDB-T-2F : IT-4F : PBD ratio (1:1:0.01) - Total 20 mg mL⁻¹ in CB - 0.7% DIO - Spin-coated at 1800 rpm and annealed at 100°C for 10 minutes 					
* HTL parameters: <ul style="list-style-type: none"> - Spin-coated at 3000 rpm and annealed at 150°C for 15 minutes 					
* ETL parameters: <ul style="list-style-type: none"> - Spin-coated at 3000 rpm without annealing 					

Table B.15 Summary of conventional PBDB-T-2F:IT-4F:PBD -based OSCs.

Devices	V_{oc} [V]	J_{sc} [mA cm ⁻²]	FF [%]	PCE_{max} (avg.)^a [%]
0%	0.866	20.8	75.2	13.5 (13.1)
1% dopant	0.846	18.8	72.5	11.6 (11.4)

^a Average PCE was obtained from 9 independent devices

Table B.16 Raw data of conventional PBDB-T-2F:IT-4F:g-C₃N₄ -based OSCs (1% dopant).

Configuration : ITO PEDOT:PSS PBDB-T-2F : IT-4F : g-C ₃ N ₄ PDINO Al Addition : 1% g-C ₃ N ₄ as dopant				
Devices No.	V_{oc} [V]	J_{sc} [mA cm ⁻²]	FF [%]	PCE [%]
1	0.853	19.6	73.5	12.3
2	0.854	19.9	72.0	12.3
3	0.857	19.8	72.6	12.3
4	0.853	19.8	73.6	12.5
5	0.858	19.6	73.0	12.3
6	0.852	19.5	73.5	12.2
7	0.858	19.6	73.0	12.3
8	0.857	19.4	73.0	12.1
9	0.844	20.2	73.5	12.5
Avg.	0.854	19.7	73.1	12.3

* Photoactive layer parameters: <ul style="list-style-type: none"> - PBDB-T-2F : IT-4F : g-C₃N₄ ratio (1:1:0.01) - Total 20 mg mL⁻¹ in CB - 0.7% DIO - Spin-coated at 1800 rpm and annealed at 100°C for 10 minutes 				
* HTL parameters: <ul style="list-style-type: none"> - Spin-coated at 3000 rpm and annealed at 150°C for 15 minutes 				
* ETL parameters: <ul style="list-style-type: none"> - Spin-coated at 3000 rpm without annealing 				

Table B.17 Summary of conventional PBDB-T-2F:IT-4F:g-C₃N₄ -based OSCs.

Devices	V_{oc} [V]	J_{sc} [mA cm ⁻²]	FF [%]	PCE_{max} (avg.)^a [%]
0%	0.866	20.8	75.2	13.5 (13.1)
1% dopant	0.853	19.8	73.6	12.5 (12.3)

^a Average PCE was obtained from 9 independent devices

Table B.18 Raw data of conventional PBDB-T-2F:Y6 -based OSCs.

Configuration : ITO PEDOT:PSS PBDB-T-2F : Y6 PDINO Al Addition : none				
Devices No.	V_{oc} [V]	J_{sc} [mA cm⁻²]	FF [%]	PCE [%]
1	0.837	25.7	73.9	15.9
2	0.835	25.6	73.7	15.8
3	0.834	25.6	73.8	15.8
4	0.838	25.9	75.0	16.3
5	0.837	25.8	74.9	16.2
6	0.835	25.8	74.9	16.2
7	0.839	25.6	73.9	15.9
8	0.837	25.6	73.5	15.7
9	0.835	24.7	76.1	15.7
Avg.	0.836	25.6	74.4	15.9

*** Photoactive layer parameters:**

- PBDB-T-2F : Y6 ratio (1:1.2)
- Total 16 mg mL⁻¹ in CF
- 0.5% CN
- Spin-coated at 2700 rpm and annealed at 110°C for 10 minutes

*** HTL parameters:**

- Spin-coated at 3000 rpm and annealed at 150°C for 15 minutes

*** ETL parameters:**

- Spin-coated at 3000 rpm without annealing

Table B.19 Raw data of conventional PBDB-T-2F:Y6:DRCN-5T -based OSCs (5% addition).

Configuration : ITO PEDOT:PSS PBDB-T-2F : Y6 : DRCN-5T PDINO Al Addition : 5% DRCN-5T				
Devices No.	V_{oc} [V]	J_{sc} [mA cm⁻²]	FF [%]	PCE [%]
1	0.855	24.7	73.8	15.6
2	0.841	24.4	76.0	15.6
3	0.840	24.4	75.9	15.6
4	0.843	25.0	74.8	15.8
5	0.841	25.0	74.8	15.7
6	0.840	25.0	74.8	15.7
7	0.842	25.2	74.5	15.8
8	0.841	25.2	74.9	15.9
9	0.840	25.2	74.8	15.8
Avg.	0.843	24.9	74.9	15.7

*** Photoactive layer parameters:**

- PBDB-T-2F : Y6 : DRCN-5T ratio (1:1.15:0.05)
- Total 16 mg mL⁻¹ in CF
- 0.5% CN
- Spin-coated at 2700 rpm and annealed at 110°C for 10 minutes

*** HTL parameters:**

- Spin-coated at 3000 rpm and annealed at 150°C for 15 minutes

*** ETL parameters:**

- Spin-coated at 3000 rpm without annealing

Table B.20 Raw data of conventional PBDB-T-2F:Y6:DRCN-5T -based OSCs (10% addition).

Configuration : ITO PEDOT:PSS PBDB-T-2F : Y6 : DRCN-5T PDINO Al Addition : 10% DRCN-5T				
Devices No.	V_{oc} [V]	J_{sc} [mA cm⁻²]	FF [%]	PCE [%]
1	0.834	25.8	72.9	15.7
2	0.846	24.8	73.6	15.5
3	0.844	24.8	73.6	15.4
4	0.855	25.0	73.5	15.7
5	0.853	25.0	73.6	15.7
6	0.851	25.0	73.7	15.7
7	0.848	24.5	74.1	15.4
8	0.846	24.5	73.8	15.3
9	0.853	25.2	73.1	15.7
Avg.	0.848	25.0	73.5	15.6

*** Photoactive layer parameters:**

- PBDB-T-2F : Y6 : DRCN-5T ratio (1:1.1:0.1)
- Total 16 mg mL⁻¹ in CF
- 0.5% CN
- Spin-coated at 2700 rpm and annealed at 110°C for 10 minutes

*** HTL parameters:**

- Spin-coated at 3000 rpm and annealed at 150°C for 15 minutes

*** ETL parameters:**

- Spin-coated at 3000 rpm without annealing

Table B.21 Raw data of conventional PBDB-T-2F:Y6:DRCN-5T -based OSCs (20% addition).

Configuration : ITO PEDOT:PSS PBDB-T-2F : Y6 : DRCN-5T PDINO Al				
Addition : 20% DRCN-5T				
Devices No.	V_{oc} [V]	J_{sc} [mA cm ⁻²]	FF [%]	PCE [%]
1	0.845	24.5	72.1	14.9
2	0.842	24.5	72.1	14.9
3	0.841	24.6	72.1	14.9
4	0.843	24.8	73.6	15.4
5	0.842	24.8	73.5	15.3
6	0.841	24.8	73.3	15.3
7	0.844	24.4	72.9	15.0
8	0.842	24.4	72.9	15.0
9	0.842	24.4	72.7	14.9
Avg.	0.842	24.6	72.8	15.1

* Photoactive layer parameters:				
- PBDB-T-2F : Y6 : DRCN-5T ratio (1:1:0.2)				
- Total 16 mg mL ⁻¹ in CF				
- 0.5% CN				
- Spin-coated at 2700 rpm and annealed at 110°C for 10 minutes				
* HTL parameters:				
- Spin-coated at 3000 rpm and annealed at 150°C for 15 minutes				
* ETL parameters:				
- Spin-coated at 3000 rpm without annealing				

Table B.22 Summary of conventional PBDB-T-2F:Y6:DRCN-5T -based OSCs.

Devices	V_{oc} [V]	J_{sc} [mA cm ⁻²]	FF [%]	PCE_{max} (avg.)^a [%]
0%	0.838	25.9	75.0	16.3 (15.9)
5%	0.841	25.2	74.9	15.9 (15.7)
10%	0.855	25.0	73.5	15.7 (15.6)
20%	0.843	24.8	73.6	15.4 (15.1)

^a Average PCE was obtained from 9 independent devices

Table B.23 Raw data of conventional PBDB-T-2F:Y6:M2 -based OSCs (1% dopant).

Configuration : ITO PEDOT:PSS PBDB-T-2F : Y6 : M2 PDINO Al Addition : 1% M2 as dopant				
Devices No.	V_{oc} [V]	J_{sc} [mA cm⁻²]	FF [%]	PCE [%]
1	0.837	24.3	72.8	14.8
2	0.842	23.7	72.6	14.5
3	0.840	24.6	70.8	14.7
4	0.842	24.7	70.5	14.6
5	0.842	24.2	71.3	14.6
6	0.842	24.6	71.4	14.8
7	0.839	24.7	71.4	14.8
8	0.835	24.6	71.8	14.8
9	0.836	24.6	70.6	14.5
Avg.	0.840	24.5	71.5	14.7

*** Photoactive layer parameters:**

- PBDB-T-2F : Y6 : M2 ratio (1:1.2:0.01)
- Total 16 mg mL⁻¹ in CF
- 0.5% CN
- Spin-coated at 2700 rpm and annealed at 110°C for 10 minutes

*** HTL parameters:**

- Spin-coated at 3000 rpm and annealed at 150°C for 15 minutes

*** ETL parameters:**

- Spin-coated at 3000 rpm without annealing

Table B.24 Raw data of conventional PBDB-T-2F:Y6:M2 -based OSCs (5% dopant).

Configuration : ITO PEDOT:PSS PBDB-T-2F : Y6 : M2 PDINO Al Addition : 5% M2 as dopant				
Devices No.	V_{oc} [V]	J_{sc} [mA cm ⁻²]	FF [%]	PCE [%]
1	0.838	24.4	70.9	14.5
2	0.835	24.7	70.3	14.5
3	0.834	24.9	70.3	14.6
4	0.836	24.7	70.1	14.5
5	0.835	24.1	71.9	14.5
6	0.842	24.6	70.1	14.5
7	0.840	24.8	69.8	14.5
8	0.841	24.8	70.3	14.7
9	0.840	24.7	70.5	14.6
Avg.	0.838	24.6	70.5	14.6

* Photoactive layer parameters: <ul style="list-style-type: none"> - PBDB-T-2F : Y6 : M2 ratio (1:1.2:0.05) - Total 16 mg mL⁻¹ in CF - 0.5% CN - Spin-coated at 2700 rpm and annealed at 110°C for 10 minutes 				
* HTL parameters: <ul style="list-style-type: none"> - Spin-coated at 3000 rpm and annealed at 150°C for 15 minutes 				
* ETL parameters: <ul style="list-style-type: none"> - Spin-coated at 3000 rpm without annealing 				

Table B.25 Summary of conventional PBDB-T-2F:Y6:M2 -based OSCs.

Devices	V_{oc} [V]	J_{sc} [mA cm ⁻²]	FF [%]	PCE_{max} (avg.)^a [%]
0%	0.838	25.9	75.0	16.3 (15.9)
1% dopant	0.835	24.6	71.8	14.8 (14.7)
5% dopant	0.841	24.8	70.3	14.7 (14.6)

^a Average PCE was obtained from 9 independent devices